Evaluation of the VPI & SU Fluid Film Bearing Test Rig

by

Erik Evan Swanson

Thesis submitted to the Faculty of

Virginia Polytechnic Institute and State University

in partial fulfillment of the requirements for the degree of

MASTER OF SCIENCE

in

Mechanical Engineering

APPROVED:

R.G. Kirk, Chairman

F.J. Pierce

R.H. Plaut

March, 1992
Blacksburg, Virginia

Evaluation of the VPI & SU

Fluid Film Bearing Test Rig

by

Erik Evan Swanson

Chairman: R.G. Kirk
Department of Mechanical Engineering

(ABSTRACT)

The design of advanced, state-of-the-art turbomachinery requires accurate analytical tools for predicting rotor response and evaluating stability. One of the required tools is a reliable analytical code for predicting the performance of fluid-film bearings. This work presents an initial evaluation of a test rig for verifying such codes. This presentation includes background information on the techniques and terminology of fluid-film bearing analysis and two basic approaches to experimental evaluation of fluid-film bearings. To establish one such code, NPADVT, as a useful tool for evaluating the performance of the test rig, comparisons between six published, experimental evaluations of fluid-film bearings for static characteristics and the corresponding NPADVT analysis are presented. With the code thus anchored, and its limits established, experimental data generated with the test rig are compared to appropriate analyses and the test rig shown to be essentially functional. Finally, experimental static results for a pocket bearing generated with the test rig are presented and compared with analysis.

Acknowledgements:

I would like to acknowledge the support of my parents and thank them for giving me an innate curiosity about the world that has made this thesis possible.

I would also like to thank Dr. Kirk for his support and assistance with this work, John Nicholas of Rotating Machinery Technology for supplying the test bearing, Ingersoll-Rand/Torrington for donating the test rig and NASA Marshall for granting me a Graduate Research Fellowship.

In addition, I would also like to thank the many outstanding teachers I have had the privilege of learning from throughout my formal education. Finally, I would like to thank the "working men" in the maintenance department of the Stone Container - Hopewell papermill with whom I worked as an undergraduate while in the Co-Op program. Without some of the skills they taught me, I would never have been able to complete the experimental portion of this work.

Erik Swanson

Blacksburg, Virginia

March 14, 1992

Table of Contents

Chapter 1

Introduction and Literature Review 1

1.1 Purpose and Scope of Work 1

1.2 Approaches to Fluid-Film Bearing Analysis 5

1.2.1 Fluid-Film Bearing Geometry Definitions 6

1.2.2 The Reynolds Equation 9

1.2.3 Computer Based Solutions 10

1.3 Bearing Analysis With Code NPADVT 16

1.4 Published Results for Axial-Groove Bearings 21

1.5 Published Results for Pocket Bearings 23

Chapter 2

Experimental Approach 24

2.1 Approaches to Test Rig Design 24

2.2 Floating Bearing Rigs 26

2.2.1 Advantages to Floating Bearing Paradigm 27

2.2.2 Disadvantages to the Floating Bearing Paradigm 28

2.3 Dual Rigid Bearing Mounts 31

2.4 Rigid Mount, Single Test Bearing 32

2.4.1 Advantages to Rigid Bearing Paradigm 32

2.4.2 Concerns with Rigid Bearing Paradigm 33

Chapter 3

Comparisons: NPADVT vs. Published Experimental Results 36

3.1 Overview 36

3.2 Comparison for Tonnesen/Hansen 39

3.2.1 Data 39

3.2.2 Discussion of Results 48

3.3 Comparison for Lund/Tonnesen 49

3.3.1 Data 50

3.3.2 Discussion of Results 60

3.4 Comparison for Someya #2 60

3.4.1 Data 61

3.4.2 Discussion of Results 71

3.5 Comparison for Someya #3 72

3.5.1 Data 72

3.5.2 Discussion of Results 79

3.6 Comparison for Someya #5 79

3.6.1 Data 80

3.6.2 Discussion of Results 83
3.7 Comparison for Andrisano 83
3.7.1 Data 84
3.7.2 Discussion of Results 92

Chapter 4

VPI & SU Test Rig 94
4.1 Introduction and Orientation 94
4.2 Rig History 95
4.2.1 Summary of Test Rig Capabilities 98
4.3 Detailed Description of Test Rig 99
4.3.1 Mechanical Details 99
4.3.2 Magnetic Loading System 103
4.3.3 Air Turbine Drive 106
4.3.4 Test Bearing Oil System 107
4.3.5 Other Instrumentation 108
4.4 Sensor Calibration 110
4.5 Uncertainty Analysis 115
4.5.1 Discussion of Approach Employed 115
4.5.2 Zeroth Order Error Analysis 118
4.5.3 Sensitivity Analysis 126

4.5.4 First Order Analysis 135

4.5.5 N^{th} Order Analysis 137

Chapter 5

VPI Experimental Results and Comparisons for a Two-Axial-Groove Bearing 139

5.1 Introduction 139

5.2 VPI & SU Test Bearing and Oil 140

5.3 Experimental Procedure 142

5.4 Experimental Two-Axial-Groove Data 145

5.4.1 Data 145

5.4.2 Discussion of Results 154

5.5 Comparisons Between Experimental Results 155

5.5.1 Repeated Test Comparisons 156

5.5.2 Discussion of Repeated Tests 161

5.5.3 Removal/Reinstallation Repeatability 162

5.5.4 Discussion for Removal/Reinstallation Comparison 164

5.5.5 Comparisons for Variable Feed Pressure 164

5.5.6 Discussion for Feed Pressure Comparisons 167

5.5.7 Comparisons between NPADVT and VPI Data 168

5.5.8 Discussion for Comparisons to NPADVT 186

5.6 Comments and Discussion 188

Chapter 6

VPI Results and Comparisons for Pocket Bearing 192

6.1 Introduction 192

6.2 Pocket Bearing and Oil 193

6.3 Experimental Procedure 195

6.4 Experimental Pocket Bearing Data and Comparisons 196

6.4.1 Data 196

6.4.2 Discussion of Results 200

6.4.3 Comparisons For Repeated Tests 201

6.4.4 Discussion of Repeated Tests 205

6.4.5 Comparisons Between NPADVT and VPI for Pocket Bearing 206

6.4.6 Discussion of NPADVT vs. VPI for Pocket Bearing 217

6.4.7 Comparison Between Pocket and Plain Bearing 218

6.4.8 Comments on Bearing Type Comparison 220

6.4.9 Comments and Discussion for Pocket Bearing 221

Chapter 7

Conclusions and Recommendations 223

7.1 Conclusions for NPADVT 223

7.2 Conclusions for the VPI & SU Test Rig 224

7.3 Recommendations for NPADVT 225

7.4 Recommendations for Test Rig 227

7.4.1 Thermal Growth Effects 228

7.4.2 Other Misalignment Effects 230

7.4.3 Data Acquisition 231

7.4.4 Oil System 234

7.4.5 Speed Control 235

7.4.6 Miscellaneous Instrumentation Upgrades 237

7.4.7 Rig Mechanical 238

7.4.8 Miscellaneous Recommendations 240

7.4.9 Priorities 242

References 247

Appendix A 250

Appendix B 254

B.1 Confidence Areas 254

B.2 Analysis of Variance Output 257

B.3 Sample Uncertainty Calculations 259

B.3.1Sample Calculation #1 - Bearing Centerline Estimation 259

B.3.2 Sample Calculation #2 - Estimation of Number of Samples 260

Vita 263

List of Figures

Fig. 1: Two-Axial-Groove Bearing Geometry 7

Fig. 2: Additional Geometry for Pocket Bearing 7

Fig. 3: Fluid-Film Bearing Geometric Parameter Definitions 8

Fig. 4: Fluid-Film Analysis Geometry 8

Fig. 5: Typical NPADVT Grid 19

Fig. 6: NPADVT Flowchart 20

Fig. 7: Floating Bearing/Fixed Shaft Test Rig 25

Fig. 8: Floating Shaft/Fixed Bearing Test Rig 25

Fig. 9: X-Eccentricity Ratio for Tonnesen, 6.67 Hz 42

Fig. 10: Y-Eccentricity Ratio for Tonnesen, 6.67 Hz 42

Fig. 11: X-Eccentricity Ratio for Tonnesen, 26.67 Hz 43

Fig. 12: Y-Eccentricity Ratio for Tonnesen, 26.67 Hz 43

Fig. 13: X-Eccentricity Ratio for Tonnesen, 80 Hz 44

Fig. 14: Y-Eccentricity Ratio for Tonnesen, 80 Hz 44

Fig. 15: X-Eccentricity Ratio for Tonnesen, 133.3 Hz 45

Fig. 16: Y-Eccentricity Ratio for Tonnesen, 133.3 Hz 45

Fig. 17: Percent Error for Tonnesen, 6.67 Hz 46

Fig. 18: Percent Error for Tonnesen, 26.67 Hz 46

Fig. 19: Percent Error for Tonnesen, 80 Hz 47

Fig. 20: Percent Error for Tonnesen, 133.33 Hz 47

Fig. 21: X-Eccentricity Ratio for Lund, 33.33 Hz 52

Fig. 22: Y-Eccentricity Ratio for Lund, 33.33 Hz 52

Fig. 23: X-Eccentricity Ratio for Lund, 58.33 Hz 53

Fig. 24: Y-Eccentricity Ratio for Lund, 58.33 Hz 53

Fig. 25: X-Eccentricity Ratio for Lund, 83.33 Hz 54

Fig. 26: Y-Eccentricity Ratio for Lund, 83.33 Hz 54

Fig. 27: X-eccentricity for Lund, 108.33 Hz 55

Fig. 28: Y-eccentricity for Lund, 108.33 Hz 55

Fig. 29: Percent error for Lund, 33.33 Hz (Stationary Probes) 56

Fig. 30: Percent error for Lund, 33.33 Hz (Rotating Probes) 56

Fig. 31: Percent error for Lund, 58.33 Hz (Stationary Probes) 57

Fig. 32: Percent error for Lund, 58.33 Hz (Rotating Probes) 57

Fig. 33: Percent error for Lund, 83.33 Hz (Stationary Probes) 58

Fig. 34: Percent error for Lund, 83.33 Hz (Rotating Probes) 58

Fig. 35: Percent error for Lund, 108.33 Hz (Stationary Probes) 59

Fig. 36: Percent error for Lund, 108.33 Hz (Rotating Probes) 59

Fig. 37: X-Eccentricity Ratio for Someya Test 2, 50 Hz 63

Fig. 38: Y-Eccentricity Ratio for Someya Test 2, 50 Hz 63

Fig. 39: X-Eccentricity Ratio for Someya Test 2, 100 Hz 64

Fig. 40: Y-Eccentricity Ratio for Someya Test 2, 100 Hz 64

Fig. 41: X-Eccentricity Ratio for Someya Test 2, 150 Hz 65

Fig. 42: Y-Eccentricity Ratio for Someya Test 2, 150 Hz 65

Fig. 43: X-Eccentricity Ratio for Someya Test 2, 200 Hz 66

Fig. 44: Y-Eccentricity Ratio for Someya Test 2, 200 Hz 66

Fig. 45: X-Eccentricity Ratio for Someya Test 2, 250 Hz 67

Fig. 46: Y - Eccentricity Ratio for Someya Test 2, 250 Hz 67

Fig. 47: Percent Error for Someya Test 2, 50 Hz 68

Fig. 48: Percent Error for Someya Test 2, 100 Hz 68

Fig. 49: Percent Error for Someya Test 2, 150 Hz 69

Fig. 50: Percent Error for Someya Test 2, 200 Hz 69

Fig. 51: Percent Error for Someya Test 2, 250 Hz 70

Fig. 52: X-Eccentricity Ratio for Someya Test 3, 26.7 Hz 74

Fig. 53: Y-Eccentricity Ratio for Someya Test 3, 26.7 Hz 74

Fig. 54: X-Eccentricity Ratio for Someya Test 3, 66.7 Hz 75

Fig. 55: Y-Eccentricity Ratio for Someya Test 3, 66.7 Hz 75

Fig. 56: X-Eccentricity Ratio for Someya Test 3, 100 Hz 76

Fig. 57: Y-Eccentricity Ratio for Someya Test 3, 100 Hz 76

Fig. 58: Percent Error for Someya Test 3, 26.7 Hz 77

Fig. 59: Percent Error for Someya Test 3, 66.7 Hz 77

Fig. 60: Percent Error for Someya Test 3, 100 Hz 78

Fig. 61: X-Eccentricity Ratio for Someya Test 5 81

Fig. 62: Y-Eccentricity Ratio for Someya Test 5 81

Fig. 63: Percent Error for Someya Test 5 82

Fig. 64: X-Eccentricity Ratio for Andrisano, 10 Hz 86

Fig. 65: Y-Eccentricity Ratio for Andrisano,10 Hz 86

Fig. 66: X-Eccentricity Ratio for Andrisano, 20 Hz 87

Fig. 67: Y-Eccentricity Ratio for Andrisano, 20 Hz 87

Fig. 68: X-Eccentricity Ratio for Andrisano, 30 Hz 88

Fig. 69: Y-Eccentricity Ratio for Andrisano, 30 Hz 88

Fig. 70: X-Eccentricity Ratio for Andrisano, 40 Hz 89

Fig. 71: Y-Eccentricity Ratio for Andrisano, 40 Hz 89

Fig. 72: Percent Error for Andrisano, 10 Hz 90

Fig. 73: Percent Error for Andrisano, 20 Hz 90

Fig. 74: Percent Error for Andrisano, 30 Hz 91

Fig. 75: Percent Error for Andrisano, 40 Hz 91

Fig. 76: VPI & SU Fluid Film Bearing Test Rig 96

Fig. 77: Test Rig Sketch 97

Fig. 78: Shaft/Magnet Arrangement 105

Fig. 79: Uncertainty Analysis Geometry 120

Fig. 80: Percent X-Eccentricity Ratio Change per Hz 127

Fig. 81: Percent Y-Eccentricity Ratio Change per Hz 127

Fig. 82: Absolute Shaft X Position Change (mm) per Hz 128

Fig. 83: Absolute Shaft Y Position Change (mm) per Hz 128

Fig. 84: Percent X-Eccentricity Change per Degree C 129

Fig. 85: Percent Y-Eccentricity Change per Degree C 129

Fig. 86: Absolute Shaft X Position (mm) Change per Degree C 130

Fig. 87: Absolute Shaft Y Position (mm) Change per Degree C 130

Fig. 88: Percent X-Eccentricity Ratio Change per N load 131

Fig. 89: Percent Y-Eccentricity Change per N Load 131

Fig. 90: Absolute Shaft Position (mm) Change per N Load 132

Fig. 91: Absolute Shaft Position (mm) Change per N Load 132

Fig. 92: First 16.7 Hz Test (Cd = 0.15 mm) 147

Fig. 93: First 33.3 Hz Test (Cd = 0.148 mm) 147

Fig. 94: First 58.3 Hz Test (Cd = 0.146 mm) 148

Fig. 95: First 83.3 Hz Test (Cd = 0.158) 148

Fig. 96: Second 16.7 Hz Test (Cd = 0.156 mm) 149

Fig. 97: Second 33.3 Hz Test (Cd = 0.152 mm) 149

Fig. 98: Second 58.3 Hz Test (Cd = 0.149 mm) 150

Fig. 99: Second 83.3 Hz Test (Cd = 0.148 mm) 150

Fig. 100: 33.3 Hz, 0.069 MPa Test (Cd = 0.154 mm) 151

Fig. 101: 33.33 Hz, 0.137 MPa Test (Cd = 0.154 mm) 151

Fig. 102: 33.3 Hz, 0.172 MPa Test (Cd = 0.153 mm) 152

Fig. 103: 33.33 Hz Test after removal/reinstallation (Cd = 0.149 mm) 152

Fig. 104: 83.3 Hz Test, after removal/reinstallation (initial Cd = 0.149 used) 153

Fig. 105: 16.7 Hz Repeated Tests - Actual Data 157

Fig. 106: 16.7 Hz Repeated Tests - Normalized Data 157

Fig. 107: 33.3 Hz Repeated Tests - Actual Data 158

Fig. 108: 33.3 Hz Repeated Tests - Normalized Data 158

Fig. 109: 58.3 Hz Repeated Tests - Actual Data 159

Fig. 110: 58.3 Hz Repeated Tests - Normalized Data 159

Fig. 111: 83.3 Hz Repeated Tests - Actual Data 160

Fig. 112: 83.3 Hz Repeated Tests - Normalized Data 160

Fig. 113: Comparison for Removal/Reinstallation, 33.3 Hz 163

Fig. 114: Comparison for Removal/Reinstallation, 83.3 Hz 163

Fig. 115: Comparison for Oil Feed Pressure - Actual Data 166

Fig. 116: Comparison for Oil Feed Pressure - Normalized to 0.034 MPa, 5500 N . . . 166

Fig. 117: 16.7 Hz X-Position Comparison (First Test Series) 170

Fig. 118: 16.7 Hz Y-Position Comparison (First Test Series) 170

Fig. 119: 16.7 Hz X-Position 1500 N Normalized Comparison (First Test Series) 171

Fig. 120: 16.7 Hz Y-Position 1500 N Normalized Comparison (First Test Series) 171

Fig. 121: 33.3 Hz X-Position Comparison (First Test Series) 172

Fig. 122: 33.3 Hz Y Position Comparison (First Test Series) 172

Fig. 123: 33.3 Hz X-Position 1500 N Normalized Comparison (First Test Series) 173

Fig. 124: 33.3 Hz Y-Position 1500 N Normalized Comparison (First Test Series) 173

Fig. 125: 58.3 Hz X-Position Comparison (First Test Series) 174

Fig. 126: 58.3 Hz Y-Position Comparison (First Test Series) 174

Fig. 127: 58.3 Hz X-Position, 1500 N Normalized (First Test Series) 175

Fig. 128: 58.3 Hz Y-Position, 2000 N Normalized (First Test Series) 175

Fig. 129: 83.3 Hz X-Position Comparison (First Test Series) 176

Fig. 130: 83.3 Hz Y-Position Comparison (First Test Series) 176

Fig. 131: 83.3 Hz X-Position 1500 N Normalized Comparison (First Test Series) 177

Fig. 132: 83.3 Hz Y-Position 1500 N Normalized Comparison (First Test Series) 177

Fig. 133: 16.7 Hz X-Position Comparison (Second Test Series) 178

Fig. 134: 16.7 Hz Y-Position Comparison (Second Test Series) 178

Fig. 135: 16.7 Hz X-Position 1500 N Normalized Comparison (Second Test Series) . . 179

Fig. 136: 16.7 Hz Y-Position 1500 N Normalized Comparison (Second Test Series) . . 179

Fig. 137: 33.3 Hz X-Position Comparison (Second Test Series) 180

Fig. 138: 33.3 Hz Y-Position Comparison (Second Test Series) 180

Fig. 139: 33.3 Hz X-Position 1500 N Normalized Comparison (Second Test Series) . . 181

Fig. 140: 33.3 Hz Y-Position 2000 N Normalized Comparison (Second Test Series) . . 181

Fig. 141: 58.3 Hz X-Position Comparison (Second Test Series) 182

Fig. 142: 58.3 Hz Y-Position Comparison (Second Test Series) 182

Fig. 143: 58.3 Hz - Position, 1500 N Normalized (Second Test Series) 183

Fig. 144: 58.3 Hz Y-Position, 2000 N Normalized (Second Test Series) 183

Fig. 145: 83.3 Hz X-Position Comparison (Second Test Series) 184

Fig. 146: 83.3 Hz Y-Position Comparison (Second Test Series) 184

Fig. 147: 83.3 Hz X-Position 2000 N Normalized Comparison (Second Test Series) . . 185

Fig. 148: 83.3 Hz Y-Position 2000 N Normalized Comparison (Second Test Series) . . 185

Fig. 149: First 16.7 Hz Test (Cd = 0.163 mm) 197

Fig. 150: First 33.3 Hz Test (Cd = 0.166 mm) 197

Fig. 151: First 58.3 Hz Test (Cd = 0.156 mm) 198

Fig. 152: Second 16.7 Hz Test (Cd = 0.169 mm) 198

Fig. 153: Second 33.3 Hz Test (Cd = 0.169 mm) 199

Fig. 154: Second 58.3 Hz Test (Cd = 0.166 mm) 199

Fig. 155: 16.7 Hz Repeated Tests (as Recorded) 202

Fig. 156: 16.7 Hz Repeated Tests (5500 N Normalized) 202

Fig. 157: 33.3 Hz Repeated Tests (as Recorded) 203

Fig. 158: 33.3 Hz Repeated Tests (5500 N Normalized) 203

Fig. 159: 58.3 Hz Repeated Tests (as Recorded) 204

Fig. 160: 58.3 Hz Repeated Tests (5500 N Normalized) 204

Fig. 161: 16.7 Hz Pocket X-Position Comparison (First Test Series) 207

Fig. 162: 16.7 Hz Pocket Y-Position Comparison (First Test Series) 207

Fig. 163: 16.7 Hz Pocket X-Position 1500 N Normalized Comparison (First Test Series) 208

Fig. 164: 16.7 Hz Pocket Y-Position 1500 N Normalized Comparison (First Test Series) 208

Fig. 165: 33.3 Hz Pocket X-Position Comparison (First Test Series) 209

Fig. 166: 33.3 Hz Pocket Y-Position Comparison (First Test Series) 209

Fig. 167: 33.3 Hz Pocket X-Position 1500 N Normalized Comparison (First Test Series) 210

Fig. 168: 33.3 Hz Pocket Y-Position 1500 N Normalized Comparison (First Test Series) 210

Fig. 169: 58.3 Hz Pocket X-Position Comparison (First Test Series) 211

Fig. 170: 58.3 Hz Pocket Y-Position Comparison (First Test Series) 211

Fig. 171: 58.3 Hz Pocket X-Position 1500 N Normalized Comparison (First Test Series) 212
Fig. 172: 58.3 Hz Pocket Y-Position 1500 N Normalized Comparison (First Test Series) 212
Fig. 173: 16.7 Hz Pocket X-Position Comparison (Second Test Series) 213
Fig. 174: 16.7 Hz Pocket Y-Position Comparison (Second Test Series) 213
Fig. 175: 16.7 Hz Pocket X-Position 1500 N Normalized Comparison (Second Test Series) 214
Fig. 176: 16.7 Hz Pocket Y-Position 1500 N Normalized Comparison (Second Test Series) 214
Fig. 177: 33.3 Hz Pocket X-Position Comparison (Second Test Series) 215
Fig. 178: 33.3 Hz Pocket Y-Position Comparison (Second Test Series) 215
Fig. 179: 58.3 Hz Pocket X-Position Comparison (Second Test Series) 216
Fig. 180: 58.3 Hz Pocket Y-Position Comparison (Second Test Series) 216
Fig. 181: Comparison Between Plain and Pocket Bearings, 33.3 Hz (NPADVT) 219
Fig. 182: Comparison Between Pocket and Plain Bearings, 33.3 Hz (Experimental) . . . 219
Fig. 183: Shaft Deflection Measurement Locations 252
Fig. 184: Two Standard Deviation Area 256

List of Tables

Table I - Description of Published Bearings 22

Table II - Published Bearings, Mechanical Details 37

Table III - Published Bearings, Operating Conditions 37

Table IV - Uncertainty Data for Shaft Center Position Estimation 121

Table V - Bearing Centerline Estimation Uncertainty 121

Table VI - Uncertainty Data for Load Estimation 125

Table VII - Load Estimate Uncertainty 125

Table VIII - Control Repeatability 134

Table IX - Two A.G. Control Repeatability Errors 134

Table X - Expected Y Experimental Scatter from Repeatability 136

Table XI - N^{th} Order Y Scatter and Uncertainty 138

Table XII - Immediate Rig Improvement/Study Items 244

Table XIII - 1 Year Rig Improvement/Study Items 245

Table XIV - Long Term Rig Improvement/Study Items 246

Chapter 1

Introduction and Literature Review

1.1 Purpose and Scope of Work

All rotating systems are supported on some form of bearing. With the exception of aircraft engines, most high-speed turbomachinery is supported on some form of fluid-film bearing. This machinery includes compressors, turbines, generators, pumps, and marine propulsion systems. Although a few machines use hydrostatic bearings, the bulk of these bearings are hydrodynamic. As this equipment is used at ever higher speeds and loads, the rotor dynamic analysis of the equipment becomes ever more crucial. In most cases, a linearized, steady-state analysis is employed due to the computational requirements of a complete transient analysis, which would actually

calculate all system forces and reactions at each time step and include non-linearities. Any analysis of the dynamic characteristics of a dynamic system requires some description of the support system's properties. In the field of rotor dynamics, this need usually translates to a description of the bearing system; thus, accurate, easy to apply bearing analyses are required by both the designer and the analyst. In most rotor dynamic analyses, the non-linear fluid-film bearing stiffness and damping functions are linearized by using gradients of the functions at some operating position [17], and small shaft motions are assumed. This simplified approach seems to be adequate in most cases, as evidenced by the success turbomachinery designers have had in increasing operating speeds and loads.

A portion of this work is an attempt to provide some of the missing experimental verification of one such code, NPADVT, to establish it as a useful yardstick for evaluating the VPI & SU rotor dynamics lab fluid-film bearing test rig (hereafter referred to as the "VPI rig"). This code, based on the original 1977 work of Ref. 22, was developed by Nicholas and Kirk [13, 22]. This code is a design oriented code which can be used to model a variety of hydrodynamic bearings. The experimental verification will be based on six published experimental data sets for plain journal bearings of 45 mm to 100 mm in diameter.

The primary purpose of this work is evaluation of the VPI rig's operational status. Comparisons between NPADVT analysis and VPI rig experimental data for a 101.6 mm diameter plain journal bearing will be used to demonstrate that the test rig generates valid data. After this demonstration, comparisons will be made between experimental data for the plain bearing modified by the addition of a pocket and NPADVT's analysis of this bearing. Experimental data for this type of bearing are not currently available in the published literature.

All of the comparisons will employ the static shaft locus as the dependent variable. Although a static comparison may seem limiting, it actually has considerable relevance to dynamic properties, since linearized stiffness coefficients are essentially the gradients of the static shaft locus at the operating point [17]. Thus, if the analytical static shaft locus is not similar to the experimental static shaft locus for the same bearing and conditions, the predicted dynamic coefficients are going to be different.

Another standard of comparison, proposed in Ref. 26 as the ideal method, is pressure profiles. Although there is appeal to using this approach, since it is the integrated effect of the pressure profile which controls both the static and dynamic characteristics, complete experimental pressure profiles are difficult to obtain. This

approach will not be employed in this work; the VPI rig does not have the required pressure probes and most of the published data do not include pressure profiles.

The remainder of Chapter 1 and the entirety of Chapter 2 present a considerable amount of essential background information for the reader unfamiliar with fluid-film bearing analysis and testing. This background information includes a brief history of fluid-film bearing analysis, a general discussion of the approach used in NPADVT, and a description of several approaches to fluid-film bearing test rig design. It is hoped that this background information will give the reader some appreciation for the analytical approach and its limitations, as well as an understanding of the two basic experimental approaches used in fluid-film bearing testing. Following this background information, Chapter 3 will present six comparisons between published works and the corresponding NPADVT analyses. Following this anchoring of NPADVT to published data, the VPI rig will be described, instrumentation calibration issues will be discussed, and the results of an uncertainty analysis will be presented in Chapter 4. In Chapter 5, the VPI rig results for a 101.6 mm plain, two-axial-groove bearing are presented and examined for internal consistency and for appropriate agreement with NPADVT. This discussion will demonstrate that the VPI rig is generally producing reasonable data with the exception of a non-repeatable displacement zero. Chapter 6 will present experimental results for a pocket bearing

and comparisons to NPADVT. Finally, Chapter 7 will discuss some conclusions about both NPADVT and the VPI rig. A number of recommendations for work on both the VPI rig and NPADVT will also be presented.

1.2 Approaches to Fluid-Film Bearing Analysis

One approach to developing fluid-film bearing coefficients is to run a set of experiments and measure the coefficients. Although such an approach could be warranted in a few cases, in general it is far too time consuming, expensive and difficult to test every variation of every bearing design or modification. To eliminate this need, there are several analytical approaches to fluid-film bearing analysis available. The first real analytical treatment of hydrodynamic fluid-film bearings is Osbourne Reynolds' "On the Theory of Lubrication and its Application to Mr. Beauchamp Tower's Experiments ..." [28]. This work, published in 1886, introduces the so called "Reynolds Equation", which forms the basis for most fluid-film bearing analysis. This partial differential equation cannot be solved in closed form unless various simplifying assumptions are made. These simplified versions of the equation provided the analytical basis for fluid-film bearing analysis until the advent of the digital computer. With a computer, several numerical techniques, most notably finite difference methods and finite element methods, allow more accurate solutions. Currently, the state-of-the-art bearing analyses generally employ computer codes

which implement a finite element based solution to the generalized Reynolds equation and some auxiliary assumptions or equations (i.e., a form of the energy equation and turbulence corrections). While these codes seem to give fairly accurate results (i.e., the results are not so grossly inaccurate that they do not solve real world problems [23]), they do not always agree well with experimental results. Also, experimental results are not available in the open literature for some bearing geometries (pocket bearings, for example). Although NPADVT is in use at several locations, thorough experimental verification of the code is lacking. Thus to use it as a yardstick for evaluation of the VPI rig requires that the missing experimental verification be supplied. The remainder of this section will introduce the nomenclature of bearing analysis and discuss the various solution techniques.

1.2.1 Fluid-Film Bearing Geometry Definitions

Figure 1 shows the typical geometry of a two-axial-groove bearing. Figure 2 shows the geometry of a typical pocket bearing modification to the bearing of Fig. 1. Figure 3 shows the location of several other geometric parameters used to describe the shaft location within a bearing. Figure 4, which is taken from Ref. 1, shows the geometry used in the analytical treatments described below.

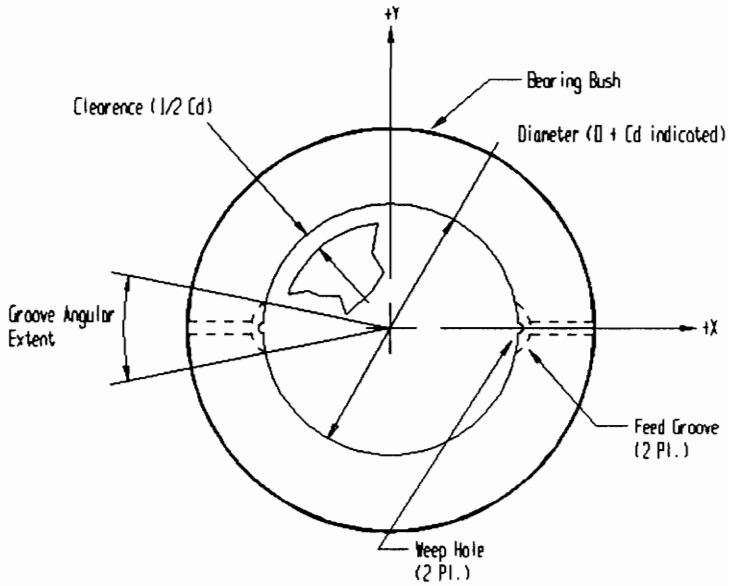

Fig. 1: Two-Axial-Groove Bearing Geometry

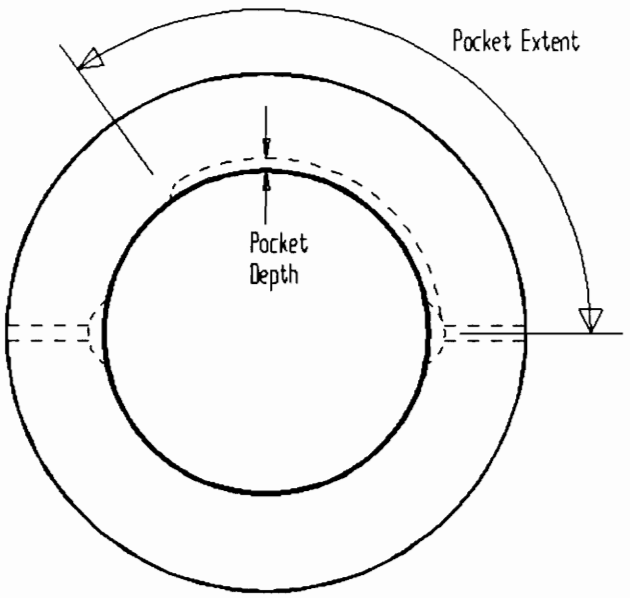

Fig. 2: Additional Geometry for Pocket Bearing

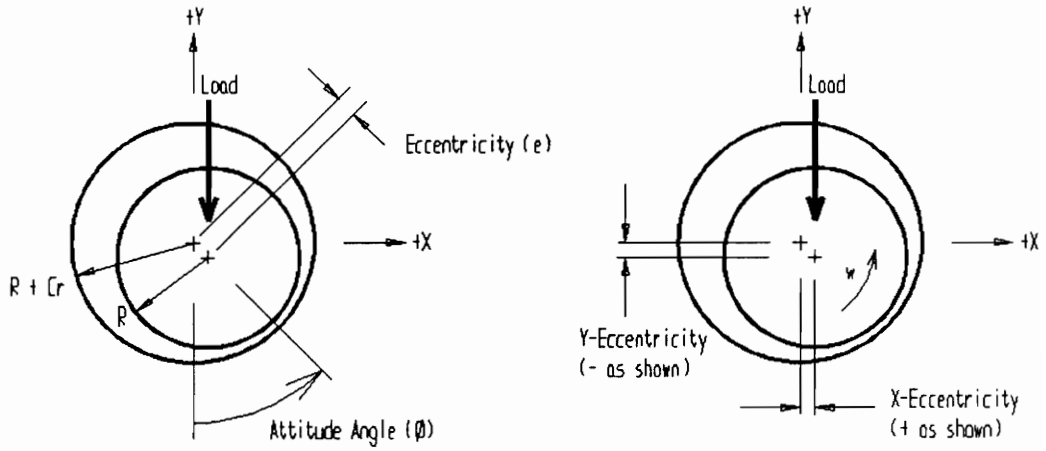

Fig. 3: Fluid-Film Bearing Geometric Parameter Definitions

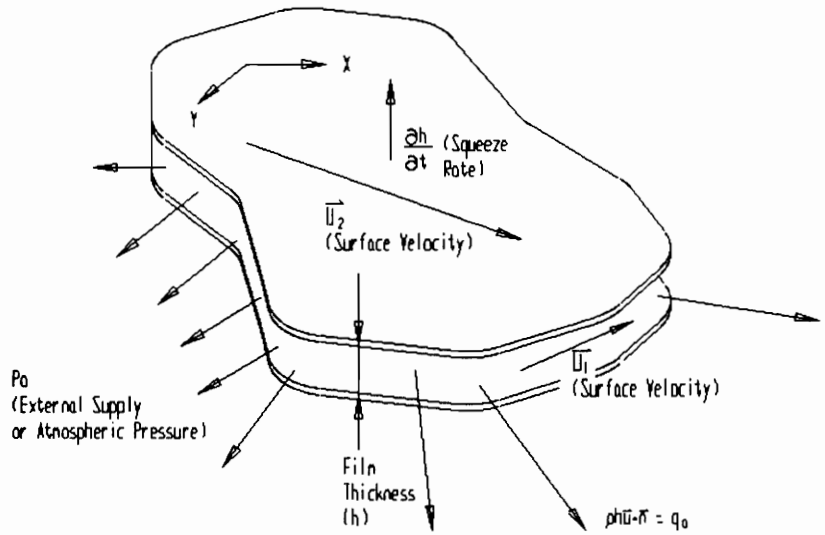

Fig. 4: Fluid-Film Analysis Geometry

1.2.2 The Reynolds Equation

The analytical approaches employed in fluid-film bearing analyses are generally based on one of the manifestations of the so called "Reynolds Equation," originally developed by Osbourne Reynolds in 1886 [28]. As developed by Reynolds, this equation does not allow for compressible lubricants. However, the form of the equation used as the starting point for most analyses, the generalized Reynolds equation, relaxes the compressibility restriction. The generalized Reynolds equation can be derived from the Navier-Stokes equations [24]. The generalized Reynolds equation may be written as follows (using the geometry definitions of Fig. 4):

$$\frac{\partial}{\partial x}\left(\frac{\rho h^3}{\mu}\frac{\partial p}{\partial x}\right) + \frac{\partial}{\partial z}\left(\frac{\rho h^3}{\mu}\frac{\partial p}{\partial z}\right) = 6U\frac{\partial(\rho h)}{\partial x} + 12\rho V_0 \qquad (1)$$

Equation (1) assumes that:

1. The film height h, is small compared to the width and length,
2. There is no variation of pressure across the film,
3. The flow is laminar,
4. There are no external forces,
5. Inertia forces are small compared to shear forces,

6. No slip at the boundaries,

7. Shear along the film in the x direction and squeeze in the y direction constitute the dominant velocity gradients.

In early analyses, several approximate solutions to this equation were utilized, allowing designers to make rough predictions about the performance and characteristics of bearings. These approximations include the "Long Bearing Solution" (by Sommerfeld), which assumes an infinitely long bearing, and the "Short Bearing Solution" (by Ocvirk), which assumes an infinitely short bearing. Other closed form approaches have been advanced by Pinkus, Sternlicht, Ocvirk, Kirk and Gunter.

1.2.3 Computer Based Solutions

With the digital computer, it has become feasible to generate more exact solutions to the Reynolds equation using any of several numerical techniques. The two most common approaches are the finite difference approach [19, 24, 29] (historically, the first approach to be employed) and the finite element approach [for example, Refs. 1, 2, 4, 5, 22, and 29]. The finite difference is perhaps more intuitively obvious, as it

makes direct use of some form of the Reynolds equation. This approach, however, is not employed in NPADVT, and will not be discussed.

The finite element approach offers the advantages that it directly handles the irregular geometries found in many bearing designs as well as mixed flow and pressure boundary conditions such as would be found in a hydrostatic bearing [2, 4]. The ability to easily handle varied geometry is extremely important for bearing analyses, since the most interesting bearings from an applications standpoint are bearings with features such as steps, offsets, and separate partial arc pads, all of which may or may not be symmetric with regards to bearing centerlines (both axial and radial), and may not be concentric with the shaft. Bearings may also exhibit axial misalignment. A good, general purpose program must be capable of handling a number of these cases. It has also been suggested that the finite element approach may be more accurate than the finite difference approach for the same amount of computational effort [1, 22].

The analytical approach embodied in NPADVT is described in Ref. 1, which is in large part based on the work of Ref. 4. This finite element approach begins with the form of the generalized Reynolds equation in three dimensions (from Ref. 4) shown in Eq. (2):

$$\nabla \cdot \left(\frac{\rho h^3}{12\mu} \nabla p \right) = \nabla \cdot \left(\rho h \overline{\mathbf{U}} + \frac{\rho^2 h^3}{12\mu} \overline{\mathbf{F}} \right) + \frac{\partial}{\partial t}(\rho h) + \rho \upsilon \tag{2}$$

The solution to Eq. (2) can be shown through variational calculus to be equivalent to a minimization of an equivalent functional (with geometry definitions as in Fig. 4), shown in Eq. (3) [1]:

$$J(P) = \iint_A \left\{ \frac{\rho h^3}{24\mu} \left[\left(\frac{\partial P}{\partial x} \right)^2 + \left(\frac{\partial P}{\partial y} \right)^2 \right] - \rho h \left[U_x \frac{\partial P}{\partial x} + U_y \frac{\partial P}{\partial y} \right] + \frac{\partial}{\partial t}(\rho h) P \right\} dA + \int_{C_q} \left[(q_x n_x + q_y n_y) P \right] dC \tag{3}$$

To perform this analysis, the bearing surface is divided into two-dimensional, three node, triangular elements by first breaking the surface into quadrilaterals, then into triangles by adding a diagonal which is approximately aligned with the expected pressure gradient (this alignment maximizes accuracy [1, 22]). A typical grid for half of a two-axial-groove bearing, and the grid for a pocket bearing are shown in [figure ??]. NPADVT performs this division and computes element thicknesses automatically for each geometry the code can handle. Within each element, viscosity, lubricant film thickness, and bounding surface velocities are assumed to be constant and the boundary flow is assumed to be uniform. The film pressure is assumed to be a function of only the nodal pressures and linear interpolation functions. A pressure or

flow condition is then specified for each element boundary (c_q is the boundary with a specified mass rate of flow). The set of element functionals is then minimized by solving the system of equations resulting from differentiating with respect to the unknown nodal pressures. This technique results in the global fluidity matrices introduced in Ref. 4, shown in the flow balance given below (note that each term is actually a matrix or a vector):

Flow =	Pressure Effect	x Pressure
	+ Shear Effect	x Surface Velocity
	+ Body Force Effect	x Body Forces
	+ Expansion Effect	x Density Change
	+ Squeeze Effect	x Film Thickness Change
	+ Diffusion Effect	x Diffusion Velocity

Given sufficient boundary conditions, this set of equations results in a tridiagonal system that can be readily solved to yield the unknown pressures and flows. Not all of the effects given above are necessarily present in a given application. NPADVT, for example, has no diffusion, density change, or body force effects. Other equations or assumptions must be added to this formulation to account for the fact that viscosity can vary dramatically with temperature and to correct for turbulence. Auxiliary

equations may also be added to account for factors such as mechanical and/ or thermal deformations of the bearing.

One approach to the viscosity-temperature effect is to ignore this variation and simply assume a constant viscosity [6]. This approach is not very interesting, other than as a starting place for a more sophisticated analysis. The opposite extreme, the so called "thermo-hydrodynamic" (THD) approach, can take into account the full three-dimensional variation of temperature within the lubricant film, the shaft, the bearing, and the bearing housing. This approach is also not extremely useful to the designer or analyst. This method requires a more sophisticated, and hence more difficult to solve, mathematical description of the lubricant film, as well as energy equations and heat transfer equations, all of which are coupled. Closely related is the "elasto-hydrodynamic" (EHD) approach, wherein an attempt is also made to fully account for the mechanical deformation of the components due to applied loads and thermal effects. The problem with these approaches is that they require an immense amount of computation, which tends to place these codes beyond the capabilities of desktop PC's for everyday design and analysis purposes, especially if there is an attempt to do justice to turbulence effects. These codes also require a great deal more information from the user, such as material properties as well as thermal and mechanical boundary conditions, which may not be readily available. Perhaps most

importantly, the uncertainty in some of these properties and boundary conditions is likely to cancel out any improvements in the solution accuracy. Although several investigators have applied THD and EHD analyses to hydrodynamic bearings, the difficulties mentioned tend to make these approaches (especially in their complete form) primarily of research interest only. It will be suggested, however, that an attempt to include a simple description of localized, thermally induced mechanical deformation might be important.

The most productive approaches to bearing analysis thus fall between these two extremes. The basic finite element solution to the Reynolds equation is employed, some form of an approximate energy equation is used to obtain the temperature effect on viscosity, some simple turbulence correction is included, and there may be some attempt to include the gross effects of mechanical deformation (this is especially important in the analysis of tilting pad bearings, where the pads which support the lubricant films generally undergo significant mechanical deformation). This is the approach employed in NPADVT.

1.3 Bearing Analysis With Code NPADVT

NPADVT is a simple example of a finite element based, hydrodynamic, fluid-film bearing analysis code. This code is based on the work of Ref. 22, modified to include global temperature-viscosity effects and a greater variety of geometries. This code is representative of the bearing analysis codes in use at many turbomachinery manufacturers. This code directly analyzes (see Ref. 13 for a description of the geometry for each bearing type):

1. Plain Axial-Groove Bearings
2. Multi-Pocket Taper Pocket Bearings
3. Multi-Pocket Step Pocket Bearings
4. Pressure Dam Bearings
5. Anti-rotation Bearings
6. Double Pocket Bearings
7. Taper Land Bearings.

The code is also able to account for a fixed, user defined deformation to the housing due to mechanical compression during installation. This application flexibility is achieved through the use of a finite element approach [22].

NPADVT begins its analysis by obtaining the bearing and operating conditions from a data file. An approximate thermal solution, using basic journal bearing theory, generates an initial guess for the fluid viscosity to use in the iterative finite element analysis. The bearing geometry data is then used to establish the finite element grid. The grid consists of 50 circumferential nodes and 5 axial nodes per bearing pad (a 2-axial-groove bearing has 2 pads). As shown in Fig. 5, this grid represents half of a symmetric bearing, effectively doubling the number of elements used to model the bearing. The grid shown in this figure represents a typical grid for a plain axial-groove bearing. In the case of a pocket bearing, the nodes closest to the pocket boundaries are aligned with the boundaries. Convergence studies in Ref. 22 suggest that this grid should be accurate to within less than 5% error. After establishing the mesh, the finite element subroutine iteratively generates an updated shaft position and computes the power loss caused by fluid shear using the finite element approach outlined above. The program then computes a revised temperature rise through the bearing by performing a global energy balance, assuming that all energy dissipated in the bearing must be removed by the lubricant, thereby raising its temperature. This revised average temperature is used for the next iteration. Generally only three or four temperature iterations are required. To generate linearized dynamic stiffness and damping coefficients (most rotor dynamic analyses assume a linear system perturbed about some operating point), the program gives the shaft small perturbations in

displacement and velocity about the operating position. See Fig. 6 for a flowchart of this procedure.

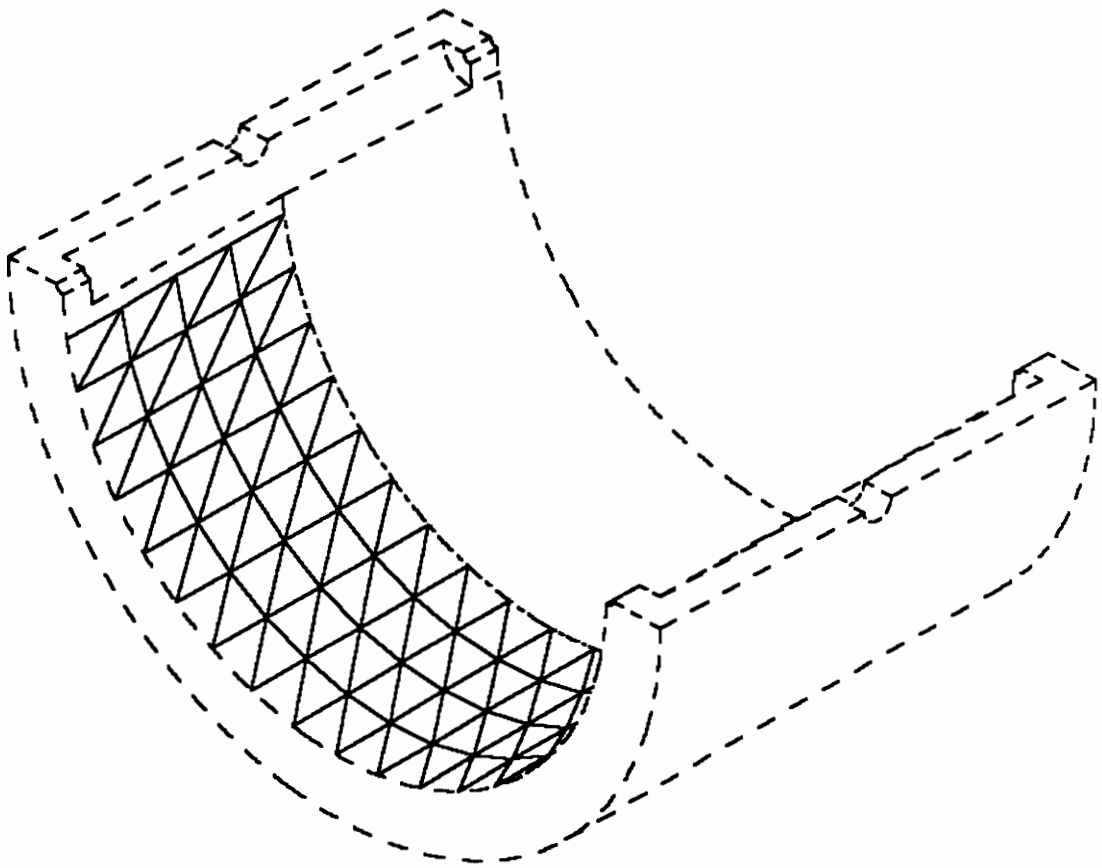

Fig. 5: Typical NPADVT Grid

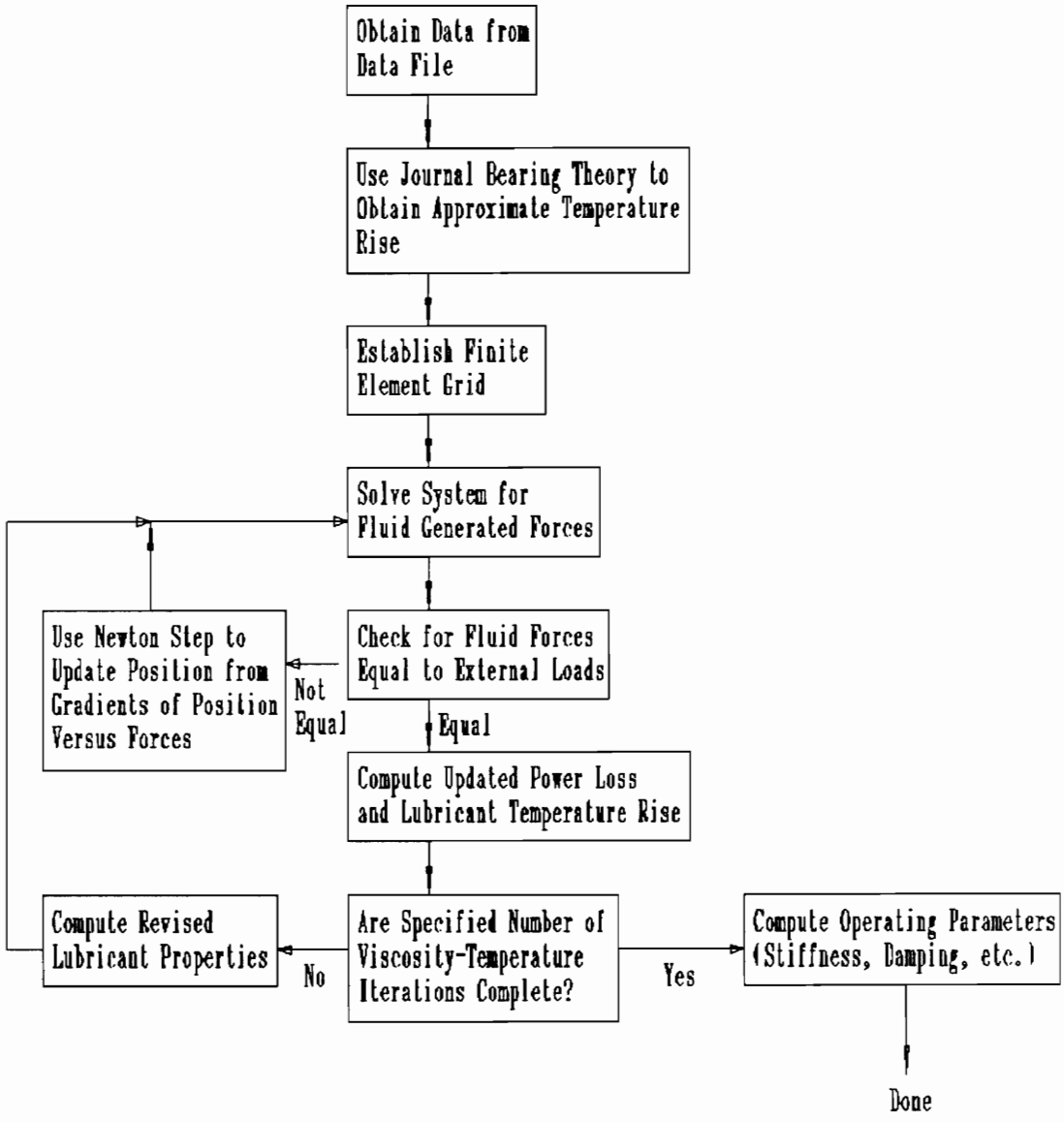

Fig. 6: NPADVT Flowchart

1.4 Published Results for Axial-Groove Bearings

Although the body of published works on the subject of journal bearings is quite large, there is relatively little good published experimental data for the static characteristics of axial-groove bearings to use in verifying NPADVT. Of the sources surveyed, only six data sets contained both a good description of the bearing geometry, lubricant properties and the shaft center locus as a function of one or more of load, speed and lubricant viscosity. Of these data sets, three are from Ref. 29, and the other three are from journal articles [3, 18, 30]. The bearings used in these works are described in Table I.

The VPI test bearing is a two-axial-groove (2 A.G.) bearing, 101.6 mm in diameter, with a length to diameter ratio of 0.5625, and a nominal (diametral) clearance to diameter (C_d/D) ratio of 0.00125. Thus, several of the published bearings are very similar to the VPI test bearing. Further descriptions of the published speeds, loads, etc. will be saved for Chapter 5, where comparisons between NPADVT and the published data will be made.

Table I - Description of Published Bearings

Author	Diameter(mm)	L/D	C/R	Type
Lund/ Tonnesen	100	0.55	0.00137	2 A.G.
Tonnesen/ Hansen	100	0.55	0.00150	2 A.G.
Andrisano	45	1.0	0.00133	1 A.G.
Someya #2	100	1.0	0.00210	2 A.G.
Someya #3	100	0.5	0.00280	2 A.G.
Someya #5	50	0.5	0.00132	2 A.G.

Note: The first two data sets are from the same test rig, all others are from different test rigs.

1.5 Published Results for Pocket Bearings

In the sources examined, no experimental results for the shaft locus of a pocket bearing were located. Thus, the data generated in this work will be new, previously unavailable data.

Chapter 2

Experimental Approach

2.1 Approaches to Test Rig Design

Before proceeding to the evaluation of NPADVT and the VPI rig, it is beneficial to examine the basic approaches used for fluid-film bearing test rig design. There are essentially two approaches to the design of test rigs for fluid-film bearings: 1) floating bearing and 2) fixed bearing. Fig. 7 is a sketch of a rig designed under the floating bearing paradigm. Fig. 8 is a sketch of a rig designed under the fixed bearing paradigm.

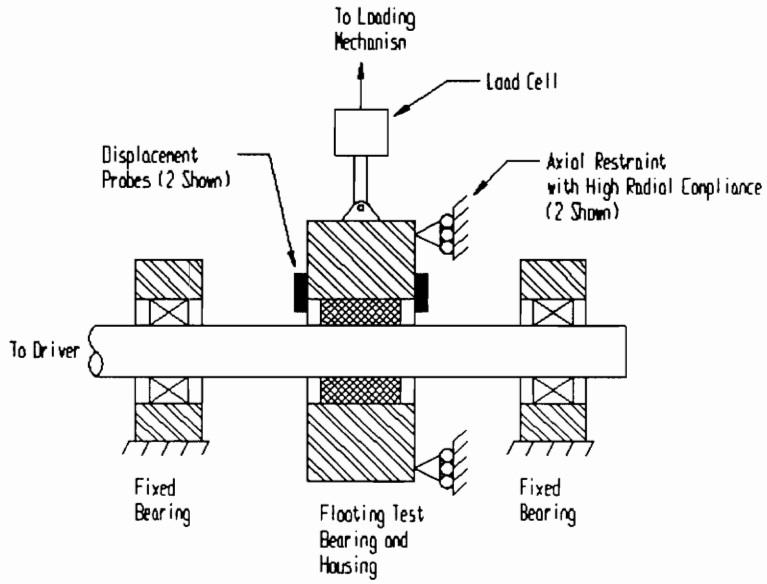

Fig. 7: Floating Bearing/Fixed Shaft Test Rig

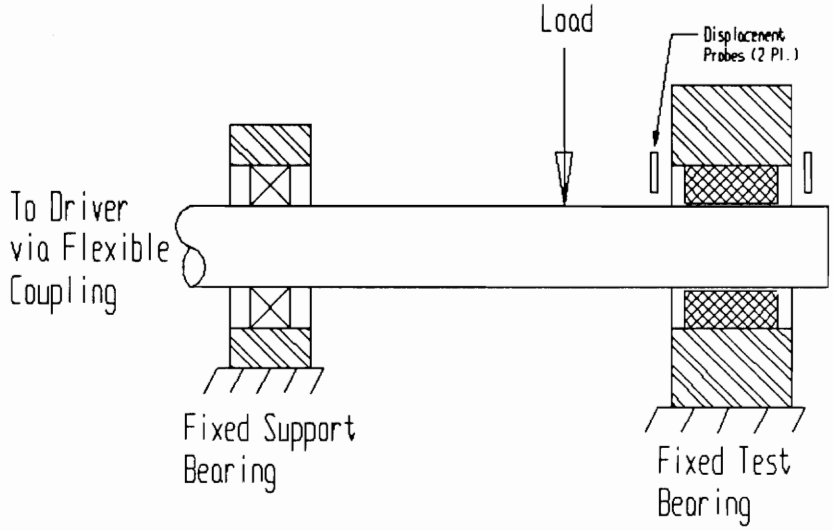

Fig. 8: Floating Shaft/Fixed Bearing Test Rig

2.2 Floating Bearing Rigs

The approach to fluid-film bearing test rig design most prevalent in the literature over the last twenty years is the floating bearing/rigid shaft approach [3, 6, 9, 10, 12, 18, 26, 29 and 30]. This design paradigm is essentially an inversion of the usual rotor-bearing system geometry; the shaft is supported by two anti-friction or hydrostatic bearings (occasionally, but much less commonly, support is provided by two fluid-film bearings - usually tilting pad bearings smaller than the test bearing). The test bearing and its housing float on the shaft between the two support bearings (in one case, the test bearing was instead cantilevered off the end of the shaft [9]). Some form of axial restraint with low radial stiffness and damping is employed to locate the bearing axially and encourage angular alignment with the shaft. Loads are applied to the test bearing housing through load cells. The relative response between the housing and shaft is measured with non-contact displacement probes. For static shaft locus as a function of any static variable such as speed, load, viscosity, inlet geometry, etc., these measurements are sufficient. For dynamic loading, hydraulic, pneumatic or electromagnetic shakers, either in line with the main loading device or separate, and load cells are added. Accelerometers are also added to the housing in an attempt to be able to subtract out the effects of the mass of the bearing housing and test bearing.

2.2.1 Advantages to Floating Bearing Paradigm

The biggest advantage of the floating bearing/rigid test bearing approach is the relative ease with which the non-rotating bearing can be loaded. A common means of obtaining the load is a combination of deadweight and air bellows [10, 12, 18, 26, 29, and 30]. Assuming the bellows is properly designed and constructed, this approach would seem to have the advantages that off axis loading should be minimized and small dynamic variations in housing position are readily accommodated. The ability to accommodate slight variations in shaft position with constant load is important for reducing problems with mechanical run-out or studying instabilities such as whirl. As another approach, in Ref. 9, Ferron employed a horizontal hydrostatic pad to reduce off axis loading, and vertical, pneumatic loading .

Another potential advantage to loading a floating bearing against a rigid shaft is pointed out by Hinton in Ref. 12. In this article, he suggests that if the loading mechanism is rigid, operation is possible even under conditions of speed and load where the bearing is unstable. In the floating bearing, rigid shaft approach, large excursions which would be damaging and unsafe with a conventional rotor-bearing system geometry are eliminated by fixing the bearing in place. Such a loading system forces the bearing to a given eccentricity and attitude angle and holds it there. This

feature would allow studying bearings over a wider range of operating conditions, as well as evaluation of non-load supporting elements such as seals.

There are several other possible advantages to following the floating bearing design paradigm. For example, such a rig has the ability to test non-load supporting rotor system elements such as seals and dampers. Another possible advantage is that with the fixed shaft, slip-rings for on-shaft instrumentation can be readily accommodated.

2.2.2 Disadvantages to the Floating Bearing Paradigm

Although the floating bearing paradigm offers some advantages, there are several disadvantages to such a rig. Perhaps the most apparent is the fact that the floating test bearing paradigm does not in fact model the actual system geometry. As a result, it is not inconceivable that effects which would occur in service might not be seen, or might be misinterpreted due to the inversion of the system geometry. One example of such a possibility is bearing stability. If the loading system and housing mounting system do not exhibit sufficient radial compliance, a bearing which would become unstable in actual applications could appear to be stable at the same operating conditions due to the additional stiffness and damping from the housing support

system. Other similar discrepancies between actual application and results from a floating bearing test rig could be readily imagined.

The floating bearing is also a more complex dynamic system than a system with rigid bearings and a floating shaft. Not only are there the flexible shaft effects to consider, but there are also three bearings and support effects which could be significant (again, depending on the loading and mounting systems' radial compliances). Some of these effects, especially the support damping, may be difficult to quantify. Ideally, most of these effects are eliminated from measurements by the fact that the test bearing is mounted on load cells, which allows loads on the bearing to be directly measured, thus decoupling it from the rotor. However, one factor which may be very difficult to isolate in dynamic testing is the inertia of the floating system. This inertia manifests itself as a variable bias error between the measurements of the applied load, as measured by load cells in the loading system, and the load actually applied between the bearing and the shaft. The method generally employed to try to separate the inertia effects from load applied between the bearing surface and the shaft is based on taking acceleration data for the bearing housing simultaneously with the measurements of loading force. This data, assuming the mass of the floating system can be established, allows the Newtonian relationship force=mass x acceleration to be used to eliminate the inertial component from the measured loading. Although high quality

accelerometers may be employed on the housing to minimize the errors in acceleration measurement, the mass of the floating system is difficult to establish. The housing and bearing can be weighed quite accurately, but it is difficult to specify the amount of oil present in the housing during operation. One possible solution might be to design the loading system such that the load cells in this system could measure the bearing/housing/oil tare weight for static conditions. Although this approach could measure the weight of the oil under static conditions, in operation the amount of oil present may be different. To make matters even worse, this oil is itself moving. There is also some evidence to suggest that the inertial effects due to the oil may not be limited to the addition of mass. Reference 27 discusses some theoretical results for a conventional fixed bearing/floating shaft geometry, suggesting that the effects of oil inertia could increase the effective shaft mass by as much as six to ten times, especially with short and/or light shafts. Although this research was aimed primarily at a fixed bearing/floating shaft geometry, it does suggest that subtracting out all inertia effects could be extremely difficult. The problems of separating the shaft-bearing effects from all other effects would seem to make dynamic measurements with this type of test rig more difficult than at first appears.

There are also some points of concern even with regards to static measurements. One of these is the fact that there are several loads on the bearing housing which are not

measured. These loads include the oil feed and drain piping, as well as instrumentation cables and the bearing axial and angular positioning mechanisms. Considerable care would be required to insure that these secondary load paths do not affect the measured load. Calibration would not seem to provide the whole answer, since the whole housing moves around to some degree in operation, which might change the calibrated bias errors. Finally, there is also the possibility of shaft bending and misalignment effects causing changes in expected bearing geometry and thus generating errors in the shaft position measurement.

2.3 Dual Rigid Bearing Mounts

Another approach to bearing response testing is to use two identical, rigidly mounted test bearings, loaded by an auxiliary bearing and unbalance weights [8, 11]. This approach is the only direct method (i.e., using only unbalance excitation) to obtain enough information to directly evaluate four stiffness and four damping coefficients for a bearing unless assumptions of symmetry are introduced [21]. This approach, however, ignores the possibility of added mass coefficients. It is also difficult to obtain two identical bearings. Similar test rigs are employed in studies focusing on instability and flexible shaft effects, such as in Ref. 15. In these studies, the system operates with gravity and unbalance loading only. The dual bearing test rig design

paradigm is not often employed for the type of static testing which is the focus of this work, and will not be discussed further.

2.4 Rigid Mount, Single Test Bearing

The final bearing test rig design paradigm to examine is the (single) rigidly mounted test bearing, floating shaft approach. A schematic of such a rig is shown in Fig. 8. This design paradigm is the approach used for the VPI rig. With this approach, the shaft is supported only by the test bearing and a second non-test bearing, and loaded directly [16, 21, and 31]. A small hydro-static or anti-friction bearing is usually employed as the shaft support bearing. The test and support bearing centerlines are located as far apart as practical and the loading system is generally between the bearings, as close to the test bearing as possible.

2.4.1 Advantages to Rigid Bearing Paradigm

This design paradigm has several advantages over the floating bearing paradigm. Foremost is the fact that it closely resembles actual application geometry, thus minimizing the questions of modeling accuracy. With this approach, it is also possible to make the mounting system stiff enough for shaft effects to dominate over

support and bearing housing effects, assuming the rig is securely mounted. The concerns of alternate loading paths bypassing the load measurement device can also be avoided. Even in the case that the bearing housing is mounted on load cells, the motion across feedlines, etc. is negligible, if the load cells are extremely stiff, and any loading path from cables, feedlines, etc. can be calibrated out.

2.4.2 Concerns with Rigid Bearing Paradigm

The biggest problem with the rigid bearing/floating shaft paradigm is applying a load to the bearing. Since the bearing is fixed, the load must be applied to the shaft, which in turn then loads the bearing. Gravity loads (i.e., heavy rotors), and unbalance loading are not very flexible, the rig must be stopped in order to change load, and the load is either static or shaft synchronous. With a single test bearing, excitation with shaft synchronous loading (i.e., unbalance) does not give enough information to evaluate all eight dynamic bearing coefficients. Even with static testing, it is not very convenient to be required to stop the rig every time the load is to be changed. There would also be the likelihood that the rotor would require balancing every time weights are added. One early solution was the use of an auxiliary bearing (hydrostatic or anti-friction) to apply the desired load. The rig of Ref. 16, for example, makes use of an anti-friction bearing to apply a static load and

a non-shaft synchronous alternating load. The alternating load is reported not to have worked very well. Even assuming this approach had been successful, the addition of a third bearing to the system makes the system dynamics rather complex. This approach would also require that the test bearing be mounted on load cells. The VPI rig (to be described later), and the rig of Ref. 21 both use a non-contact magnetic loading device which eliminates many of the complications of mechanically coupling the load to the shaft.

A related problem is that of the support bearing characteristics. For the data generated by such a test rig to have meaning, either it must be possible to account for the support bearing effects or the test bearing must be mounted on load cells. Also, as mentioned above, if the housing and rig are not securely mounted to a massive foundation, the rigid bearing assumption is violated. This effect is not as great a problem if the applied load is measured at the test bearing; however, a massive foundation is desirable from the viewpoint of reducing inertia effects.

With this design paradigm, differential thermal growth is perhaps a greater concern than with a floating bearing test rig, but it should not be too difficult to eliminate or allow for this effect. Alignment is also more critical with this test approach, but is perhaps easier to control. Shaft bending must also be allowed for through some

combination of measurement and analysis. This bearing test rig design does not allow as great a range of operating condition as a floating bearing approach, as operation of bearings in an unstable region is highly undesirable, both from the standpoints of damage to the rig and of safety. This fact is not necessarily a great problem, as most of the useful data on a bearing are recorded in stable regions. This design also does not generally have the flexibility to test non-load carrying rotor system elements such as seals and dampers. With a magnetic loading system though, it may be possible to operate the magnets as a magnetic bearing in addition to a loading device, eliminating both of these weaknesses. Reference 21 contains a brief discussion of this possibility. Finally, depending on bearing clearances, it may be difficult to reliably use slip rings for on-shaft instrumentation, such as pressure probes, due to the range of possible shaft motion, unless the shaft is bored through to the support bearing end.

Chapter 3

Comparisons: NPADVT vs. Published Experimental Results

3.1 Overview

To evaluate NPADVT for use as a yardstick for evaluating the VPI rig, the program's analysis results will be compared to six published experimental data sets in this chapter. The published results consist of two studies performed on a test rig located at the Technical University of Denmark (Ref. 18, by Lund and Tonnesen in 1984, and Ref. 30, by Tonnesen and Hansen in 1981), a study performed at the University of Bologna in Italy (Ref. 3 by A.O. Andrisano in 1988), and three data sets from test rigs located at various facilities in Japan (Ref 29, published in 1988). The bearings involved in these studies are shown in Table II. The experimental conditions for each of these studies are presented in Table III.

Table II - Published Bearings, Mechanical Details

Author	Diameter(mm)	L/D ratio	C_d/D ratio	Material	Type
Lund/Tonnesen	100	0.55	0.00137	*	2-Axial-Groove
Tonnesen/Hansen	100	0.55	0.00150	Bronze, SAE64	2-Axial-Groove
Someya #2	100	1.0	0.00210	ASTM B23/SS41	2-Axial-Groove
Someya #3	100	0.5	0.00280	ASTM B23/SS41	2-Axial-Groove
Someya #5	50	0.5	0.00132	ASTM B23/SS41	2-Axial-Groove
Andrisano	45	1.0	0.00133	Bronze	1-Axial-Groove

notes: All except the Andrisano bearing are horizontally fed, the Andrisano bearing is vertically fed.

ASTM B23 is a babbitt alloy

* It is not clear if this bearing is steel or bronze

Table III - Published Bearings, Operating Conditions

Author	Sommerfeld Range (NPADVT)	Load Range (N)	Speed Range (Hz)	Oil Density (kg/m^3)	Kinematic Viscosity @ 40 deg (m^2/Sec)
Lund/ Tonnesen	0.1376 - 0.8658	2600 - 9600	33.3 - 108.3	850	32.3×10^{-6}
Tonnesen/ Hansen	0.0309 - 12.63	200 - 9000	6.67 - 133.3	858	15.0×10^{-6}
Someya #2	0.0393 - 0.78	4740 - 48000	50 - 250	865	31.6×10^{-6}
Someya #3	0.0540 - 2.21	367 - 4500	26.67 - 100	862	31.6×10^{-6}
Someya #5	0.1251 - 0.8905	485 - 1600	25 - 83.6	871	22.2×10^{-6}
Andrisano	0.0416 - 0.5371	660 - 3000	10 - 40	770	52.6×10^{-6}

Note: Sommerfeld numbers are those generated in the NPADVT analysis

Comparisons: NPADVT vs. Published Experimental Results

All five bearings were modeled as best as possible with NPADVT. Full geometric data, including feed groove extent were available only for the Lund/Tonnesen, Tonnesen/Hansen and Someya #3 test bearings. In the remaining cases, the angular extent of the feed groove was assumed to be 10 degrees (15 degrees for Andrisano), the weep hole was assumed to be very small, and the oil inlet hole diameter was assumed to be on the order of the feed groove width (for Someya test #3, the weep hole diameter and feed diameter were specified). In all cases, the bearing diameter, ratio of length to diameter, clearance ratio, oil pressure, approximate oil inlet temperature, and oil properties were available. Generally four viscosity-temperature iterations were employed with NPADVT (more iterations sometimes diverged, possibly indicating a numerical instability). No real attempt was made to match NPADVT oil outlet temperatures to the published results for two reasons. The first reason is that NPADVT ignores heat loss other than through the rise in oil temperature, a thermal boundary condition that does not match well to the experimental boundary conditions. The second is the discussion in Ref. 18, which suggests that exact thermal boundary conditions are less important to the accuracy of the solution than modelling the fluid mechanics precisely (NPADVT, for example, ignores some cavitation effects).

3.2 Comparison for Tonnesen/Hansen

The oldest data set for the static characteristics of a two-axial-groove bearing to be used in this work is Ref. 30, a 1981 Journal of Lubrication Technology paper by Tonnesen and Hansen of the Technical University of Denmark, Department of Machine Elements. While this paper is primarily oriented towards thermal effects in the oil film, the static shaft locus as a function of load and speed is reported. Sufficient data are also presented to allow the bearing and lubricant conditions to be modeled (previous works reviewed did not include sufficient information for modeling purposes). The test rig employs a floating bearing/rigid shaft approach, and uses a combination of dead weight and pneumatic loading. The displacement data were recorded with both stationary and shaft-mounted rotating probes, which were found to be in close agreement (within several percent) when corrections were made for shaft deflection; thus the displacement data should be reliable.

3.2.1 Data

The data used for comparison purposes is that of Tonnesen's Fig. 4B. This figure plots the shaft locus as a function of speed and load for an oil with a viscosity of 12.9 mPa•s at 40 degrees. The temperature-viscosity relationship for this oil is assumed to

be the same as for an ISO 15 oil from Ref. 3 (which has the correct viscosity at 40 degrees). This assumption is made since Tonnesen only included the 40 degree viscosity for the test oil. From this data, an equation of the form of Eq. (4) was used for the temperature-viscosity relationship for this oil.

$$\mu(T) = \frac{A}{\left(\frac{T}{10}\right)^B} \tag{4}$$

The bearing model is as follows:

Diameter:	100 mm
Length:	55 mm
C_d/D ratio:	0.0015
Weep Hole Dia:	0.127 mm
Oil Inlet Dia:	3.175 mm
Grooves:	0 and 180 degrees from horizontal
	10 degrees of arc width
	(actual groove is 1.5 mm deep)

The data scaled from Tonneson's Fig. 4B and the NPADVT results for shaft eccentricity for the four speeds examined are graphically compared in Fig. 9 through Fig. 16. In Fig. 17 through Fig. 20, the same data are presented as a percentage

error (100 x (experimental - NPADVT) / experimental). It should be noted that the percentage error plots for small eccentricity values may be misleading, as a small absolute error can generate a large percentage error

Comparisons: NPADVT vs. Published Experimental Results

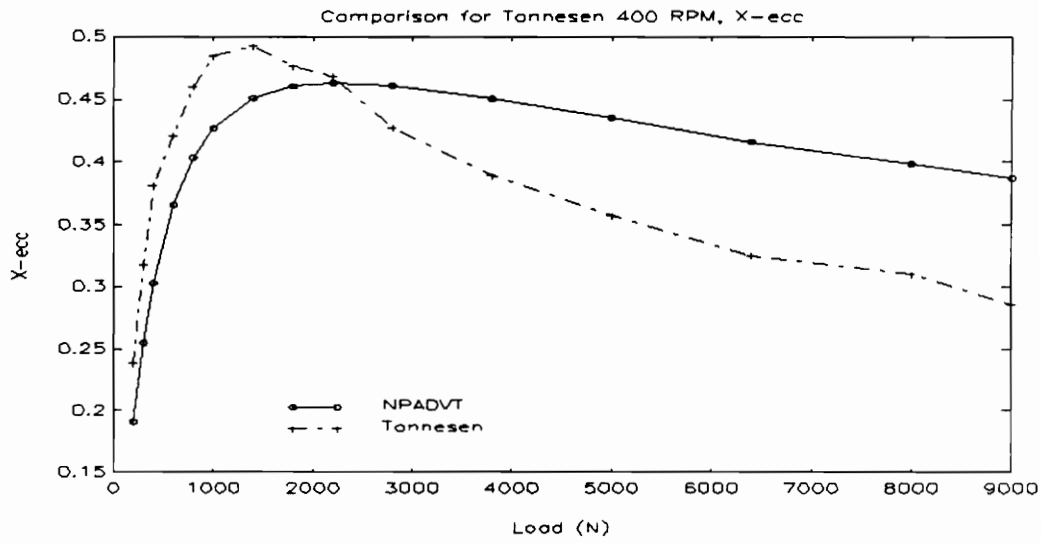

Fig. 9: X-Eccentricity Ratio for Tonnesen, 6.67 Hz

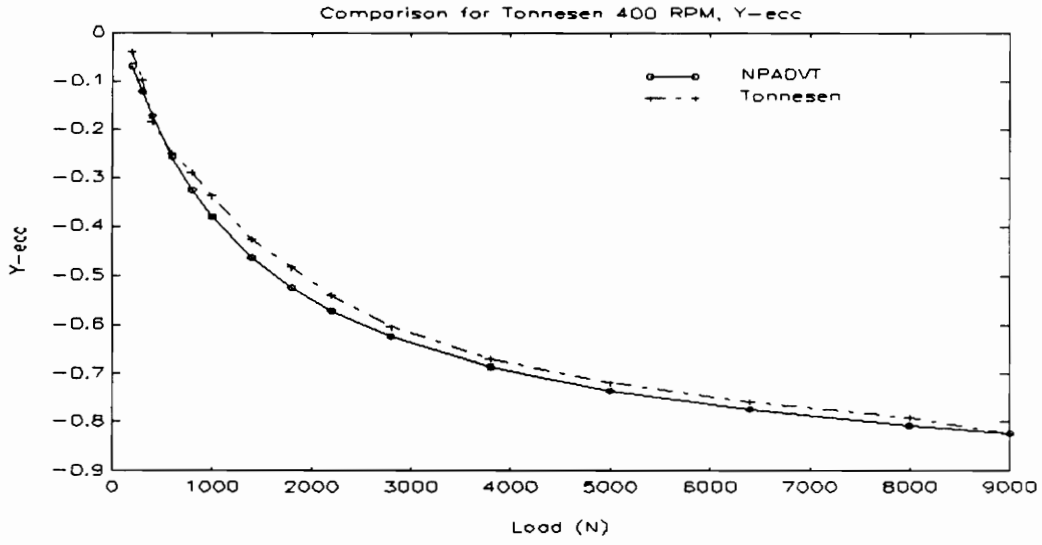

Fig. 10: Y-Eccentricity Ratio for Tonnesen, 6.67 Hz

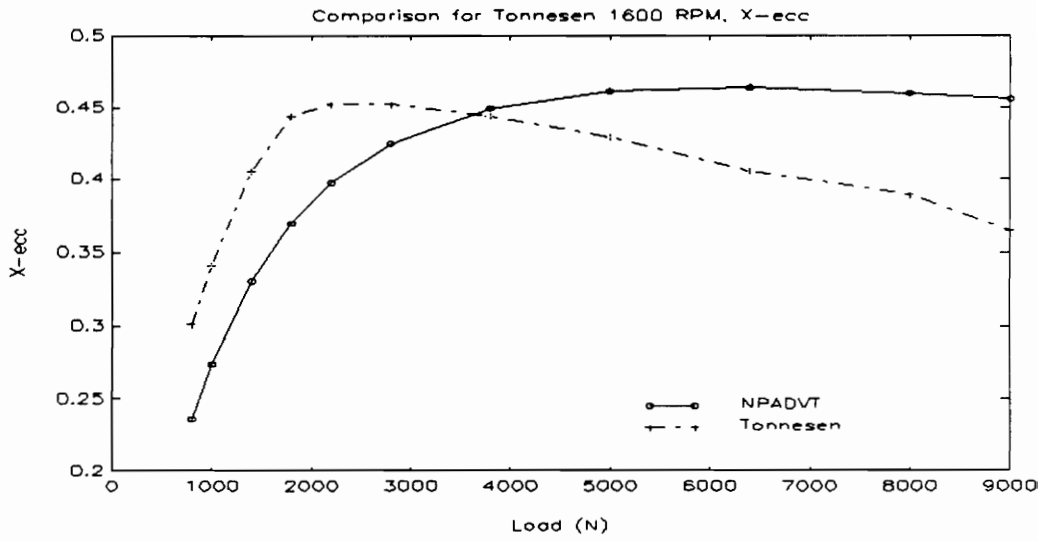

Fig. 11: X-Eccentricity Ratio for Tonnesen, 26.67 Hz

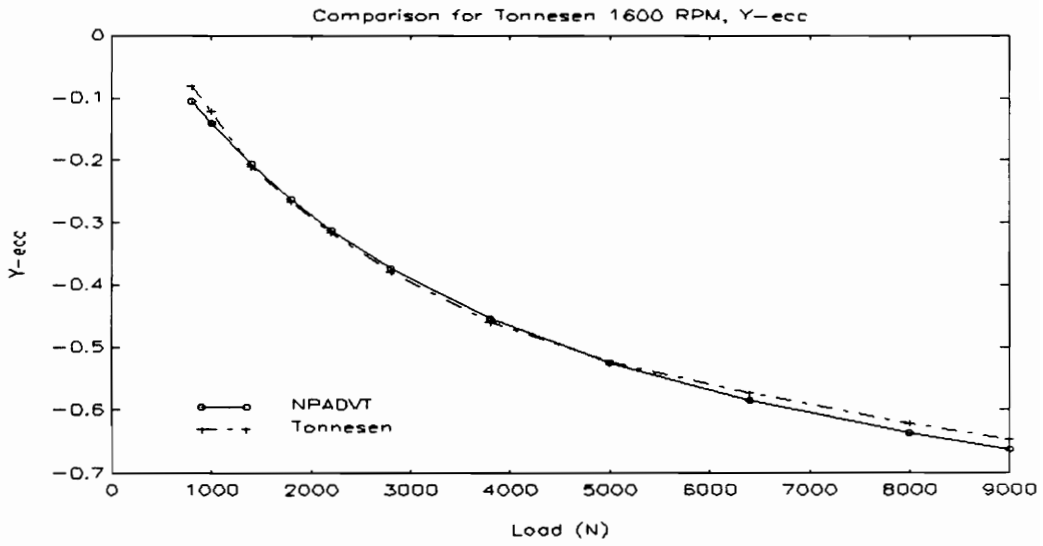

Fig. 12: Y-Eccentricity Ratio for Tonnesen, 26.67 Hz

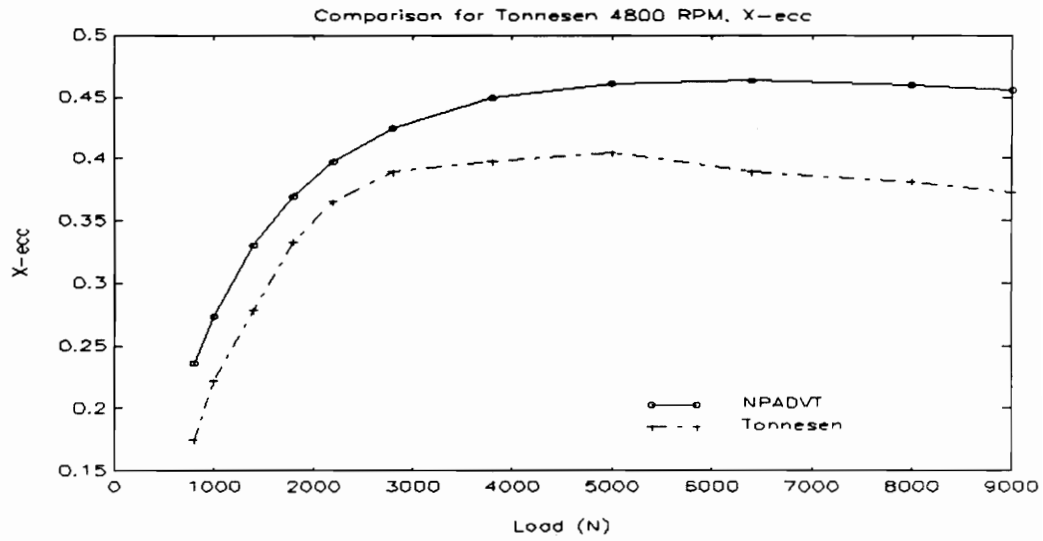

Fig. 13: X-Eccentricity Ratio for Tonnesen, 80 Hz

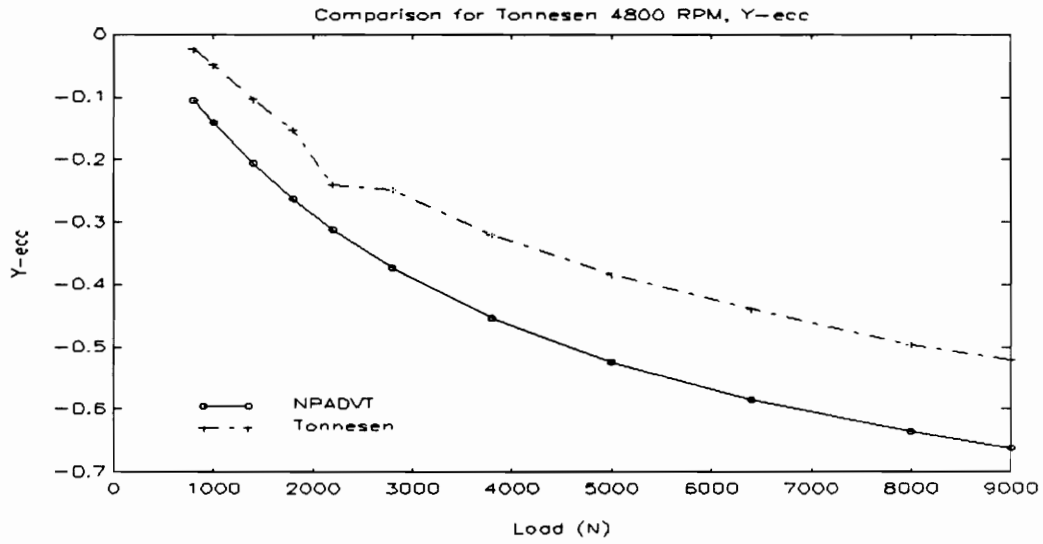

Fig. 14: Y-Eccentricity Ratio for Tonnesen, 80 Hz

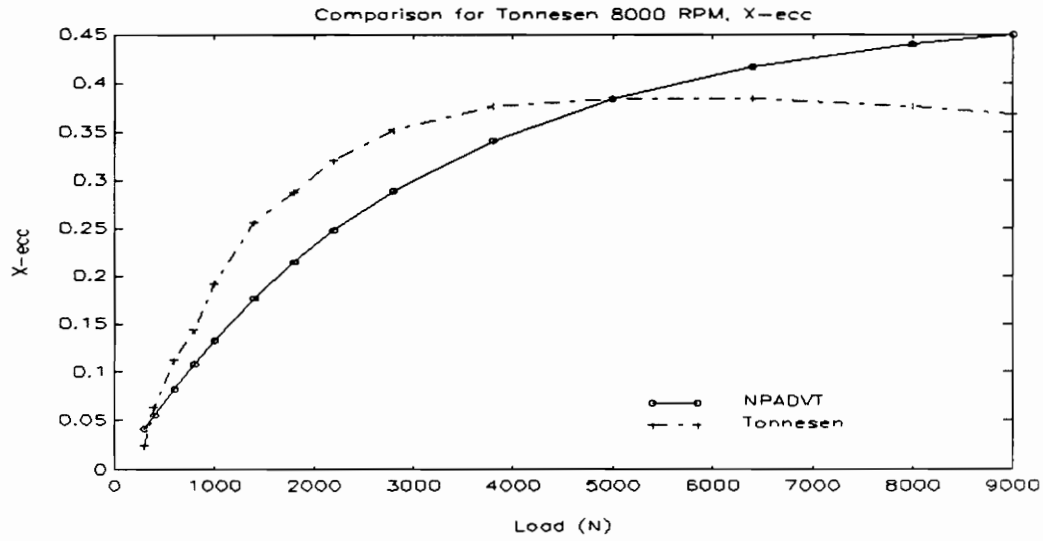

Fig. 15: X-Eccentricity Ratio for Tonnesen, 133.3 Hz

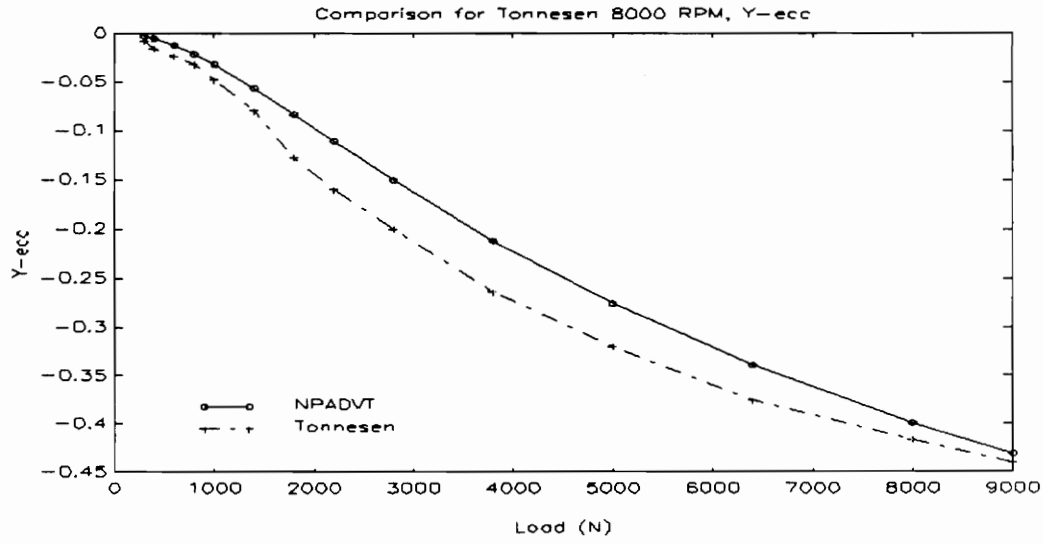

Fig. 16: Y-Eccentricity Ratio for Tonnesen, 133.3 Hz

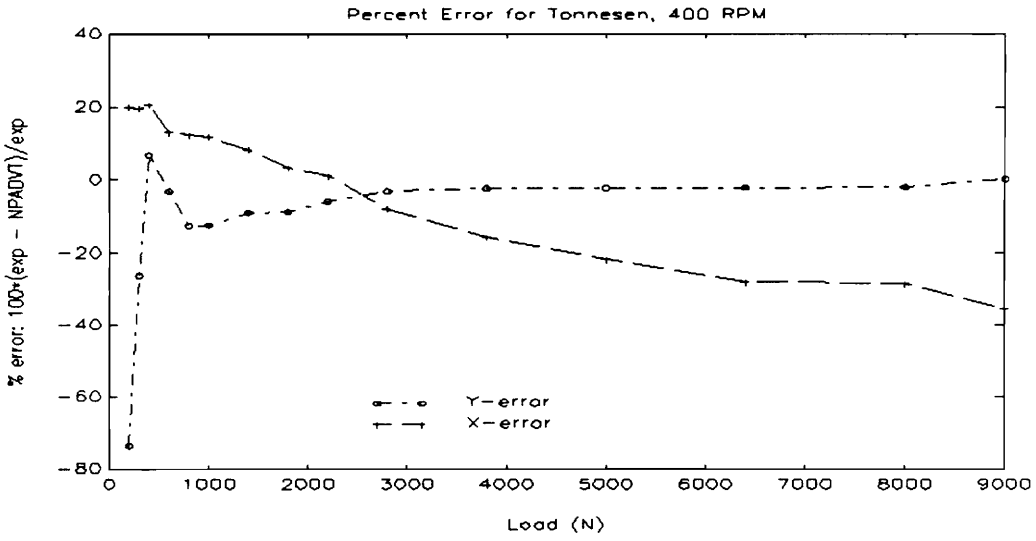

Fig. 17: Percent Error for Tonnesen, 6.67 Hz

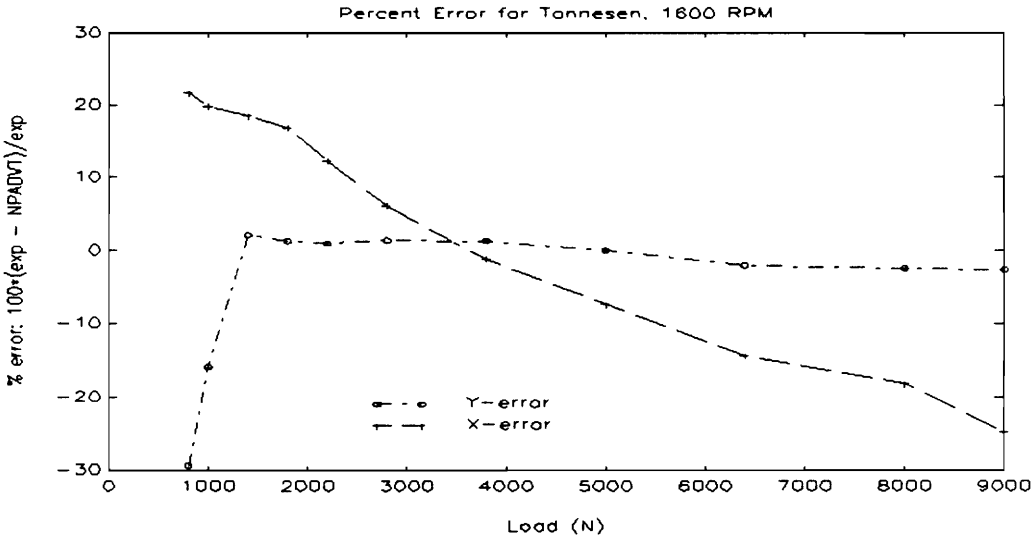

Fig. 18: Percent Error for Tonnesen, 26.67 Hz

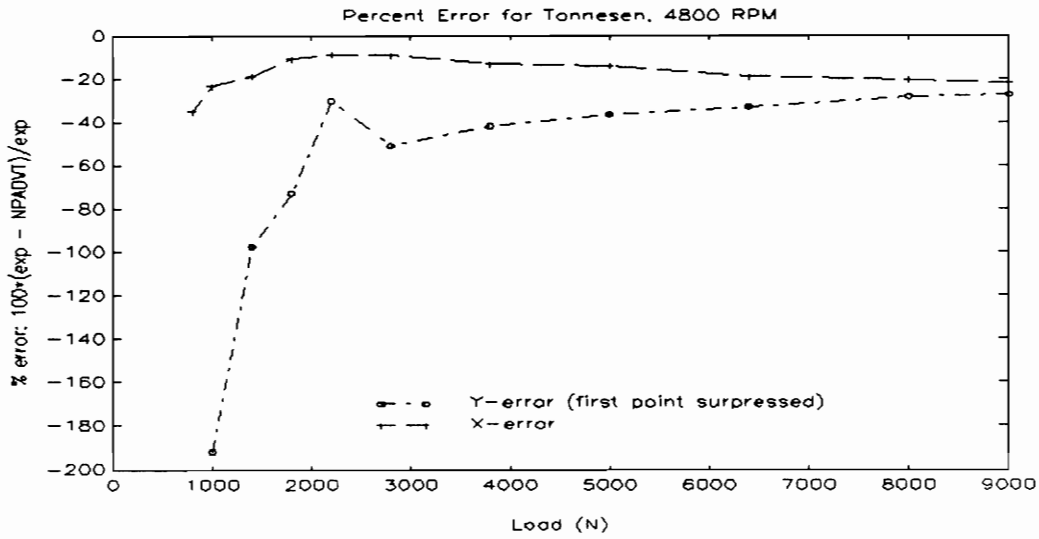

Fig. 19: Percent Error for Tonnesen, 80 Hz

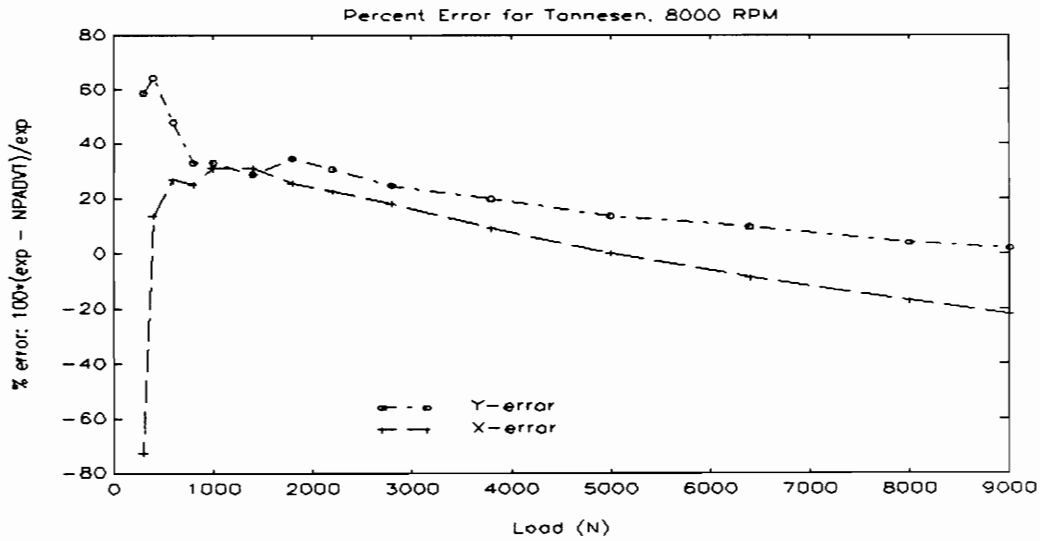

Fig. 20: Percent Error for Tonnesen, 133.33 Hz

3.2.2 Discussion of Results

These four comparisons tend to suggest that NPADVT, despite using a very crude thermal model and neglecting some fluid effects, does a credible job of predicting the static operating point. The Y (in line with the load) shaft loci are generally in good agreement with the experimental results, both in percentage error as well as the general shape, with increasing percentage error as the eccentricity approaches zero. It is even possible that some of the error seen is due to experimental zero offsets, as experimentally determining the center of an operating bearing is difficult. The fact that the major differences occur at the lowest loads is not surprising. The low eccentricities associated with lighter loads are likely to be the most sensitive to effects not considered in the analysis. The X shaft loci, on the other hand, do not show good agreement nor do zero offsets really explain the differences. In general, the analytical points do not show good agreement in either shape or percentage error for this axis.

Although the results would be usable from a load carrying standpoint, or an estimate of running clearances, the most important use of an analytical bearing analysis is to obtain dynamic coefficients. The Y locus (related to resistance in line with applied load) shows sufficiently good agreement that a stiffness evaluated by taking the gradient of the curve with respect to load (this would be the "direct" stiffness) would

seem likely to be accurate enough for most analyses. The inaccuracy that would be introduced would seem likely to be on the order of the modeling error and unmodeled effects. Unfortunately, the gradient of the analytical X locus with regard to load in the Y direction, i.e.,the cross-coupled stiffness, is likely to be quite different from the actual value. This fact is particularly evident in the percentage error plots, which show the analytical curve initially deviating below, then above the experimental curve. This deviation is particularly troubling from a rotor dynamic analyst's point of view, as some instabilities are driven by the magnitude and sign of the system cross-coupled stiffness (for a discussion of these effects, see Ref. 25 or Ref. 32). This point will be discussed further in the conclusions to this work.

3.3 Comparison for Lund/Tonnesen

An investigation made using the same rig as above is reported in Ref. 18, a 1984 Journal of Tribology article by Lund and Tonnesen of the Technical University of Denmark. This work is the application of an approximate thermal analysis of a journal bearing. Both shaft mounted and stationary displacement probes were again employed, with the uncertainty in measurements estimated as plus or minus five percent. Comparisons between a theoretical analysis with a somewhat more

sophisticated treatment of thermal conditions than employed in NPADVT and the experimental data are also presented. As noted in Table II, the bearing may be steel or bronze. The article only lists the thermal conductivity of the bearing material as 50 W/m °C, which could be either a steel or a bronze. The article refers to Ref. 30 as providing the details of the test rig construction; in this article, a bronze bearing is specified.

3.3.1 Data

The experimental data used for comparison purposes is from Fig. 8 in Ref. 18, which presents the measured journal locus as a function of load for 33.33, 58.33, 83.33 and 108.33 Hz. This plot is not corrected for shaft bending, but a correction equation is specified; all comparisons will be made to the corrected data. The loads used in developing the results in this figure vary from 2600 N to 9600 N by 1000 N steps (at 33.33 Hz, the 9600 N and 8600 N load are not included; at 83.33 and 108.33 Hz, the 9600 N point is omitted). The oil used is specified as having a viscosity of 18.3 mPa•s at 50 degrees. Sufficient data are available in Ref. 18 to specify a two parameter, exponential temperature-viscosity relationship as in Eq. (4). The oil specific heat was also specified as 2000 J/kg•K. The bearing model is as follows:

Diameter:	100 mm
Length:	55 mm
C_d/D ratio:	0.00137 (33.33, 58.33 Hz)
	0.00134 (83.33, 108.33 Hz)
Weep Hole Dia:	0.254 mm
Oil Inlet Dia:	3.175 mm
Grooves:	0 and 180 degrees from horizontal
	10 degrees of arc width

The data scaled from Lund's Fig. 8 and the NPADVT results for shaft eccentricity for the four speeds examined are graphically compared in Fig. 21 through Fig. 28. In Fig. 29 through Fig. 36, the same data are presented as a percentage error (100 x (experimental - NPADVT) / experimental). Note that in the legends for these figures, "rotating" refers to the set of displacement probes in the test rig shaft, while "stationary" refers to the set of displacement probes on the bearing housing.

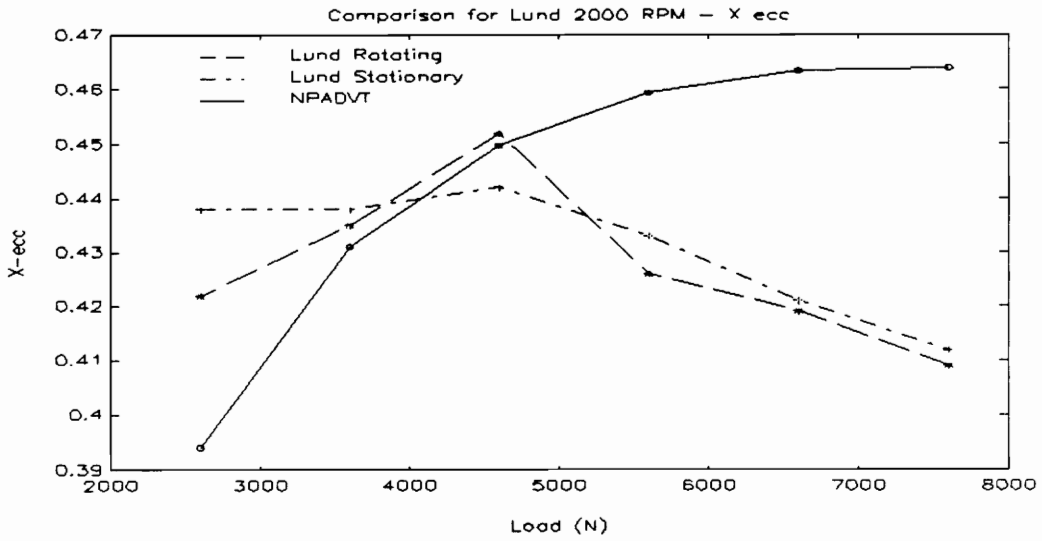

Fig. 21: X-Eccentricity Ratio for Lund, 33.33 Hz

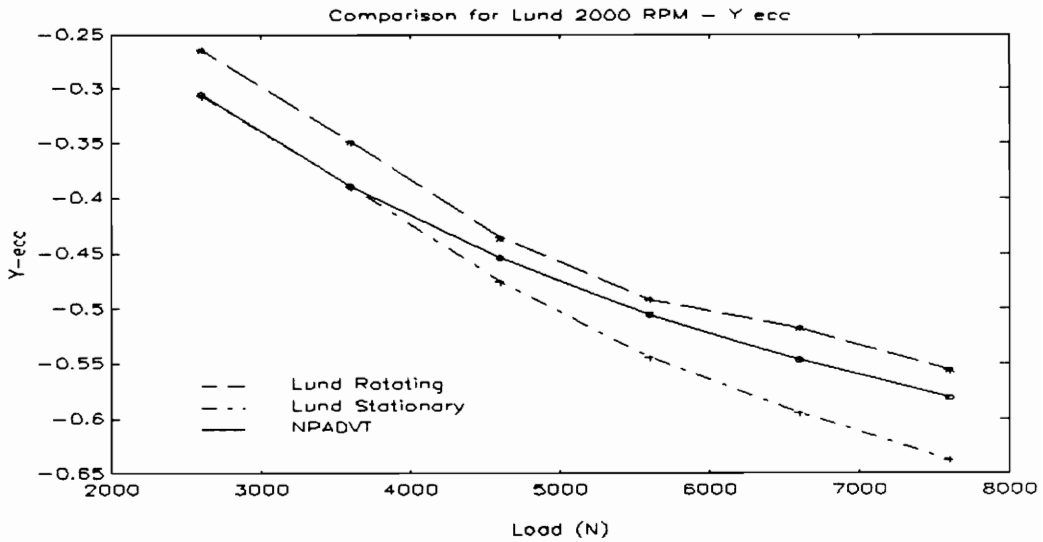

Fig. 22: Y-Eccentricity Ratio for Lund, 33.33 Hz

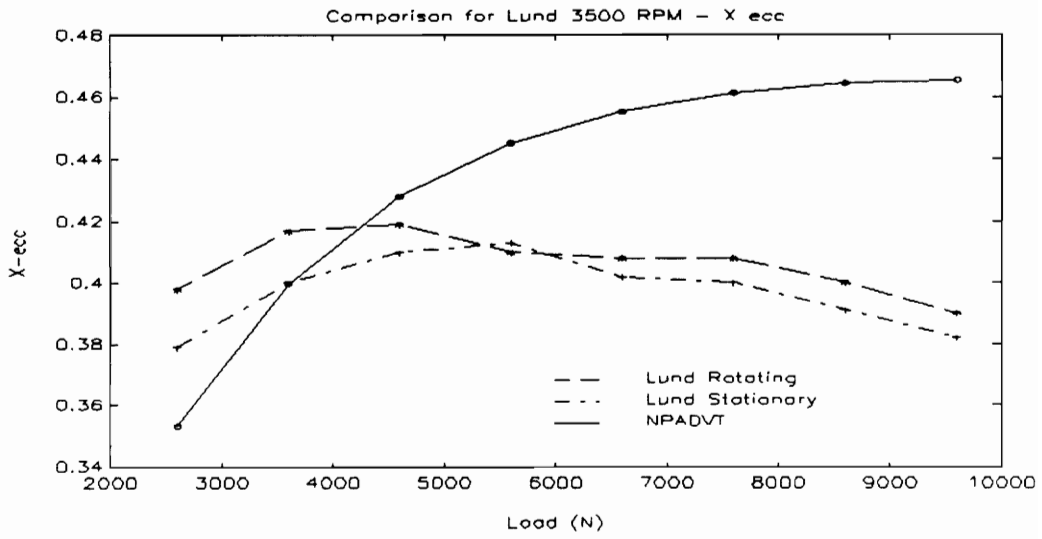

Fig. 23: X-Eccentricity Ratio for Lund, 58.33 Hz

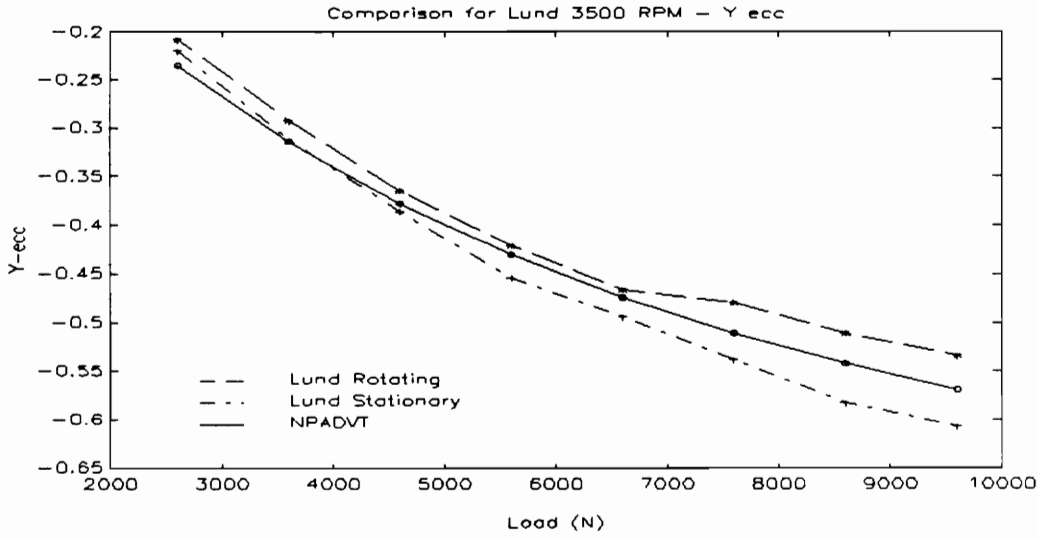

Fig. 24: Y-Eccentricity Ratio for Lund, 58.33 Hz

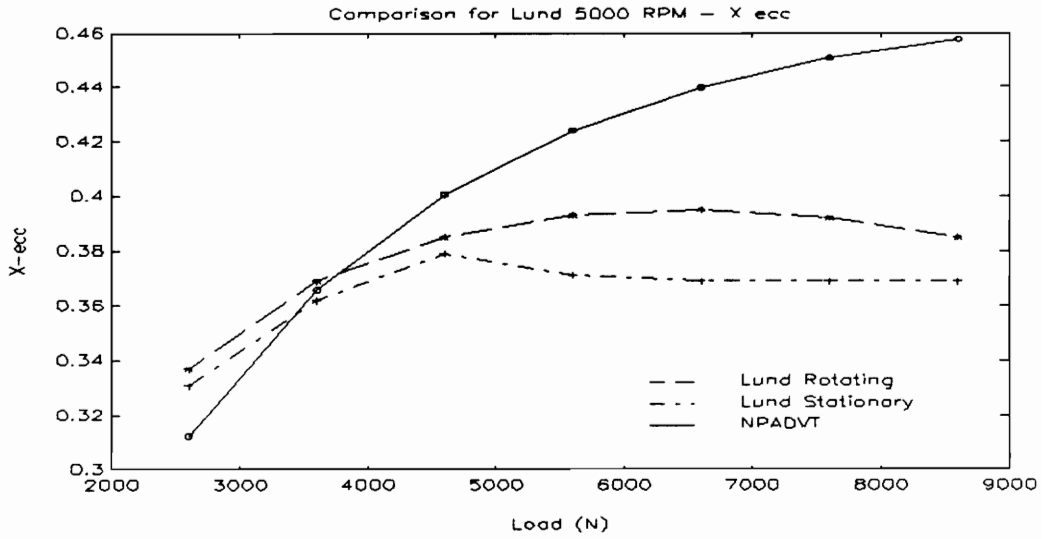

Fig. 25: X-Eccentricity Ratio for Lund, 83.33 Hz

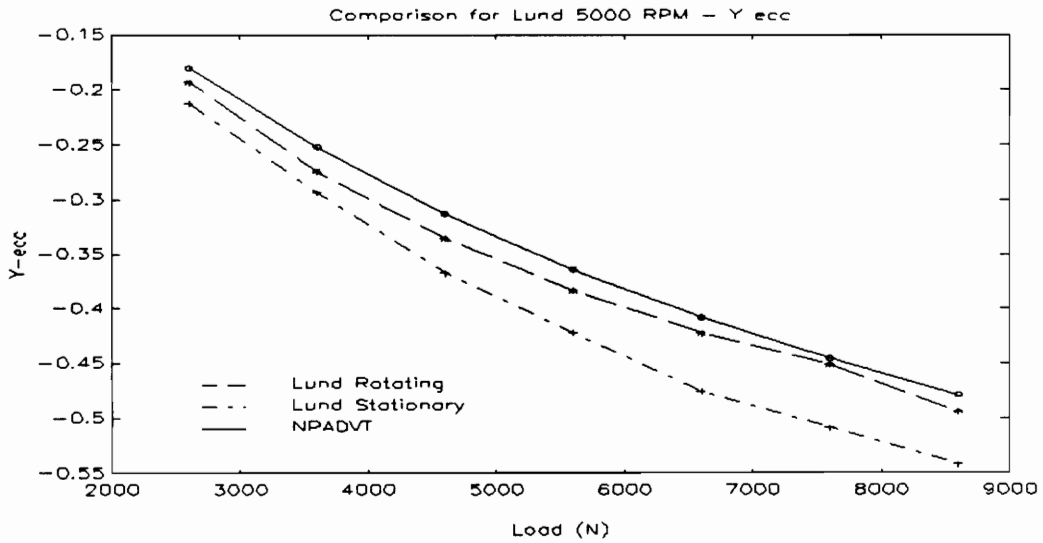

Fig. 26: Y-Eccentricity Ratio for Lund, 83.33 Hz

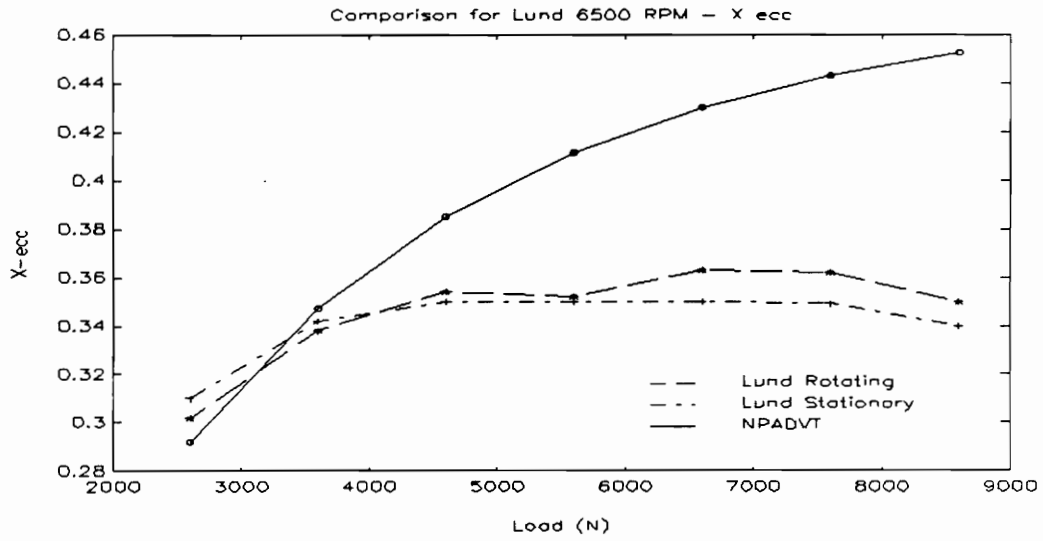

Fig. 27: X-eccentricity for Lund, 108.33 Hz

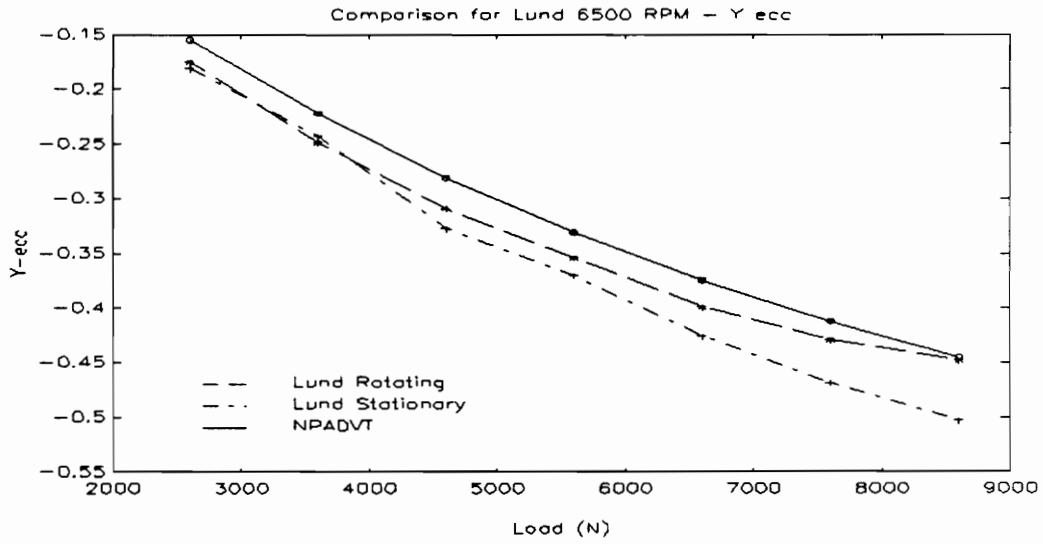

Fig. 28: Y-eccentricity for Lund, 108.33 Hz

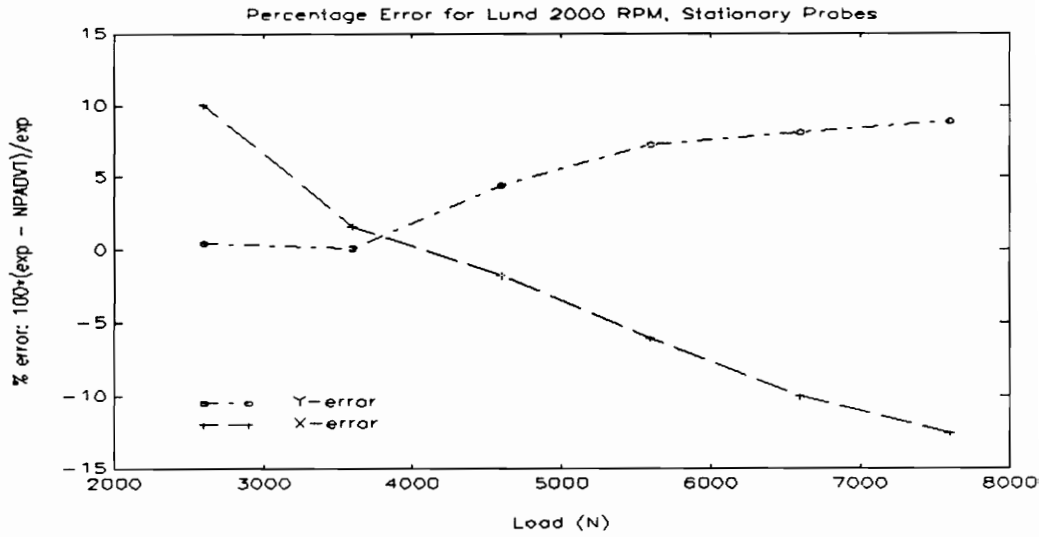

Fig. 29: Percent error for Lund, 33.33 Hz (Stationary Probes)

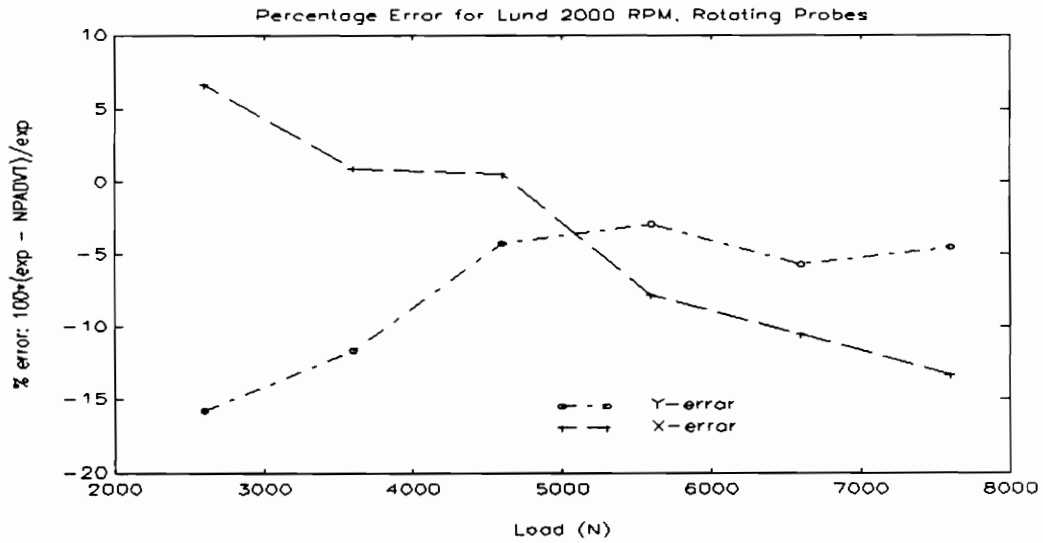

Fig. 30: Percent error for Lund, 33.33 Hz (Rotating Probes)

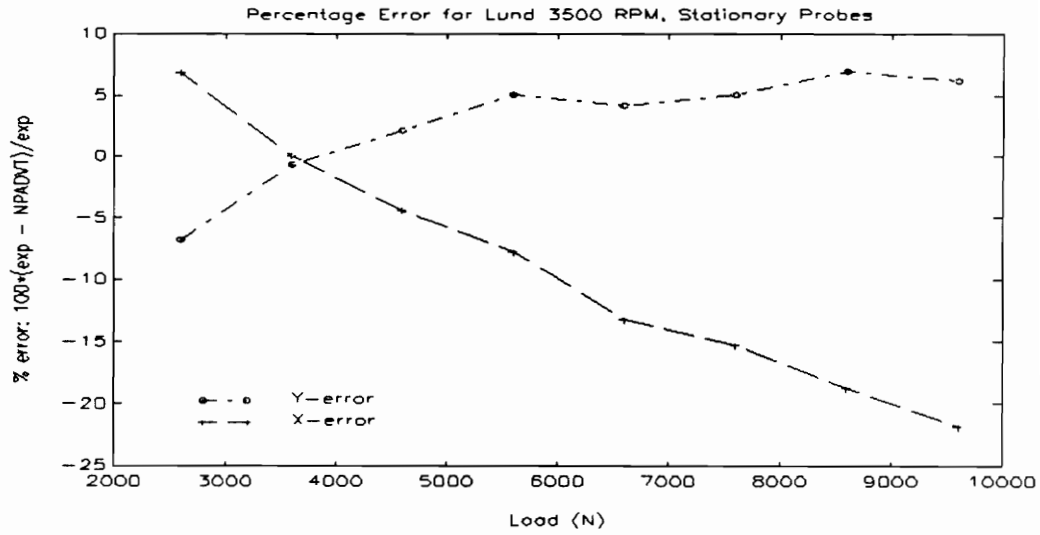

Fig. 31: Percent error for Lund, 58.33 Hz (Stationary Probes)

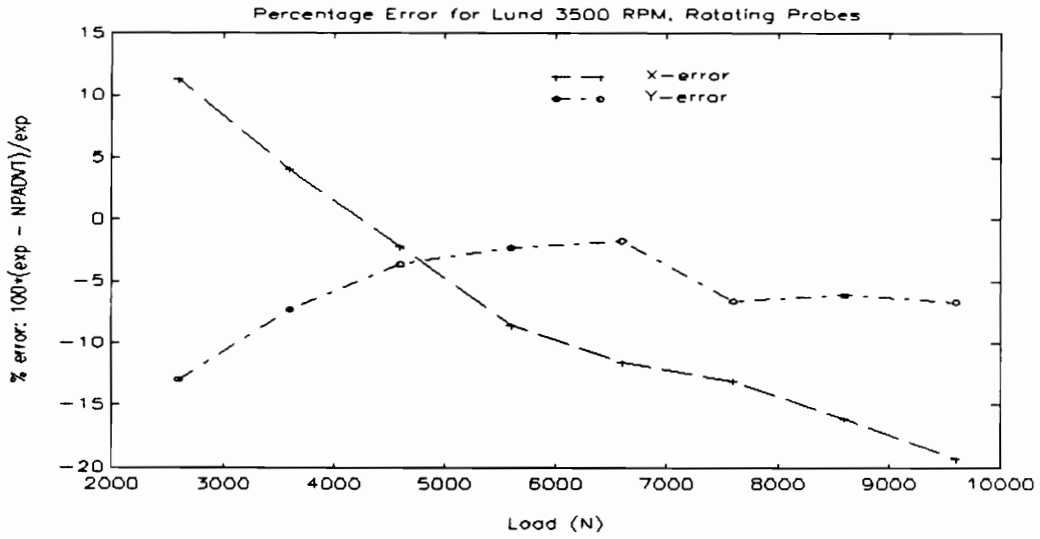

Fig. 32: Percent error for Lund, 58.33 Hz (Rotating Probes)

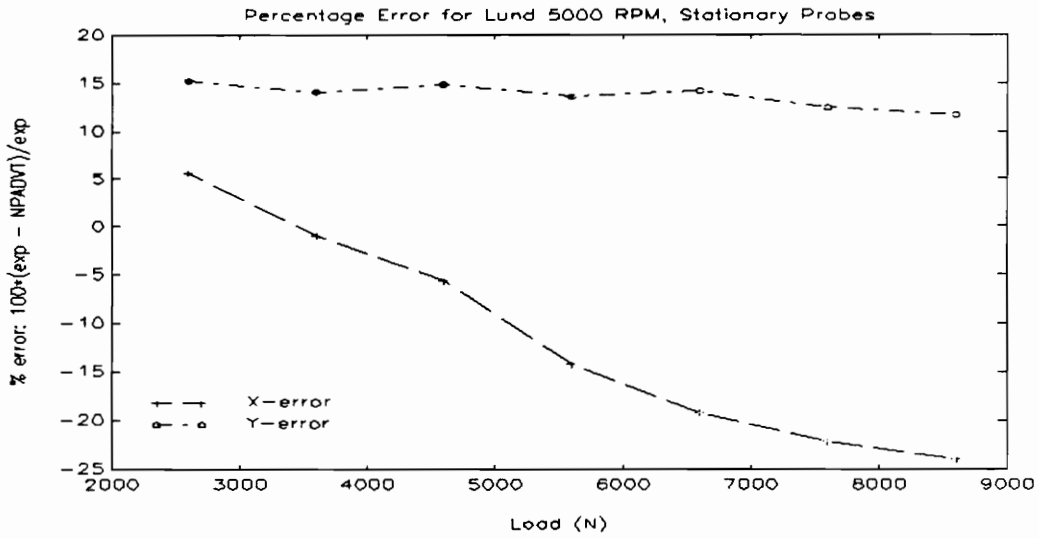

Fig. 33: Percent error for Lund, 83.33 Hz (Stationary Probes)

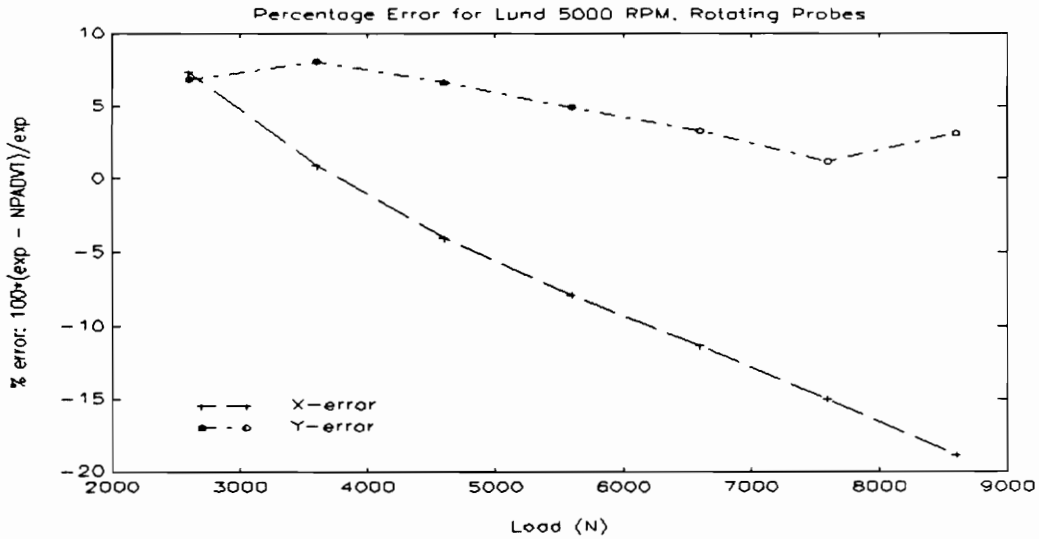

Fig. 34: Percent error for Lund, 83.33 Hz (Rotating Probes)

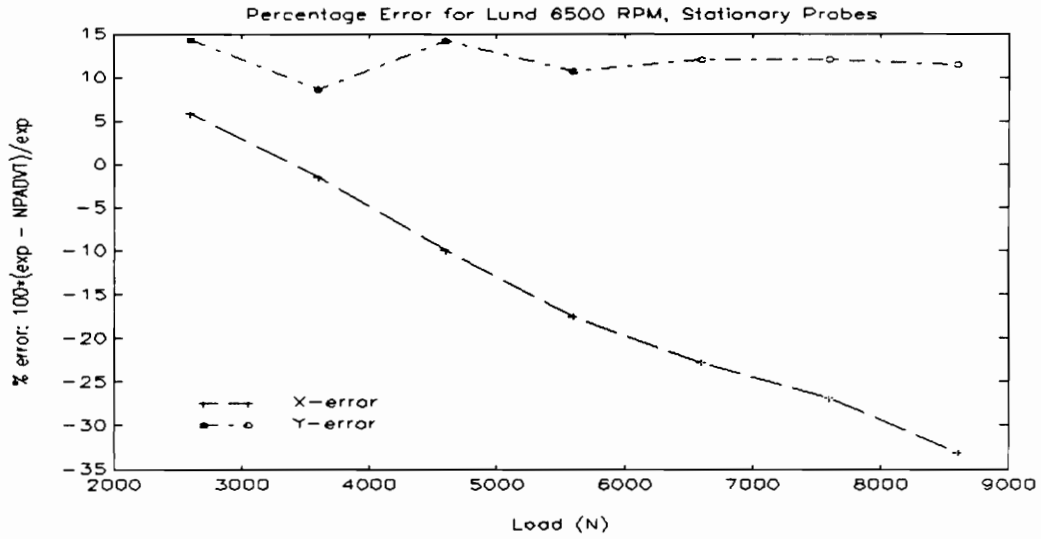

Fig. 35: Percent error for Lund, 108.33 Hz (Stationary Probes)

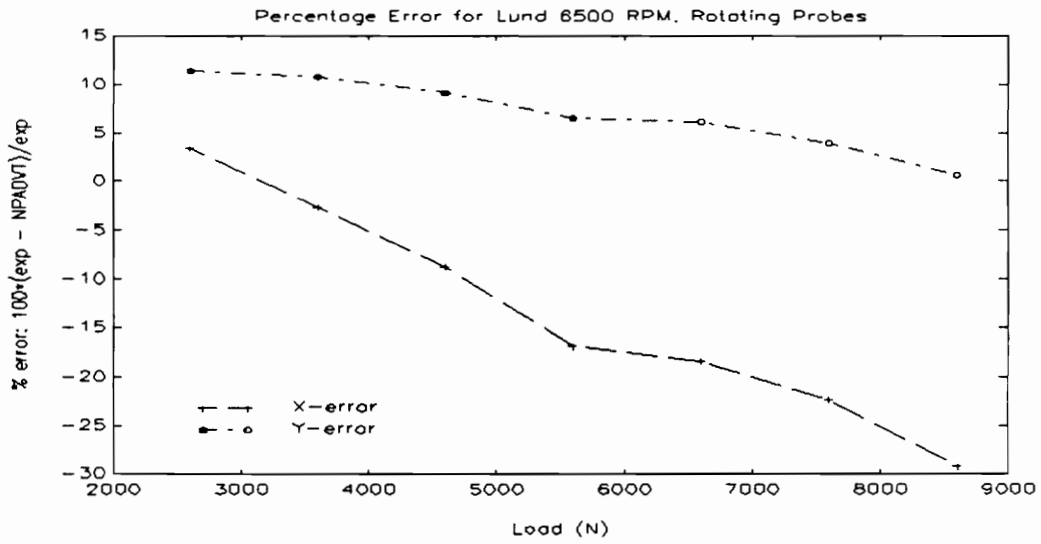

Fig. 36: Percent error for Lund, 108.33 Hz (Rotating Probes)

3.3.2 Discussion of Results

The plots of Fig. 21 through Fig. 36 again suggest problems with the cross-coupled effect, as pointed out in the discussion of the comparisons of Ref. 30 results. The analytical X-positions generated by NPADVT, although generally within 20% of the experimental results, do not exhibit the same trends as the experimental results. Interestingly, the results from both Ref. 30 and Ref. 18, which were obtained with the same test rig, both exhibit the same trends in the x-position error. In both cases, the NPADVT results are too small at low loads, and too large at higher loads. This effect does not seem to be an artifact of the test rig, as the same trends will be seen in the comparisons for Ref. 29. The Y-position generally exhibits closer agreement, both in position and general shape. In addition, the comparison between experimental data and an analysis with a more sophisticated thermal model than NPADVT in Ref. 18 shows similar trends. The implications of these trends have been discussed above, and will be discussed further in the conclusions.

3.4 Comparison for Someya #2

Reference 29 is a compilation of Japanese work in the area of fluid-film bearings. Three of the eleven experimental data sets are for plain axial-groove bearings, contain sufficient information and are applicable to this work. The results are not identified

as to researcher or location. The first of the data sets to be examined is experimental data set two. The test rig employed is of the floating bearing/rigid shaft type. Loading is by air bellows. Both dynamic as well as static data are presented in tabular as well as graphical form.

3.4.1 Data

The data used for comparison purposes, are from Ref. 29's Tables 3.2.1 and 3.2.2. These tables present the operating conditions as a function of a Sommerfeld number (Eq. (5),) computed by assuming an effective oil temperature based on inlet and outlet oil temperatures.

$$S = \frac{\mu N}{P}\left(\frac{R}{C}\right)^2 \tag{5}$$

Where:

μ = Viscosity
N = Revolutions per Second
P = Load per Unit Projected Area
R = Shaft Radius
C = Radial Clearance

This somewhat artificial Sommerfeld number will be the independent variable for the comparisons (the Sommerfeld number computed by NPADVT is generally slightly different for the same input conditions). The oil used is identified as #90 Turbine oil, with a viscosity of 27.37 mPa•s at 40 degrees. Sufficient data was provided to fit a

two parameter temperature-viscosity equation as in Eq. (4). The bearing model used is as follows:

Diameter:	100 mm
Length:	100 mm
C_d/D ratio:	0.00210
Weep hole Dia:	0.2 mm
Oil inlet Dia:	6.35 mm
Grooves:	0 and 180 degrees from horizontal
	10 degrees of arc width

The data from Ref. 5 and the NPADVT results for shaft eccentricity versus the Sommerfeld number reported in Ref. 5 for speeds of 50, 100, 150, 200 and 250 Hz are graphically compared in Fig. 37 through Fig. 46. Fig. 47 through Fig. 51 present the same data as a percentage error (100 x (NPADVT - experimental) / NPADVT). Note that the percentage error is expressed somewhat differently than before. This change is required because one of the experimental points is reported as having a 90 degree attitude angle, which corresponds to a zero y-position; the previous expression for percent error will not work for this case.

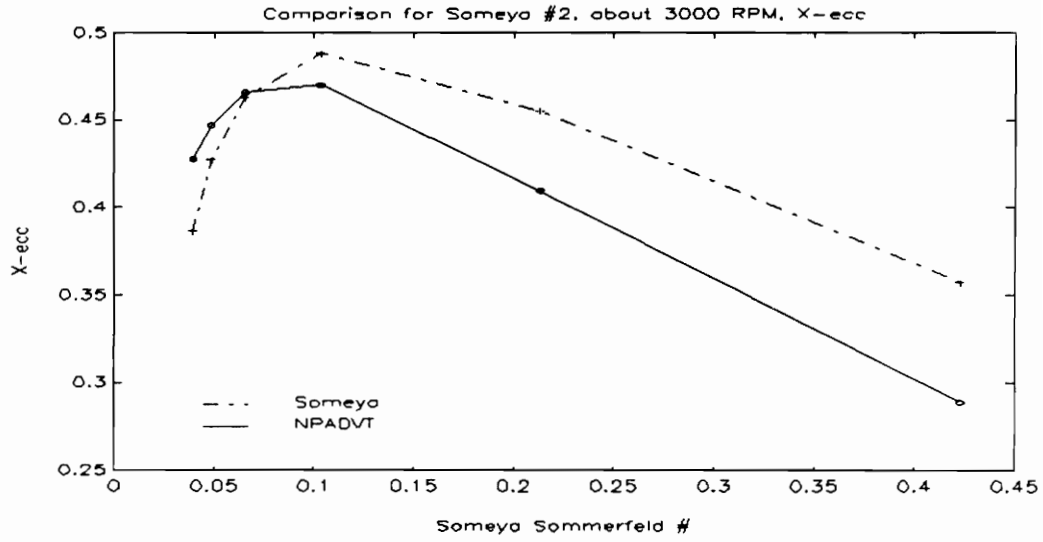

Fig. 37: X-Eccentricity Ratio for Someya Test 2, 50 Hz

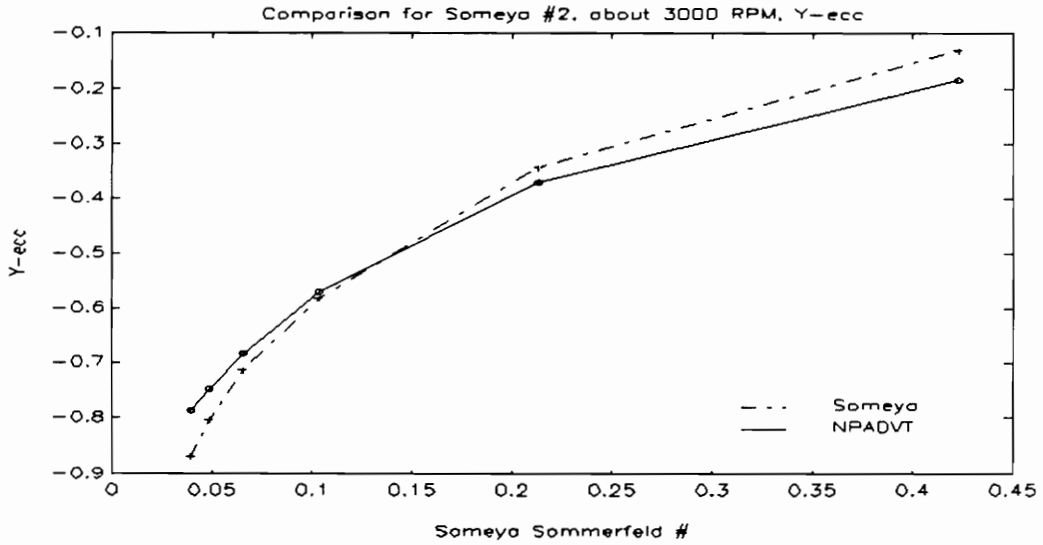

Fig. 38: Y-Eccentricity Ratio for Someya Test 2, 50 Hz

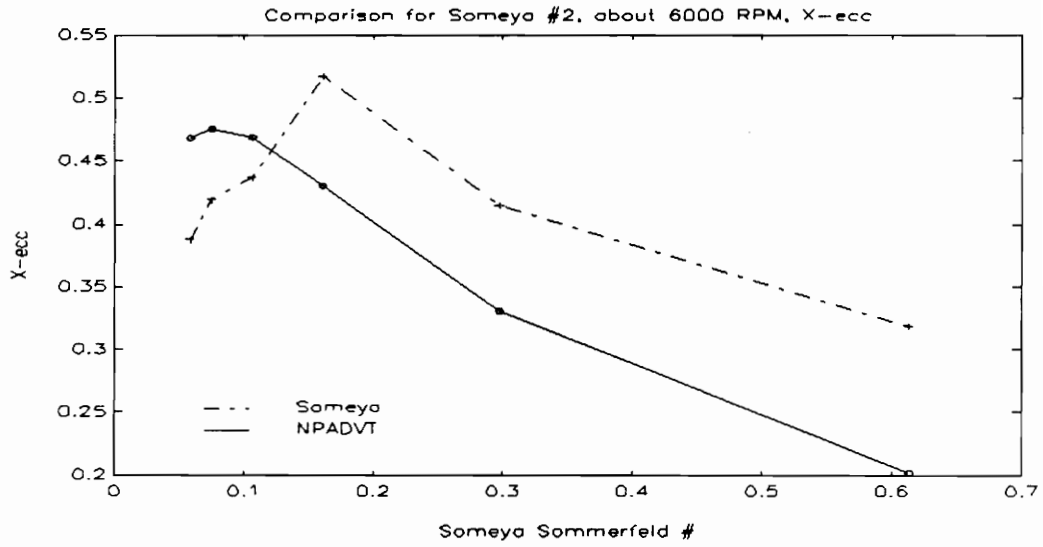

Fig. 39: X-Eccentricity Ratio for Someya Test 2, 100 Hz

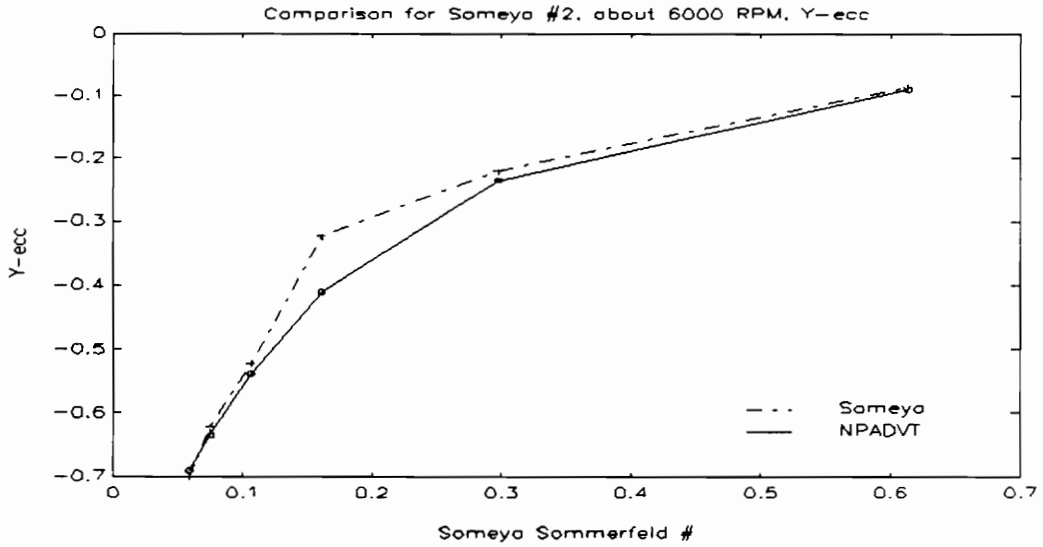

Fig. 40: Y-Eccentricity Ratio for Someya Test 2, 100 Hz

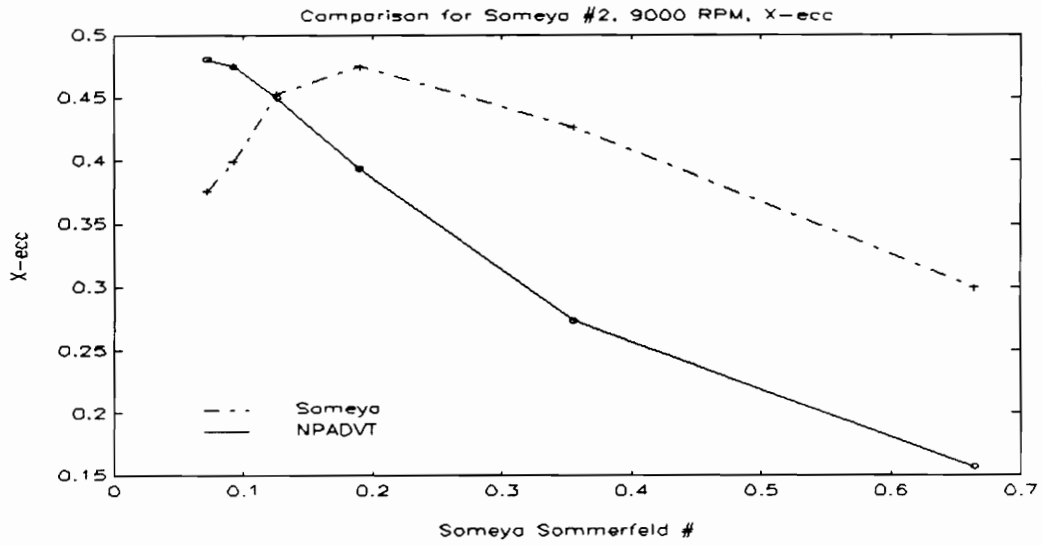

Fig. 41: X-Eccentricity Ratio for Someya Test 2, 150 Hz

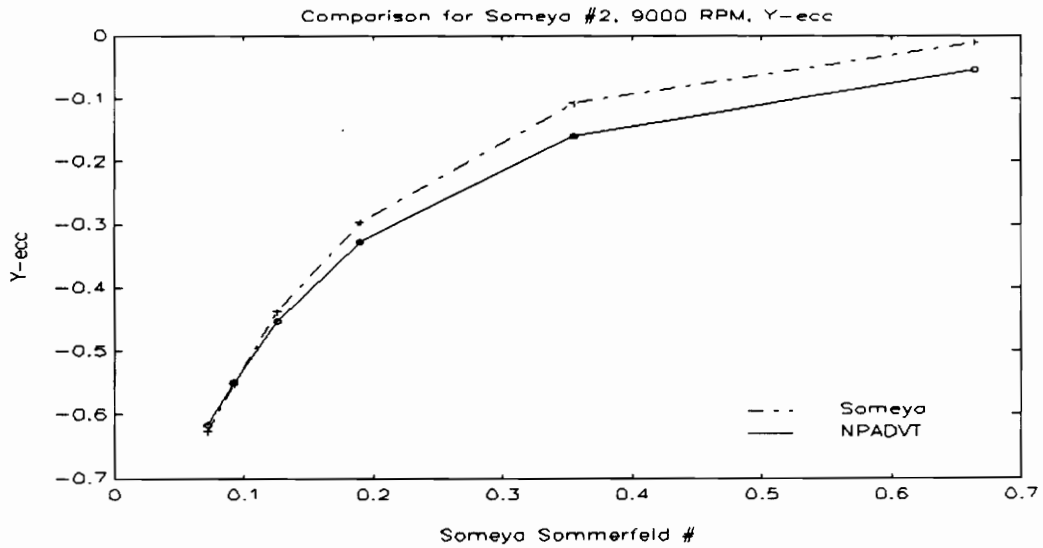

Fig. 42: Y-Eccentricity Ratio for Someya Test 2, 150 Hz

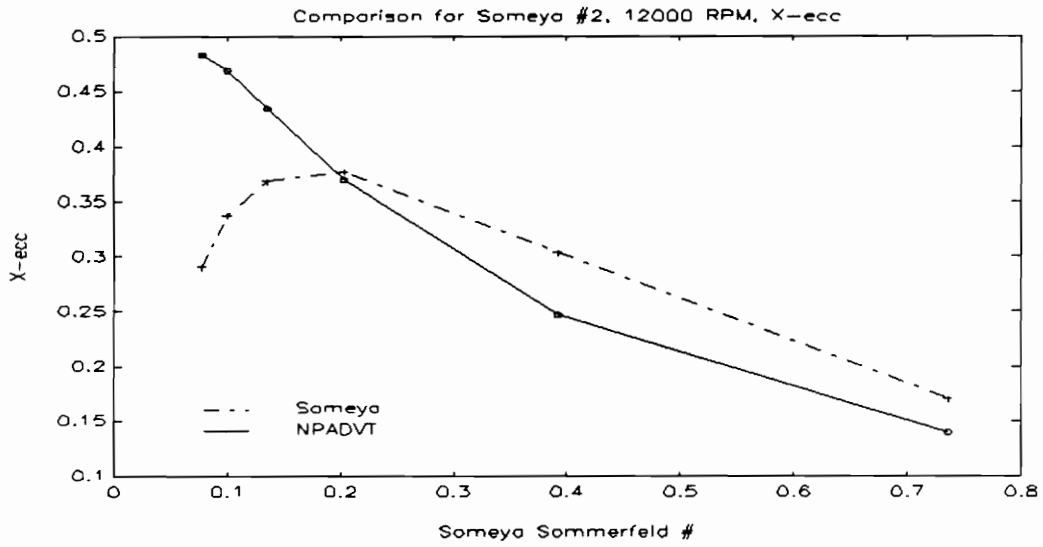

Fig. 43: X-Eccentricity Ratio for Someya Test 2, 200 Hz

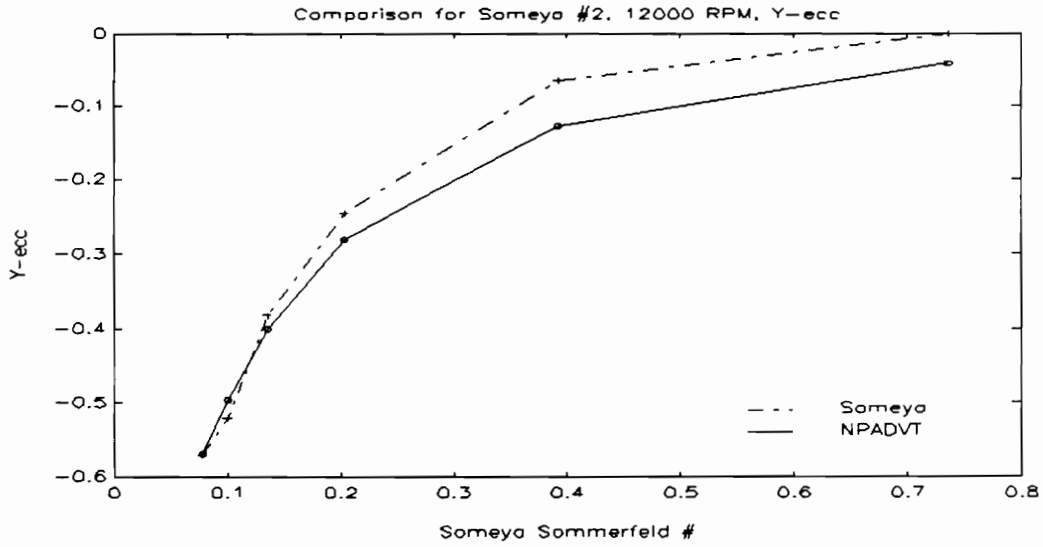

Fig. 44: Y-Eccentricity Ratio for Someya Test 2, 200 Hz

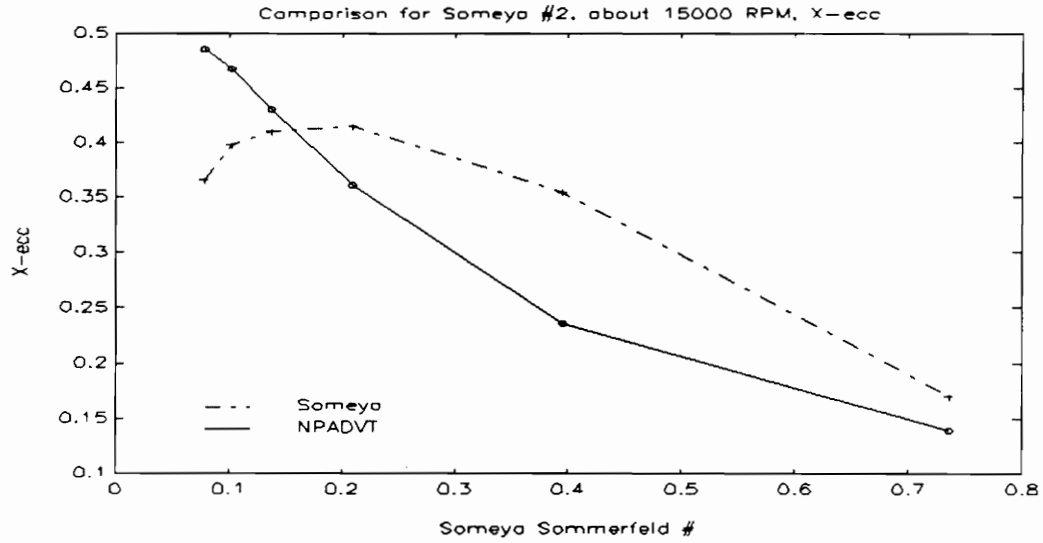

Fig. 45: X-Eccentricity Ratio for Someya Test 2, 250 Hz

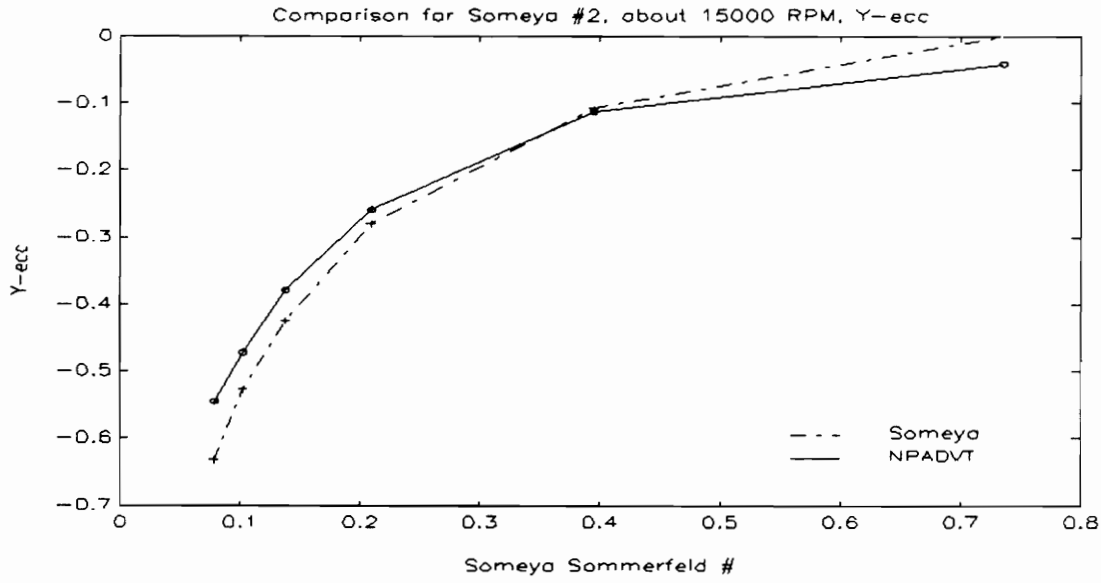

Fig. 46: Y - Eccentricity Ratio for Someya Test 2, 250 Hz

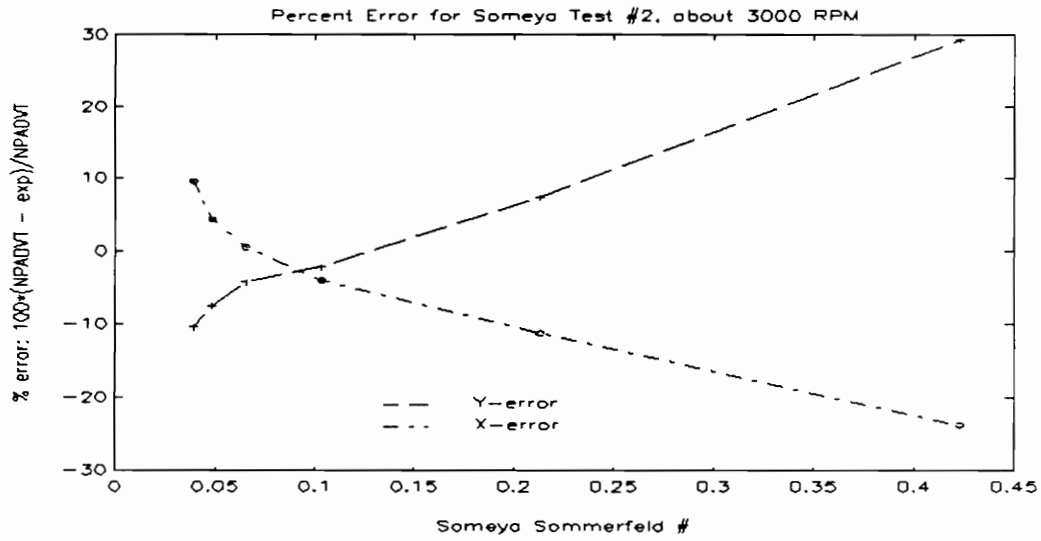

Fig. 47: Percent Error for Someya Test 2, 50 Hz

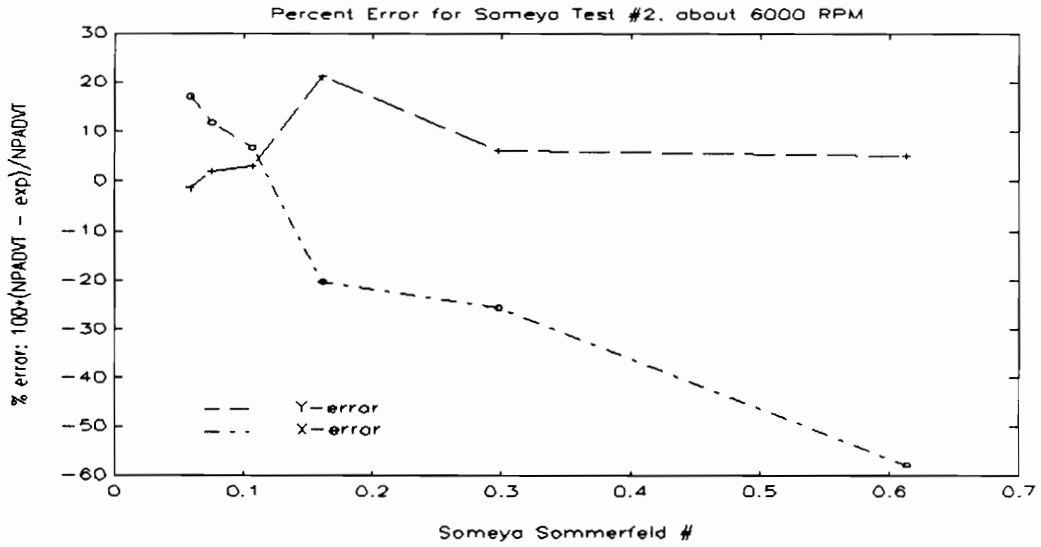

Fig. 48: Percent Error for Someya Test 2, 100 Hz

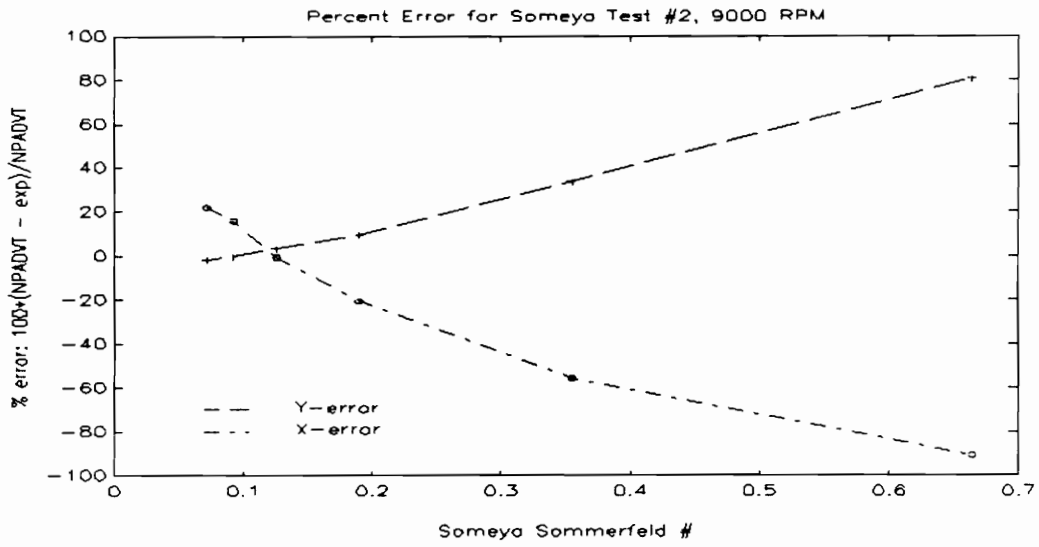

Fig. 49: Percent Error for Someya Test 2, 150 Hz

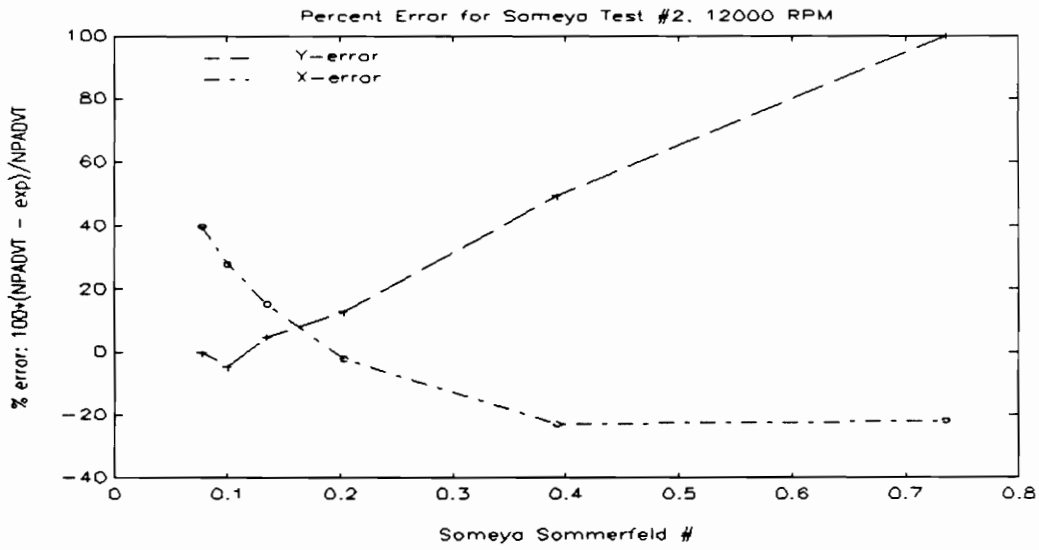

Fig. 50: Percent Error for Someya Test 2, 200 Hz

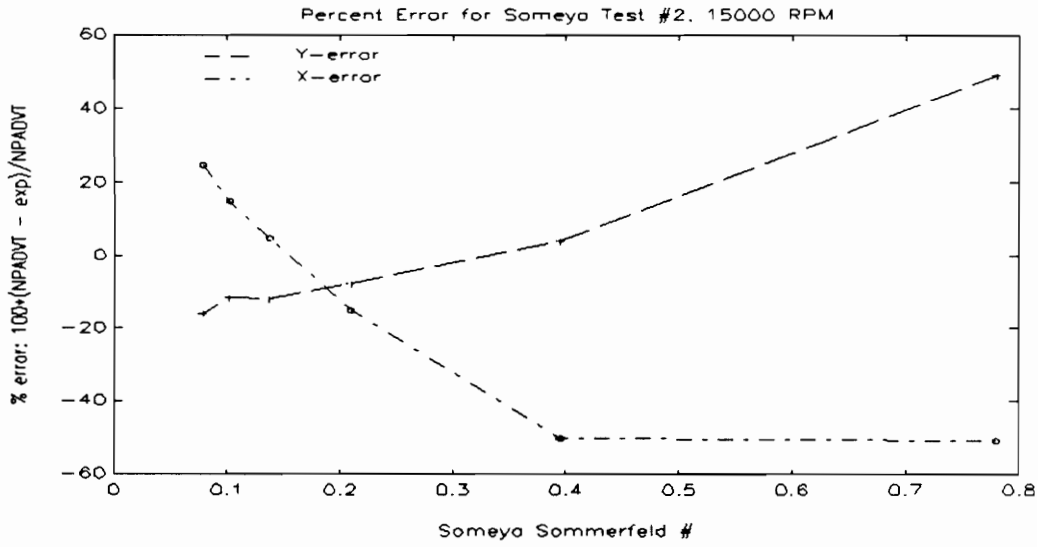

Fig. 51: Percent Error for Someya Test 2, 250 Hz

3.4.2 Discussion of Results

The NPADVT analysis for this bearing does not agree with the experimental results as well as the previous comparisons. Part of this is likely to be due to modeling error, as no data were presented in Ref. 29 for the feed groove extent, weep hole diameter and inlet hole diameter. This source of error would be in accord with the fact that the error is most apparent at larger Sommerfeld numbers (corresponding to relatively lighter loading), where the effects of feed groove extent would be most noticeable. Other than an attempt to get the NPADVT temperature rise through the bearing to be reasonably close to the experimental temperature rise by varying the weep hole size, no attempt was made to match results by varying groove extent or oil inlet hole diameter. Zero offsets do not seem to provide an explanation of the differences either, as the NPADVT results are both larger and smaller than the experimental data. In general, the results exhibit similar trends as before. The NPADVT predicted Y-position is generally close and has the right general shape (especially at the lower Sommerfeld numbers); the X-position generally exhibits the wrong shape, even if the absolute position is close.

3.5 Comparison for Someya #3

The second data set from Ref. 29 used as a basis for comparison to the NPADVT analysis is experimental data set number three. These data were obtained with a floating bearing/rigid shaft test rig with pneumatic loading. Again, both tabular and graphical results are presented for static and dynamic characteristics.

3.5.1 Data

The data set used is that of Tables 3.3.1 and 3.3.2, which present the static operating characteristics as a function of Sommerfeld number. Since the oil temperature, etc. is consistent from speed to speed, the results will be presented for 26.7, 66.7, and 100 Hz as a function of load. The oil used for this set of experiments is identified as an ISO 32 oil, with a viscosity of 18.4 mPa•s at 50 degrees. Sufficient data are presented for a two parameter viscosity-temperature relationship of the form of Eq. (4). The geometric data for this bearing are also more complete than for the previous data set. The bearing model used is as follows:

Diameter:	100 mm
Length:	50 mm
C_d/D ratio:	0.0028

Weep Hole Dia:	2 mm
Oil Inlet Dia:	15 mm
Grooves:	0 and 108 degrees from horizontal
	10 degrees of arc width
	(actual groove is 1 mm deep)

The data from Ref. 29 and the NPADVT results for shaft position for 26.7, 66.7, and 100 Hz as a function of load are presented in Fig. 52 through Fig. 57. Fig. 58 through Fig. 60 present the comparison as a percent error (100 * (exp - NPADVT) / exp).

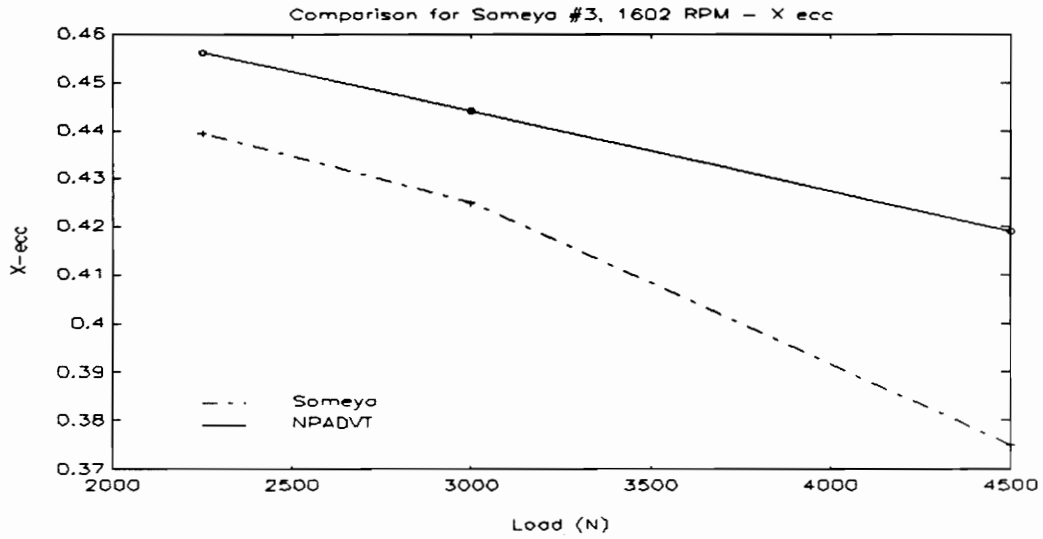

Fig. 52: X-Eccentricity Ratio for Someya Test 3, 26.7 Hz

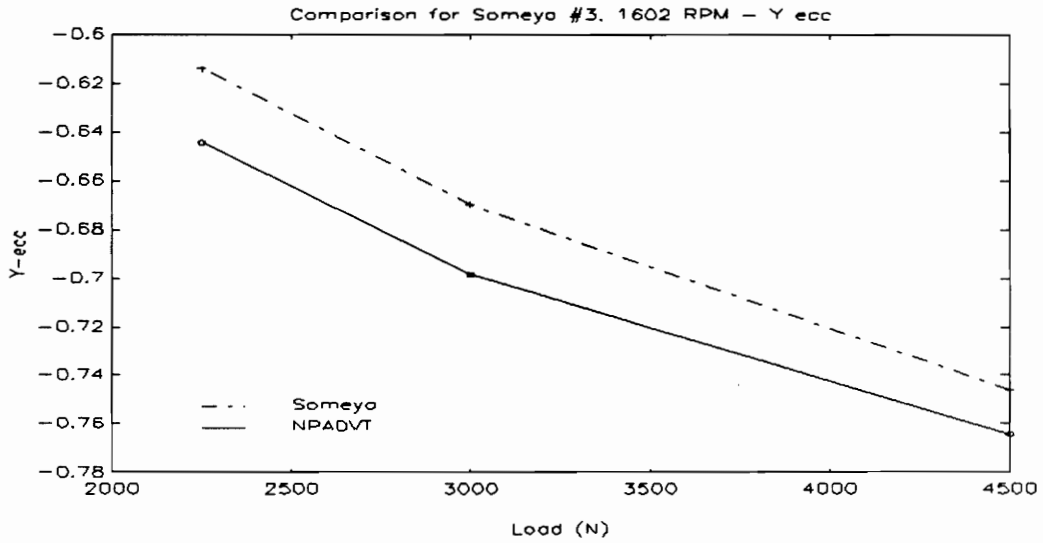

Fig. 53: Y-Eccentricity Ratio for Someya Test 3, 26.7 Hz

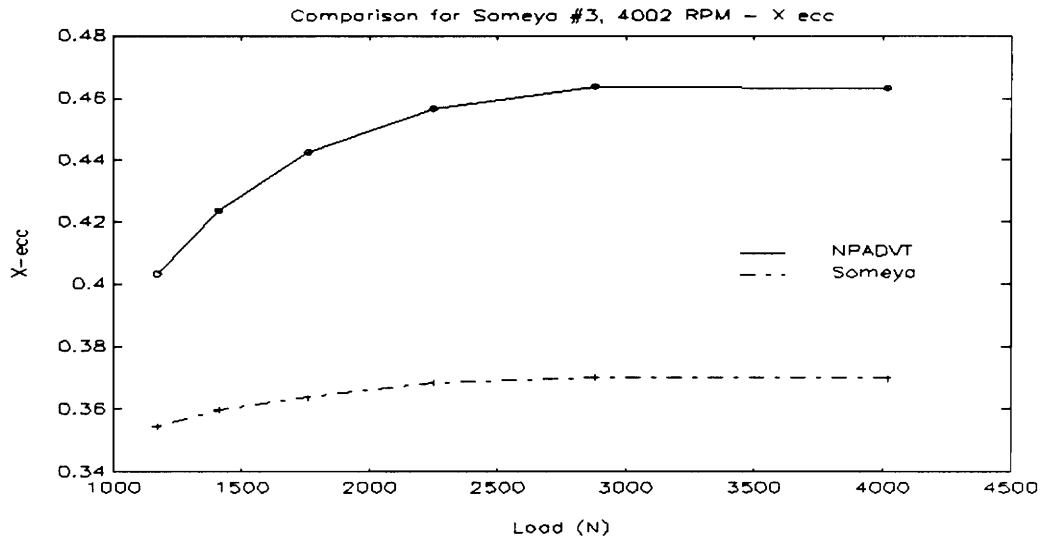

Fig. 54: X-Eccentricity Ratio for Someya Test 3, 66.7 Hz

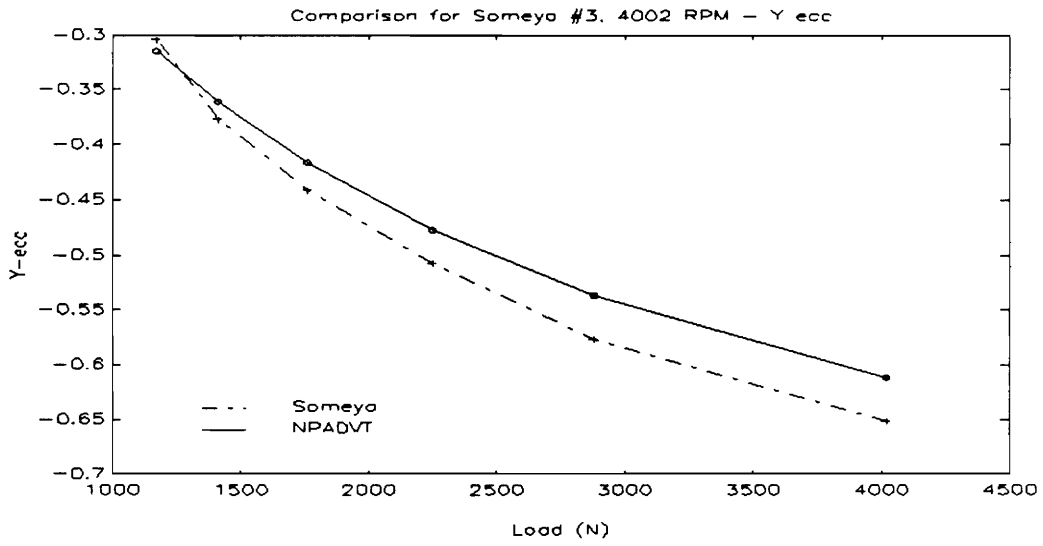

Fig. 55: Y-Eccentricity Ratio for Someya Test 3, 66.7 Hz

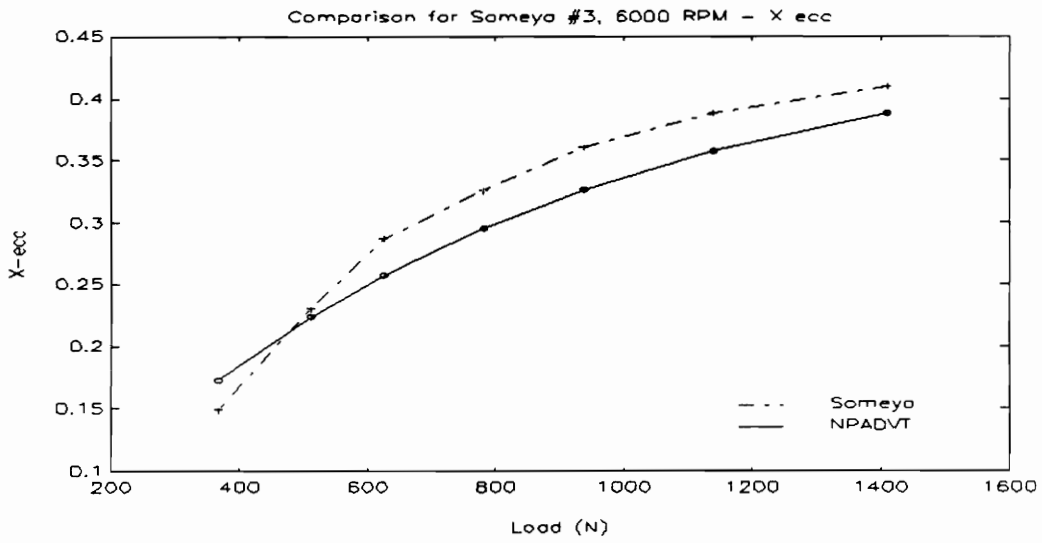

Fig. 56: X-Eccentricity Ratio for Someya Test 3, 100 Hz

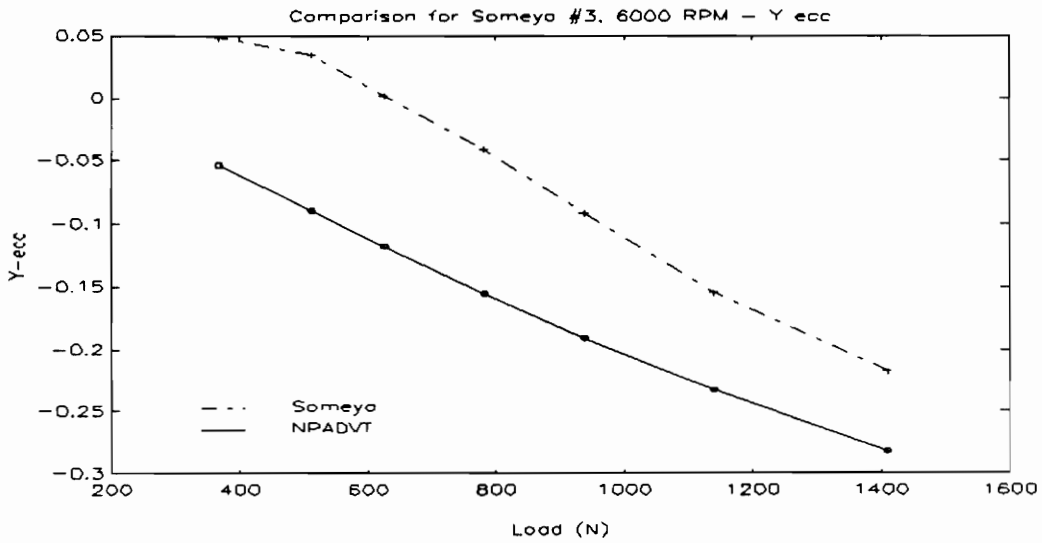

Fig. 57: Y-Eccentricity Ratio for Someya Test 3, 100 Hz

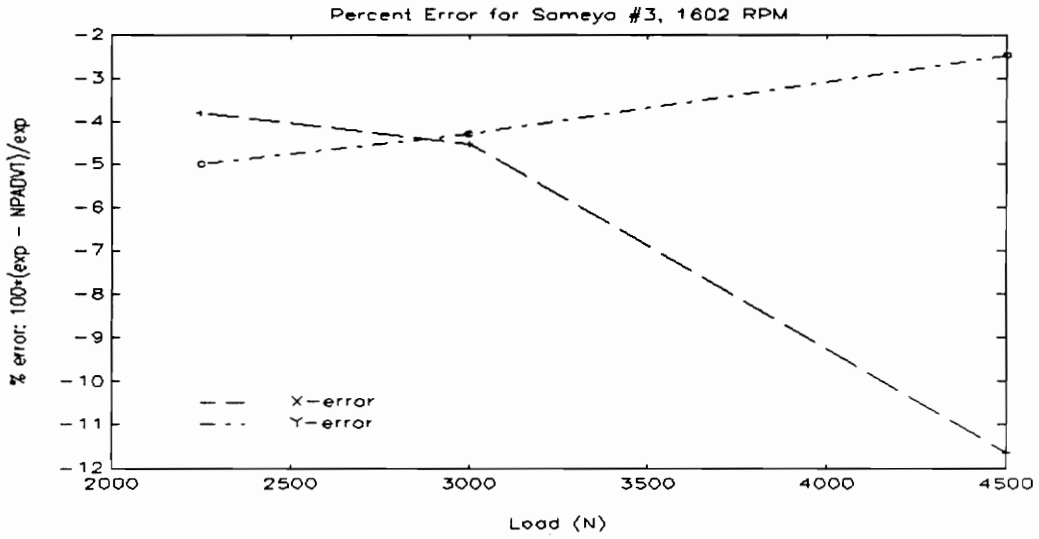

Fig. 58: Percent Error for Someya Test 3, 26.7 Hz

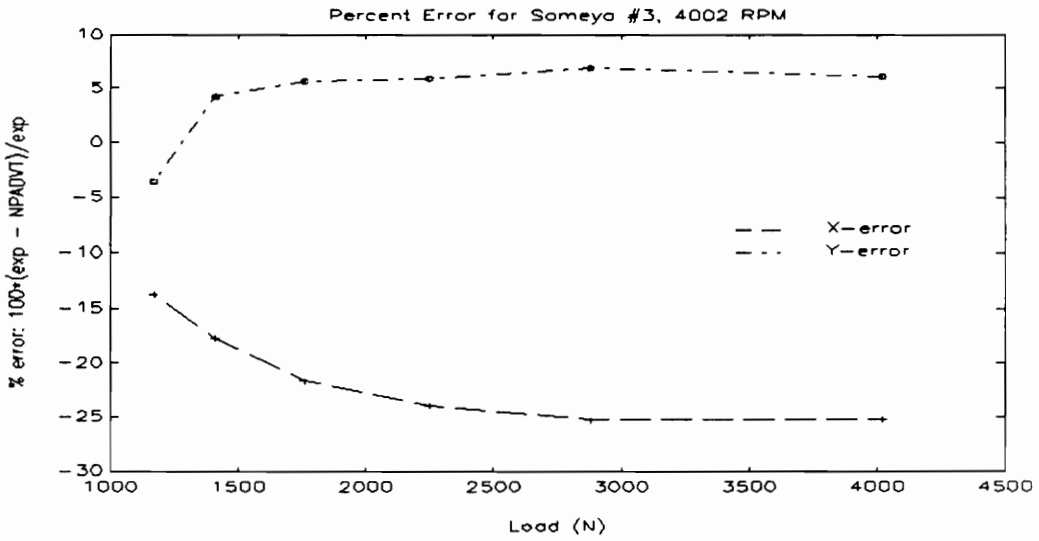

Fig. 59: Percent Error for Someya Test 3, 66.7 Hz

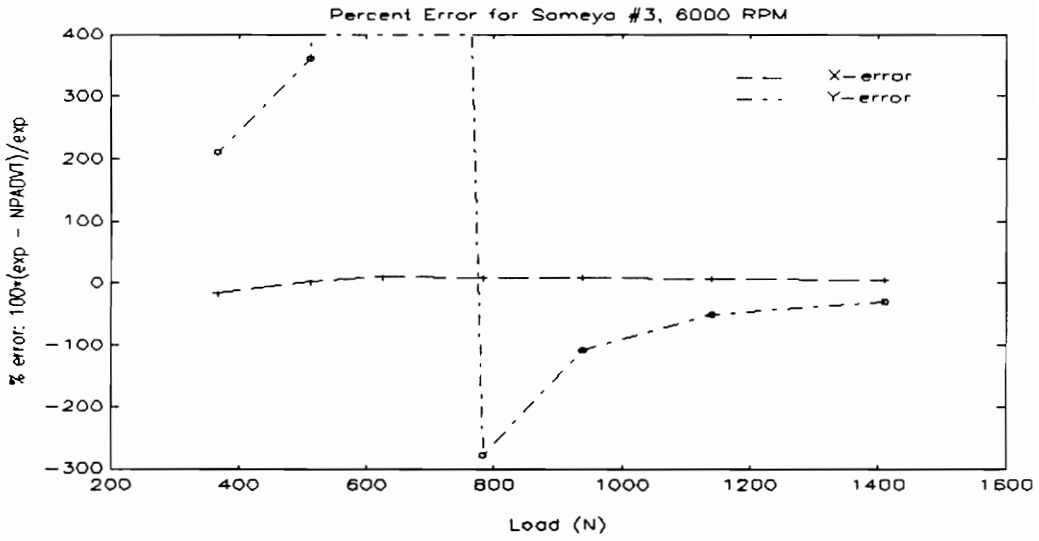

Fig. 60: Percent Error for Someya Test 3, 100 Hz

3.5.2 Discussion of Results

The results for this set of comparisons are interesting. At lower Sommerfeld numbers, the NPADVT results look quite good. It would also appear that some of the differences between experimental and NPADVT results could be caused by zero offsets. The Sommerfeld numbers in this data set are somewhat larger (0.2 to 2.21) than in the previous data set. In general, with the exception of the 26.7 Hz Y-position and the 66.7 Hz X-position, the NPADVT analyses yield very good predictions (the percent error plots may be a bit misleading at the lower eccentricities). It is not apparent why the 26.7 Hz Y-position and the 66.7 Hz X-position do not follow in line with the rest of the comparisons. Modeling error does not quite seem to be the answer, nor are these two Sommerfeld numbers close to each other.

3.6 Comparison for Someya #5

The final experimental data set from Ref. 29 is that for test bearing number five. These data were obtained with a floating bearing/rigid shaft type test rig, with manual mechanical static loading. Results for static and dynamic characteristics are presented in both tabular and graphical form.

3.6.1 Data

The oil used is identified as a #90 Turbine oil, with a viscosity of 13.41 mPa•s at 50 degrees. Sufficient data were once again presented for a two parameter equation of the form of Eq. (4) for the viscosity-temperature relationship for the oil. The bearing geometry data presented did not include feed groove details, so nominal dimensions were assumed. The bearing model is as follows:

Diameter:	50 mm
Length:	50 mm
C_d/D ratio:	0.00132
Weep Hole Dia:	0.1 mm
Oil Inlet Dia:	3.8 mm
Grooves:	0 and 180 degrees from horizontal
	10 degrees of arc width

The comparisons between the experimental data of Ref. 29, tables 3.5.1 and 3.5.2 and the appropriate NPADVT analysis are presented below in Fig. 61 and Fig. 62. As with test bearing number two above, the independent variable is the nominal Sommerfeld number reported in Ref. 29. Fig. 63 presents the comparison as a percentage error (100*(experimental - NPADVT) /experimental)).

Comparisons: NPADVT vs. Published Experimental Results

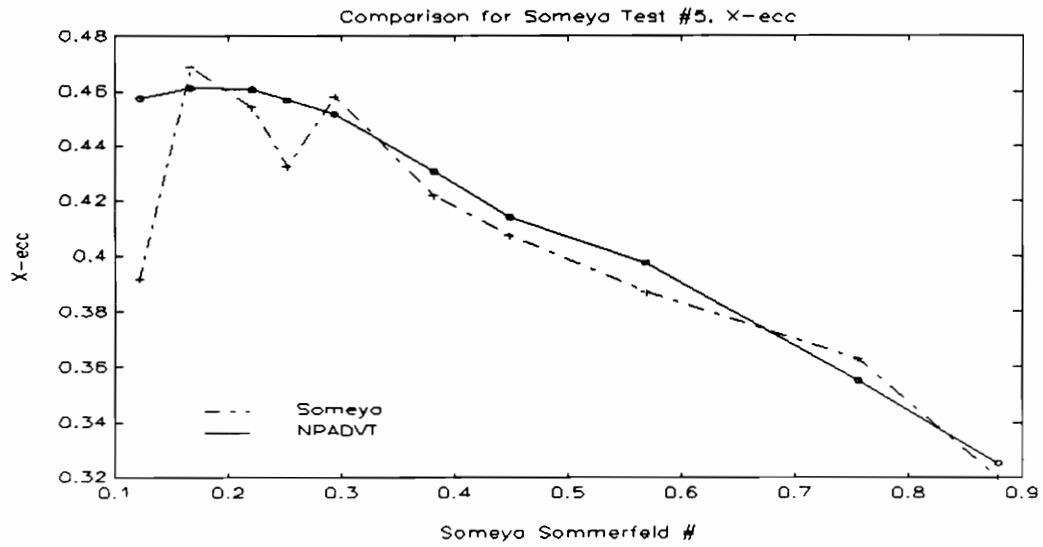

Fig. 61: X-Eccentricity Ratio for Someya Test 5

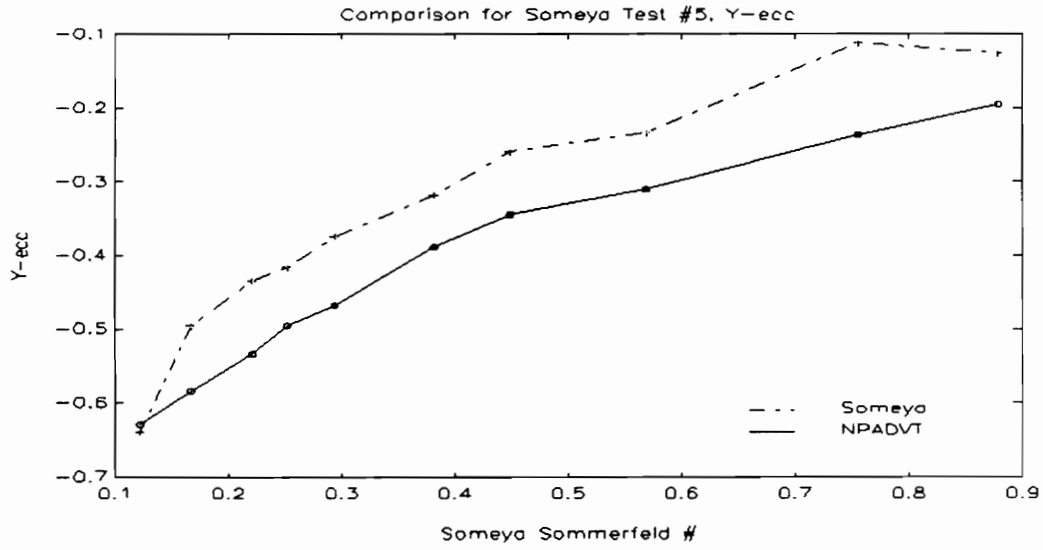

Fig. 62: Y-Eccentricity Ratio for Someya Test 5

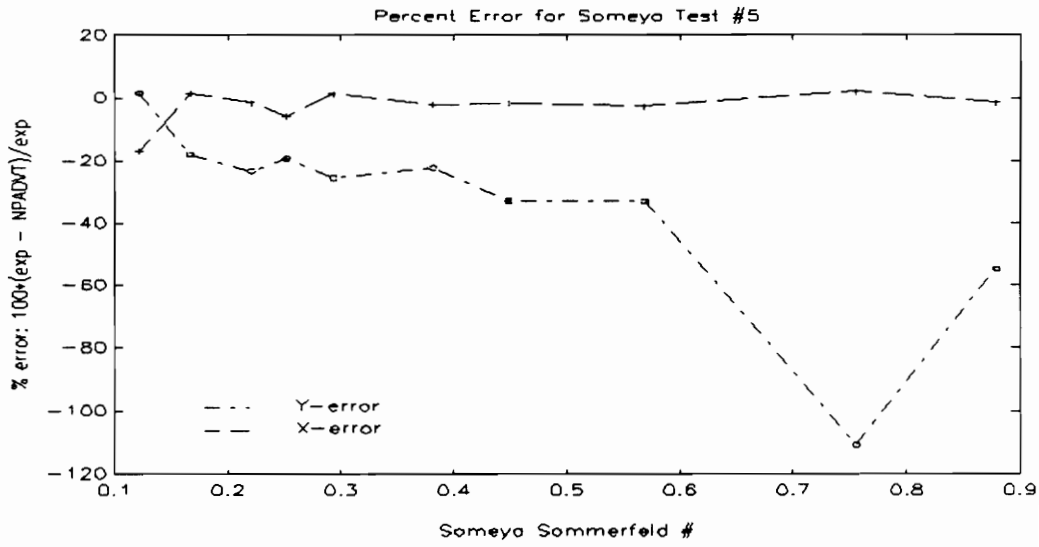

Fig. 63: Percent Error for Someya Test 5

3.6.2 Discussion of Results

The comparison for this set of experimental data does not show the same trends as the previous comparisons. The X-position is not only close in absolute terms, but it also generally has the correct shape. The Y-position seems to be about the right shape, but the percent error for Sommerfeld numbers greater than 0.5 is high; this difference could be caused by a zero offset. These seemingly anomalous results could also be the result of a number of other factors; among them, this bearing is only half the diameter of the other bearings examined. The smaller diameter could result in different mechanisms dominating the difference between experimental results and NPADVT analysis than in the larger bearings. The effects of cavitation or feed grooves, for example, might be more significant in the smaller bearing.

3.7 Comparison for Andrisano

The final experimental data set to be examined is from Ref. 3, A.O. Andrisano's 1988 Journal of Tribology article. Although this article primarily focuses on a fairly sophisticated investigation of the surface temperature of a rotating shaft, results are presented for shaft locus as a function of load and speed. This work made use of a floating bearing/rigid shaft test rig at the University of Bologna (Italy). This rig is

loaded with dead weight through a link mechanism. This set of results is especially interesting because the feed geometry is a single groove, located at the top of the bearing (the other data sets used two horizontal grooves). Although it was hoped that this data would shed light on the possibility of problems with feed groove effects not modeled in NPADVT, the experimental data exhibit some unusual trends that prevent strong conclusions from being reached.

3.7.1 Data

The data used for comparison purposes, are those of Andrisano's Fig. 9. This figure presents relative eccentricity as a function of load and speed for an ISO 46 oil with a viscosity of 25.96 mPa•s at 50 degrees. Two temperature-viscosity points are presented, which allows a relation of the form of Eq. (4) to be specified. A nominal lubricant specific heat and density are also presented. The bearing model used is as follows:

Diameter:	45 mm
Length:	45 mm
C_d/D ratio:	0.00133
Weep Hole Dia:	0.635 mm
Oil Inlet Dia:	5.08 mm

Groove: 90 degrees from horizontal

15 degrees of arc width

The data scaled from Andrisano's Fig. 9, and the NPADVT results for shaft eccentricity ratio for 10, 20, 30 and 40 Hz are graphically compared in Fig. 64 through Fig. 71. Fig. 72 through Fig. 75 present the same data as a percentage error (100 x (experimental - NPADVT) / experimental).

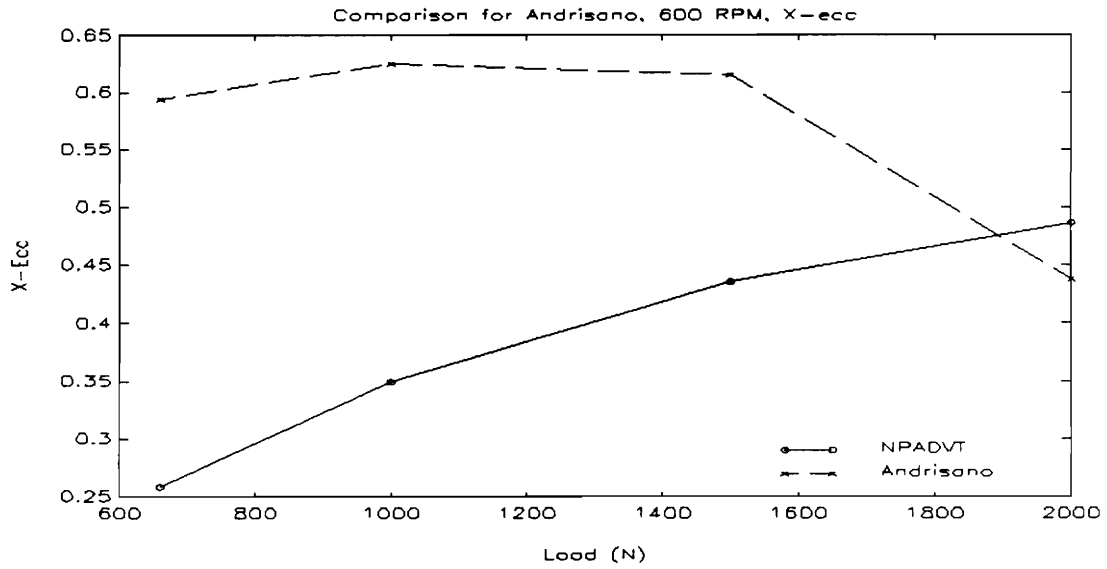

Fig. 64: X-Eccentricity Ratio for Andrisano, 10 Hz

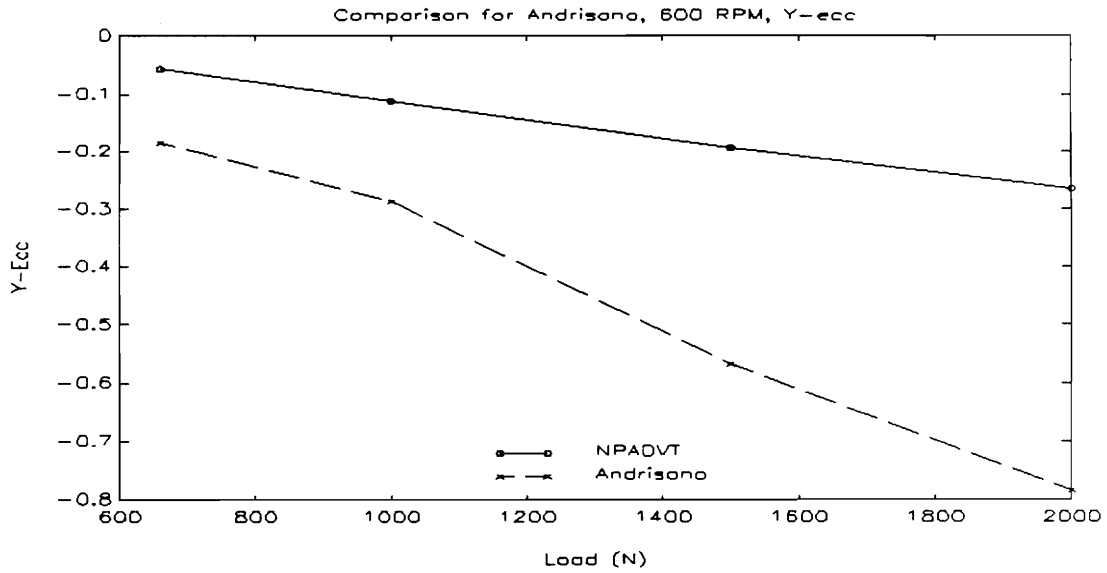

Fig. 65: Y-Eccentricity Ratio for Andrisano,10 Hz

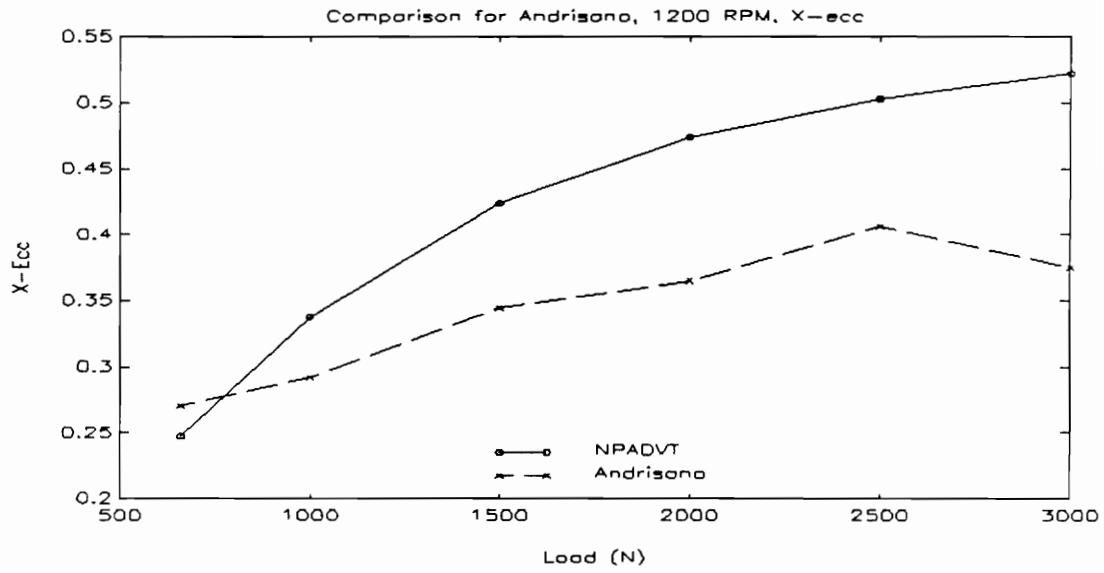

Fig. 66: X-Eccentricity Ratio for Andrisano, 20 Hz

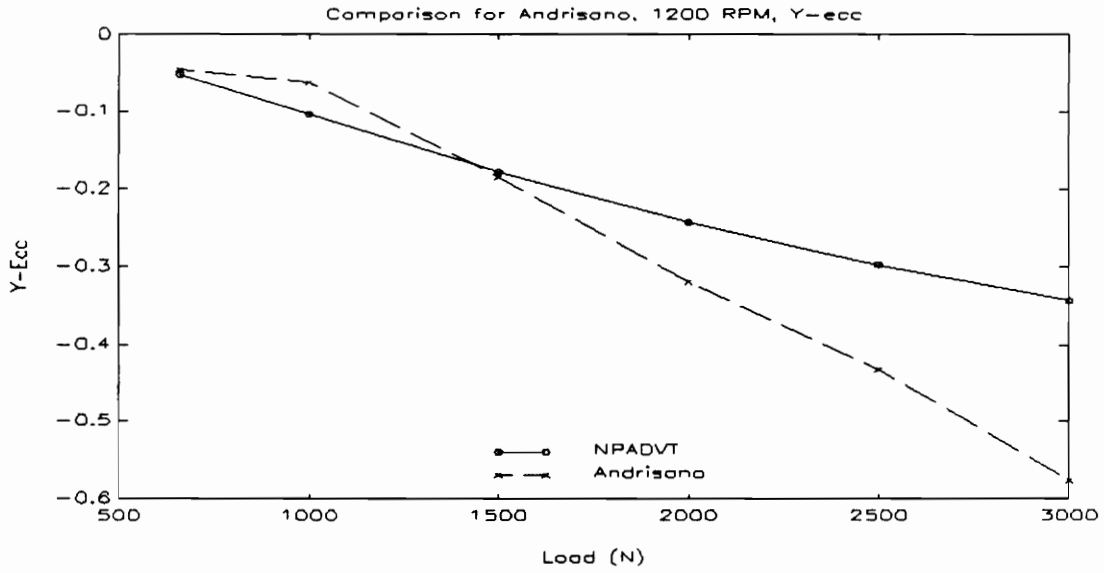

Fig. 67: Y-Eccentricity Ratio for Andrisano, 20 Hz

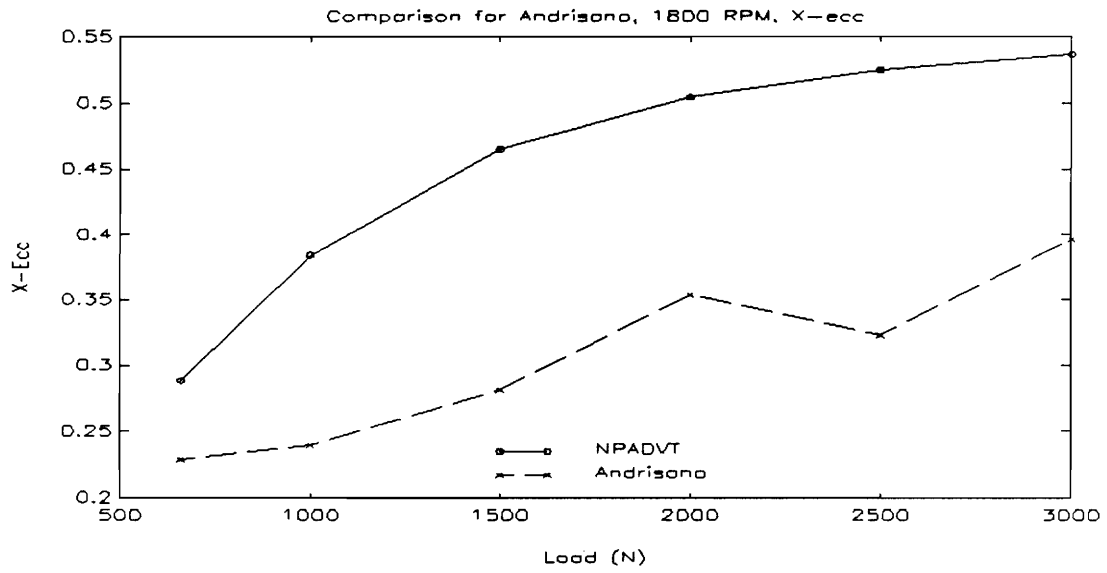

Fig. 68: X-Eccentricity Ratio for Andrisano, 30 Hz

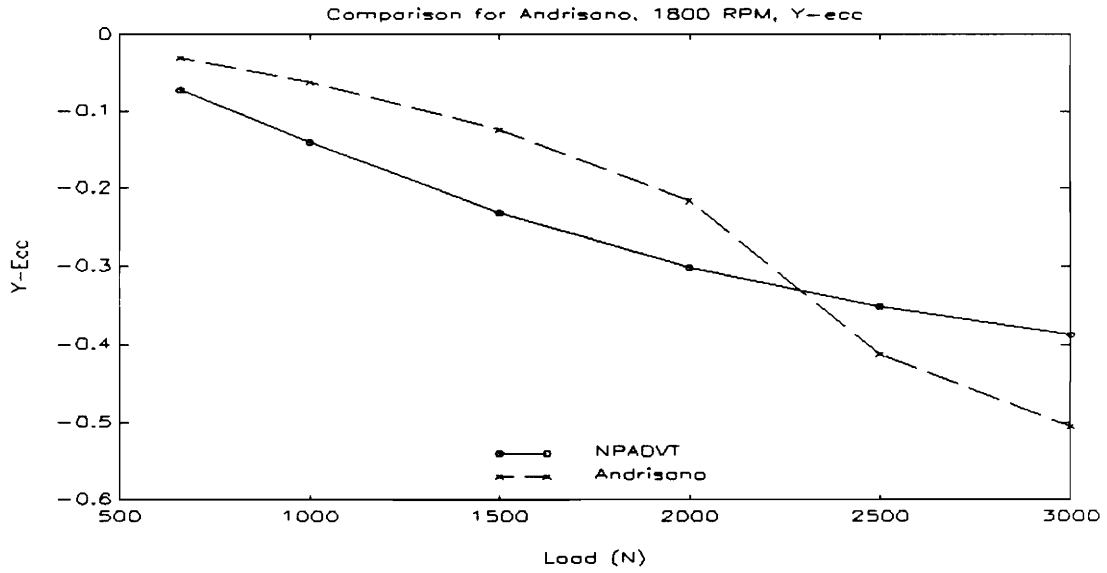

Fig. 69: Y-Eccentricity Ratio for Andrisano, 30 Hz

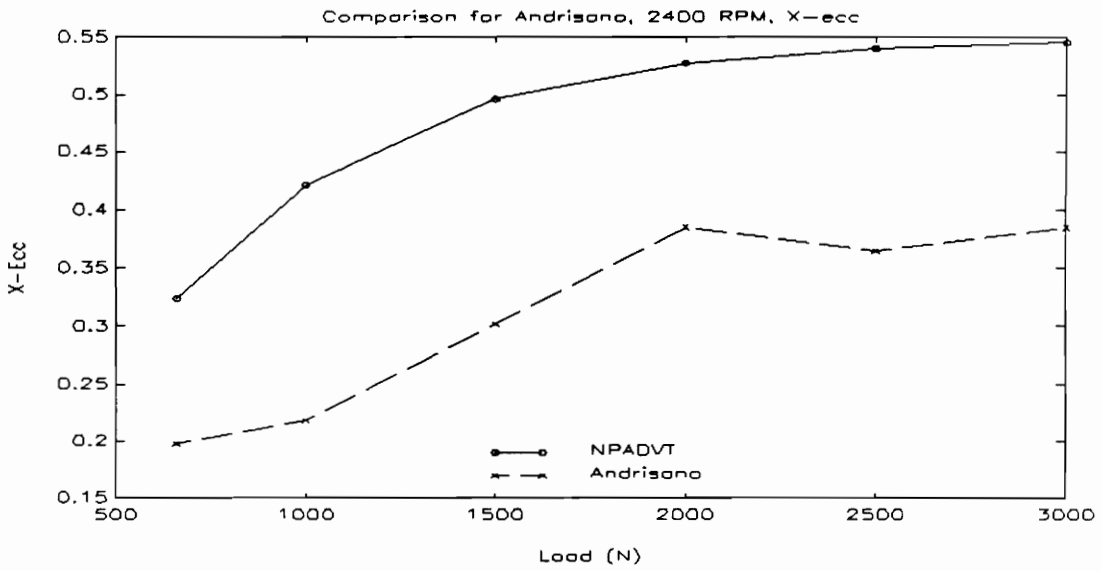

Fig. 70: X-Eccentricity Ratio for Andrisano, 40 Hz

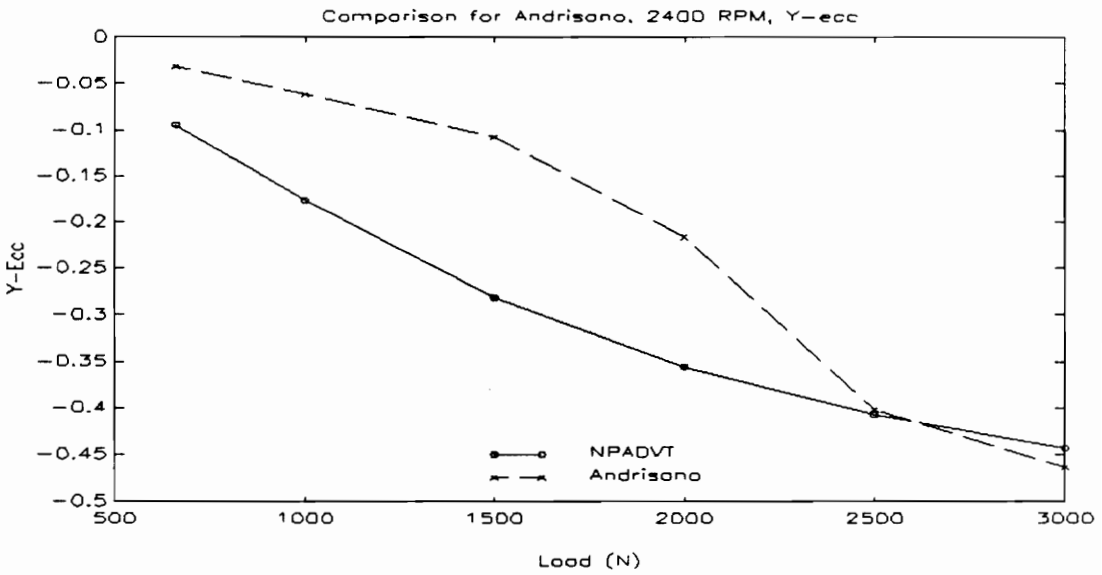

Fig. 71: Y-Eccentricity Ratio for Andrisano, 40 Hz

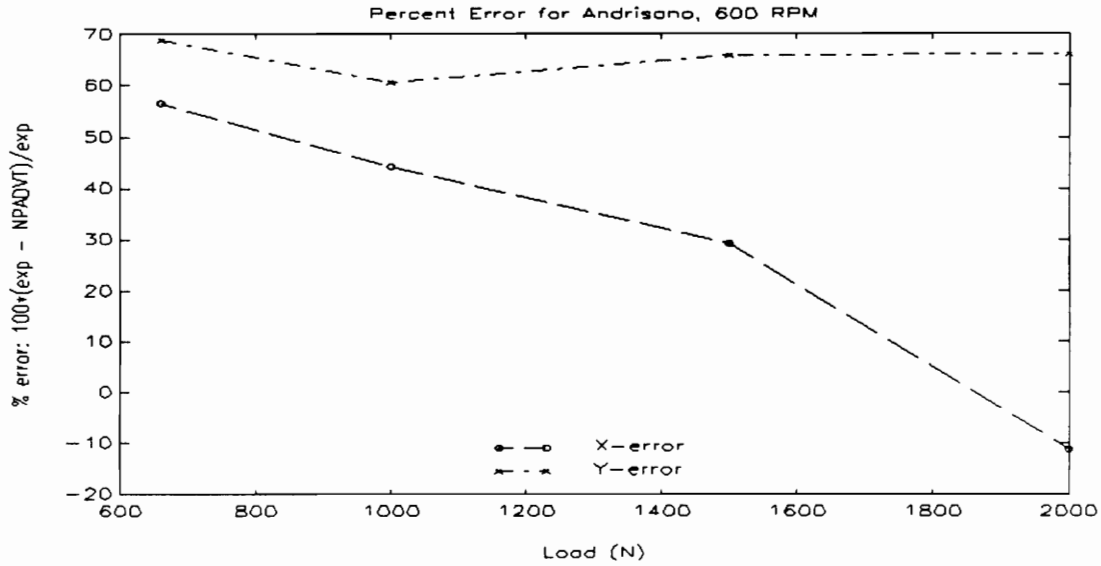

Fig. 72: Percent Error for Andrisano, 10 Hz

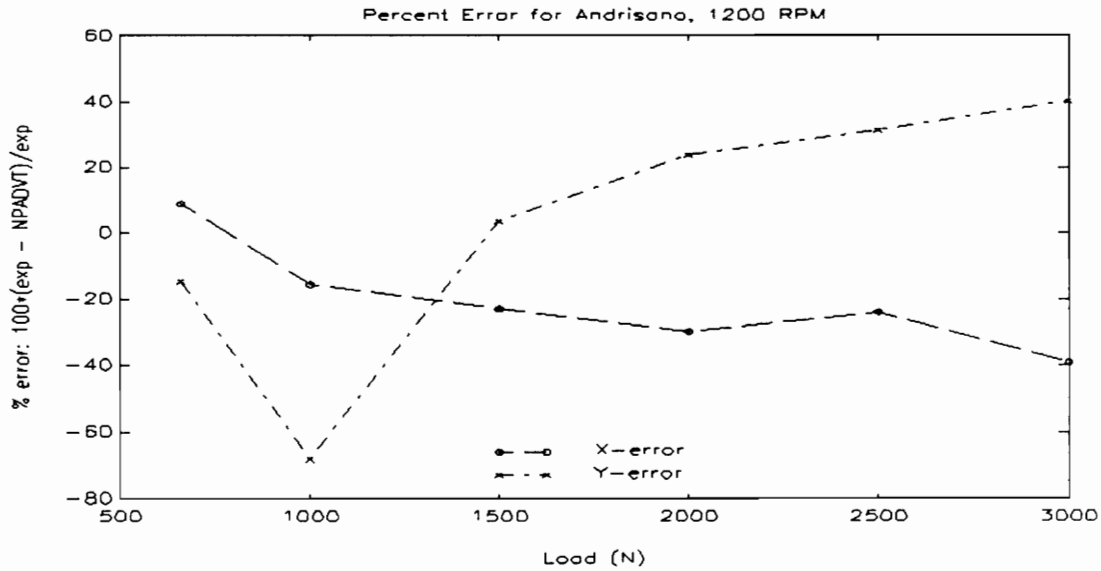

Fig. 73: Percent Error for Andrisano, 20 Hz

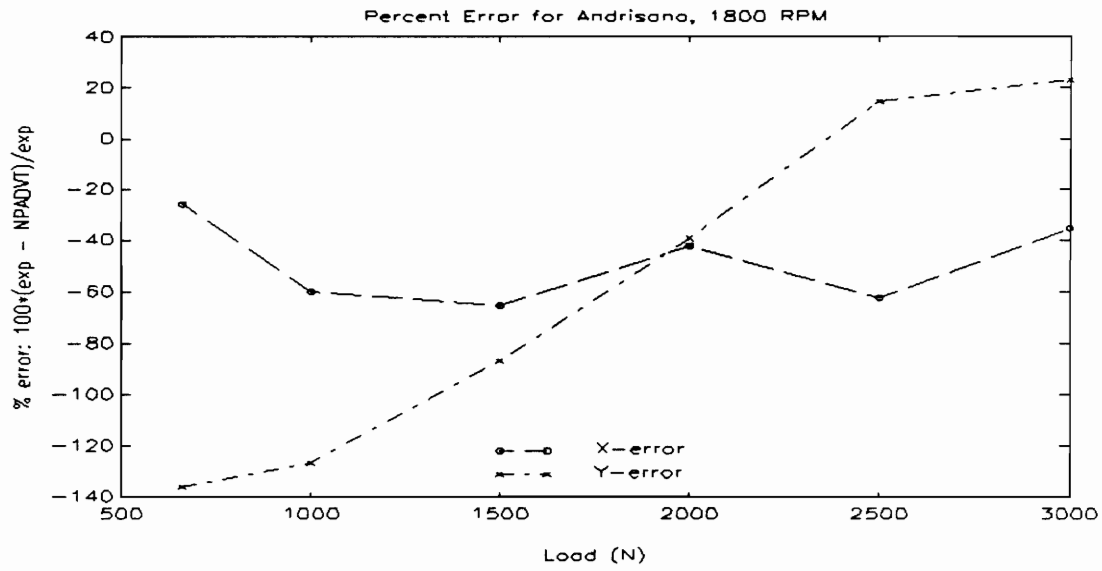

Fig. 74: Percent Error for Andrisano, 30 Hz

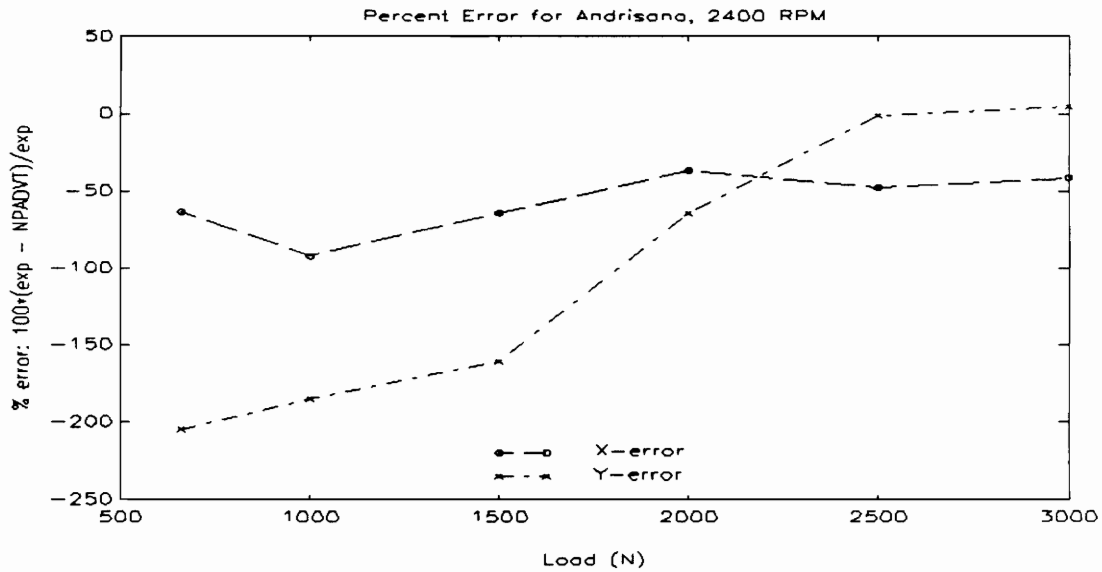

Fig. 75: Percent Error for Andrisano, 40 Hz

3.7.2 Discussion of Results

As mentioned in the introductory remarks to this data set, the data exhibit some unusual trends. In particular, the X-eccentricity ratio does not change smoothly as load increases; rather, for some reason, it exhibits a discontinuity at 2500 N load for 20, 30, and 40 Hz (the 10 Hz data does not include loads above 2000 N). This discontinuity is not simply the point at which the X-eccentricity ratio begins to reduce with increasing load, as would be expected for a plain journal bearing. In the 20 Hz (Fig. 66) case, the X-eccentricity ratio does begin to decrease, but for the 30 Hz and 40 Hz (Fig. 68 and Fig. 70) cases, the X-eccentricity ratio decreases at 2500 N, then increases again at 3000 N. This behavior is unusual. One possibility is that discrete test runs were employed for each load/speed point (or so the article implies), which could easily result in zero shifts, or slightly different thermal conditions. Uncertainties in the shaft position measurements do not really provide the answer. Although they are not specified, they would have to be on the order of 20 percent to explain the unusual behavior.

Despite this possible problem, it was hoped that the difference between the two oil grooves at 0 and 180 degrees employed in the other works reviewed, and the single groove at 90 degrees employed in this work, might shed some light on the influence

of feed groove effects. Unfortunately, none of the NPADVT results are sufficiently close to the Andrisano experimental results to draw strong conclusions. The differences are not altogether surprising, as the NPADVT model is not very refined - it spreads 50 nodes out over 345 degrees of arc width, as opposed to 50 nodes over 180 degrees of arc for the other bearings examined (50 circumferential nodes is the maximum allowed in the current version of NPADVT). Indeed, this model would begin to diverge if many more than 5 temperature-viscosity iterations were employed (one possible solution to the limitation on number of nodes would be to use a smaller arc for the active pad, as much of the top of the bearing is most likely cavitated - this has not been explored). Even so, some general observations are possible. There is some support for the possibility of feed groove effects, as the X-eccentricity ratio results are in general closer than the Y-eccentricity results. The X-eccentricity ratio results do not, however, exhibit the correct shape relative to the experimental results. Later results presented for the VPI rig will show that the pressure effect does not seem to be the cause of the discrepancy between analysis and experiment. The comparison with the data of Ref. 3 does, however, point out the need for a higher limit on the number of circumferential nodes for bearings with pads encompassing such a large angular extent.

Chapter 4

VPI & SU Test Rig

4.1 Introduction and Orientation

This Chapter is devoted to describing the VPI rig in preparation for the presentation of results from the rig in Chapter 5 and 6. Both a summary description and a more detailed description are included in this chapter. This chapter also discusses instrumentation calibration issues and includes an uncertainty analysis for displacement and load.

4.2 Rig History

The VPI & SU rotor dynamics research laboratory fluid-film bearing test rig (VPI Rig), shown in Fig. 76 and Fig. 77, was designed and constructed in the mid-1980's by a major turbomachinery manufacturer to support the development of new compressor bearings. The rig was only run briefly before this program was discontinued. The rig was eventually donated to the university in the spring of 1989.

This test rig is of the fixed test bearing/floating shaft type. During the spring of 1990, as an undergraduate research project, the author restored it to a temporary working configuration and determined that it was still functional. The rig has since been permanently mounted on a large (7700 Kg+) reinforced concrete pedestal. In addition, adequate instrumention and automatic controls for operation and test control have been added.

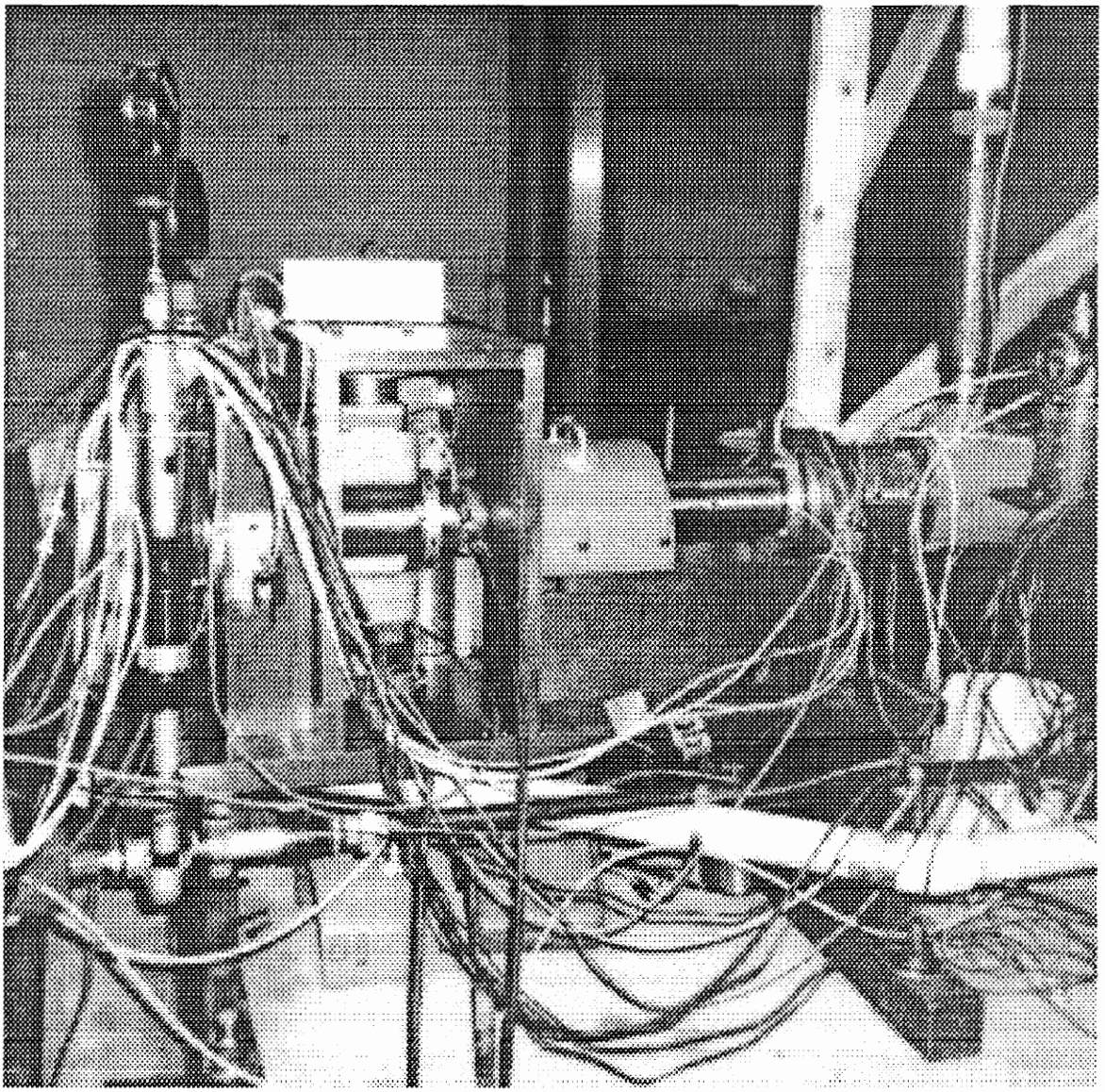

Fig. 76: VPI & SU Fluid Film Bearing Test Rig

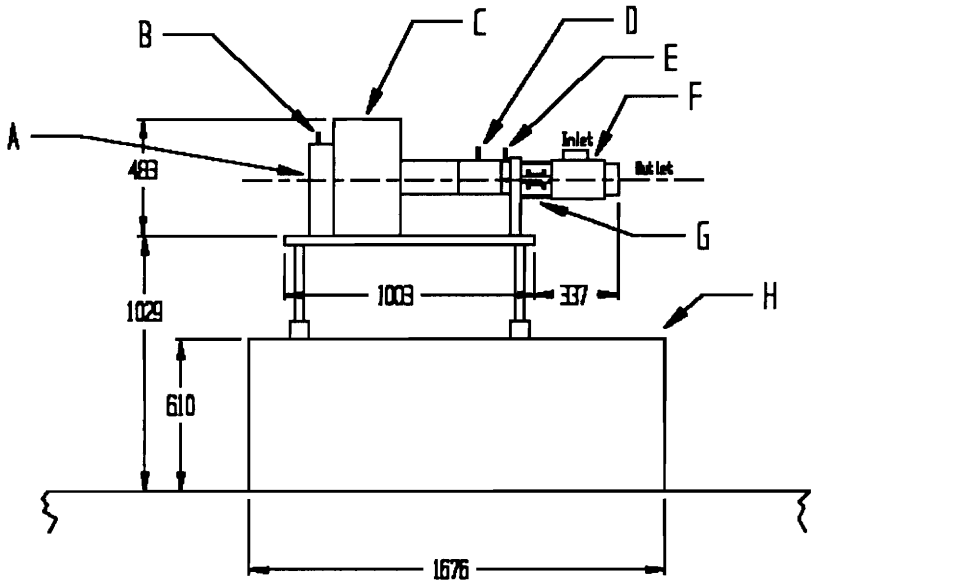

Legend

A - Test Bearing Housing
B - Shaft Displacement Probes (Inboard and Outboard of Bearing)
C - Loading Magnets Housing
D - Key Phasor Pickup
E - Rear Shaft Displacement Probes
F - Air Turbine
G - High Speed Coupling and Torque Sensor
H - Reinforced Concrete Foundation

Fig. 77: Test Rig Sketch

4.2.1 Summary of Test Rig Capabilities

Speed range: 3 Hz - 530 Hz,

Driver: 30 kW air turbine,

Loading: Approx. 6.9 kN shaft load; 5.7 kN bearing load; two axis loading (up-down, left-right),

Test Bearing Capacity: 203 mm Dia. by 90 mm deep cavity, shaft designed to accept sleeves to adapt to bearing diameter,

Oil System: 0.04 m^3 heated oil reservoir, 500 cm^3/s vane oil pump with a pressure rating of 0.61 MPa,

Instrumentation: Shaft position (3 planes), oil temperature and pressure, bearing temperatures, shaft speed, shaft load, and turbine output torque,

Data Acquisition: Combination of stand alone and microcomputer hardware,

Control and Supervisory: Air turbine speed controlled by a custom PC based controller and two pneumatically operated valves, separate overspeed/overtorque shut-off controller, air turbine shut-down for low oil level in test bearing and support bearing sump, or test bearing low oil pressure. Test bearing oil temperature control with commercial PID controller operating a pneumatic valve controlling water flow through

an oil to water heat exchanger, oil sump temperature with proportional heater controller.

4.3 Detailed Description of Test Rig

The detailed description of the test rig will be broken into 5 sections:

1) mechanical details
2) magnetic loading system
3) air turbine drive
4) test bearing oil system
5) other instrumentation.

4.3.1 Mechanical Details

The VPI rig, shown in Fig. 76, and schematically in Fig. 77 is designed using the rigid bearing mount/floating shaft paradigm. The test rig, constructed for the most part of type 410 stainless steel, has an estimated mass in the vicinity of 450 Kg, and is in turn securely bolted to a 7700+ Kg reinforced concrete foundation. This combination provides a very rigid bearing support. For static testing, the rig is essentially fixed in place. Mechanically, the rig is also extremely stiff, constructed from 25 mm and 38 mm plate, securely bolted together. The bearing housing is a

single piece of stainless steel, 330 mm wide by 375 mm tall by 127 mm deep. The shaft is also fabricated from type 410 Stainless Steel, treated to Rc 36/39 (yield strength of 1200 MPa vs. 500 MPa for untreated). It is 101.6 mm in diameter over most of the 0.762 m span between bearing centerlines. It necks down to 29 mm at the rear support bearing and to 31.8 mm at the test bearing (this end accepts the sleeve to adapt to bearing diameter). At the loading magnets, the shaft is cut down to 63.5 mm diameter to accommodate the laminates required to reduce eddy-current losses in the magnetic loading system. These laminates, of 0.36 mm thick Hiperco 50 (a high performance magnetic alloy), bring the shaft outside diameter to 108 mm diameter for the length of the magnetic loading system (described in the next section). The measured shaft slope due to load, across the test bearing sleeve (assumed to be rigid), is $6x10^{-4}$ mm/mm. The maximum shaft deflection relative to the bearing centerline is 0.095 mm at the loading magnets. Appendix A contains a detailed sketch of the measured shaft deflection.

The rear support bearing is a 30 mm ID by 50 mm OD, duplex angular contact ball bearing, mounted in a spherical housing to facilitate alignment. This bearing is lubricated and cooled by an oil mist lubrication system and is rated for continuous operation at the rig's maximum speed and load. This bearing has an experimentally

determined stiffness of 35 MN/m. The bearing is sealed on either side with a windback seal.

The test bearing is mounted in a carrier housing which matches the test bearing OD to the test rig bearing cavity ID of 203 mm. The fits on this housing are between line-to-line and 0.025 mm loose. The cavity of the bearing housing is approximately 70 mm deep, with openings for oil drains on the bottom, an offset oil inlet on the top, and a removable front cover. The shaft seal is again a windback design. The shaft is aligned to be parallel to the housing bore to 5.7 mm/mm. This alignment was performed with the test bearing in place with the following procedure:

1) load shaft down lightly and note dial indicator reading at 3 O'Clock position.

2) rotate shaft and note dial indicator reading at 9 O'Clock position.

3) adjust rear support bearing horizontal position until these two readings match.

4) balance shaft weight with up magnet and load shaft to the left.

5) adjust rear support bearing until 12 O'Clock and 6 O'Clock readings match

6) check horizontal position

This procedure was performed with the test rig at "cold" conditions. After the rig warms to operating temperature (43.3 degree oil temperature), the bearing housing grows by approximately 0.08 mm. To allow for this increase, the rear support bearing

was adjusted upwards by approximately 0.05 mm. With this adjustment, the warm bearing clearance, as indicated by a lift check, agreed with the original cold clearance plus an allowance for thermal growth.

The 30 kW, 3 Hz to 530 Hz air turbine drive is mounted to the rear bearing housing support through a four arm strain bridge (see Fig. 77). The turbine output shaft and the test rig shaft are coupled through a floating, double diaphragm coupling which offers very little resistance to shaft angular motion. The air turbine employs grease lubricated bearings and is rated for continuous operation at maximum speed. The compressed air for the air turbine drive is supplied from a large diesel compressor located outside the building through approximately 45 m of 50 mm diameter PVC pipe. Air filters, a shut-off valve and two pneumatically operated throttling valves (for speed control) are located several meters above the air turbine drive on a wooden support structure. This arrangement allows a reasonably long length of vertical PVC pipe to be attached to the air turbine in an attempt to minimize the influence of the air supply piping on the torque reading from the torque bridge. Unfortunately, the wooden structure is not rigid enough, and moves enough to measurably change the torque bridge zero. The torque bridge zero is also strongly affected by temperature changes. The rig electrical power and water supplies are also attached to this structure.

4.3.2 Magnetic Loading System

A magnetic loading system is employed to load the shaft, which in turn loads the test bearing (see Fig. 78). This non-contact loading approach eliminates some of the mechanical difficulties of loading a bearing via a rotating shaft. As designed, the loading system consists of four axial electromagnets arranged at right angles, thereby allowing loads to be applied in any arbitrary radial direction. Currently, only three magnets are installed (up, down, and left). These magnets are capable of applying a static load of up to 6900 N to the shaft at a nominal 0.5 mm air gap. Depending on the location of the test bearing centerline, between 80 and 85 percent of this load is applied to the test bearing. Each magnet is mounted on a 8900 N capacity load cell to provide a measurement of applied load. The specifications on these load cells suggest a maximum combined bias and random uncertainty of plus or minus approximately 32 N. This uncertainty, and means of reducing it, will be discussed in greater detail in a later section.

The loading magnets are constructed around a U-shaped piece of solid Hiperco 50, with 700 turns of wire around each leg. The eddy-current losses, due to the solid core and the inductance due to the large number of turns, limits the applied load to static or almost static (less than a few Hertz). This limitation applies only to the

loading magnets; the rotating portion of the shaft is laminated, and thus would be able to operate at reasonably high frequencies. At the maximum load of 6900 N, the magnets require 7.2 A at 58 volts.

As currently configured, the loading system does not include a true feedback control system. Loads are set manually or under computer control by increasing the current supplied to the magnets until the desired load, as sensed through a data acquisition card in the PC, is obtained. This approach is adequate for the static tests associated with this work.

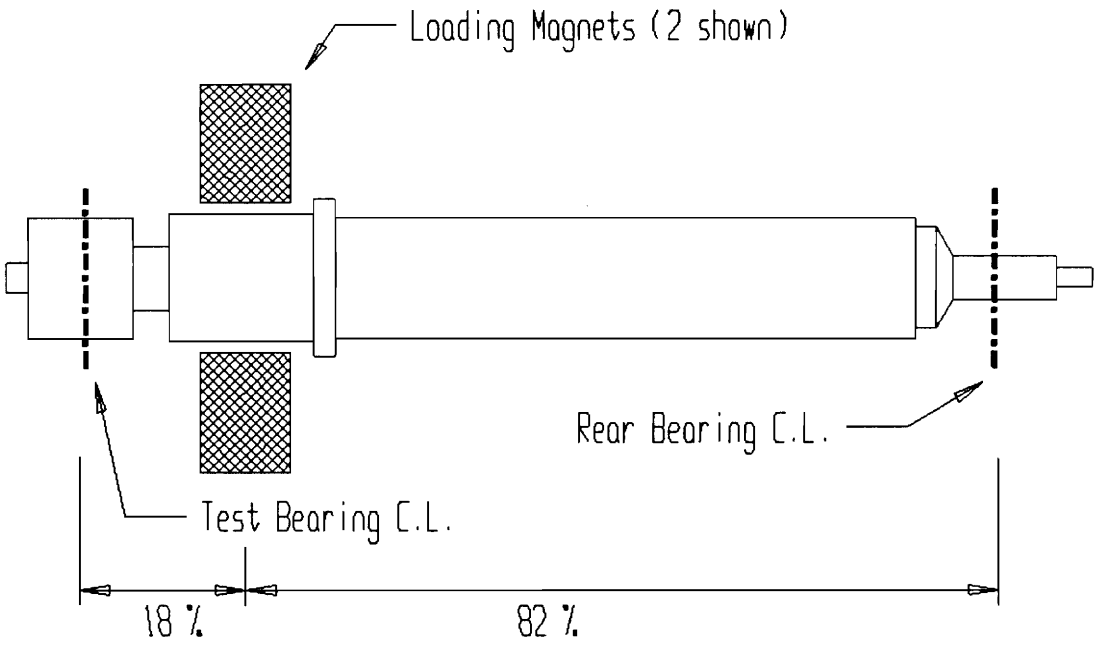

Fig. 78: Shaft/Magnet Arrangement

4.3.3 Air Turbine Drive

The air turbine drive system is a single stage, 30 kW air turbine, rated for continuous operation at up to 583 Hz, Minimum operational speed is in the vicinity of 3 Hz. The air turbine is mounted on a four arm torque bridge to provide a means of monitoring the turbine output torque. This measured torque, however, is greater than that caused by losses in the test bearing alone. Additional losses in the support bearing, seals, magnetic loading system, and shaft windage increase the drive torque above the bearing torque. A custom PC based control system, with feedback from the turbine speed pickup (a 30 tooth gear), is employed to control speed by modulating two pneumatically operated control valves (32 mm and 20 mm) in the air supply line. This system controls the operating speed to within plus or minus 0.4 Hz. The turbine speed pickup is also connected to a separate overspeed shut-down controller. This controller will shut off the air supply with a solenoid valve if the speed reaches an operator set limit value. This controller also contains the signal conditioning and readout for the torque bridge. Automatic shut-down with this shut-off valve also occurs for low oil level in either the test bearing oil sump or the support bearing oil mist system, as well as for low oil pressure at the test bearing oil inlet. The operator may also manually close this shut-off valve.

4.3.4 Test Bearing Oil System

The oil system for the test bearing consists of a 0.04 m^3 heated sump, a 500 cm^3/sec vane oil pump with a pressure rating of 0.6 MPa, an oil to water shell and tube heat exchanger and a commercial PID control system which regulates cooling water flow to control oil temperature based on feedback from a thermocouple located in the bearing oil inlet passage. The oil is filtered through a single 10 micron filter. The supply temperature is generally held to within ± 1 degree C of the setpoint temperature. Pressure at the bearing housing inlet is controlled with a spring loaded bypass valve, which maintains the supply pressure very close to the initial pressure setpoint. Flow measurement is provided by a variable cross-section flow meter (rotameter). Pressure is measured with an analog pressure gauge at the inlet to the bearing housing. The oil reservoir temperature is maintained above the bearing supply temperature with proportional (electrical) control of the tank heater. This elevated temperature allows the bearing oil inlet temperature to be controlled by modulating the water flow through the heat exchanger. Oil supply and exit temperatures at the test bearing are measured with type J thermocouples connected to the PC data acquisition system.

4.3.5 Other Instrumentation

The shaft displacement is measured at three axial locations to allow shaft angular and radial displacements to be characterized. Two (1x, 1y) eddy-current displacement probes are installed just inboard of the rear shaft support bearing. Four (2x, 2y) eddy-current displacement probes are installed in opposing pairs just inboard of the test bearing. Two (1x, 1y) eddy-current displacement probes are installed just outboard of the test bearing location. The dual, opposed probe approach used at the inside measuring location allows uniform diametral growth, such as could be caused by thermal expansion, or centrifugal growth, to be cancelled from displacement measurements. The magnitude of such growth can also be estimated using this approach. The use of opposed probes also has the advantage of reducing noise, thereby increasing resolution. Although it would be desirable, dual opposed probes are not installed at the outboard probe location. The combination of probes used should allow the shaft displacement at the bearing centerline to be estimated with a sufficiently low uncertainty for present purposes (see section on uncertainty analysis for details). These probes are connected to a stand-alone instrument which takes shaft synchronous readings, thus allowing electronic run-out compensation to be employed. This instrument is designed to download data to a PC and has been specially modified to allow direct PC control of data acquisition. Each sample is composed of 32 8-bit

readings per revolution for 8 revolutions, for a total of 256 readings per channel per sample. These readings are used along with a 12-bit integrated shaft centerline reading (6.29 second integration time constant), to provide a compensated average shaft centerline position.

Shaft speed is sensed with both a 30 pulse per revolution speed pickup in the air turbine as well as by a one time per revolution key-phasor pulse from the test rig shaft. The key-phasor pulse is used by the stand-alone displacement instrumentation to provide the synchronous data acquisition required to perform electrical run-out compensation.

Other test rig bearing temperatures are monitored with thermistor sensors installed on the air turbine ball bearing housings (sealed grease lubrication), as well as the test rig rear support ball bearing housing (oil mist lubrication) to enable action to be taken in the event of high bearing temperatures.

Finally, a thermistor sensor is installed in the air turbine exhaust to help diagnose any frosting problems in the turbine.

4.4 Sensor Calibration

Due to the extreme dependence of the results on the accuracy of the eddy-current displacement probes, a great deal of effort was expended in calibrating the probe/proximeter(demodulator)/amplifier/data acquisition instrument system. The probe/proximeter system specifications are given by the manufacturer as: non-linearity less than 0.02 mm, noise floor of less than 0.0025 mm (the actual noise floor seen in testing is close to an order of magnitude smaller), with a scale factor temperature effect of -3% at 65 degrees at a 1.27 mm gap setting (this figure agrees well with an experimental verification of the temperature sensitivity). The nominal probe/proximeter scale factor is 8.0 volts per millimeter. This scale factor does not give sufficient resolution with the 0.0244 volt minimum static resolution of the data acquisition equipment employed. Therefore, the output of each probe/proximeter is also passed through a times five amplifier (LM318 op amp). To verify the manufacturer's probe/proximeter specifications and check the calibration of the times five amplifiers, each of the probes was calibrated to the appropriate target (shaft or bearing sleeve). For calibration, each probe was mounted on a movable fixture and the probe measurements compared to a measurements taken with a precision dial indicator with 0.0025 mm gradations. The amplified proximeter output was connected to a 12-bit analog to digital board through a bucking power supply (the

proximeter output is negative 5 to 17 volts), and a low pass filter. These components were calibrated as a system with a calibrated 5 1/2 digit voltmeter, specified to be accurate to ± 0.0009 volts worst case. The probe calibration procedure used is as follows:

1) Allow system to warm up,
2) Set probe offset to approximately 0.7 mm,
3) Take 9 readings at 0.025 mm increments, moving away from target, and obtain a least squares calibration slope,
4) Take 9 readings at 0.025 mm increments moving towards shaft from end of previous series, and obtain least squares slope,
5) Finally, take 18 readings at 0.013 mm increments moving away from shaft, starting at initial start point, and obtain least squares calibration slope.

Each data point is the average of 1000 points on two channels, for a total of 2000 points, over a 2 second period. The standard deviation of the data set for each data point was very low, indicating that noise contamination of each reading was minimal. The slope in all cases was repeatable to better than 1 percent. The maximum deviation from linearity was 9.65×10^{-4} mm (this deviation may well be related to the dial indicator used, as it occurs at roughly the same place with each probe); the deviation from linearity is generally an order of magnitude better than this figure.

The accuracy specification for the 12-bit data acquisition system used for the bearing testing is given as $\pm 0.5\%$ of reading + 0.0192 V (this translates to ± 0.00125 mm). With these accuracy figures, the ± 0.0025 mm uncertainty in displacement measurements used in the uncertainty analysis should be a conservative figure.

The manufacturer of the load cells used to measure magnet load quotes the following inspection limits for the load cells:

Rated Capacity:	8896 N
Non-Linearity:	± 0.20 % F.S. (17.8 N)
Hysteresis:	± 0.15 % F.S. (13.3 N)
Repeatability:	± 0.05 % F.S. (4.4 N)

Since these numbers are the inspection limits which 100% of the units must satisfy, they correspond to a spread of approximately 3 standard deviations. Since the uncertainty analysis for this work is based on a 95% confidence interval, the above specifications need to be adjusted by a factor of 1.96/3.00 (the ratio of standard deviations for 95% to 99%). The resulting specifications are:

Non-Linearity:	± 11.6 N
Hysteresis:	± 8.7 N
Repeatability:	± 2.9 N

The instrumentation amplifiers used to amplify the load cell output are specified as linear to 0.005 percent of the output (approximately 14-bit accuracy). To check the calibration of the load cells, they were bolted to one of the actual loading magnet mounting plates, with a calibration fixture rather than a magnet attached, and placed in a tension testing machine. The down magnet load cell conveniently showed the best agreement with the load indicated on the tension testing machine; the maximum deviation was less than 5 N, the hysteresis was about half of the quoted figure. Thus, the manufacture's quoted specifications will be used as a conservative estimate of the load measurement uncertainty.

Since the temperature measurements are influenced by conduction and convection effects not examined in this work, and will be primarily used as reference points for the comparisons to analytical data, a several degree uncertainty in temperature is acceptable. As a result, the nominal calibration of the temperature probes was deemed adequate. A ± 1 degree uncertainty for the combination of thermocouple and data acquisition hardware should be reasonable and is assumed for all measured temperatures.

The inlet oil pressure measurements are taken with a 0 to 200 kPa dial type pressure gauge. This gauge was calibrated at 0.034 MPa by loading with a water column of

appropriate height and found to be accurate and repeatable (successive readings were correct and indistinguishable from one another). This calibration seems sufficient for present purposes. The work of Ref. 14 on the effect of supply pressure on bearing operating characteristics tends to confirm this assumption.

The RPM readings are obtained with the same instrument used for the displacement measurements. The readings are specified as accurate to within ± 1.5 RPM worst case. This specification is more than adequate for the purposes of this work. The acceptability will be confirmed in a later section on the analytically derived sensitivity of the static characteristics to several variables.

The least accurate measurement in this work should be the flow measurement. This variable is measured with a variable area type 7.5×10^{-3} cm^3 per minute flowmeter (rotameter). This flowmeter is specified as accurate to ± 4 percent of full scale, repeatable to $\pm 1\%$ of full scale. As this variable is intended for reference only, this uncertainty was deemed acceptable, and no attempt was made to calibrate this gauge.

4.5 Uncertainty Analysis

Before the experimental portion of this work was undertaken, an examination was made of the impact of the expected sensor and data acquisition system accuracy on the results to be obtained. This section will discuss this uncertainty analysis.

4.5.1 Discussion of Approach Employed

The approach used to analyze the impact of errors on the results to be obtained is that of Ref. 7. This work defines several levels of analysis:

Zeroth order -	Process is steady, all measurement errors are the result of the measurement system; this is the best that can be expected from the instruments employed.
First order -	All run-to-run variation is the result of unmeasured (or unmodeled) variations in the process itself.
N^{th} order -	Both the process and instrument errors are assumed to be random variables (instrument bias errors are random as well).

The basic equation employed in uncertainty analysis to examine the effect of measurement uncertainty on the experimental result, where the experimental result is assumed to be the result of a function of several variables, is derived from an equation of the form of Eq. (6) (if the result were measured directly, the uncertainty would be the measurement uncertainty itself):

$$r = r(x_1, x_2, x_3, \ldots, x_j) \tag{6}$$

r: experimental result

x_j: measured quantities

The uncertainty in the experimental result arising from the combined effect of the random measurement uncertainties can be approximated by a Taylor series expansion of Eq. (6) about the biased result. Assuming a linear effect of measurement uncertainties, uncorrelated measurement errors, discarding all but first order terms, and using some relationships from statistics, a root sum of squares (RSS) relationship between the measurement uncertainties and the uncertainty in the experimental result can be obtained as in Eq. (7):

$$U_r = \left[\left(\frac{\partial r}{\partial x_1} U_{x1} \right)^2 + \left(\frac{\partial r}{\partial x_2} U_{x2} \right)^2 + \ldots + \left(\frac{\partial r}{\partial x_j} U_{xj} \right)^2 \right]^{\frac{1}{2}} \tag{7}$$

U_{xj}: Uncertainty in measured xj

Note: partials are obtained either analytically, or as numerical perturbations.

Equation (7) assumes that all uncertainties are at the same confidence level (for example, 95% of all measurements will fall within the uncertainty bound about the true measurement) and uncorrelated.

Uncertainties are the result of both precision errors (such as resolution and noise), which are random and will average out given enough samples, and bias errors (primarily calibration), which remain constant or nearly constant from run to run and do not average out over multiple samples. To obtain a good estimate of the expected uncertainty, these two types of uncertainty are treated separately, then combined only as the final step. The estimated precision errors can be improved by taking multiple samples; the appropriate number of samples to take can be estimated a priori. Given the expected improvement resulting from averaging, a new "precision" uncertainty limit can be established. This figure can be combined with the bias error with the same root sum of squares technique used above. According to Ref. 5, the RSS approach can be expected to provide a 95% confidence level for the resulting uncertainty figure. This is the approach which will be used in this work. An alternative is to add the absolute values of the two uncertainty estimates, which would be expected to provide a 99% confidence level.

4.5.2 Zeroth Order Error Analysis

Since displacement probes could not be installed at the center of the bearing to obtain displacement information at this location, the displacement data from the two measurement planes either side of the bearing are combined to obtain an estimate of the shaft position at the bearing centerline. The shaft sleeve is assumed to be rigid between the inboard and outboard displacement probes and a straight line is passed through the two measurement planes. The equation for this line is then used to obtain the displacement at the bearing center.

The expected error sources with this approach are: probe calibration and precision errors, as well as errors in the measurements of test rig geometry required to fit a line and transfer between probe and bearing coordinates. Several assumptions were made concerning other error sources; these include:

- No uncompensated mechanical or electrical run-out at the probes
- Any temperature effects on probes are compensated for, or negligible (the latter is assumed)

Using the definitions shown in Fig. 79, Eq.(8) is used to calculate the test bearing centerline displacements (B_2):

$$B_2 = \frac{P_1(Ref\backslash MProbe - Ref\backslash MBrg) + P_2(Ref\backslash MBrg - Ref\backslash IProbe)}{(Ref\backslash MProbe - Ref\backslash IProbe)} \qquad (8)$$

The nominal dimensions and expected uncertainties for these quantities are as shown in Table IV. Appendix B contains sample calculations for obtaining the numbers in this table. Given the definitions above, the data reduction equation, and the calculated uncertainties, the individual contributions to the uncertainty of the displacement measurements at the test bearing (computed by taking partials of the data reduction equation - Eq. (8) - and multiplying by the appropriate uncertainty as in Eq. (7)) are as shown in Table V.

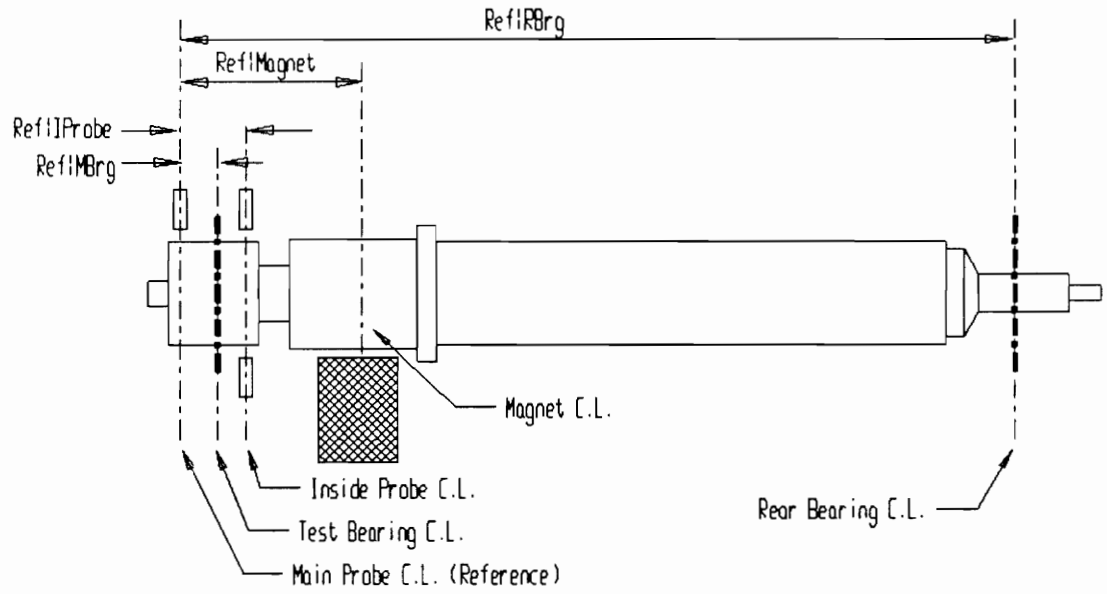

Fig. 79: Uncertainty Analysis Geometry

Table IV - Uncertainty Data for Shaft Center Position Estimation

Quantity	Nominal (mm)	Uncertainty (+/- mm)
Ref¦IProbe	67.6	0.84
Ref¦MBrg	36.8	0.41
Ref¦MProbe	0.0	0.406
Main Probes	$\pm$0.13	0.0025
Inboard Probes	$\pm$0.13	0.0013

Table V - Bearing Centerline Estimation Uncertainty

Source	Uncertainty (+/- mm)	Type of error
Test Brg Probe	1.38×10^{-3}	Random
Inboard Brg Probe	0.583×10^{-3}	Random
Ref¦MPRobe	0.963×10^{-3}	Bias
Ref¦IProbe	1.45×10^{-3}	Bias
Ref¦MBrg	0.945×10^{-3}	Bias

Using the RSS approach, the combined effect of the random errors results in an uncertainty of 1.50×10^{-3} mm in displacement measurements; the combined bias error effect is 2.35×10^{-3} mm. Although these figures are both almost two orders of magnitude smaller than the bearing radial clearance of 7.6×10^{-2}, The predicted effect of averaging various numbers of samples can be calculated to try and ensure that the dominant error be the bias error; this accuracy is the best that can be achieved with the equipment used for testing. Assuming the uncertainty above represents a 95% confidence interval, the expected standard deviation of a large sample can be computed as 7.65×10^{-4} mm. Using this figure, the expected effect of multiple samples can be computed by using the Student's t distribution to allow for the fact that small samples are involved. Appendix B again contains details of this procedure. With this approach, the following results are obtained for a 95% confidence interval as a function of the number of samples.

# of Samples	Expected Rand. Uncert. (+/- mm)
2	68.8×10^{-4}
5	9.50×10^{-4}
8	6.40×10^{-4}
10	5.47×10^{-4}
15	4.21×10^{-4}
25	3.15×10^{-4}

From this information, a target of 10 samples per data point was established. With 10 averages, the expected RSS total uncertainty is 2.41 x 10^{-3} mm. Also, the expected experimental scatter due to probe uncertainties is 0.547 x 10^{-3} mm (optimistically assuming all other effects to be insignificant). To avoid hysteretic effects, as well as to have greater confidence in the data, data sets are taken with increasing, then decreasing load to observe the loading hysteresis, then three more data points at each load are taken in random order for each test sequence. Also, the data points are obtained with two tests taken on different days.

As with displacement, it is not possible to measure the load actually applied to the bearing centerline. Instead, the loads are measured at the loading magnets, and an estimate of the load at the bearing is computed using the rig geometry. The load is assumed to be proportionally distributed between the test and support bearings. The proportionality factor is developed by experimentally determining the effective center of force for the loading magnets by measuring the load at the test bearing location with a load cell and comparing the measured load with the measured magnet load. The known rig geometry and test bearing location are then used to compute an equivalent proportionality constant for a test bearing. The equation used for this computation is Eq. (9) - geometry definitions are as in Fig. 79:

$$Brg\ Load = Mag\ Load \frac{(Ref\backslash RBrg - Ref\backslash Mag)}{(Ref\backslash RBrg - Ref\backslash MBrg)} \tag{9}$$

The nominal magnitude and uncertainties of the load cell reading, and the distance from a reference mark to the effective magnet centerline, are shown in Table VI (all other quantities are as above for the displacement measurement). After taking partial derivatives and multiplying by the appropriate magnitude (as with displacement), the resulting uncertainties are as shown in Table VII.

Assuming 10 samples as above, the random error from the load cell measurement can be expected to decrease by a factor of about 2.74, giving a resulting random uncertainty of 3.4 N. This uncertainty is the worst case, and corresponds to the expected experimental scatter. The combined effect of all load cell errors is an uncertainty of 30.3 N (95% coverage). This is the uncertainty assumed for the experimental results. It should be noted that this analysis ignores the possible effects of loading magnet residual magnetism causing a zero offset during the shunt calibration and zero procedure used by the data acquisition program.

Table VI - Uncertainty Data for Load Estimation

Quantity	Nominal	Uncertainty
Ref¦Mag	170.9 mm	3.0 mm
Load Measurement		
- Bias	±0.13%F.S.	±11.6 N
- Random (Combined)	±0.103% F.S.	±9.2 N

Table VII - Load Estimate Uncertainty

Source	Uncertainty (+/- N)	Type of error
Ref¦RBrg	1.27	Bias
Ref¦Magnet	27.6	Bias
Ref¦MBrg	2.91	Bias
Load Measurement		
- Bias	11.6	Bias
- Random	9.2	Random

4.5.3 Sensitivity Analysis

Using NPADVT, it is possible to analytically compute the expected sensitivity of the shaft position to variations in load, speed, and inlet temperature. Although it will be later shown that these results should be viewed with skepticism, they should be of the correct order of magnitude. A central difference scheme, Eq. (10), is used to generate the sensitivities to each variable presented in the figures below:

$$Sensitivity(x) = \frac{\left(\frac{Position(...,x - \delta x,...) - Position(...,x + \delta x,...)}{(x-\delta x) - (x+\delta x)} \right)}{Position(...,x,...)} \times 100 \qquad (10)$$

The results at typical speeds of 1000 RPM, 2500 RPM, 5000 RPM, 7500 RPM, and 9000 RPM for a 101.6 mm plain bearing with a nominal 0.0015 C_d/D ratio are shown in Fig. 80, Fig. 91 through ? (results are presented as both percent and absolute sensitivity). This analysis was not performed for the pocket bearing, but the magnitude of the sensitivities should be similar.

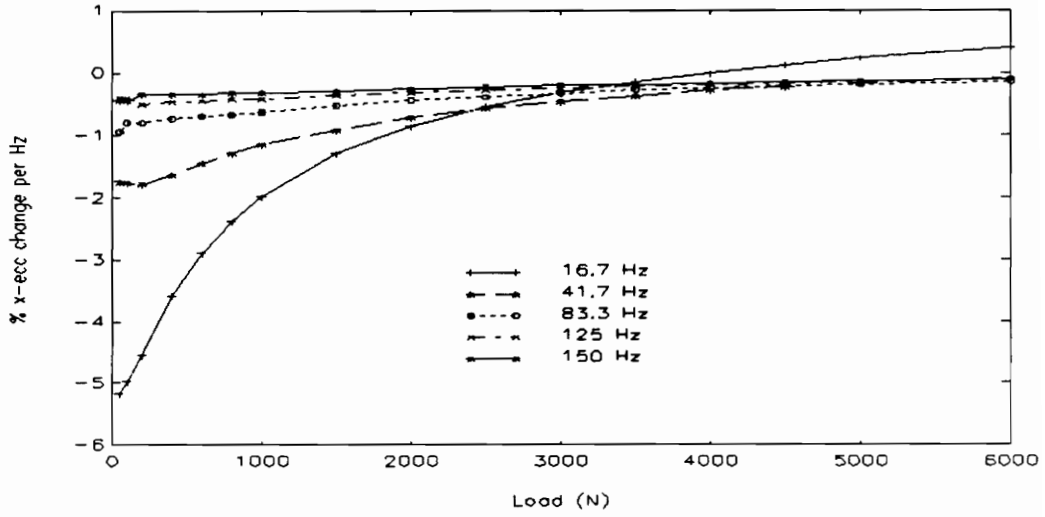

Fig. 80: Percent X-Eccentricity Ratio Change per Hz

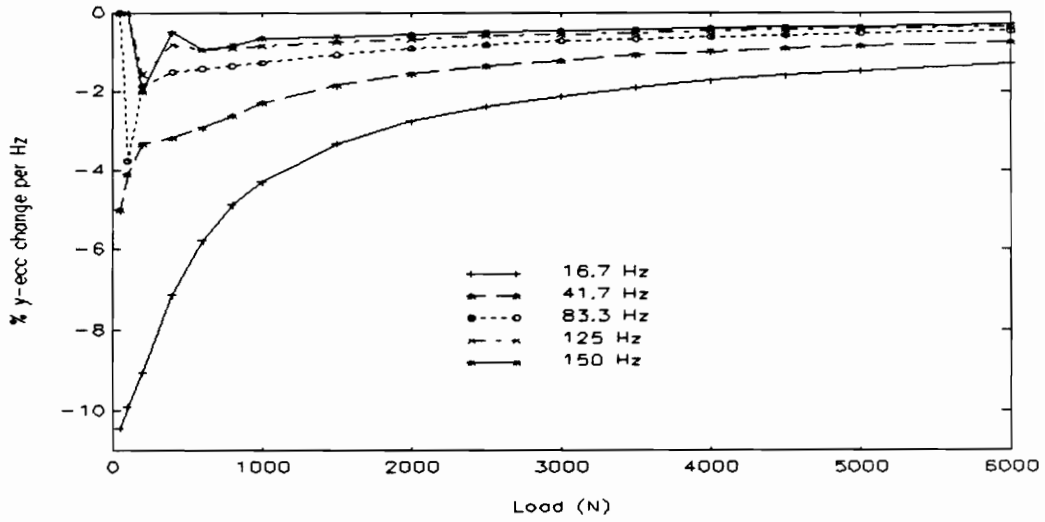

Fig. 81: Percent Y-Eccentricity Ratio Change per Hz

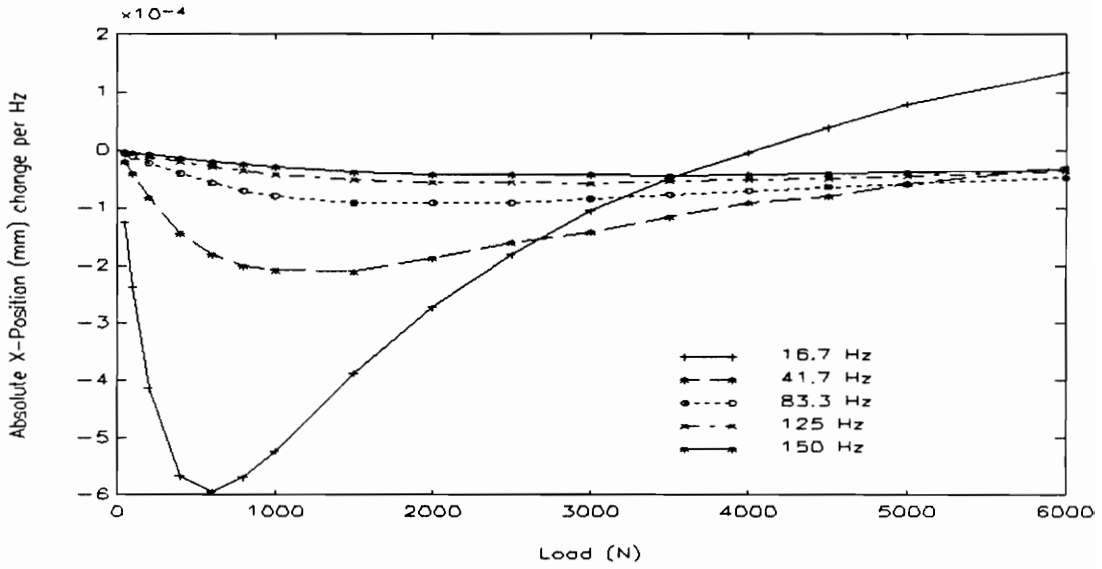

Fig. 82: Absolute Shaft X Position Change (mm) per Hz

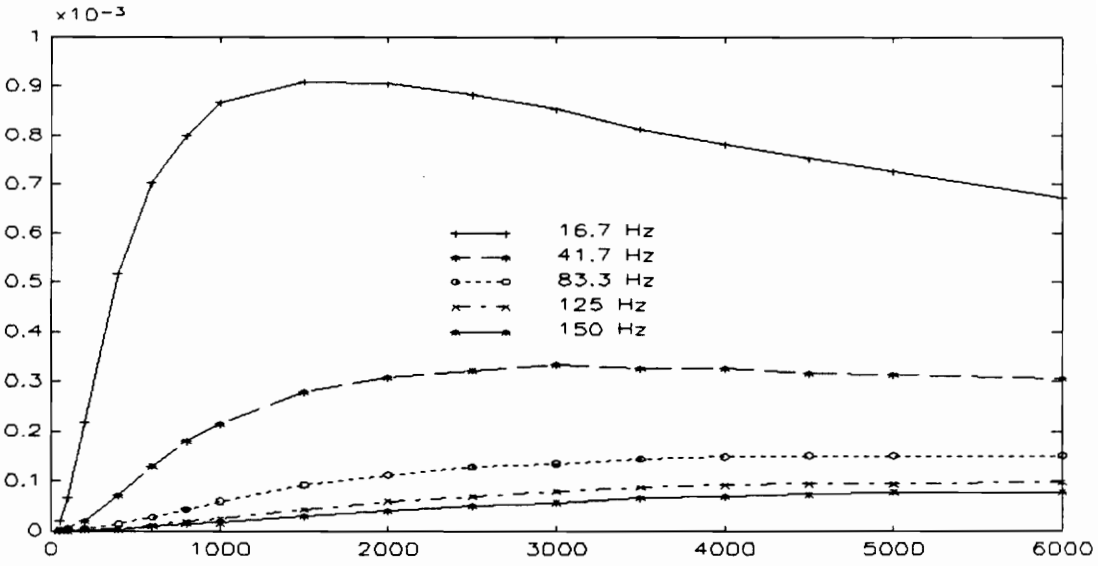

Fig. 83: Absolute Shaft Y Position Change (mm) per Hz

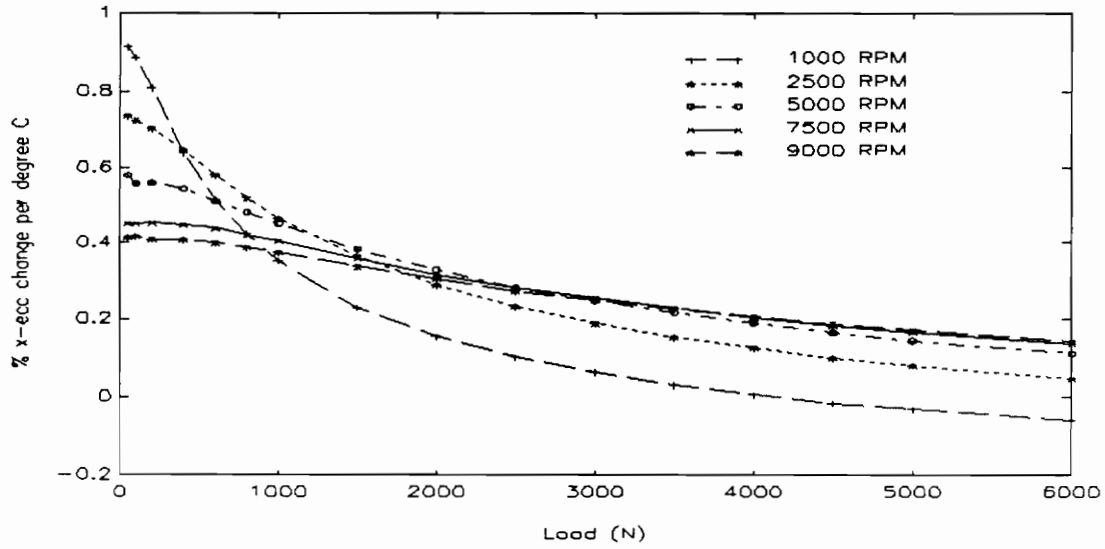

Fig. 84: Percent X-Eccentricity Change per Degree C

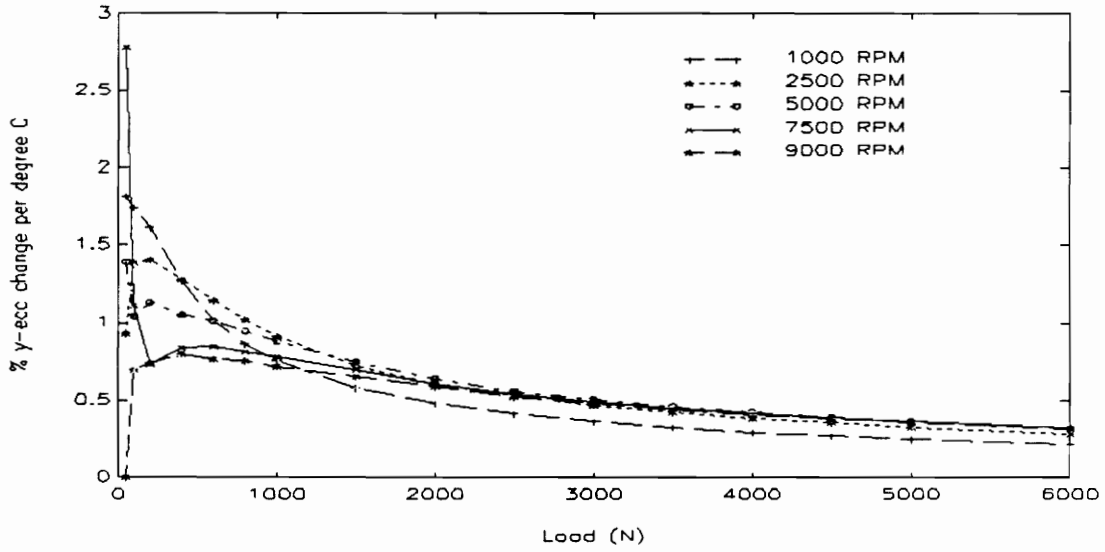

Fig. 85: Percent Y-Eccentricity Change per Degree C

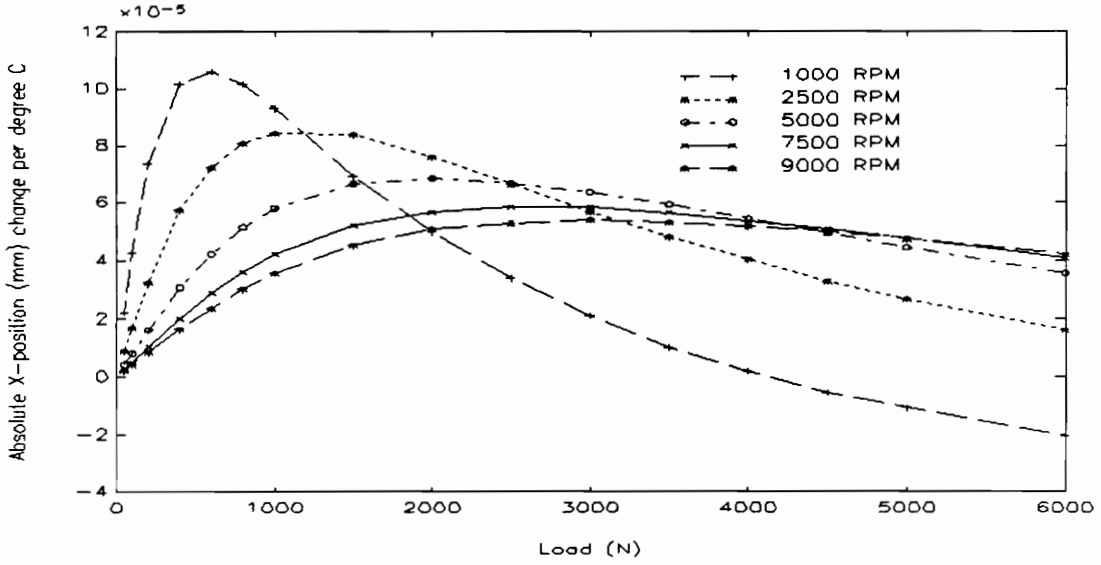

Fig. 86: Absolute Shaft X Position (mm) Change per Degree C

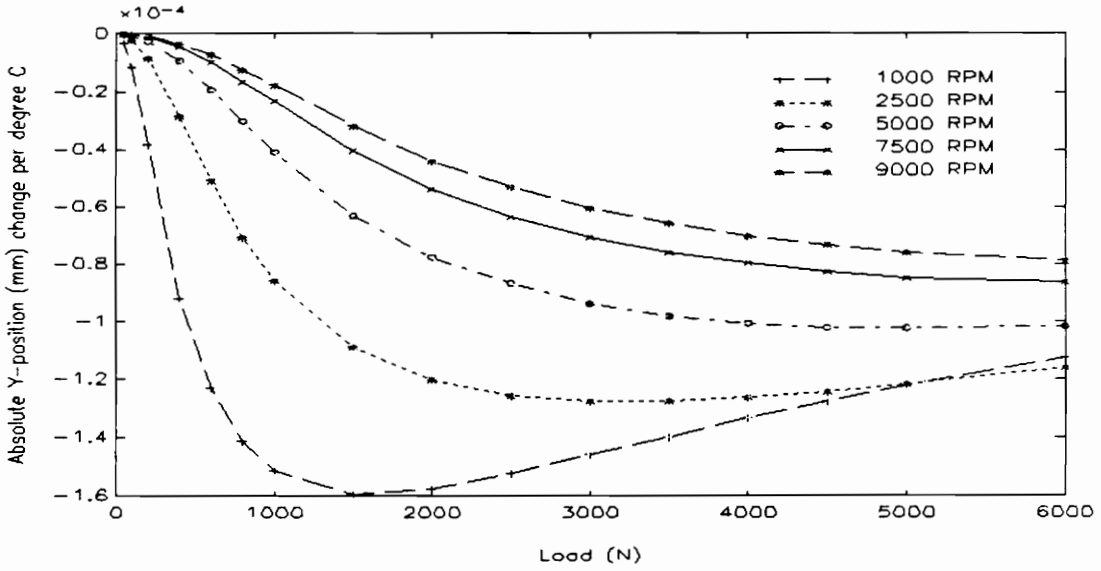

Fig. 87: Absolute Shaft Y Position (mm) Change per Degree C

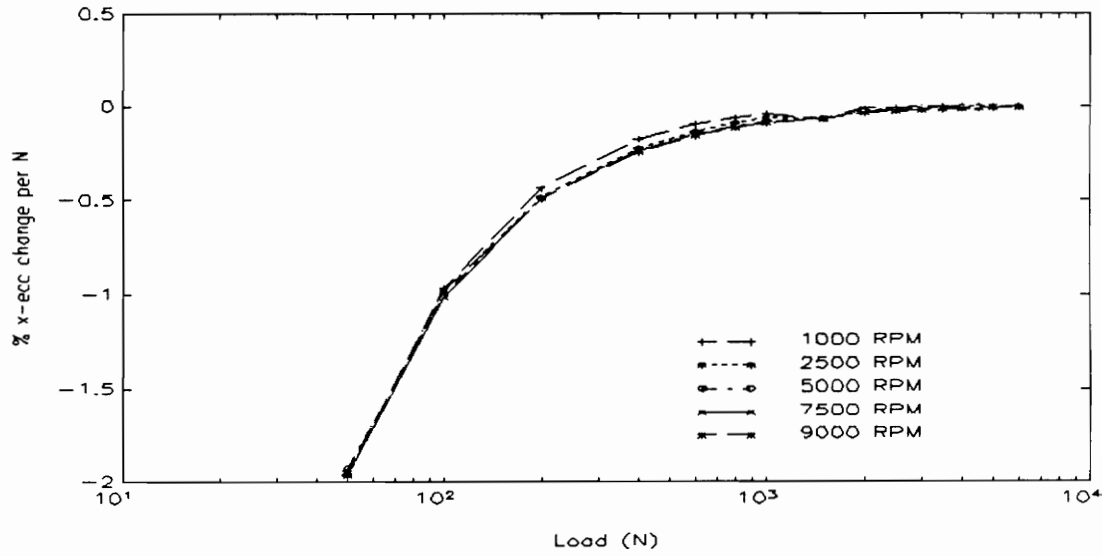

Fig. 88: Percent X-Eccentricity Ratio Change per N load

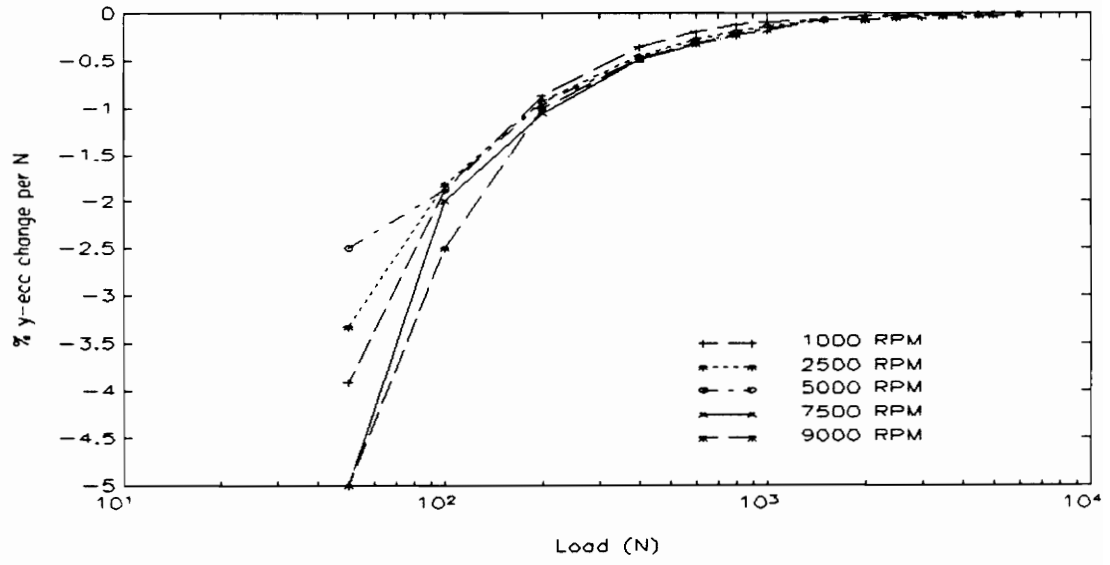

Fig. 89: Percent Y-Eccentricity Change per N Load

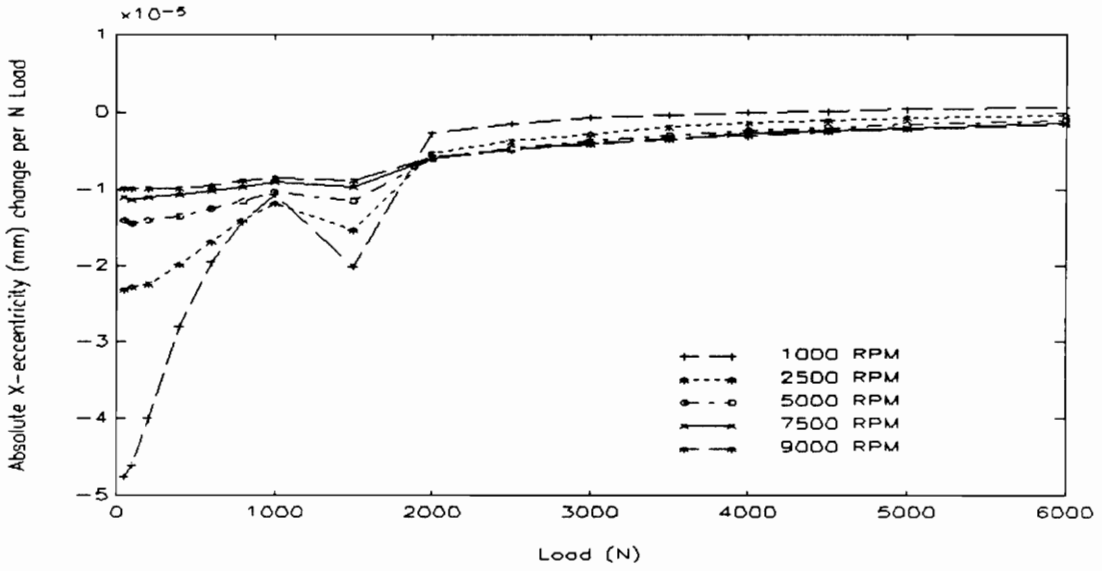

Fig. 90: Absolute Shaft Position (mm) Change per N Load

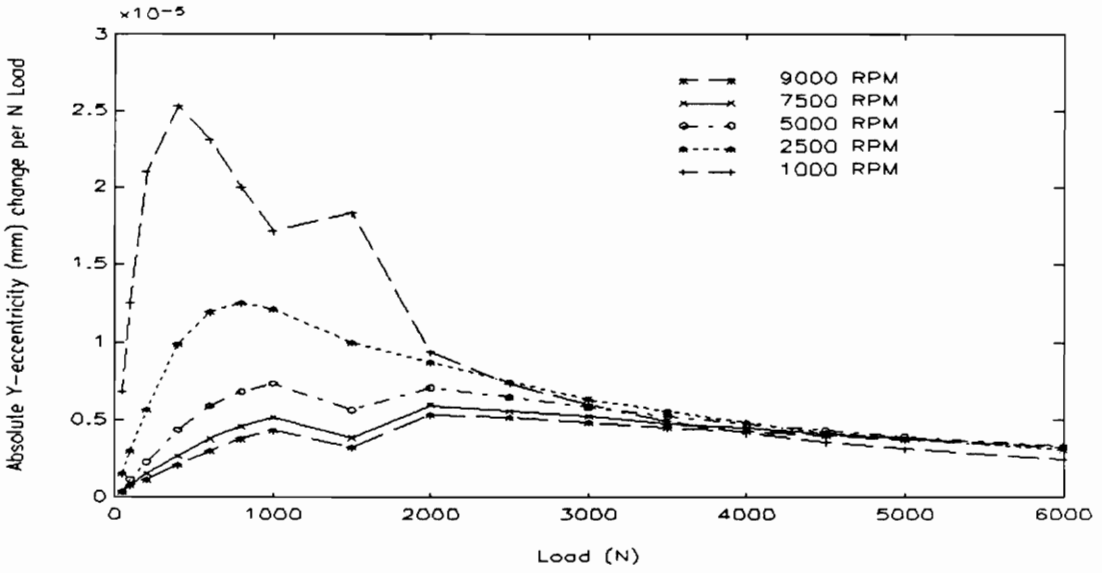

Fig. 91: Absolute Shaft Position (mm) Change per N Load

Not too surprisingly, these figures show that in general, as loading force decreases, the control of these three variables must become increasingly better to maintain a low level of scatter. For speeds of 2500 RPM and above, the results fall within a fairly narrow band; the 1000 RPM results at low loads tend to suggest that this combination will exhibit the most scatter (this combination does not correspond to the lowest Sommerfeld number, which is interesting). The attainable repeatability of these quantities is as shown in Table VIII. Given these repeatability figures, the typical and worst case absolute Y-eccentricity ratio change (always worse than the X-eccentricity ratio according to the figures above) of the results is as shown in Table IX.

Table VIII - Control Repeatability

Quantity	Repeatability
Speed	± 0.4 Hz
Temperature	± 2.5 Degrees
Load	± 10 N

Table IX - Two A.G. Control Repeatability Errors

Shaft	Error Due to		
Speed (Hz)	Speed (mm)	Temperature (mm)	Load (mm)
16.7 (Typ)	± 2.73 x 10-4	± 2.83 x 10-4	± 1.74 x 10-4
(Worst)	± 3.80 x 10-4	± 3.98 x 10-4	± 3.79 x 10-4
41.7 (Typ)	± 9.00 x 10-5	± 2.11 x 10-4	± 1.04 x 10-4
(Worst)	± 1.42 x 10-4	± 3.18 x 10-4	± 1.89 x 10-4
83.3 (Typ)	± 3.55 x 10-5	± 1.46 x 10-4	± 7.29 x 10-5
(Worst)	± 6.28 x 10-5	± 2.55 x 10-4	± 1.15 x 10-4

4.5.4 First Order Analysis

Given the expected scatter caused by repeatability limitations from the previous section, a first order uncertainty analysis can be carried out for the y-position measurements. In this uncertainty analysis, the instrumentation, etc. is assumed to be completely accurate, and all variation between repeated measurements is caused by the process and unmodeled effects. The analysis presented will only examine the effect of repeatability errors. Other effects expected to have an impact on the results include: differential thermal growth (between the test and rear support bearings), which causes misalignment; thermal growth of the test bearing, which will change the bearing load capacity; the possibility of entrained air in the oil, which can do any of a number of things; the effect of ambient conditions (temperature and barometric pressure) - changes in these quantities should have minimal impact; and the unlikely possibility of any wear of the bearing. Similar to the zeroth order analysis, the combined effect of the various process repeatability errors will be determined by the RSS technique. The results presented below in Table X are based on the average error presented in Table IX.

Table X - Expected Y Experimental Scatter from Repeatability

16.7 Hz	41.7 Hz	83.3 Hz
4.3×10^{-4} mm	2.5×10^{-4} mm	1.67×10^{-4} mm

4.5.5 N^{th} Order Analysis

Finally, all of the errors can be combined to obtain an estimate of the expected scatter due to all random effects (displacement probe precision and process repeatability), and the total measurement uncertainty using the results from the zeroth and the first order analyses and the same RSS approach. The results of these two calculations are presented in Table XI .

Table XI - N^{th} Order Y Scatter and Uncertainty

Speed (Hz)	Random Effect ($\pm$ mm)	Total Effect ($\pm$ mm)
16.7	1.13×10^{-3}	2.61×10^{-3}
41.7	1.08×10^{-3}	2.59×10^{-3}
83.3	1.06×10^{-3}	2.58×10^{-3}

Chapter 5

VPI Experimental Results and Comparisons for a Two-Axial-Groove Bearing

5.1 Introduction

With NPADVT anchored to experimental data, and its limitations explored (such as its difficulty with cross coupled stiffness), the code can be used to evaluate the VPI rig. This chapter contains a description of the test bearing and oil, the experimental approach used, the experimental results for thirteen test runs, several comparisons between repeated test conditions (to check consistency), as well as comparisons between NPADVT analysis and experimental data for eight of the tests to evaluate the rig's performance. The comparisons also provide further insight into possible weaknesses of NPADVT. The thirteen test runs consist of:

1) an initial set of four tests at 16.7, 33.3, 58.3, and 83.3 Hz

2) a repeat of these four tests

3) a set of three tests at differing oil inlet pressures for a speed of 33.3 Hz

4) a 33.3 Hz and a 83.3 Hz test after the bearing was removed and reinstalled

In all cases, loads of 500, 1000, 1500, 2000, 2500, 3000, 4000, and 5500 N are employed. Each load is repeated five times, once in order of increasing load, followed by decreasing load, followed by random ordering for the remainder of the applied loads.

5.2 VPI & SU Test Bearing and Oil

The initial VPI & SU test series is for a plain, two-axial-groove bearing with the following characteristics:

Diameter:	101.6 mm
Length:	57.15 mm
C_D/D Ratio:	0.0015 (cold) 0.00145 to 0.00155 (hot)
Weep Hole Dia:	1.6 mm
Oil Inlet Dia:	6.76 mm

Grooves:	0 and 180 degrees from horizontal
	25 degrees of arc width
	2.5 mm maximum depth

This bearing is of babbitt faced (0.43 mm thick), single piece bronze construction. It is 139.7 mm O.D. The horizontally split bearing holder which adapts the bearing to the test rig bearing cavity is fabricated from 1018 steel, and is the same width as the bearing. The bearing to holder fit is approximately line to line. The fabricator's inspection of the bearing and holder suggests that there should be minimal distortion of the bearing bush caused by installation in the holder. The bearing/holder assembly is installed in the test rig as discussed in Chapter 3.

The oil used for this test series is an ISO 32 oil. The properties of this oil and nominal inlet conditions are as follows:

Density:	863 kg/m^3 at 50° C
Specific Heat:	1.98 kJ/kg•K at 50 °C
Viscosity:	16.1 mPa•s at 40 °C 24.8 mPa•s at 50 ° C
Inlet Temp:	43 °C

Inlet Pressure: 0.034 MPa

Flow Rate: Approx. 0.6 cm^3/sec.

This rather low oil pressure (relative to the published data examined previously) is used to avoid any oil feed effects, and to minimize the entraining of air in the oil. It will be shown later that feed pressure effects seen in the testing reported in this work are minimal. The effects of entrained air should also be minimal; air bubbles were never observed in the oil feed line unless oil pressures of approximately six times the above pressure, with correspondingly higher flows rates, were employed.

5.3 Experimental Procedure

The experimental procedure for each test is as follows:

1) Warm the oil and test rig to operational temperature (43 °C) by energizing the circulation pump and oil heater and letting them operate overnight (the bearing housing takes a considerable amount of time to achieve a steady-state temperature). The data-acquisition equipment is also energized for this warm-up period.

2) Begin the test run by performing a combination displacement zero/bearing clearance check. For this procedure, the shaft is manually turned to a reference position and an automated sequence initiated.

This sequence loads the shaft down to 4000 N (bearing) load to firmly seat the shaft, then reduces the (bearing) load to 1000 N, and takes a set of displacement measurements: these become the displacement zeros. The down load is then removed and the shaft loaded up with 4000 N (bearing) load; the (bearing) load is then reduced to 1000 N and a second set of displacement measurements is taken. This load is then removed. The difference between the Y measurements, computed for the bearing centerline, is the initial bearing clearance; half of this figure is taken to be the y-coordinate of the center of the bearing. The average of the X measurements is taken to be the x-coordinate of the center of the bearing. The initial clearance and the center coordinates obtained are used by the data acquisition system to display the operating shaft eccentricity ratio and attitude angle during the test run.

3) The air turbine drive is activated and the test rig is accelerated to 8.3 Hz with only the shaft tare load. After the speed stabilizes at this speed, a "run-out" waveform is recorded. The one-time-per revolution component of this waveform is subtracted from all subsequent waveforms to cancel any effects of electrical noise on displacement measurements such as those caused by non-uniformities in the shaft (the eddy-current displacement probes are very sensitive to these effects), or

the measurement effects of the sleeve non-concentricity. The magnitude of the run-out waveform is less than 0.019 mm peak to peak. The run-out reading is taken at low speed to minimize possible effects of rotor imbalance; such imbalance would cause the magnitude of the measured waveform to increase with operating speed. This effect is not seen with the VPI rig. This absence of growth of the run-out signal confirms that it is caused by a combination of electrical effects and minor non-concentricity.

4) The operating speed is increased to the desired test speed and allowed to stabilize. The stabilization time includes the time required for the thermal spike caused by the change from resting to operating conditions to die out. For each of the test runs, the rig was operated at the maximum 5500 N load for ten to fifteen minutes to ensure thermal equilibrium had been reached in the bearing bushing.

5) The data acquisition program autoloading sequence is initiated. This procedure automatically steps through the loads in the desired sequence (increasing, decreasing and three repetitions in random order for each applied load). The routine includes a 70 second settling period, a speed check, an oil inlet temperature check, and a check that the displacement measurements have settled to a point where they vary by less than 0.05

volts - corresponding to approximately 1.27 x 10^{-3} mm - over a 20 second period. The maximum data acquisition rate is about one load point every 3 minutes, with some longer periods when the difference between successive loads is large, or the inlet temperature swings far outside established limits (the oil temperature control system just barely maintains control to ± 1 °C for a variety of reasons, and occasionally deviates outside this limit).

6) Upon completion of the autoloading sequence, the load is removed and the rig is brought to a stop. After manually rotating the shaft to a reference position, the zero/clearance procedure of step two is repeated. This step is generally completed within 2 minutes of the time the test rig is stopped. The results from this lift check are used with the data presented below.

7) The rig is now ready for the next test run.

5.4 Experimental Two-Axial-Groove Data

5.4.1 Data

The experimental data obtained with the VPI rig are presented below in Fig. 92 through Fig. 104. Unlike the previous comparisons for NPADVT

versus published data, these data are plotted against absolute shaft position (X and Y) rather than as eccentricity ratio versus load. This choice was made over non-dimensionalizing to the eccentricity ratio (dividing by the measured clearance) for two reasons: 1) the magnitude of the experimental scatter may be read directly; 2) the experimental clearance measurements are viewed with some skepticism because of the effects of thermal growth of the bearing bush, holder, and housing. The post test lift check is included with each plot for reference (except as noted). Since the measured positions are referenced to the bottom center of the bearing, the X and Y bearing center coordinates as obtained during the post-test run lift check are used to provide estimated center offsets. Note also that this estimated bearing center is to the upper right for the plots in this section. Each plot consists of the five measured points for each load, as well as an average centerline generated by connecting the average X and Y coordinate of each group of five points. This average centerline will be used in the comparisons to NPADVT analyses in later sections of this chapter.

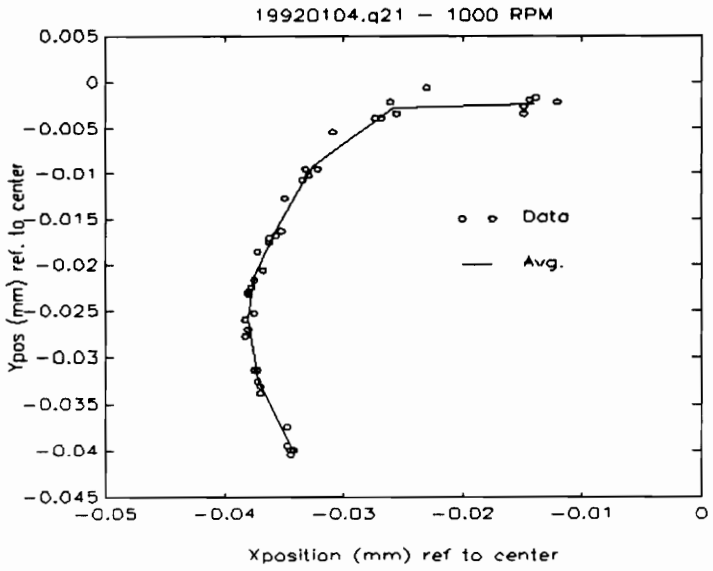

Fig. 92: First 16.7 Hz Test (Cd = 0.15 mm)

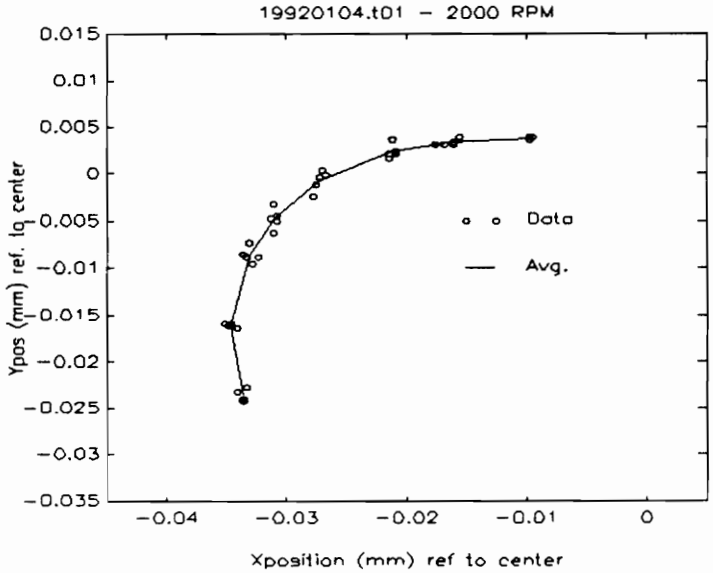

Fig. 93: First 33.3 Hz Test (Cd = 0.148 mm)

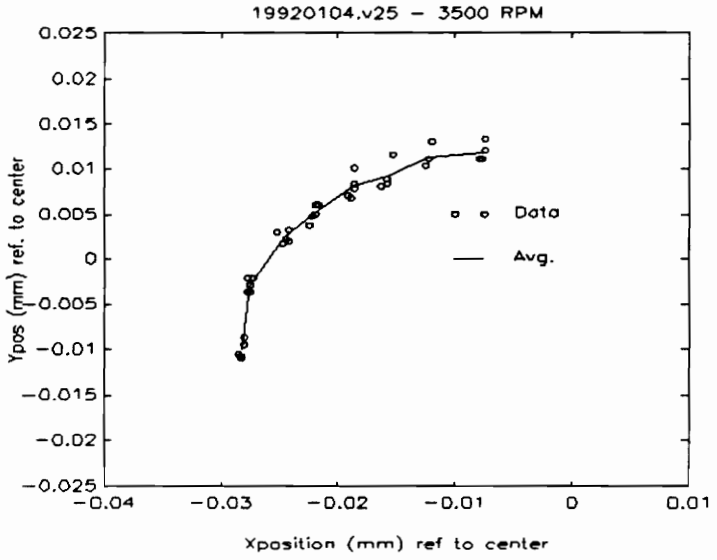

Fig. 94: First 58.3 Hz Test (Cd = 0.146 mm)

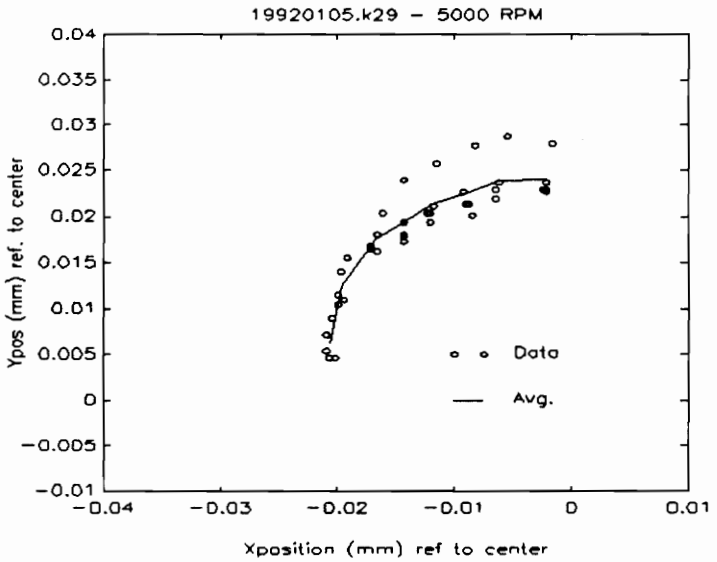

Fig. 95: First 83.3 Hz Test (Cd = 0.158)

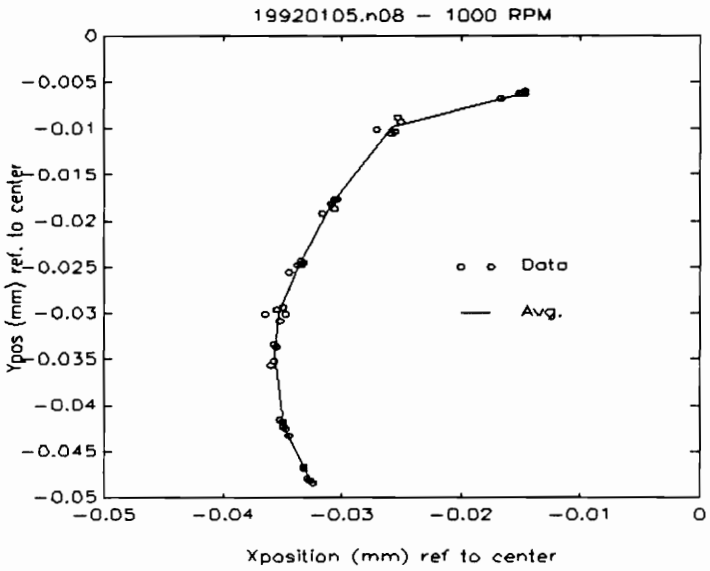

Fig. 96: Second 16.7 Hz Test (Cd = 0.156 mm)

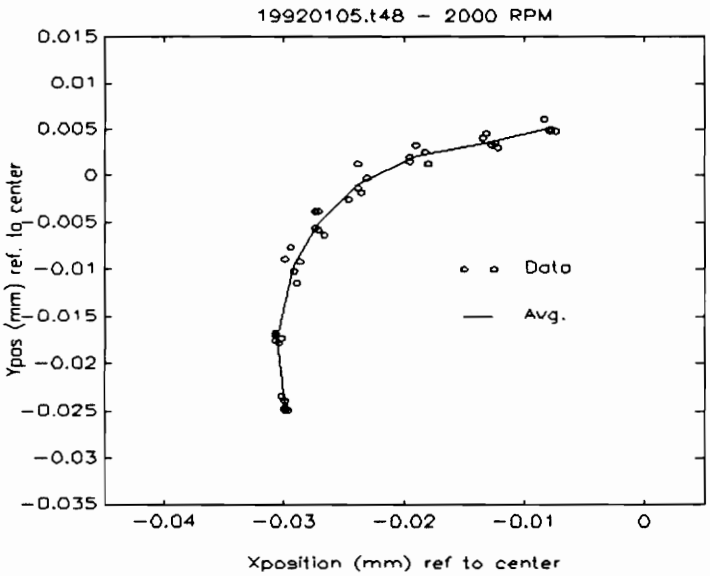

Fig. 97: Second 33.3 Hz Test (Cd = 0.152 mm)

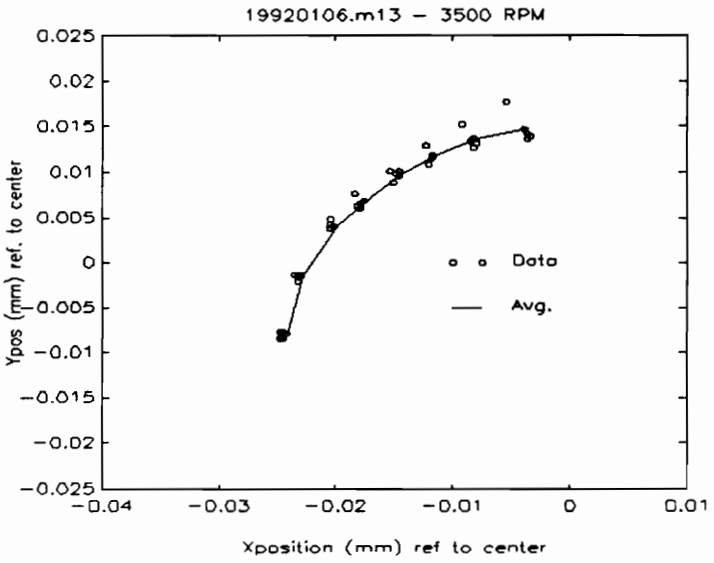

Fig. 98: Second 58.3 Hz Test (Cd = 0.149 mm)

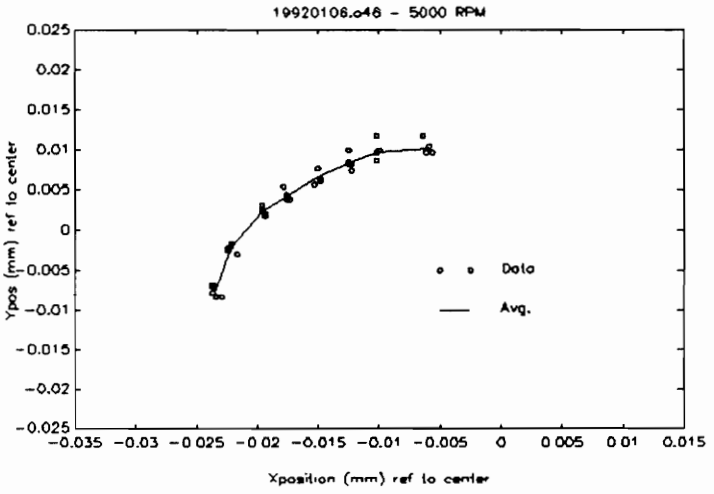

Fig. 99: Second 83.3 Hz Test (Cd = 0.148 mm)

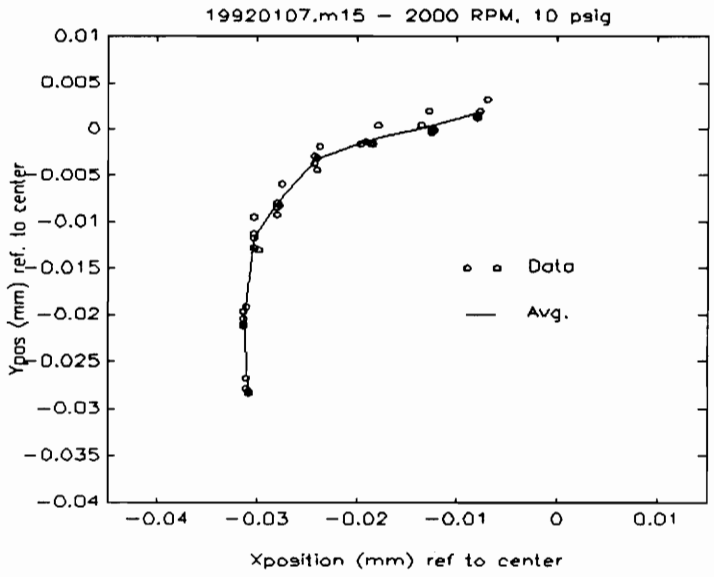

Fig. 100: 33.3 Hz, 0.069 MPa Test (Cd = 0.154 mm)

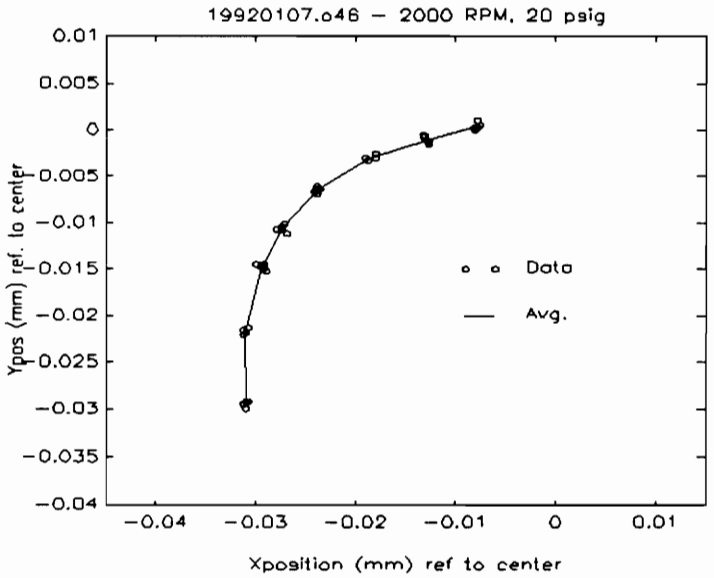

Fig. 101: 33.33 Hz, 0.137 MPa Test (Cd = 0.154 mm)

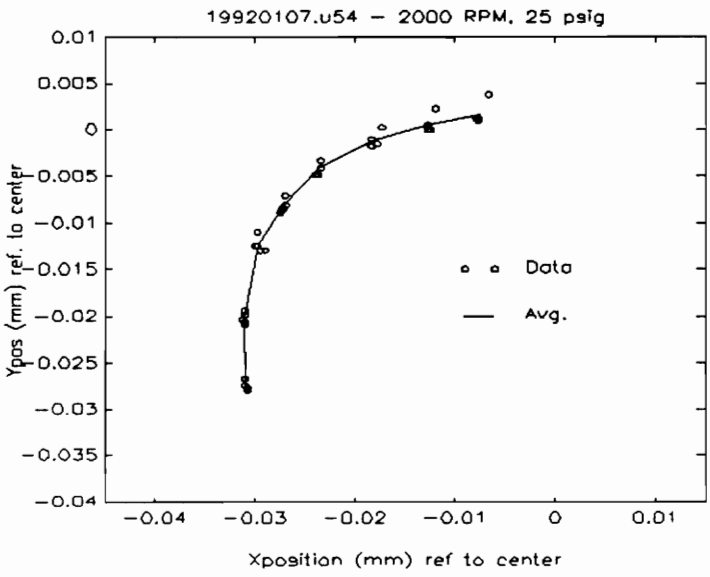

Fig. 102: 33.3 Hz, 0.172 MPa Test (Cd = 0.153 mm)

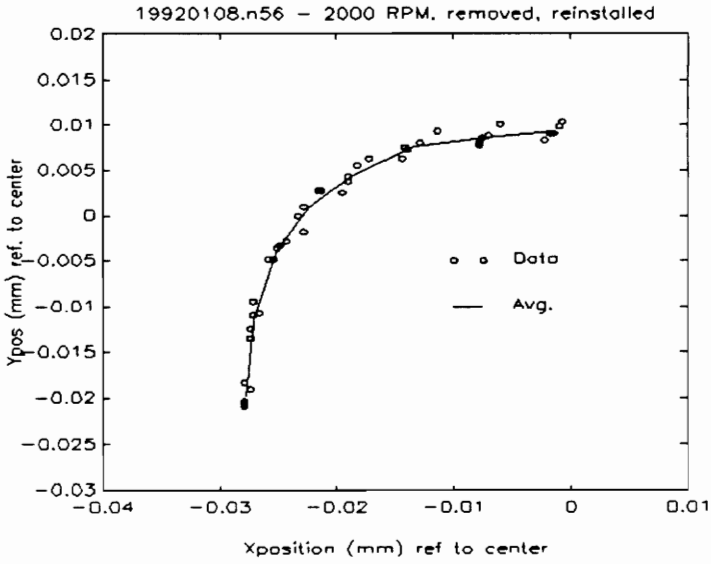

Fig. 103: 33.33 Hz Test after removal/reinstallation (Cd = 0.149 mm)

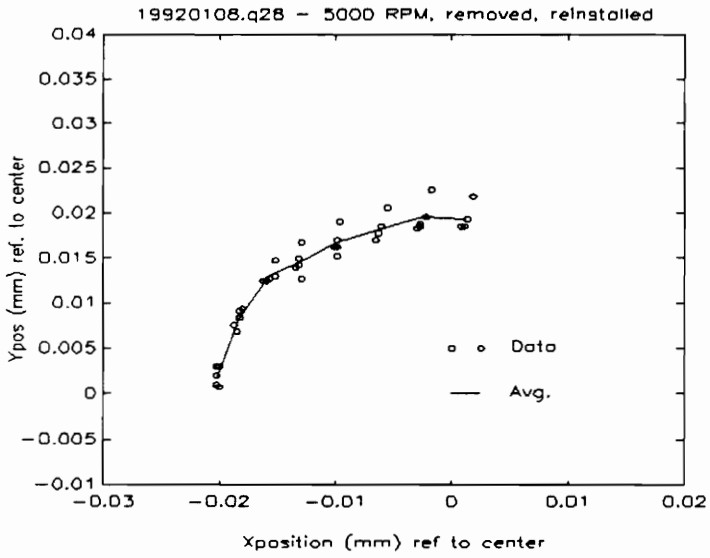

Fig. 104: 83.3 Hz Test, after removal/reinstallation (initial Cd = 0.149 used)

5.4.2 Discussion of Results

The data presented in Fig. 92 through Fig. 104 show that the VPI rig is essentially functioning correctly. The locus curve is of the general shape expected of a plain journal bearing and the operating point moves from the center of the bearing as the load is increased. An analysis of variance procedure (see Appendix B for details) on the scatter indicates that the scatter of the data is independent of the effects of speed, load, measurement axis and repeated tests. This analysis indicates that computing an average standard deviation (operating point average - measured point) is valid. Averaging the scatter over the 640 data points for the 128 speed-load-measurement axis combinations of the first eight tests yields an average scatter of 8.1×10^{-4} mm, with a standard deviation of 2.86×10^{-5} mm. This measured scatter is roughly 2 to 4 times the predicted experimental scatter of 4.3×10^{-4} to 1.7×10^{-4} mm based on process repeatability (first order analysis) from chapter 4. Thus, while the magnitude of the observed scatter is larger than the expected magnitude, it is not significantly larger, especially considering the outliers and thermal effects. This level of agreement suggests that the rig is indeed performing reasonably well at this stage of debugging.

Probably the most troubling aspect of the data is the outliers (these are especially noticeable in the 83.3 Hz data). The presence of points that do not follow the general trend is troubling. These points correspond to the first 8 load cases, increasing loads from 500 N to 5500 N. As they most likely represent some phenomena(on) other than the fluid-film effect, they will be omitted for the internal consistency comparisons (they would make the scatter of the data appear artificially larger than it really is). The effect is not merely hysteresis, as the random loading, and the decreasing loading does not exhibit this scatter. The effect of reversing the loading to start with the highest load, and then decrease loads for the initial loading, was not examined.

5.5 Comparisons Between Experimental Results

To check that the test rig is functioning in a consistent, repeatable manner, several comparisons between different tests will be made. These comparisons are: 1) between repeated tests for the same nominal conditions, 2) between tests for the bearing before and after a removal/reinstallation sequence, and 3) between tests with differing oil feed pressures.

5.5.1 Repeated Test Comparisons

In Fig. 105 through Fig. 112, the initial four tests are compared with repeated tests at the same nominal conditions. For each comparison, the average shaft locus as recorded in the test is plotted in one figure; the same data normalized at the 5500 N load are plotted in a second figure. The first 8 points of each test are omitted in these comparisons as discussed above. As with the first set of figures, these data are plotted for absolute measured shaft position as offset by the post test bearing center estimate. The area enclosed by two standard deviations for each load point is indicated with an ellipse about the mean of the four data points (see appendix B for a more complete description of this area). Again, the post test lift check clearance is also included for reference. Since the rig exhibits an unresolved, random zero shift in the displacement measurements, the normalized plots should be viewed as providing an indication of the level of repeatability that the test rig is capable of achieving. It should be noted that the difference in measured clearance between repeated tests, although small, is significant in several cases.

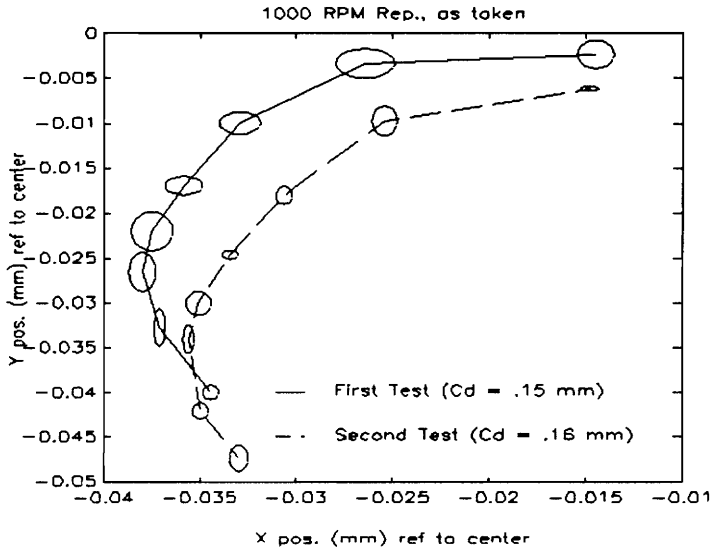

Fig. 105: 16.7 Hz Repeated Tests - Actual Data

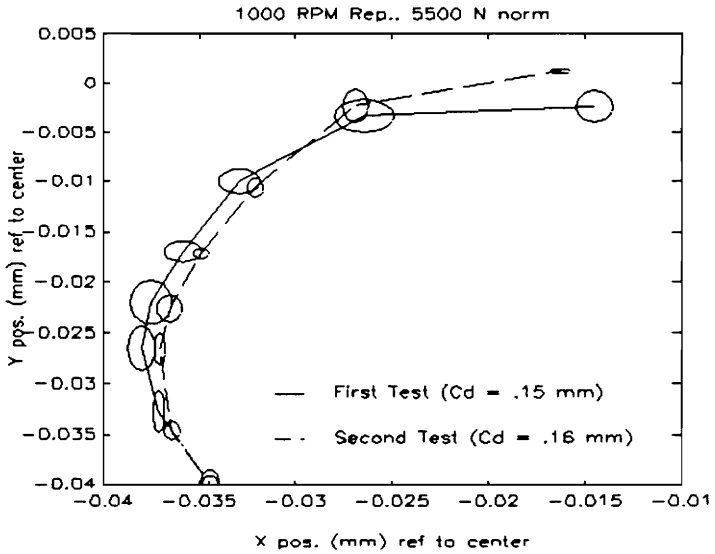

Fig. 106: 16.7 Hz Repeated Tests - Normalized Data

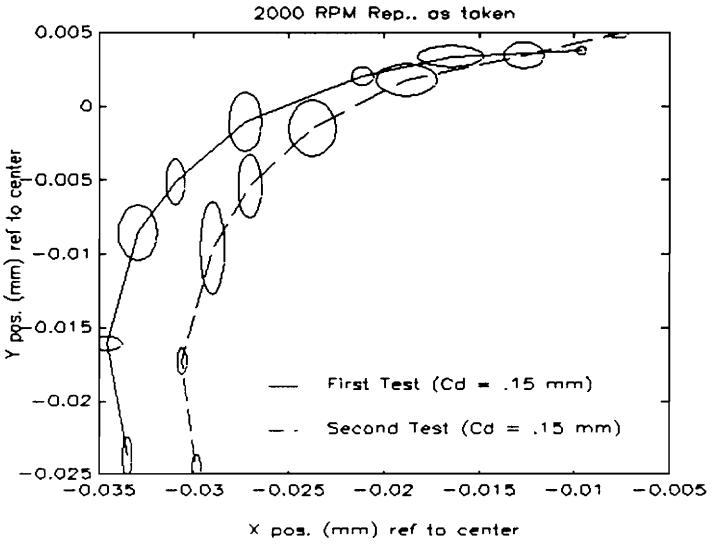

Fig. 107: 33.3 Hz Repeated Tests - Actual Data

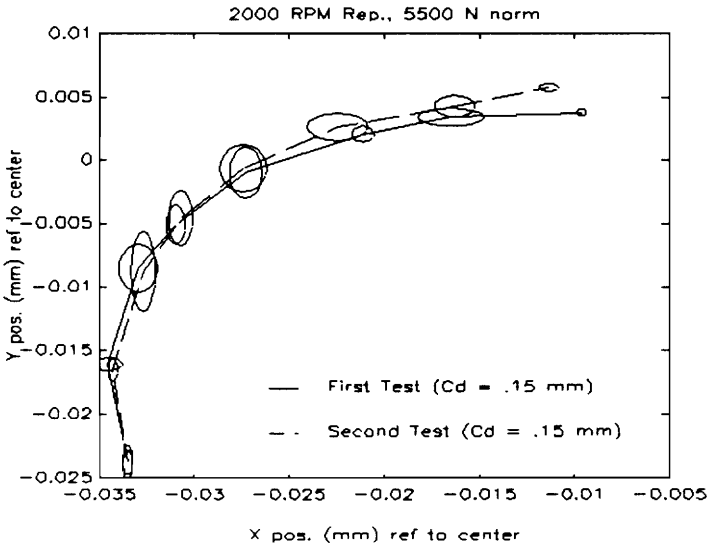

Fig. 108: 33.3 Hz Repeated Tests - Normalized Data

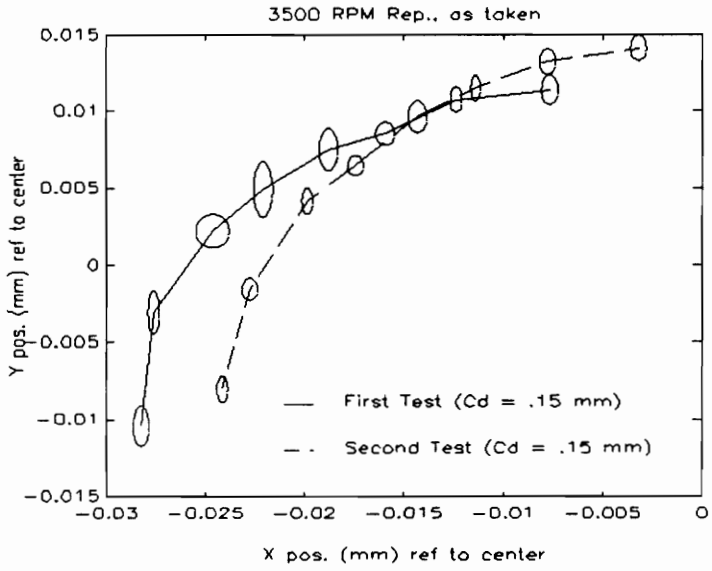

Fig. 109: 58.3 Hz Repeated Tests - Actual Data

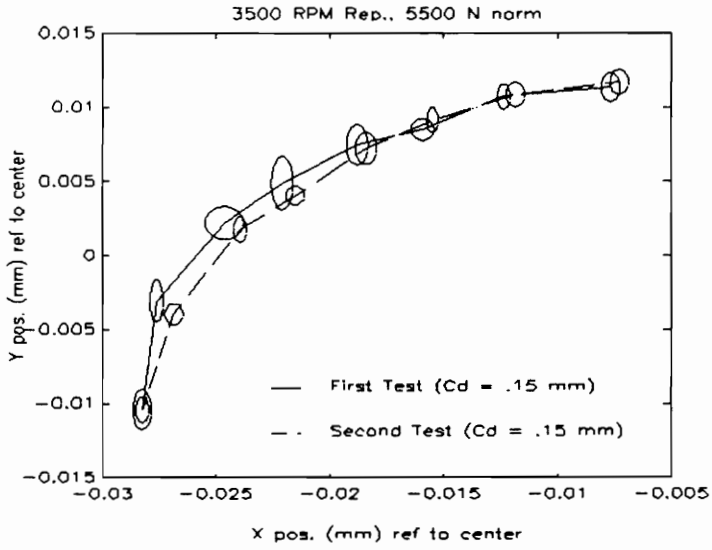

Fig. 110: 58.3 Hz Repeated Tests - Normalized Data

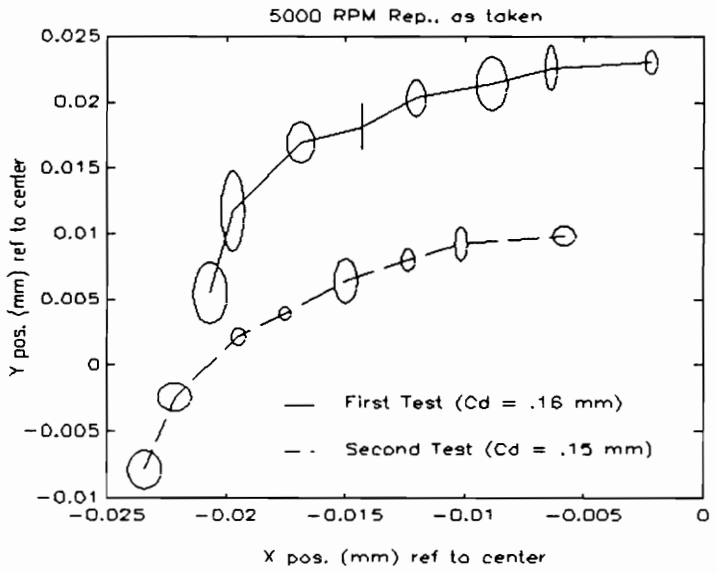

Fig. 111: 83.3 Hz Repeated Tests - Actual Data

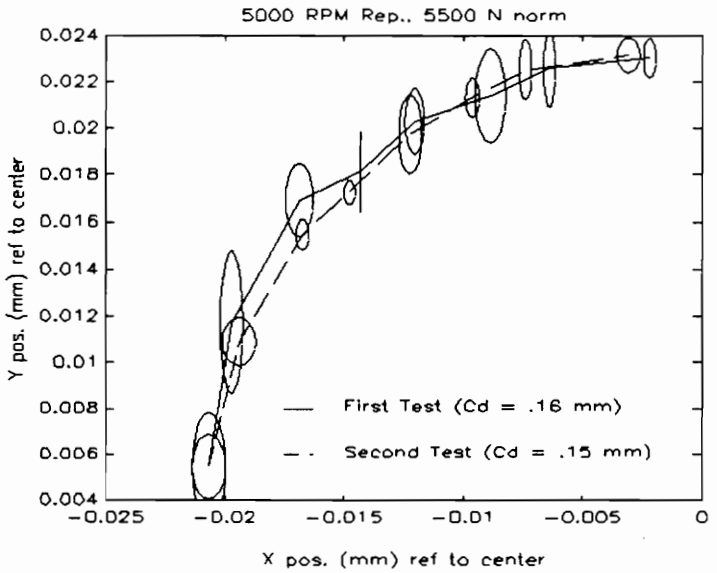

Fig. 112: 83.3 Hz Repeated Tests - Normalized Data

5.5.2 Discussion of Repeated Tests

16.7 Hz: The results for this speed show that, in general, the reproducibility of the tests is not too bad, especially given that the measured bearing clearances for the repeat tests are slightly different than the measured clearances for the initial test. The apparent y-position zero shift is most likely the result of a combination of thermal growth effects and effects not yet identified. The differences at light loads may also be in part due to variations in loading (lighter loads are most sensitive to this effect). The normalized plots show fairly good agreement (the two standard deviation areas for the two curves generally have some common portion).

33.3 Hz: The results for this speed show very good agreement, even in the data as recorded. Again the second test is (graphically and actually) further towards the top of the bearing at light loading.

58.3 Hz: The results for this speed show very good agreement when overlaid, thus supporting the hypothesis that the offset seen in the actual data plot (Fig. 109) is most likely caused by effects external to the bearing/shaft interface. The difference between

the normalized curves can mostly be explained by the observed experimental scatter.

83.3 Hz: Again, these results show fairly good repeatability if the zero offsets are ignored. Interestingly, the observed difference between the plots of the actual data is on the order of the difference in clearance measurements (0.01 mm). Also, the differences between the normalized curves is on the order of the experimental scatter.

5.5.3 Removal/Reinstallation Repeatability

To examine the effects of bearing installation variability (exact position, face clamping pressure, etc.), the bearing was removed from both the test rig and the bearing holder, wiped clean, reinstalled in the holder and the test rig, and two tests (33.3 Hz and 83.3 Hz) were conducted. Comparisons between the results for these two tests, and two tests from the initial eight tests with similar measured clearances, are show in Fig. 113 and Fig. 114. These figures are plotted for absolute shaft position normalized at 5500 N load. Again areas corresponding to plus or minus two standard deviations are indicated, as are the post test lift check clearances.

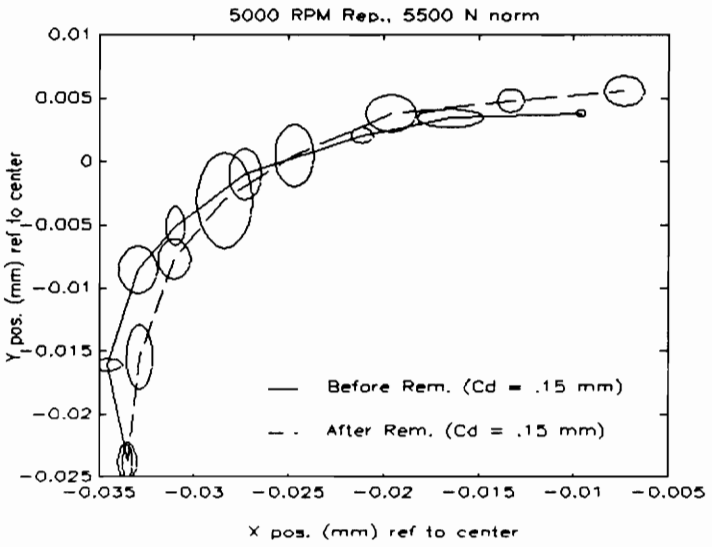

Fig. 113: Comparison for Removal/Reinstallation, 33.3 Hz

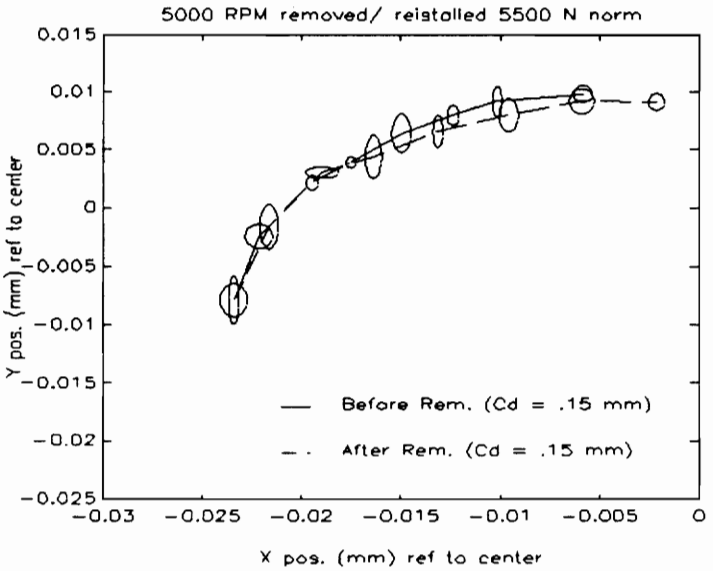

Fig. 114: Comparison for Removal/Reinstallation, 83.3 Hz

5.5.4 Discussion for Removal/Reinstallation Comparison

These two figures suggest that there are perhaps some small variable installation effects; in particular, the shaft locus is closer to the bearing center (for normalized data) after the bearing is reinstalled. This effect is most likely due to minor alignment differences. The differences, however, are still only slightly larger than the observed experimental scatter; thus comparisons between different bearings, or the same bearing after being removed and reinstalled, would seem to be valid.

5.5.5 Comparisons for Variable Feed Pressure

One of the postulated causes of differences between NPADVT analysis and the published experimental data is the effect of feed pressure. To investigate this effect, results for a nominal speed of 33.3 Hz and feed pressures of 0.034, 0.069, 0.138 and 0.172 MPa will be examined. Pressures higher than 0.172 MPa will not be examined due to visual evidence (air bubbles visible in the oil feed line) that the defoaming/settling tank capacity was being overwhelmed by the higher flow rates associated with higher feed pressures. In Fig. 115 the actual data is presented; in Fig. 116, the data is presented normalized to the

0.034 MPa, 5500 N data point. As before, ellipses indicate plus or minus two standard deviations about the mean for the data.

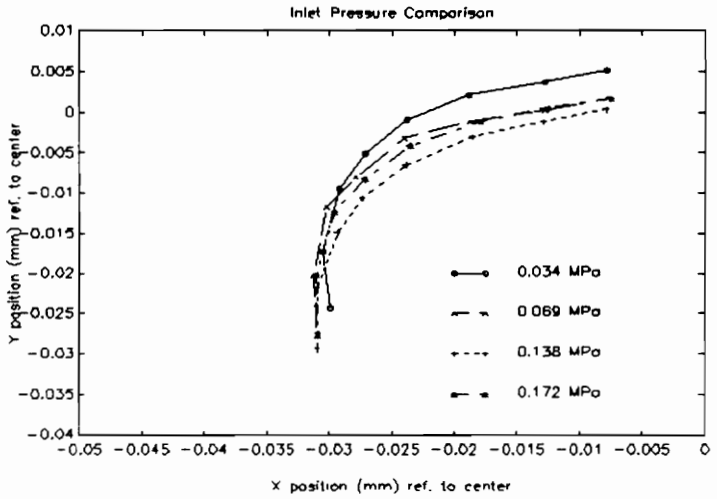

Fig. 115: Comparison for Oil Feed Pressure - Actual Data

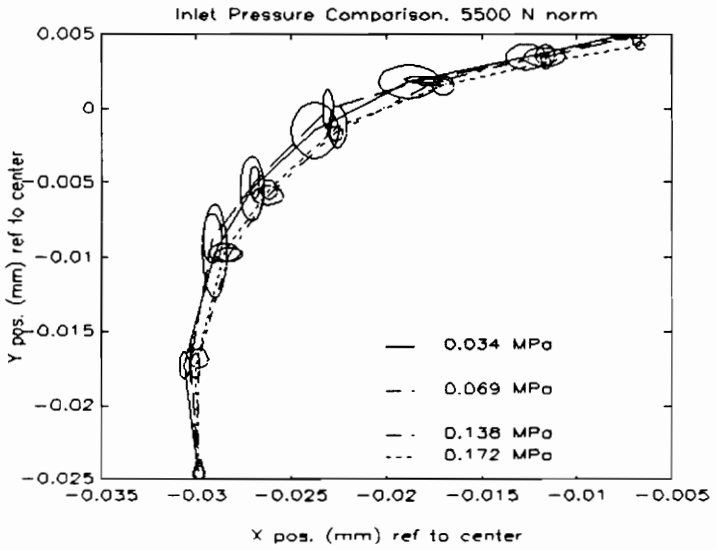

Fig. 116: Comparison for Oil Feed Pressure - Normalized to 0.034 MPa, 5500 N

5.5.6 Discussion for Feed Pressure Comparisons

In Fig. 115, there is some slight support for the contention that a rise in pressure is accompanied by a slight reduction in eccentricity ratio as is predicted by Ref. 14. Unfortunately, the effect is not consistent. In the normalized results of Fig. 116, any differences between measured position related to the pressure variation are on the order of the experimental scatter. The results presented in Ref. 14 suggest that this is about the minimum magnitude of pressure effect that would be expected over this range of pressures. Thus it is difficult to draw any conclusions without developing a means of reducing the scatter and eliminating the zero shift problem. The results do, however, suggest that within the scope of the data presented in this work, feed pressure effects do not have significant impact. It would have been helpful to have results for a greater range of pressures (the oil pump will produce pressures of up to 0.61 MPa), but as mentioned, problems with entrained air removal at the higher flow rates associated with high feed pressures preclude such an investigation.

5.5.7 Comparisons between NPADVT and VPI Data

The comparisons between the experimental data for the first eight tests and the corresponding NPADVT analysis are presented below in Fig. 117 through Fig. 148. Although it was originally hoped that the five points for a given speed for the first test could be combined with the second set of five points from the repeat on a different day to provide the ten points required to obtain the uncertainty level discussed in chapter 3, the effects of zero offsets and variable clearances make this a dubious approach. Instead, each of the tests is separately compared to an appropriate NPADVT analysis. The average shaft centerlines used in these comparisons correspond to the shaft centerlines shown in the initial set of plots in this chapter; i.e., all five repetitions are included for each load/speed point. The outlying points were included to encompass all possible effects seen in the testing. As a result, confidence limits are not included in this set of figures. The appropriate zeroth order uncertainty from chapter three for five repetitions rather than ten is $\pm$ 0.95 x 10^{-3} mm for random effects, and $\pm 2.53 \times 10^{-3}$ mm for all effects (bias and random).

The loads examined in the NPADVT analysis range from 500 N to 5250 N by steps of 250 N. The experimental loads are 500 N, 1000 N, 1500 N, 2000 N,

2500 N, 3000 N, 4000 N, and 5500 N. The omission of the exact matching maximum load in the analysis does not materially affect the conclusions that can be drawn from the plots, as the analytical shaft locus is a smoothly changing curve. These plots are presented in dimensional form as absolute shaft position relative to the center of the bearing (the plot axes correspond to the negative of the axes in Fig. 92 through Fig. 104). Because of the problems experienced in obtaining an accurate estimate of the bearing center, normalized comparisons will be presented in addition to the comparisons with the actual experimental data. This normalization is always at some low, intermediate load to avoid the possibility of problems with large differences between the analysis results and experimental data at the maximum and minimum loads.

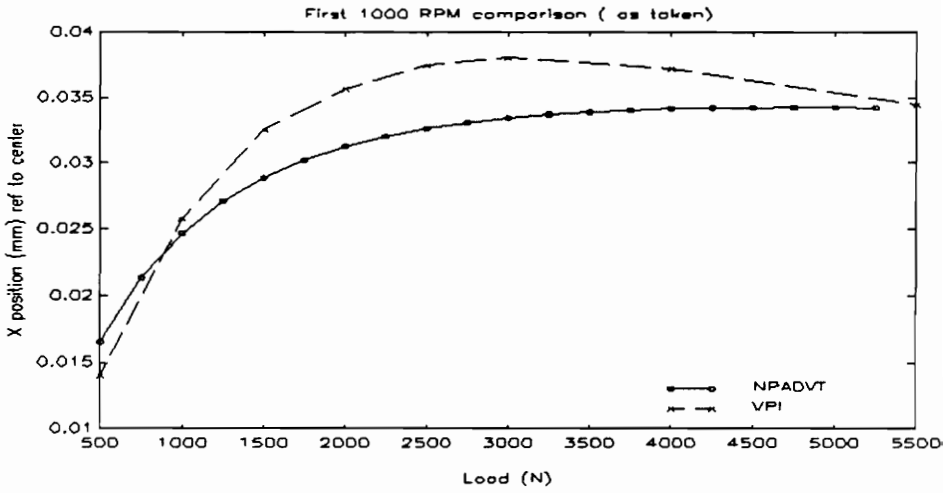

Fig. 117: 16.7 Hz X-Position Comparison (First Test Series)

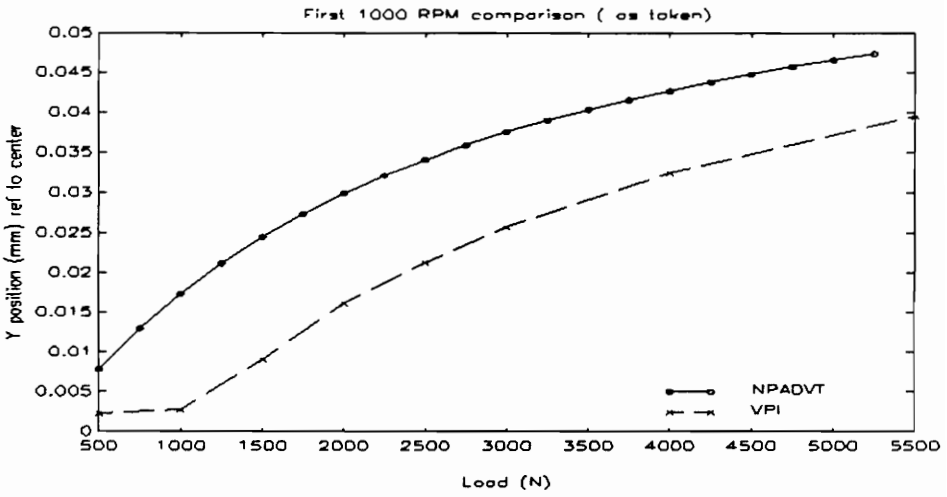

Fig. 118: 16.7 Hz Y-Position Comparison (First Test Series)

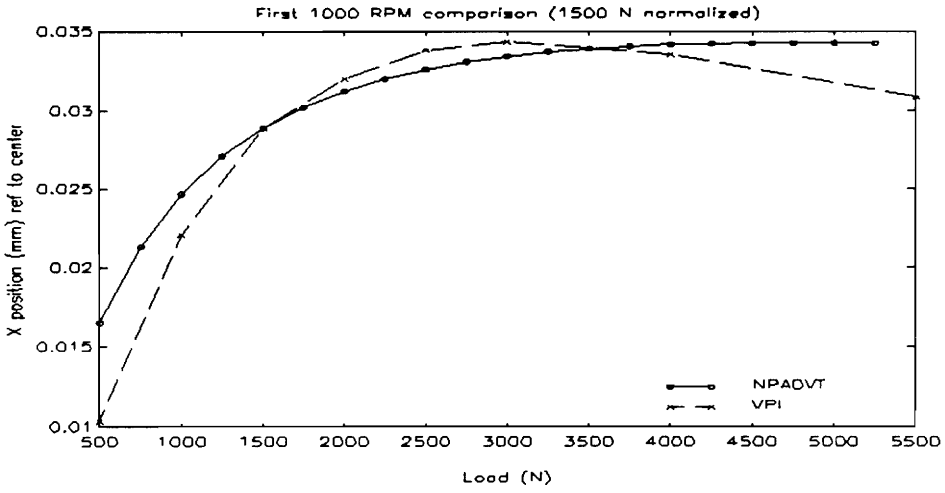

Fig. 119: 16.7 Hz X-Position 1500 N Normalized Comparison (First Test Series)

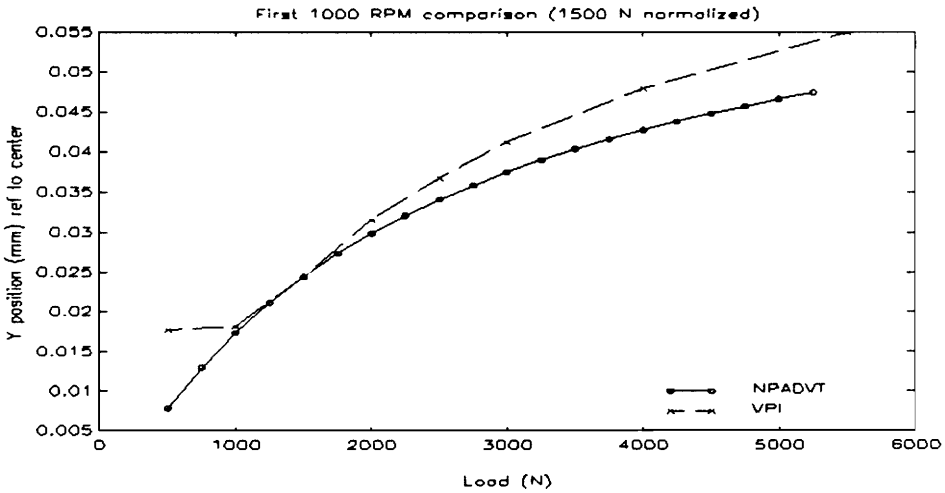

Fig. 120: 16.7 Hz Y-Position 1500 N Normalized Comparison (First Test Series)

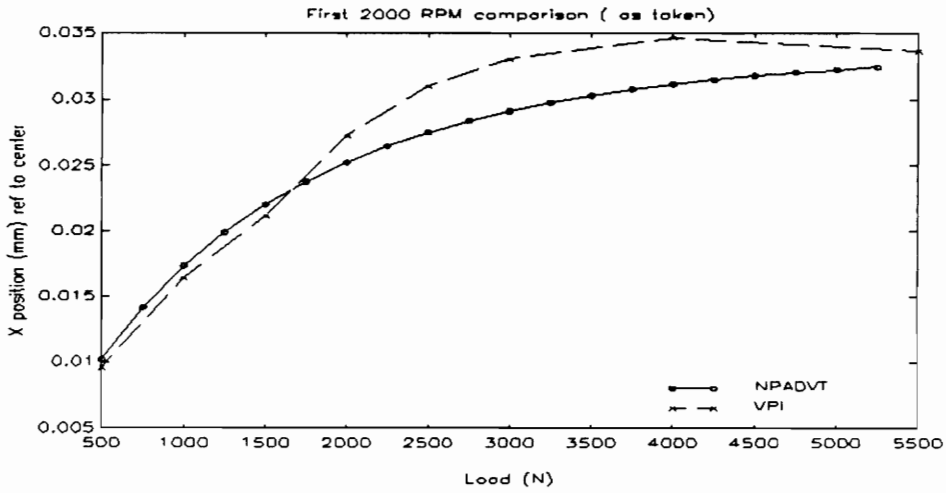

Fig. 121: 33.3 Hz X-Position Comparison (First Test Series)

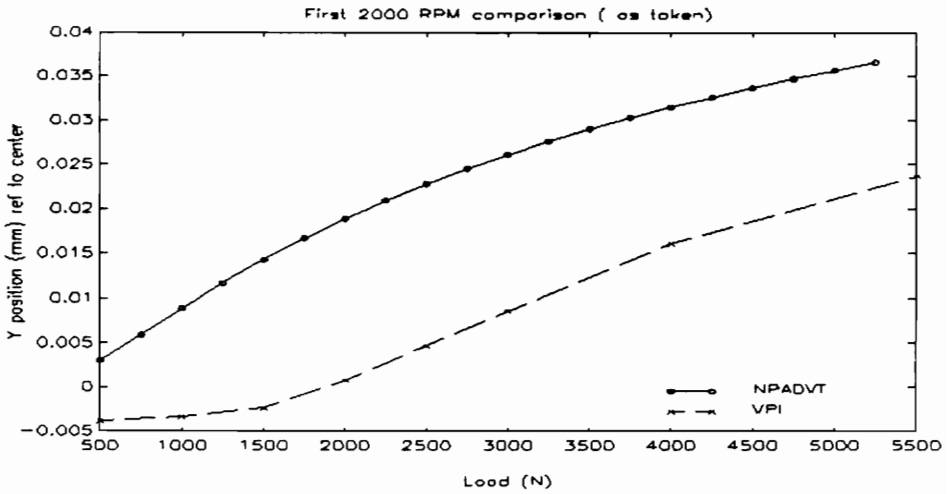

Fig. 122: 33.3 Hz Y Position Comparison (First Test Series)

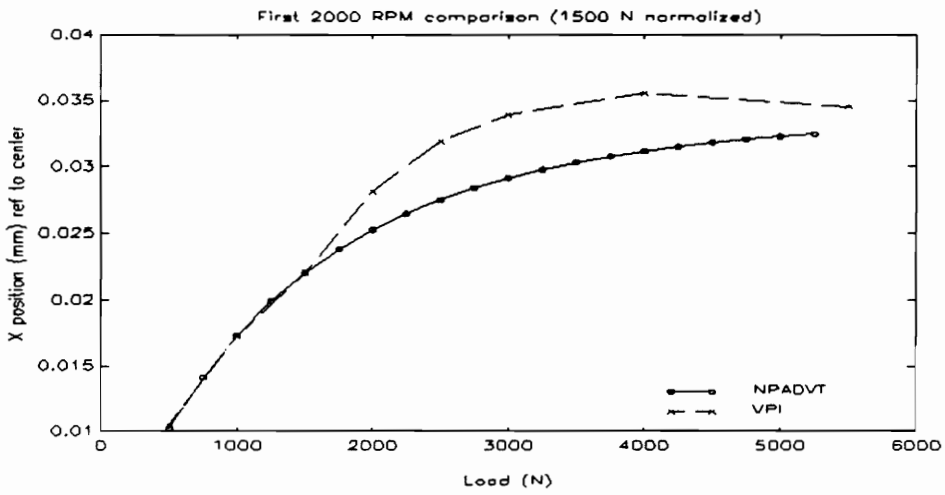

Fig. 123: 33.3 Hz X-Position 1500 N Normalized Comparison (First Test Series)

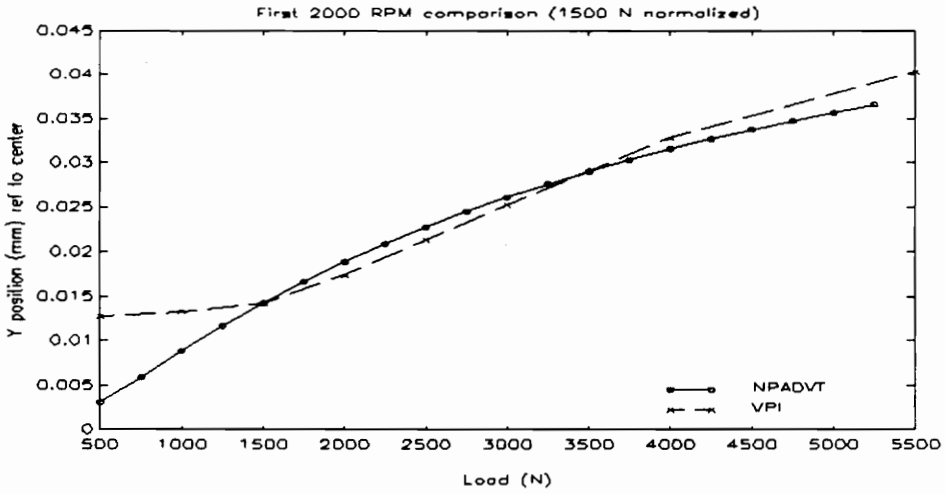

Fig. 124: 33.3 Hz Y-Position 1500 N Normalized Comparison (First Test Series)

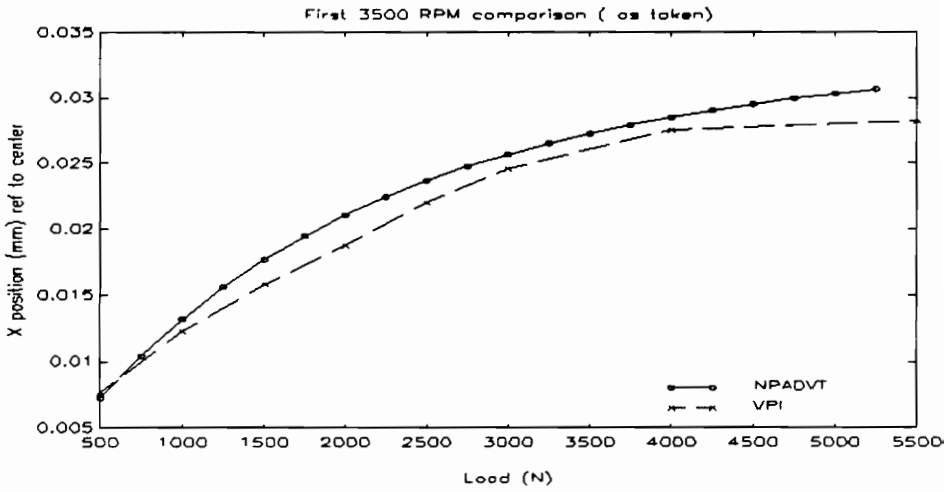

Fig. 125: 58.3 Hz X-Position Comparison (First Test Series)

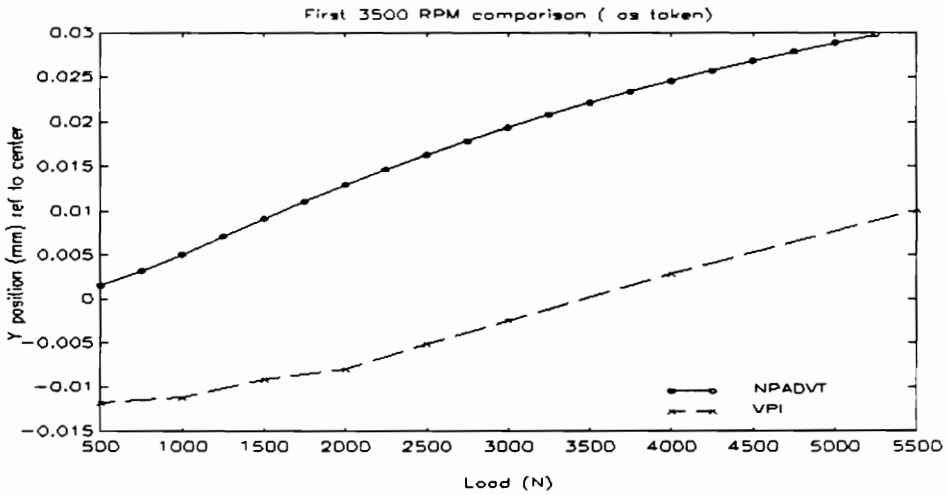

Fig. 126: 58.3 Hz Y-Position Comparison (First Test Series)

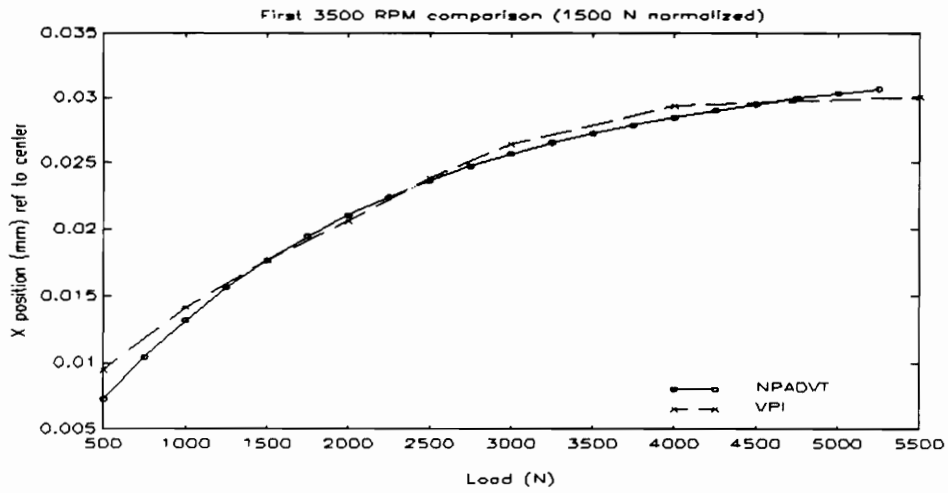

Fig. 127: 58.3 Hz X-Position, 1500 N Normalized (First Test Series)

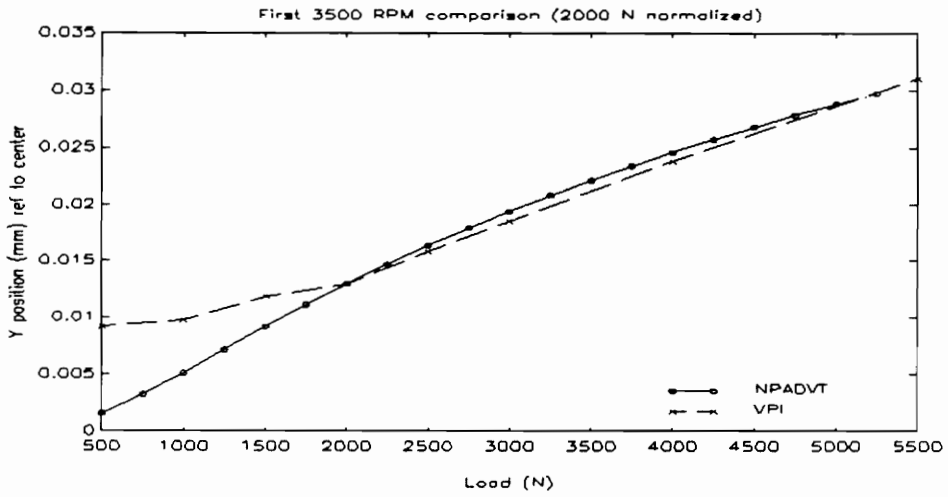

Fig. 128: 58.3 Hz Y-Position, 2000 N Normalized (First Test Series)

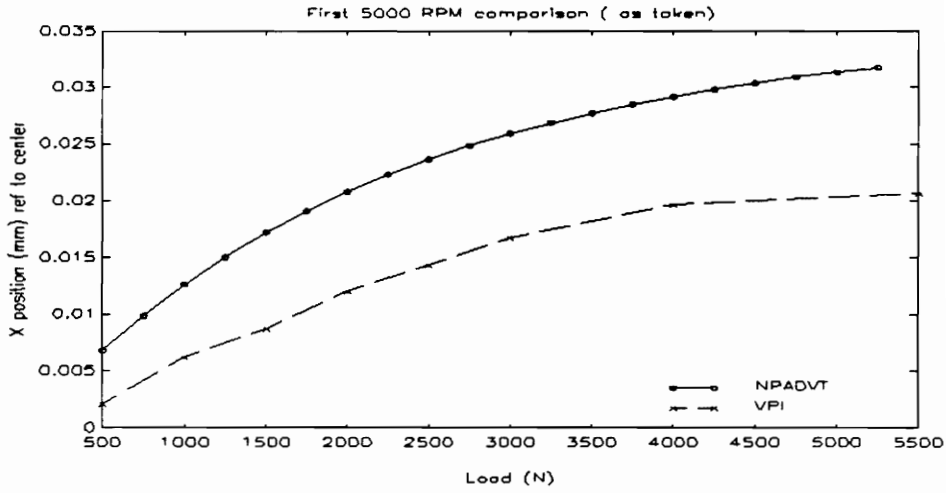

Fig. 129: 83.3 Hz X-Position Comparison (First Test Series)

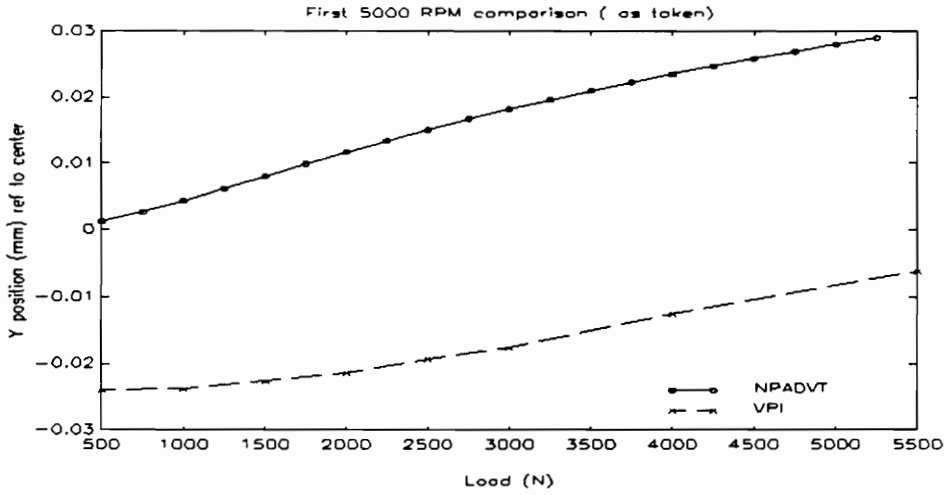

Fig. 130: 83.3 Hz Y-Position Comparison (First Test Series)

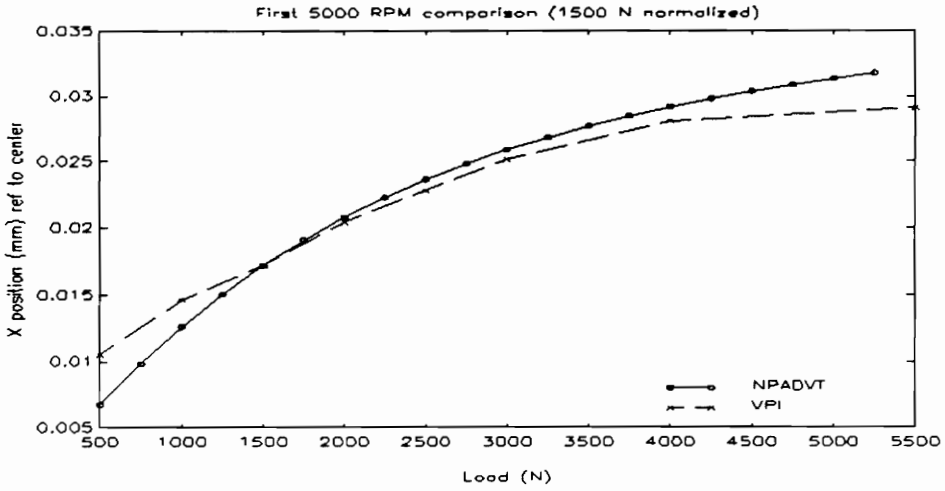

Fig. 131: 83.3 Hz X-Position 1500 N Normalized Comparison (First Test Series)

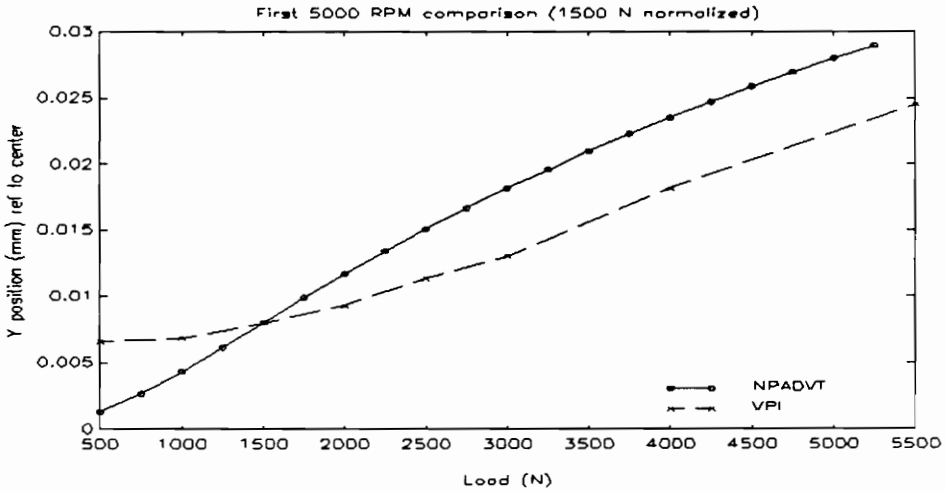

Fig. 132: 83.3 Hz Y-Position 1500 N Normalized Comparison (First Test Series)

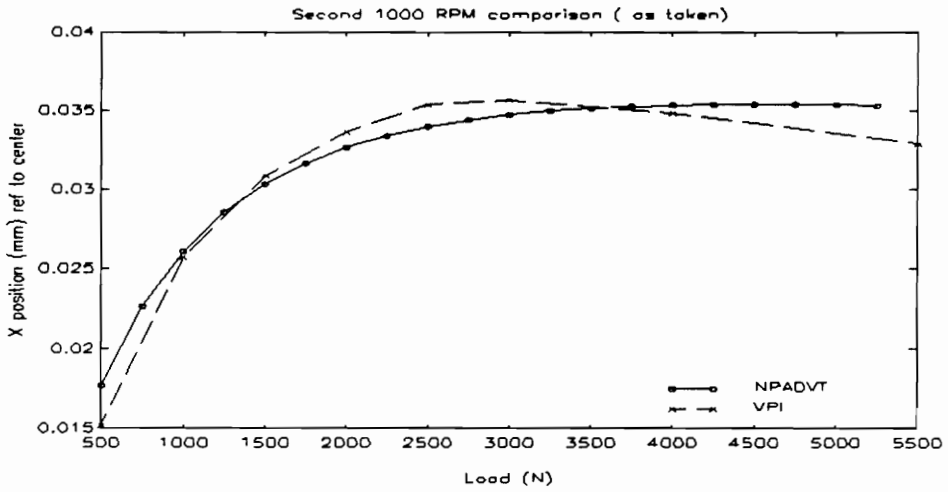

Fig. 133: 16.7 Hz X-Position Comparison (Second Test Series)

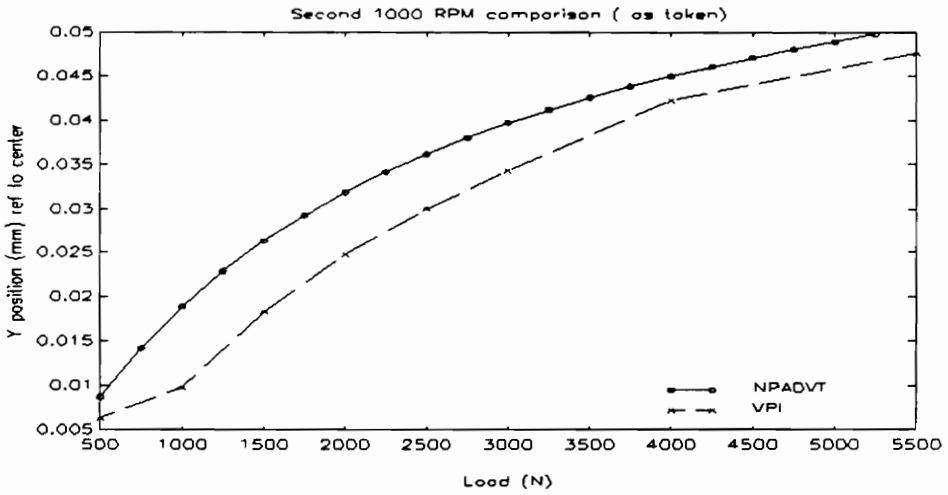

Fig. 134: 16.7 Hz Y-Position Comparison (Second Test Series)

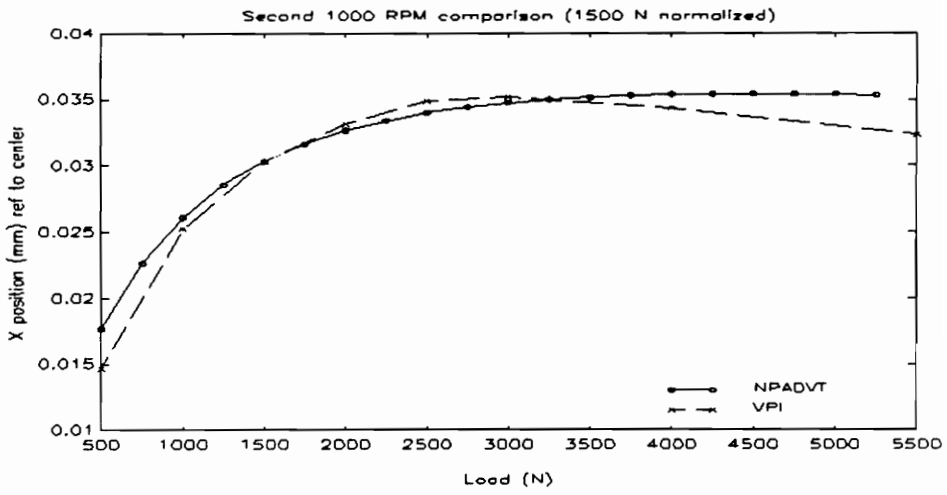

Fig. 135: 16.7 Hz X-Position 1500 N Normalized Comparison (Second Test Series)

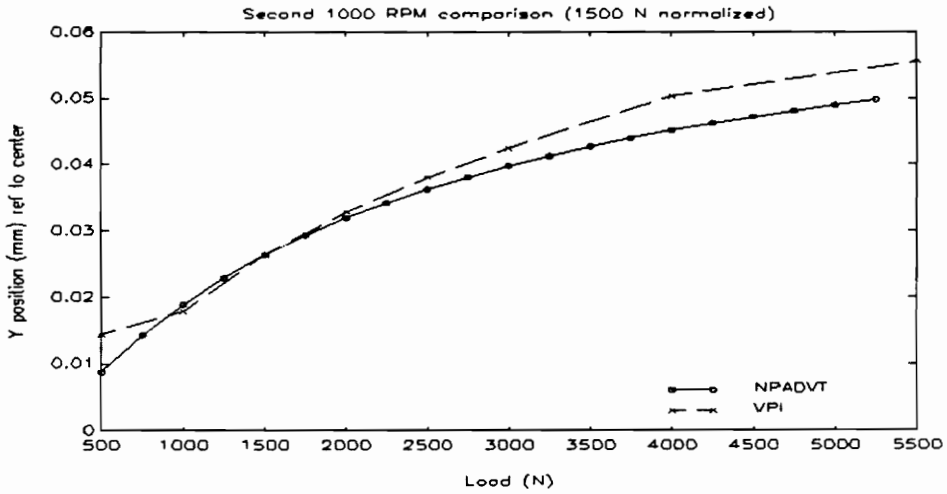

Fig. 136: 16.7 Hz Y-Position 1500 N Normalized Comparison (Second Test Series)

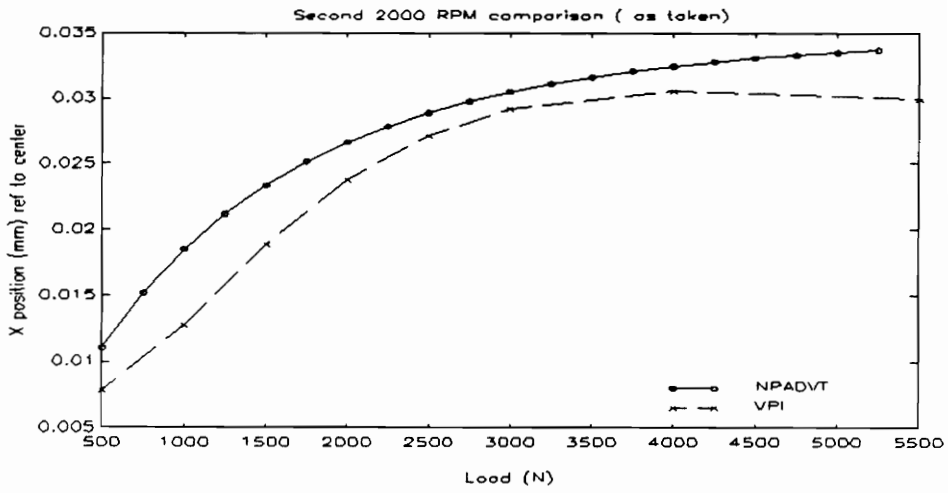

Fig. 137: 33.3 Hz X-Position Comparison (Second Test Series)

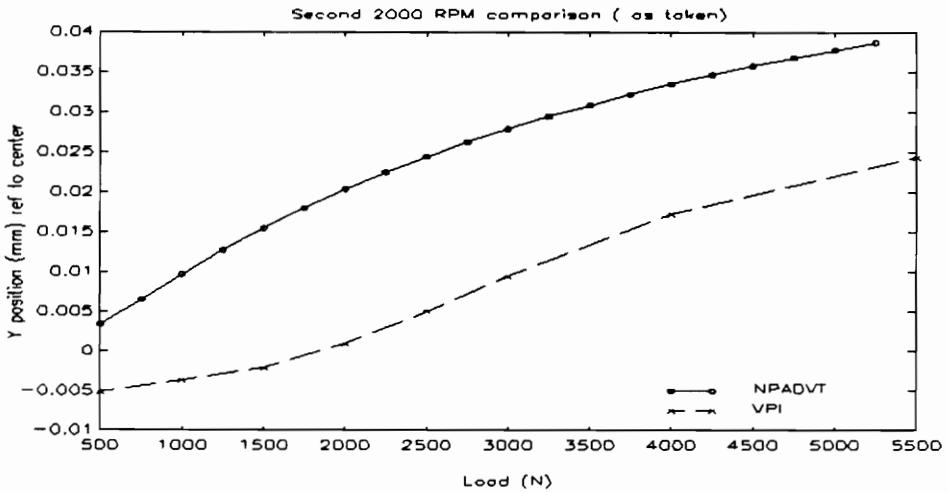

Fig. 138: 33.3 Hz Y-Position Comparison (Second Test Series)

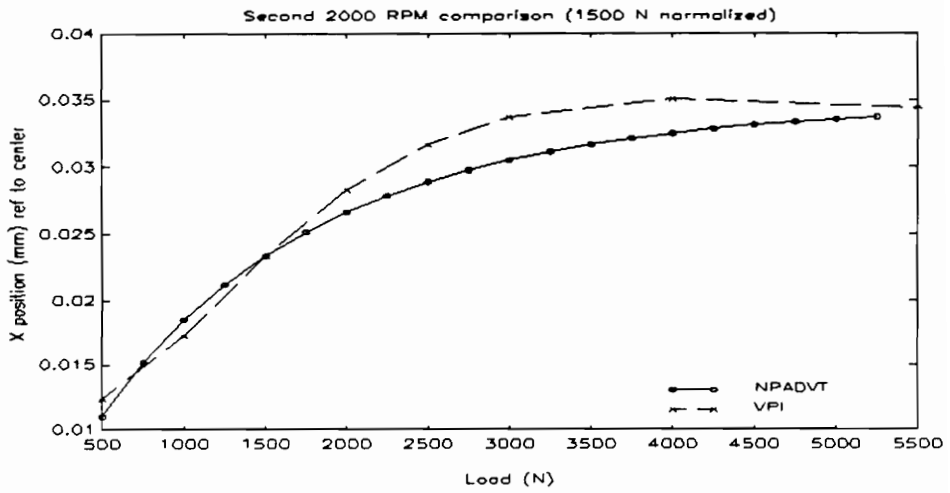

Fig. 139: 33.3 Hz X-Position 1500 N Normalized Comparison (Second Test Series)

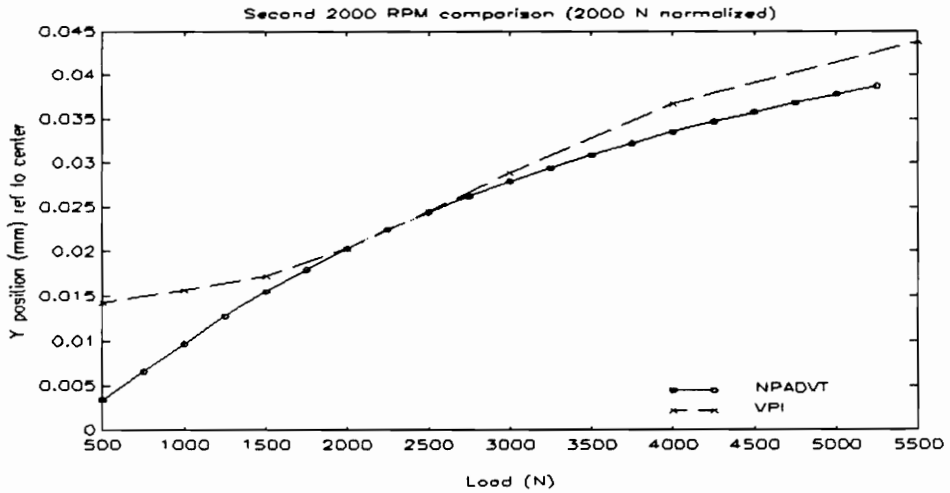

Fig. 140: 33.3 Hz Y-Position 2000 N Normalized Comparison (Second Test Series)

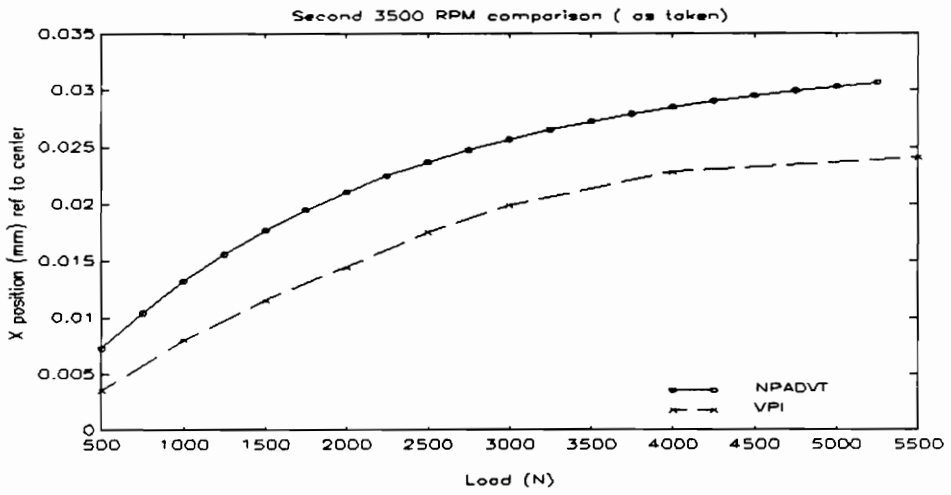

Fig. 141: 58.3 Hz X-Position Comparison (Second Test Series)

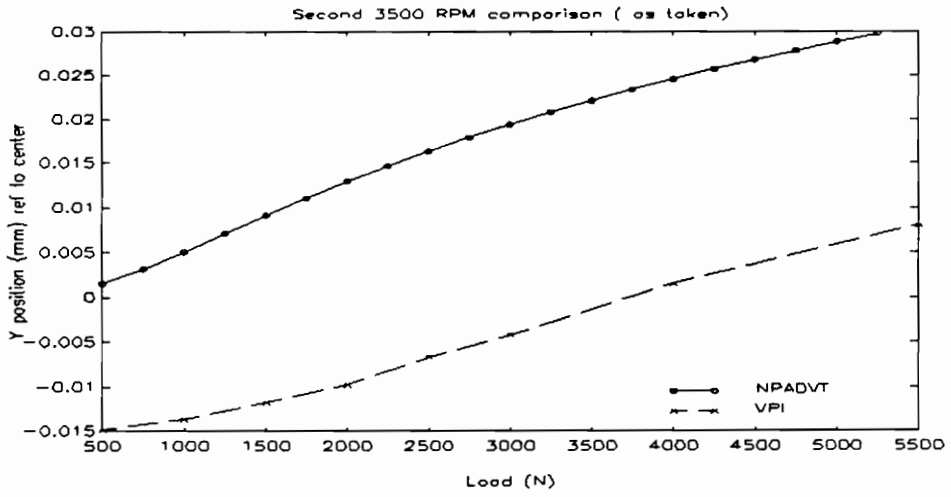

Fig. 142: 58.3 Hz Y-Position Comparison (Second Test Series)

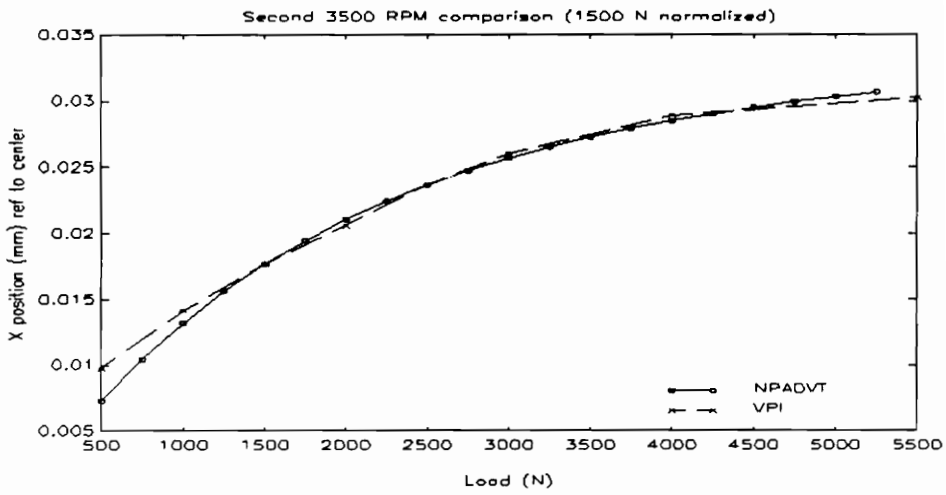

Fig. 143: 58.3 Hz - Position, 1500 N Normalized (Second Test Series)

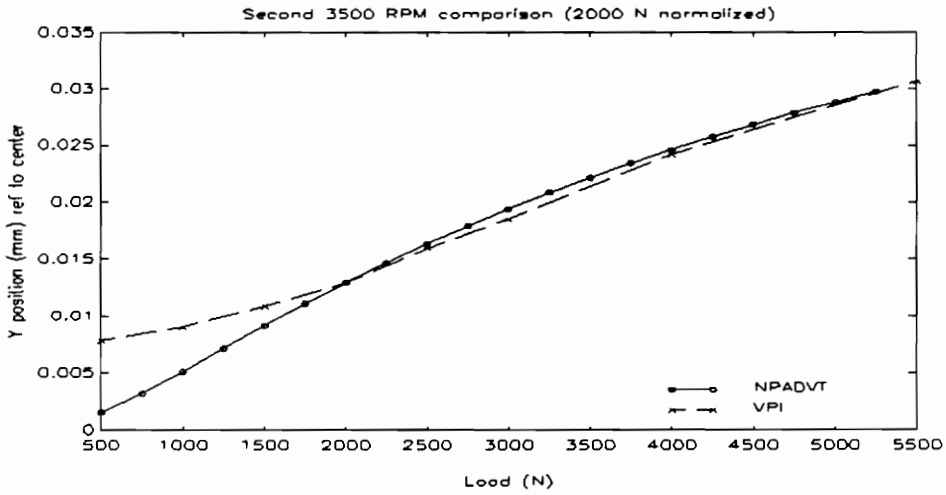

Fig. 144: 58.3 Hz Y-Position, 2000 N Normalized (Second Test Series)

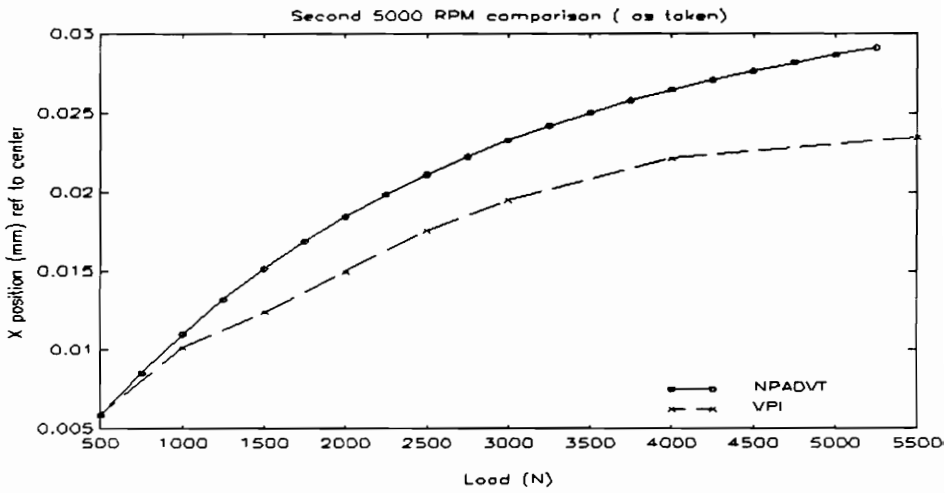

Fig. 145: 83.3 Hz X-Position Comparison (Second Test Series)

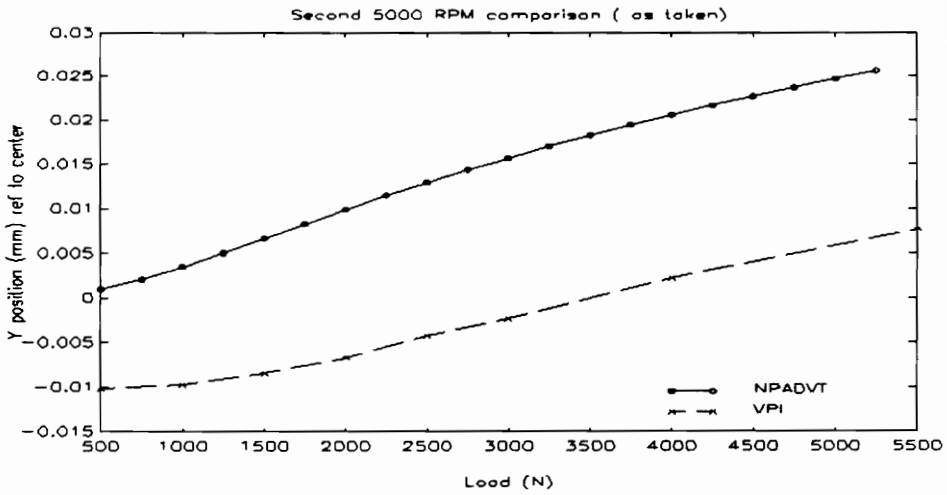

Fig. 146: 83.3 Hz Y-Position Comparison (Second Test Series)

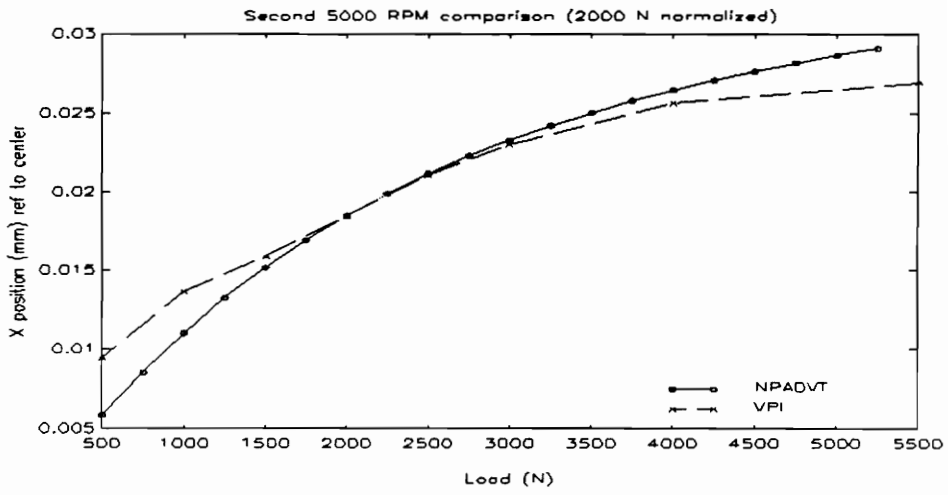

Fig. 147: 83.3 Hz X-Position 2000 N Normalized Comparison (Second Test Series)

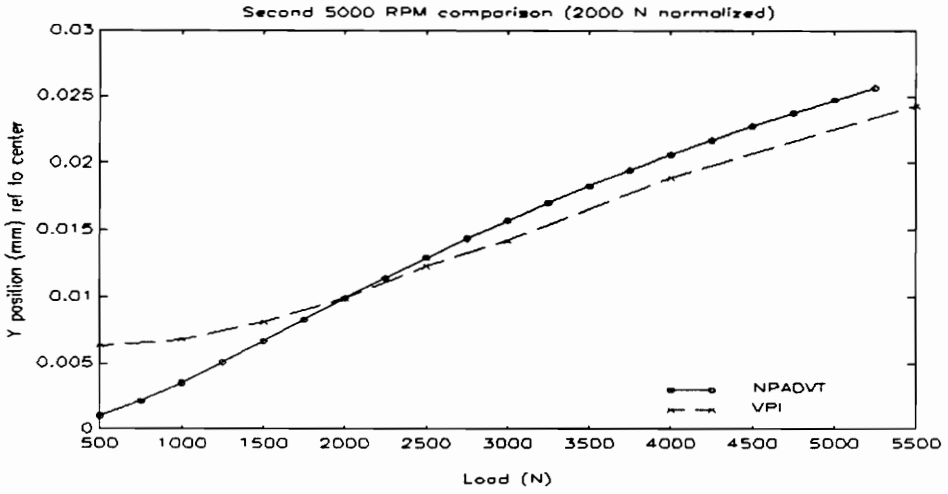

Fig. 148: 83.3 Hz Y-Position 2000 N Normalized Comparison (Second Test Series)

5.5.8 Discussion for Comparisons to NPADVT

16.7 Hz: For both tests, the x-position zero compares well. In general though, the NPADVT analysis, although close, does not exhibit the correct shape (this trend is the same as seen in the previous comparisons to published results). The y-position results are quite comparable with regards to the shape, except at light loads, where the experimental y-position exhibits a peculiar flatness. It is possible that this odd behavior is related to sleeve non-concentricity, as the thermal effects for light loads at this speed should be minimal. Surprisingly, the y-zero positions (as taken) exhibit fairly good agreement between the analytical and experimental results.

33.3 Hz: For this speed, the x-position zeros show very good agreement between analysis and experiment; the y-position zeros do not show as good agreement. The x-position at low loads also shows good agreement. As noted in previous comparisons to experiment, though, while the sign of the slope of the experimental locus changes, the analytical curve does not reflect this trend. The y-position locus again shows good agreement, except at light loads, where the experimental locus is oddly flat. The NPADVT analysis

is generally biased towards underestimating load capacity (the analytical eccentricity ratio would be too large)

58.3 Hz: As with the previous data sets, the x-position zeros show generally good agreement, while the experimental y-position zero is rather different from the NPADVT result. The normalized locus curves show good agreement between analysis and experiment. As before, however, the experimental x-locus hints at a slope reversal not seen in the analysis, and the experimental y-locus exhibits the unusual flattening at low loads. The x-locus slope reversal is not as apparent as in the previous two speeds due to the increased bearing load capacity related to the increase in speed.

83.3 Hz: For this speed, the x-position zero shows good agreement between analysis and experiment in the second test series, but not as good agreement in the first. The y-position zero does not show good agreement. In both the x-position and y-position shaft locus plots, the analytical and experimental shape show some agreement, but not as good as in previous cases. Part of the disagreement may be the results of the experimental outliers discussed previously; however, this effect does not explain all of the disagreement. The y-position curve flatness is again seen for light loads. This flattening occurs

for a greater range of loads, as would be expected for the increase in load capacity caused by the increase in speed. As before, the NPADVT results are biased towards a reduced load capacity; this could be, in part, caused by the effects for variable clearances.

5.6 Comments and Discussion

This set of experimental data, and the comparisons between experiments and between experiment and analysis, suggest that the test rig is basically functioning correctly. Ignoring the zero position fluctuations, the data is reasonably repeatable, although there is room for improvement. The comparisons between the NPADVT analysis and experiment also show the same general trends, i.e., agreement in Y, disagreement in X, as seen in the comparisons to accepted published data. Thus the rig is not grossly altering the bearing characteristics. Interestingly, Ref. 20, which is an analytical examination of thermally induced bearing deformation, shows the same trends as observed in these comparisons. In this work, it is shown that an analysis which ignores thermally induced deformation tends to predict too large an operating eccentricity; this is the trend observed in the comparisons between NPADVT and the VPI rig. It seems unlikely that the strange flattening of the locus curves seen at low loads are the results of thermal effects, as the

temperatures associated with light loads are correspondingly small. It is more likely that this anomaly is related to shaft non-concentricity.

The biggest test rig problem appears to be the zero fluctuations. It seems most likely that these are the result of effects external to the bearing/shaft interface since the normalized data show such good agreement. The relatively close agreement between most of the analytical and experimental x-position zeros suggests that the problem is worst with respect to the y-position measurements. This observation indicates that much of the problem may be related to thermal growth of the large stainless steel bearing housing which is free to expand symmetrically in the X direction, but constrained to expand only upwards in the Y direction. There is also some experimental support for this hypothesis; the housing vertical thermal growth has been measured to be between 0.051 and 0.102 mm when warmed from the lab ambient temperature of 18°C to operating temperature. The actual housing temperature probably ranges from the nominal oil temperature of 43°C to something slightly lower, depending on the operating conditions. The possibility of bearing thermal growth also cannot be ruled out, as the clearance check/zero procedure takes about two minutes; indeed, after one of the 83.3 Hz tests, the procedure failed a built in settling check (the shaft resting position also noticeably changed as viewed on

an oscilloscope connected to a pair of the inner displacement probes). The thermal growth issue also makes precise shaft alignment difficult. It is also quite likely that some of the discrepancy is due to the fact that the lift check is taken with the shaft stationary, and thus the run-out compensation values are not applied. This fact could introduce an offset that could explain some of the observed zero offsets.

Another effect which may have some impact is shaft bending. At full load, there is a significant difference between displacement measurements at the inner and outer faces of the bearing. Although the measured slope (relative to the 1000 N zero position) is on the order of hundredths of a degree, the absolute difference between the inner and outer measurements is a large percentage of the bearing clearance. The exact effect of this deflection is not apparent, but it does seem likely that it has some impact on the results. The deflection also causes problems with the zero/clearance procedure; the applied load must be large enough to firmly seat the shaft, but not so large as to cause bending; the 1000 N load used was selected from only heuristic arguments, and may not be the optimal load.

Other discussion, particularly concerning NPADVT, will be reserved for the conclusions to this work.

Chapter 6

VPI Results and Comparisons for Pocket Bearing

6.1 Introduction

With the VPI rig shown to be functional within certain limits, it is of interest to examine experimental data for a slightly different bearing geometry. Thus, the final experimental data set examined in this work is for the 101.1 mm bearing described in chapter 5 modified by machining a pocket into the upper half (see Fig. 2). The interest in testing a pocket bearing is that one easy method of enhancing the stability of a machine operating on a plain axial-groove bearing is to remove the bearing, machine a pocket into the top of the bearing, and reinstall the bearing. This is essentially the procedure followed with the VPI bearing. Thus, the results for the modified bearing should be representative of the changes expected from this modification. It turns out that the results for this bearing also exhibit some interesting

trends that may be construed as supporting the thermally induced deformation hypothesis of the previous chapter. Data for this type of bearing are also not available in the published literature. The test results presented in this chapter are for: 1) an initial three tests at speeds of 16.7, 33.3, and 58.3 Hz, and 2) a repeat of these three tests. Loads of 500, 1000, 1500, 2000, 2500, 3000, 4000 and 5500 N are examined. The 83.3 Hz speed employed in the previous chapter could not be attained with the modified bearing due to problems with entrained air in the oil (a pocket bearing has higher flow requirements than a plain bearing - the higher flow overwhelmed the settling tank's entrained air removal capability). The data as recorded, as comparisons between the original and repeated tests, and as comparisons between NPADVT and the experimental data, are presented. Comparisons will also be made between the experimental and analytical shaft loci for the original bearing and the modified bearing.

6.2 Pocket Bearing and Oil

The bearing for this test series is the original two-axial-groove bearing described in chapter five, modified by the addition of a single pocket in the upper third of the bearing. The modified bearing has the following characteristics:

Diameter:	101.6 mm

Length:	57.15 mm
C_D/D Ratio:	0.00160 to 0.00168
Pocket Extent:	0 to 110 degrees from horizontal (CCW, against rotation)
Pocket Depth:	0.254 mm
Pocket Width:	42.93 mm (Centered in bearing)
Weep Hole Dia:	1.6 mm
Oil Inlet Dia:	6.76 mm
Feed Grooves:	0 and 180 degrees from horizontal 25 degrees of arc width 2.5 mm maximum depth

The pocket to bearing surface transition at the 110 degree position is essentially as left by the milling cutter, with only minor blending of the edge. As described in the previous chapter, the bearing is of babbitt faced (0.43 mm thick), single piece bronze construction, 139.7 mm O.D. The 203.2 mm O.D. horizontally split bearing holder which adapts the bearing to the test rig bearing cavity is fabricated from 1018 steel. It is the same width as the bearing. The bearing to holder fit is approximately line to line. The fabricator's inspection of the bearing and holder suggests that there should

be minimal distortion of the bearing bush caused by installation in the holder. The bearing/holder assembly is installed in the test rig as discussed in chapter 3.

The oil used for this test series is the same ISO 32 oil used previously. For reference, the properties of this oil and nominal inlet conditions are repeated below:

Density:	863 kg/m^3 at 50° C
Specific Heat:	1.98 kJ/kg•K at 50 °C
Viscosity:	16.1 mPa•s at 40 °C 24.8 mPa•s at 50 ° C
Inlet Temp:	43 °C
Inlet Pressure:	0.034 MPa
Inlet flow rate:	0.7 to 0.8 cm^3/ s

6.3 Experimental Procedure

The tests are conducted as described previously for the plain two-axial-groove bearing tests (see chapter 5).

6.4 Experimental Pocket Bearing Data and Comparisons

The data for this bearing will be presented as recorded as well as for comparisons between repeated tests, and a comparison will be made between the unmodified and modified bearings.

6.4.1 Data

The experimental data for the pocket bearing, as obtained with the VPI rig, are presented below in Fig. 149 through Fig. 154. These data are plotted for absolute shaft position (X and Y) as offset by the bearing center coordinates as determined by the post test lift check. The clearance obtained with this lift check is also included with each plot. The estimated bearing center is to the upper left of these plots. Each plot consists of the five measured points for each load at a given speed, as well as an average shaft centerline curve. This average centerline curve is used in the comparisons to NPADVT analysis, and is generated by finding the average X and average Y coordinate for each group of five points.

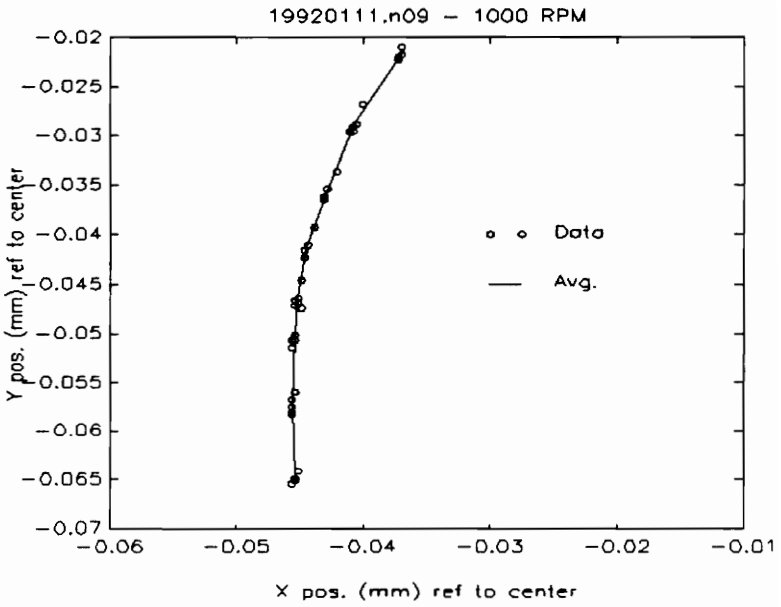

Fig. 149: First 16.7 Hz Test (Cd = 0.163 mm)

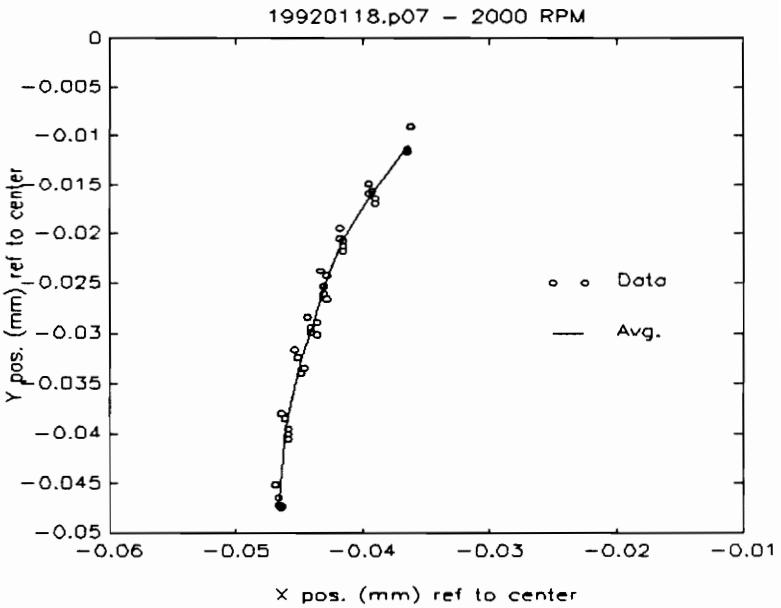

Fig. 150: First 33.3 Hz Test (Cd = 0.166 mm)

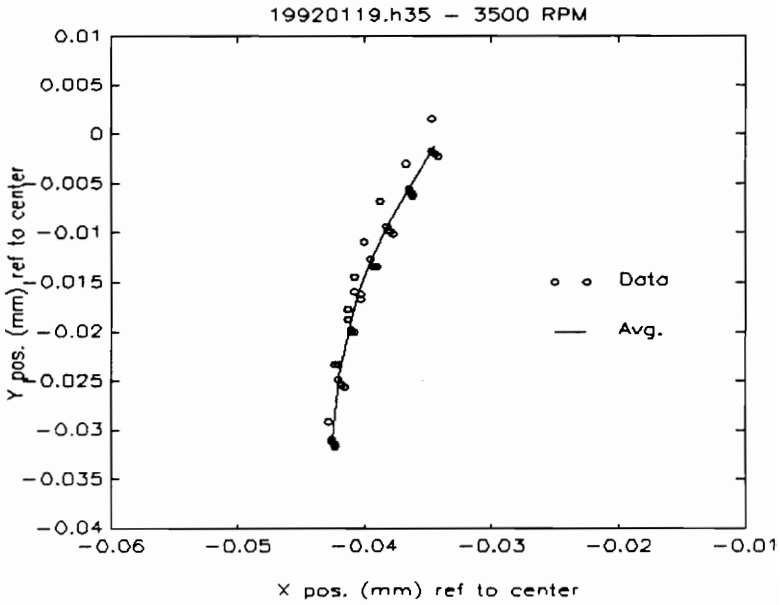

Fig. 151: First 58.3 Hz Test (Cd = 0.156 mm)

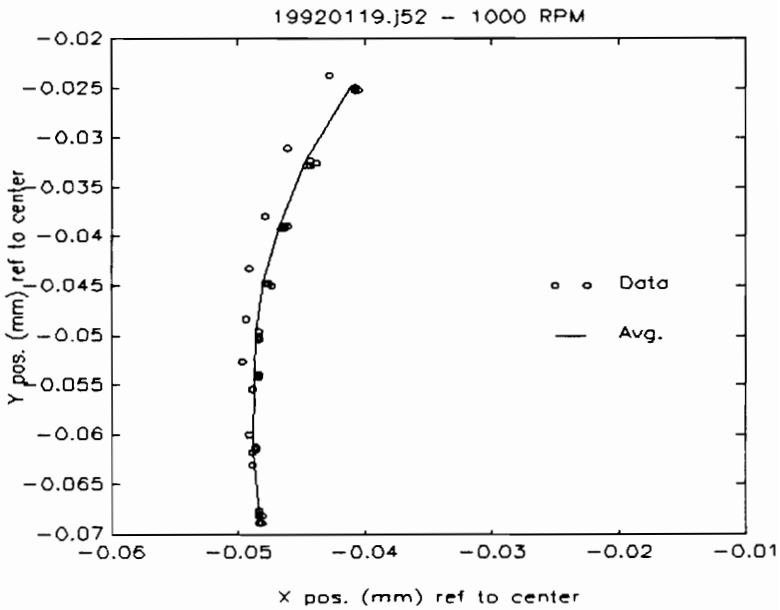

Fig. 152: Second 16.7 Hz Test (Cd = 0.169 mm)

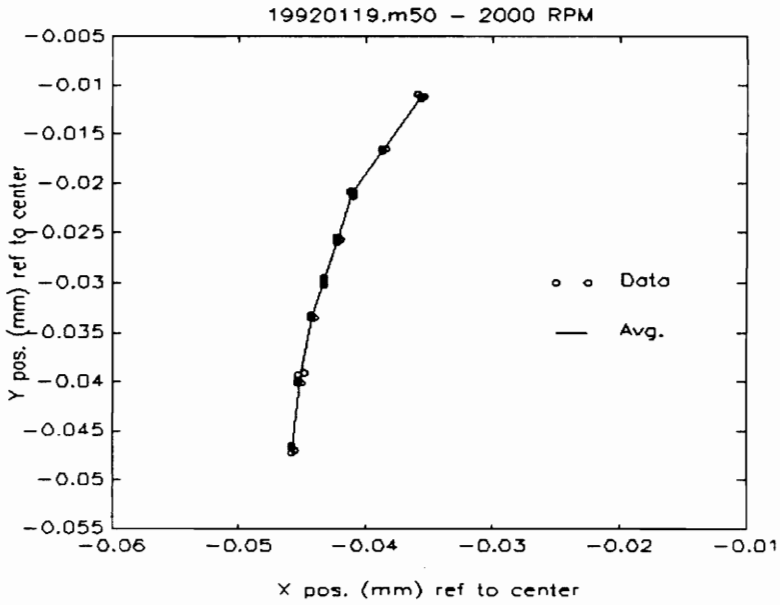

Fig. 153: Second 33.3 Hz Test (Cd = 0.169 mm)

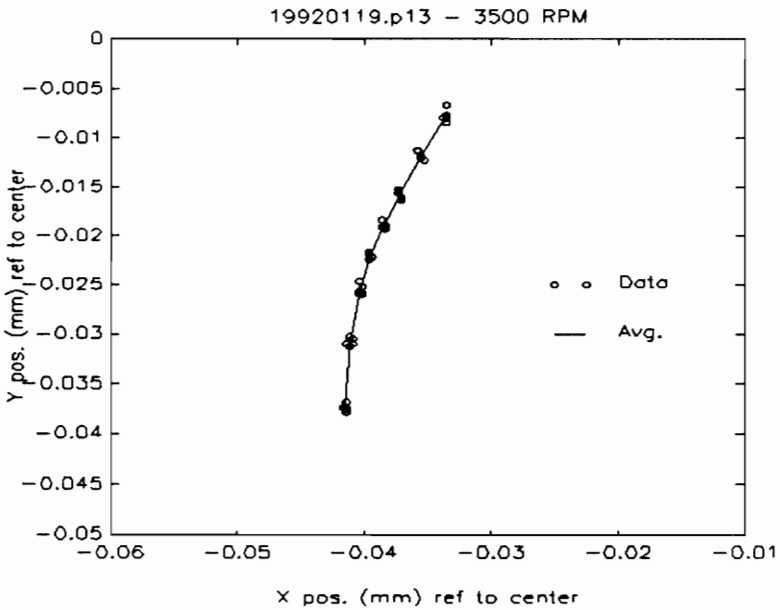

Fig. 154: Second 58.3 Hz Test (Cd = 0.166 mm)

6.4.2 Discussion of Results

The data presented in Fig. 149 through Fig. 154 show a smaller, but similar, level of scatter than the data presented in Chapter 5. The small magnitudes of the experimental scatter lends support to the idea that the rig is basically functional. Indeed, in the case of Fig. 153, the scatter is all but negligible. The outliers seen in the remaining figures are again from the first set of 8 load points. This consistent outlier behavior suggests that the mechanism causing the aberrant behavior is not tied to the bearing geometry. The behavior seen in these plots tends to support the thermal transient hypothesis, especially Fig. 152, which corresponds to 16.7 Hz data taken during a test which began as an 83.3 Hz test, and became a 16.7 Hz test after air bubbles were observed in the oil feedline. The entrained air does not explain the observed behavior, as the rig was operated at low load at 16.7 Hz for a sufficient time for the air to be eliminated, but possibly not long enough to achieve a new thermal equilibrium. In all other cases, except the initial 16.7 Hz test of Fig. 149, the rig was operated at the maximum load of 5500 N for approximately 10 minutes before the autoloading sequence was initiated.

6.4.3 Comparisons For Repeated Tests

In Fig. 156 through Fig. 160, the three initial tests are compared with repeat tests for the same nominal conditions. Due to the problem with zero position fluctuations, the data are presented as recorded, as well as normalized at 5500 N. In the 5500 N normalized plots, areas corresponding to plus or minus two standard deviations about the mean of each group of four points are indicated for each load. See appendix B for further details on these elliptical areas. Note also that the first (increasing load) 8 data points were eliminated from the data for these comparisons, since they seem to reflect some thermal effect rather than normal experimental scatter.

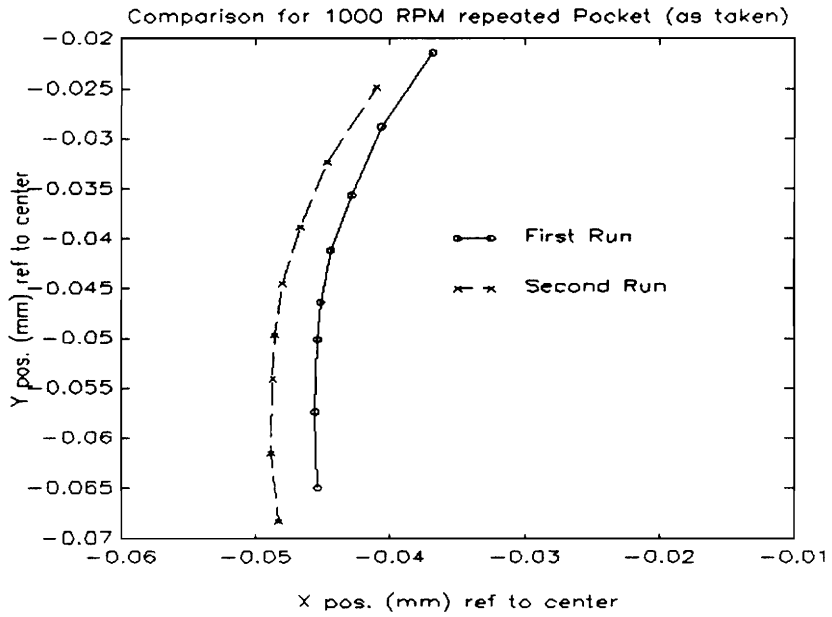

Fig. 155: 16.7 Hz Repeated Tests (as Recorded)

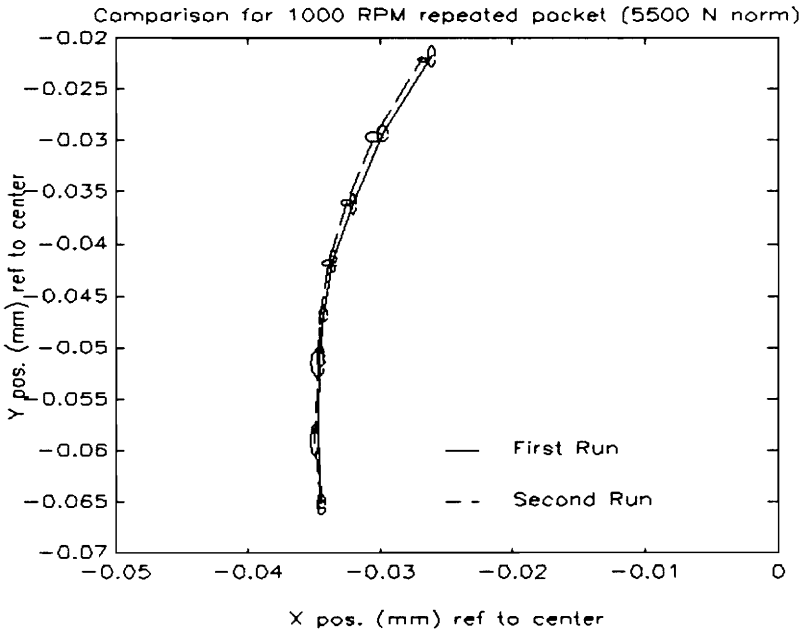

Fig. 156: 16.7 Hz Repeated Tests (5500 N Normalized)

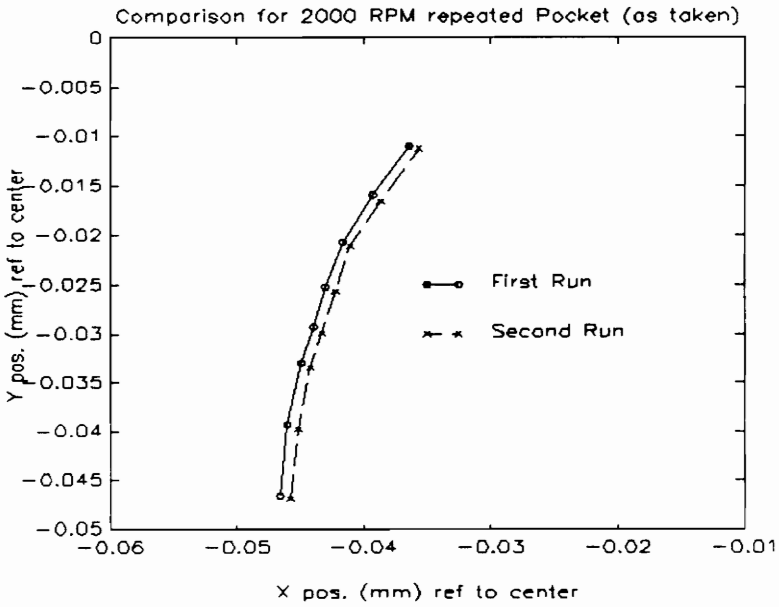

Fig. 157: 33.3 Hz Repeated Tests (as Recorded)

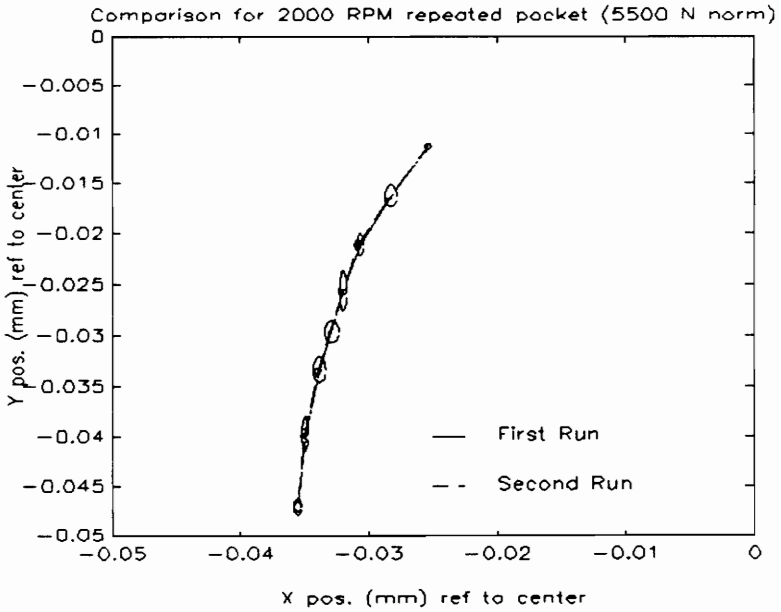

Fig. 158: 33.3 Hz Repeated Tests (5500 N Normalized)

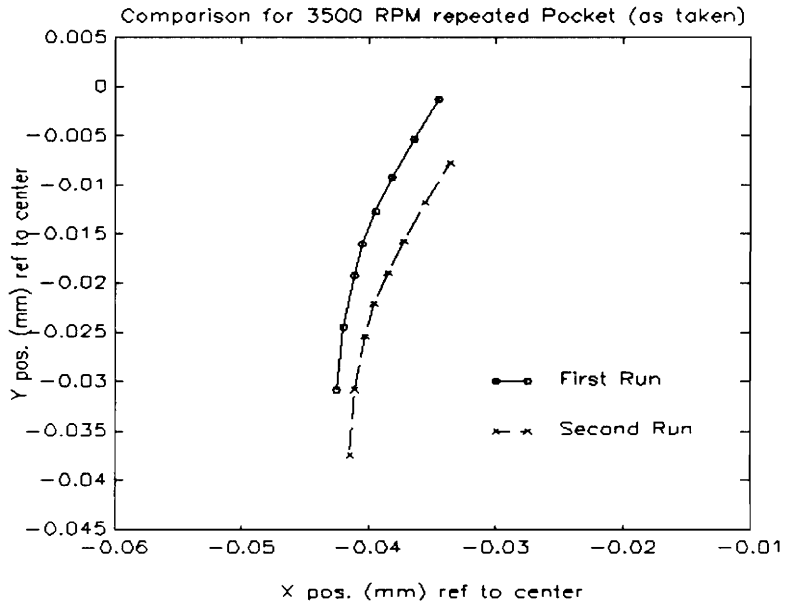

Fig. 159: 58.3 Hz Repeated Tests (as Recorded)

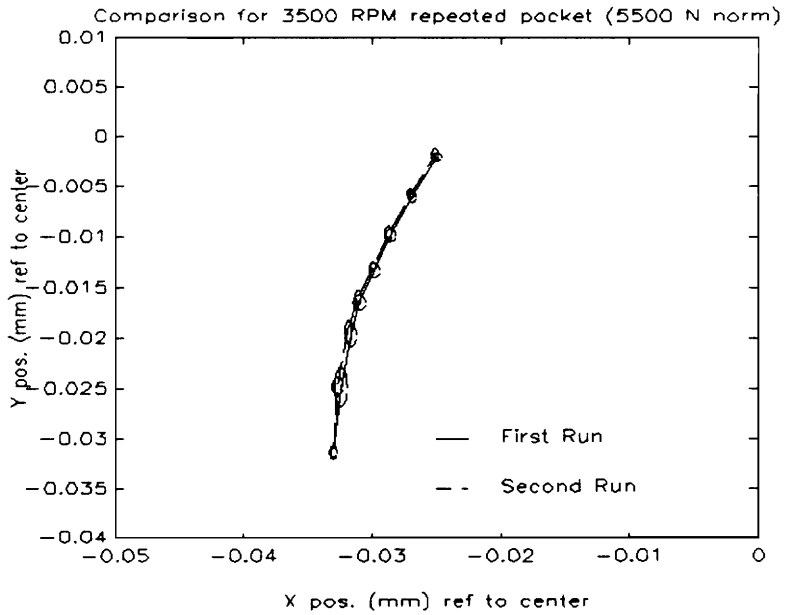

Fig. 160: 58.3 Hz Repeated Tests (5500 N Normalized)

6.4.4 Discussion of Repeated Tests

16.7 Hz: The results for this speed show very good reproducibility; the difference in zero is only slightly greater than the experimental scatter, and the normalized comparison shows that the locus shapes are almost identical. The plus or minus two standard deviation areas are contained within the same area or touching, thus indicating good agreement.

33.3 Hz: The results for this speed are phenomenally good. Even in the non-normalized plot, the curves are almost identical in both location and shape. In the normalized plots, the two curves are seen to be all but indistinguishable. This agreement is amazing, especially considering the amount of scatter observed in the first test at this speed. The effect of this scatter is evident in the different sizes of the areas corresponding to plus or minus two standard deviations for the two curves.

58.3 Hz: The results for this speed show a much larger zero position difference than do the previous two speeds. The normalized results, however, again show extremely good agreement in the shapes of the two locus curves despite the scatter observed in the first data set.

6.4.5 Comparisons Between NPADVT and VPI for Pocket Bearing

Comparisons between the experimental data and the NPADVT analysis for the same nominal conditions are presented in Fig. 161 through Fig. 180. As with the comparisons for the two-axial-groove bearing, comparisons to the actual data, as well as normalized comparisons, are presented. The normalized comparisons, however, will not be presented for the second 33.3 Hz and 58.3 Hz tests since the resulting plots would yield no new insight (the normalized plots for these two tests would be the same as the normalized plots for the same speeds for the first test series since the curves from the initial test and the repeat test are indistinguishable when normalized). As with the two-axial-groove results, these plots include data for all five repetitions of each load/speed point in generating the average centerline position. The data are plotted as absolute shaft position relative to the bearing center versus load. The NPADVT data is dimensionalized by multiplying the non-dimensional analytical result by the appropriate clearance.

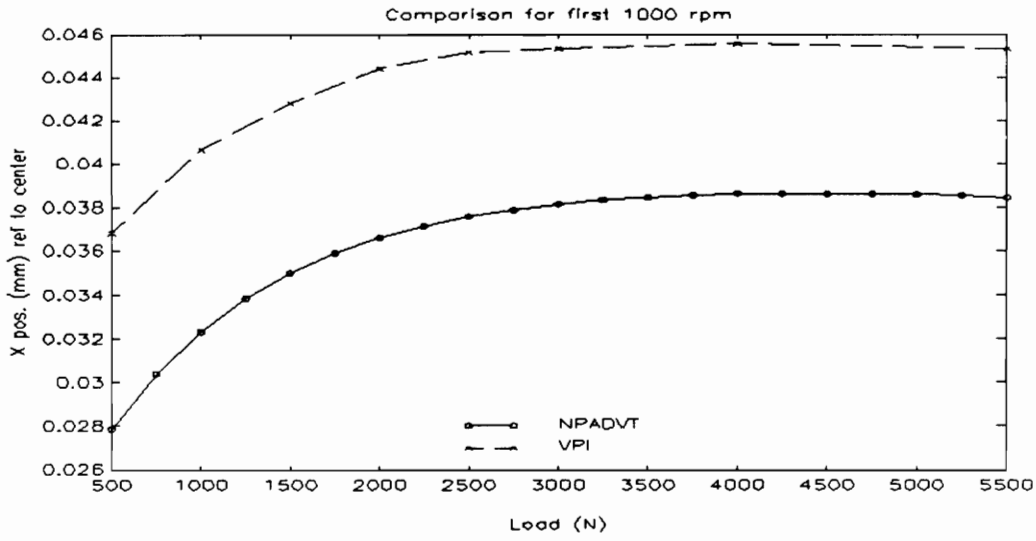

Fig. 161: 16.7 Hz Pocket X-Position Comparison (First Test Series)

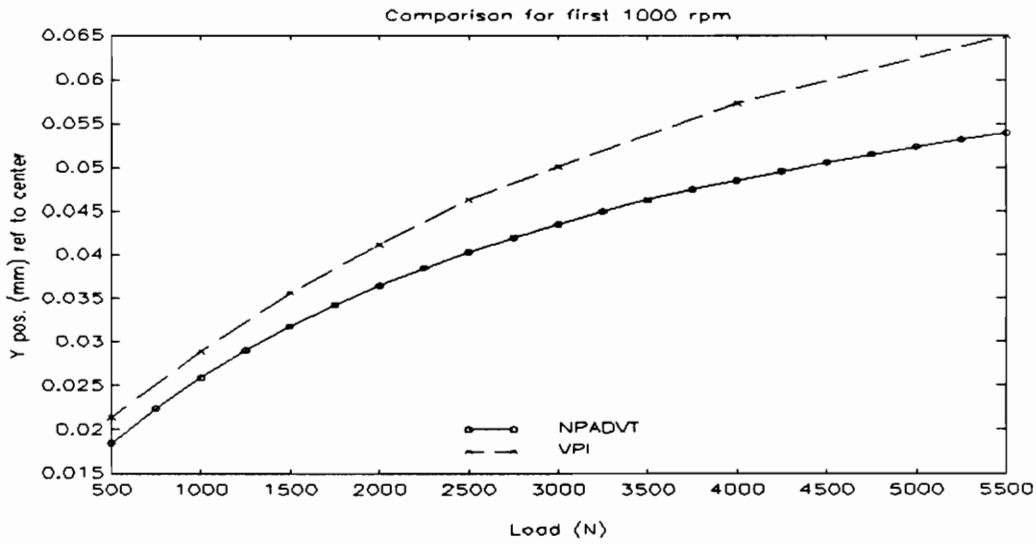

Fig. 162: 16.7 Hz Pocket Y-Position Comparison (First Test Series)

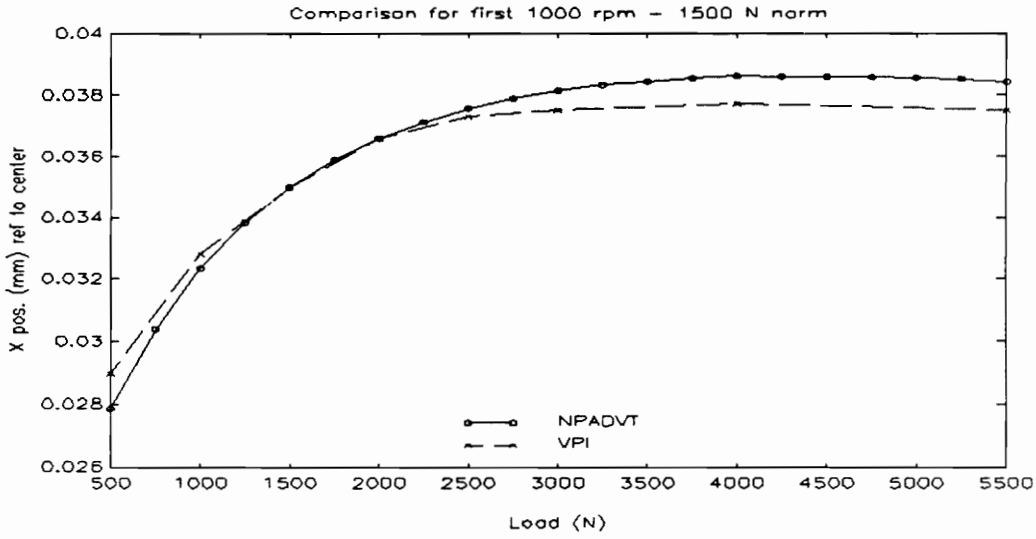

Fig. 163: 16.7 Hz Pocket X-Position 1500 N Normalized Comparison (First Test Series)

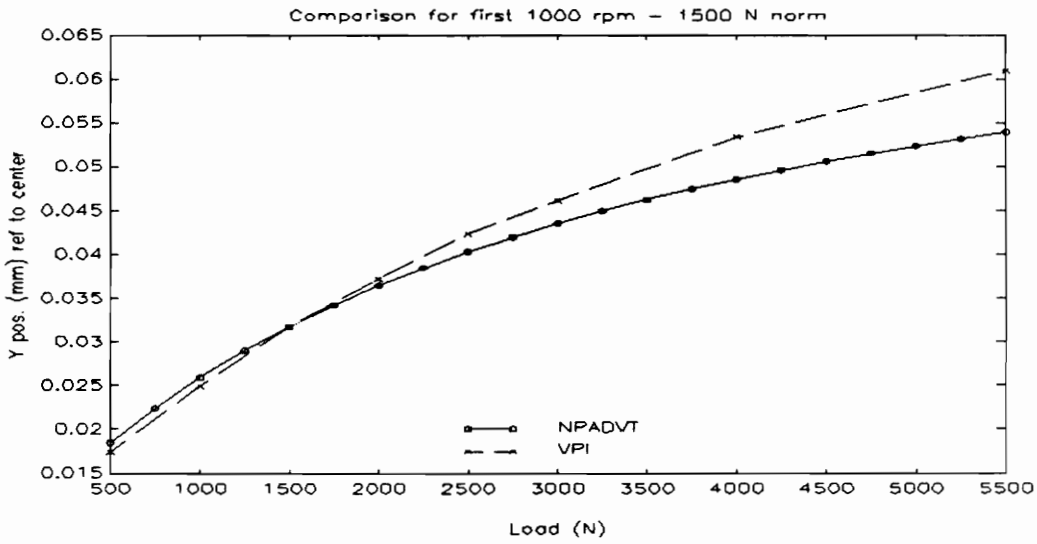

Fig. 164: 16.7 Hz Pocket Y-Position 1500 N Normalized Comparison (First Test Series)

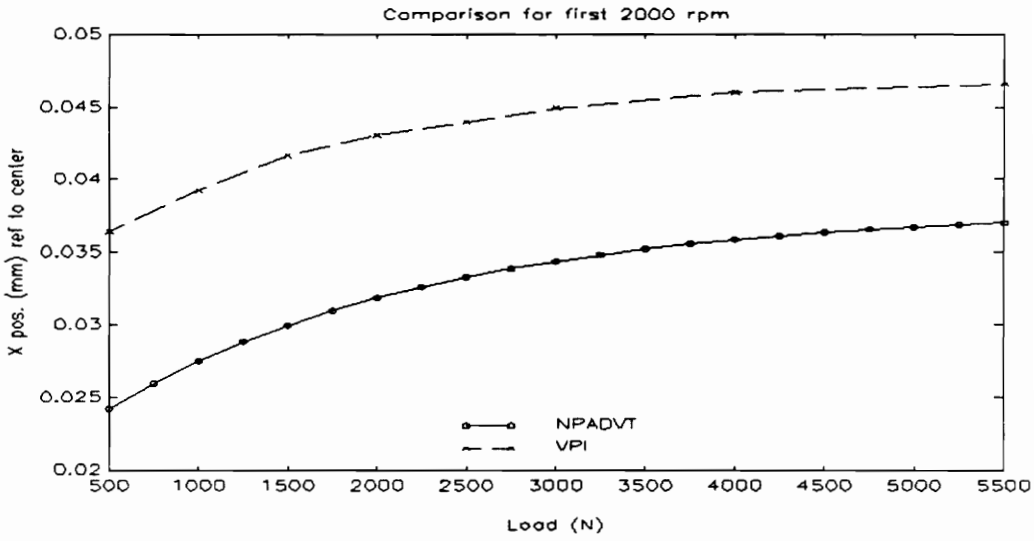

Fig. 165: 33.3 Hz Pocket X-Position Comparison (First Test Series)

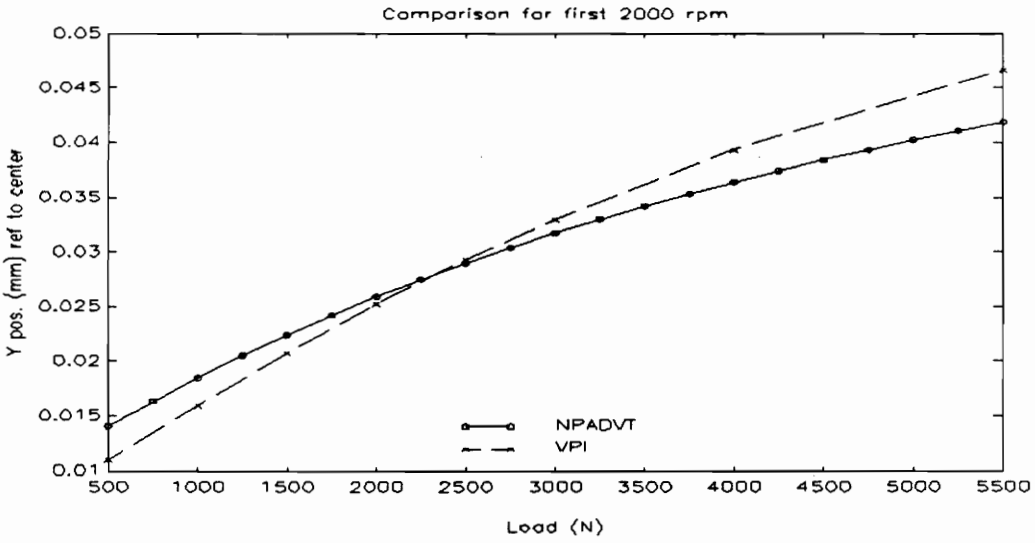

Fig. 166: 33.3 Hz Pocket Y-Position Comparison (First Test Series)

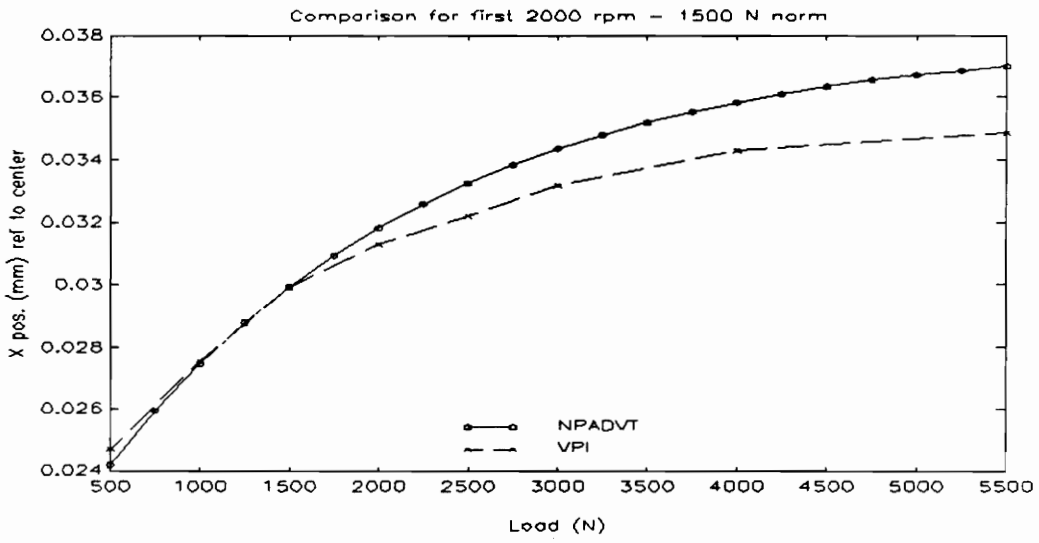

Fig. 167: 33.3 Hz Pocket X-Position 1500 N Normalized Comparison (First Test Series)

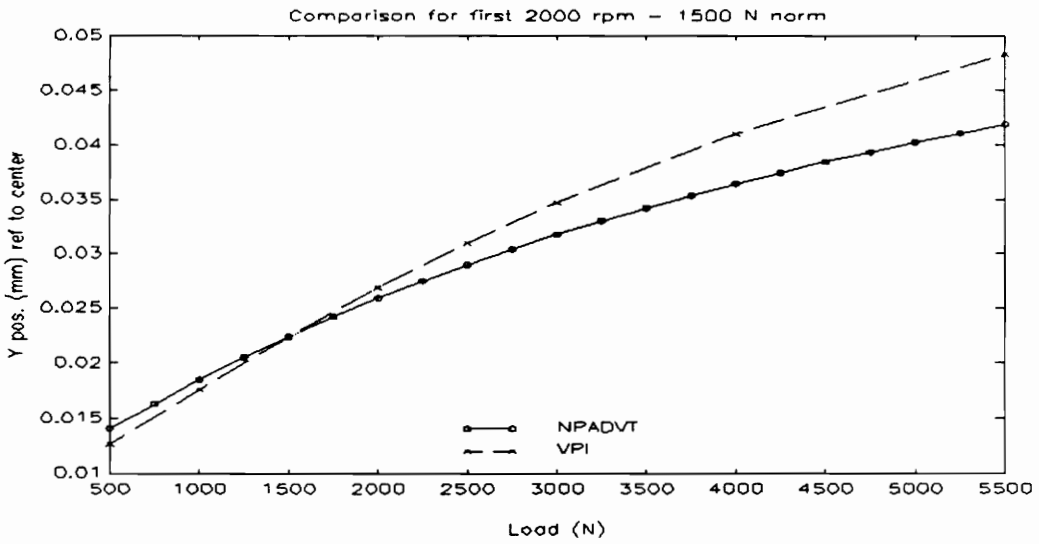

Fig. 168: 33.3 Hz Pocket Y-Position 1500 N Normalized Comparison (First Test Series)

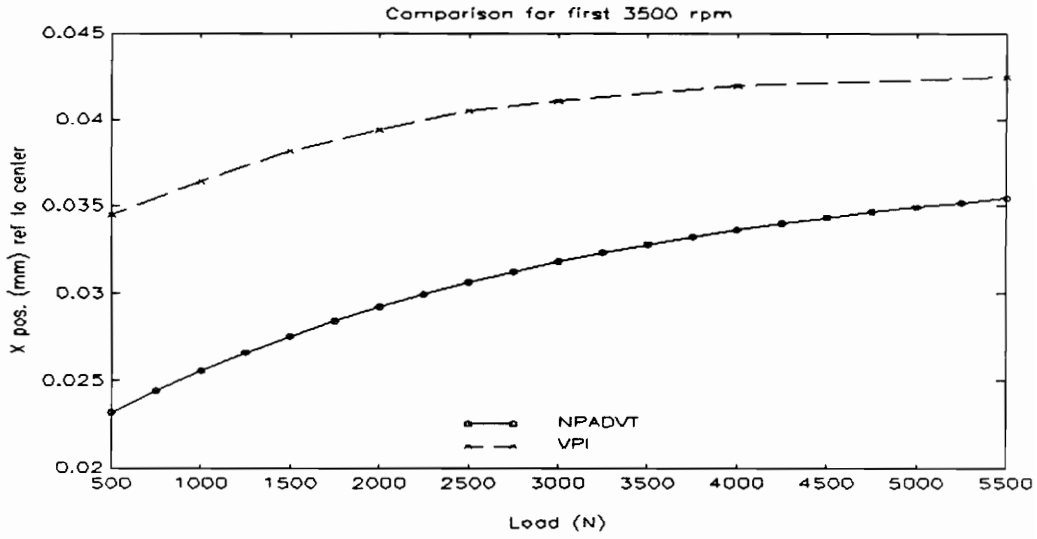

Fig. 169: 58.3 Hz Pocket X-Position Comparison (First Test Series)

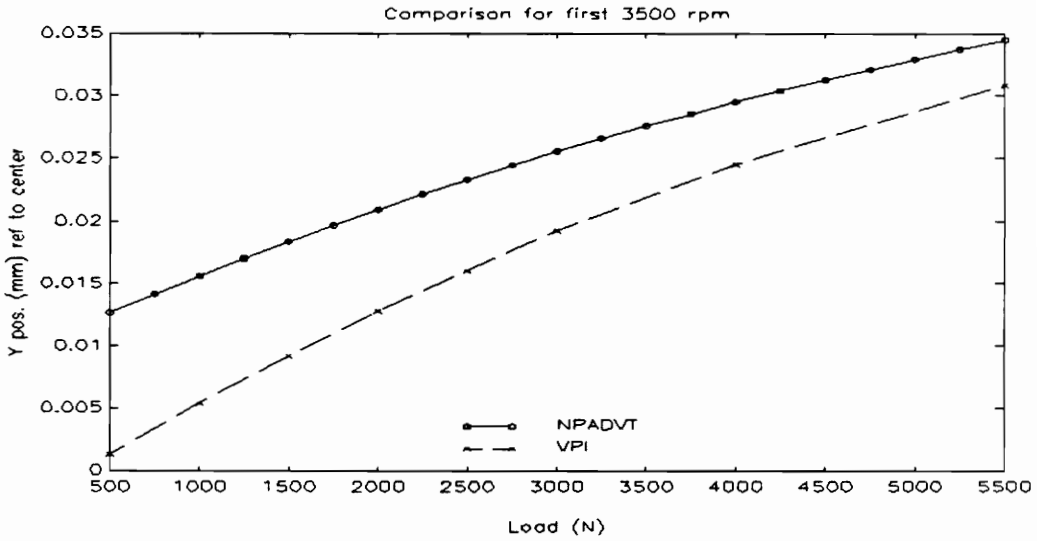

Fig. 170: 58.3 Hz Pocket Y-Position Comparison (First Test Series)

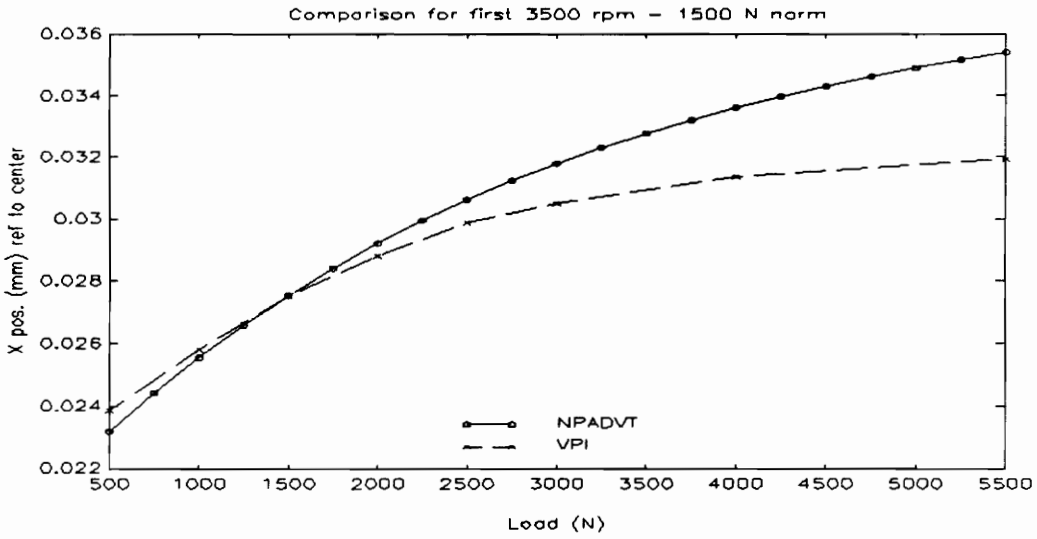

Fig. 171: 58.3 Hz Pocket X-Position 1500 N Normalized Comparison (First Test Series)

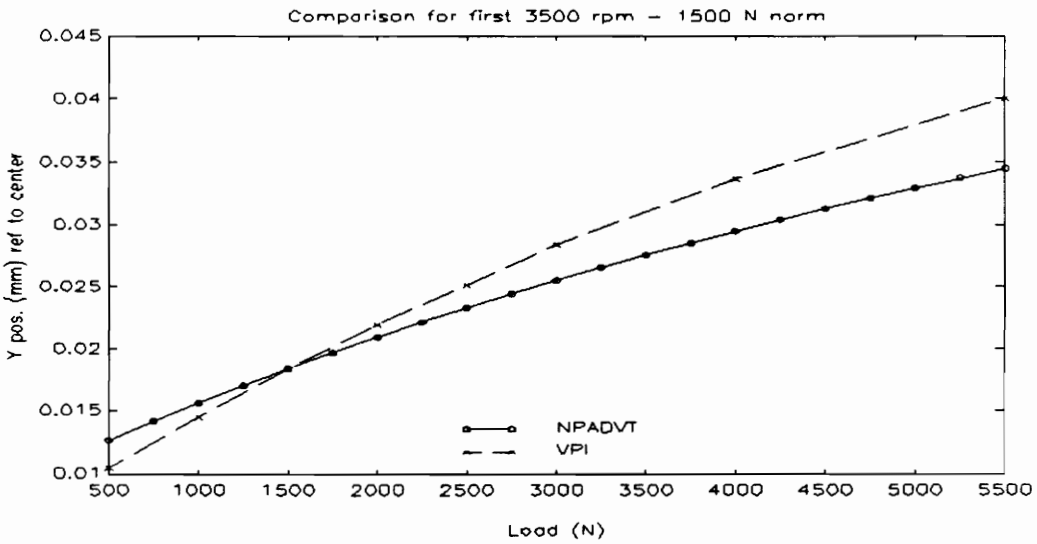

Fig. 172: 58.3 Hz Pocket Y-Position 1500 N Normalized Comparison (First Test Series)

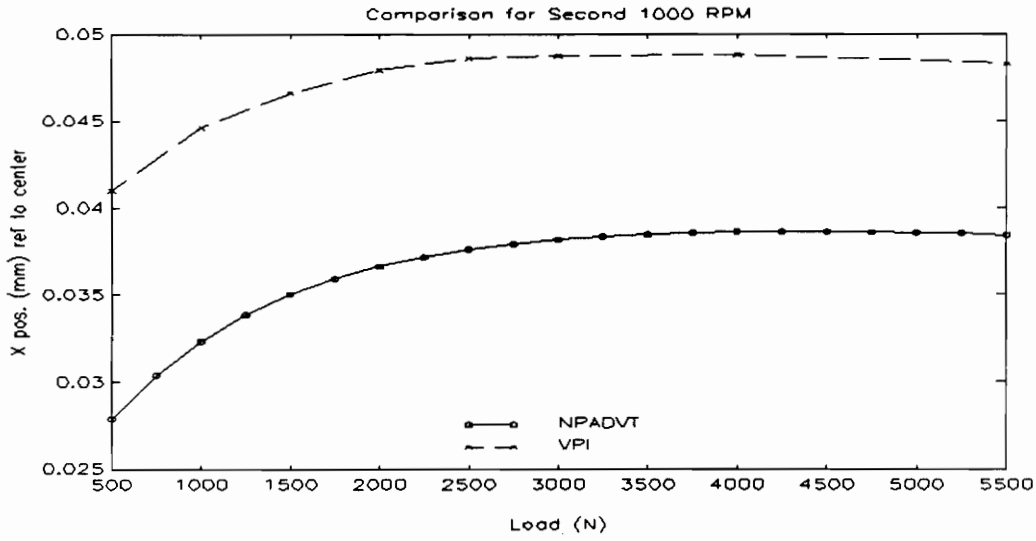

Fig. 173: 16.7 Hz Pocket X-Position Comparison (Second Test Series)

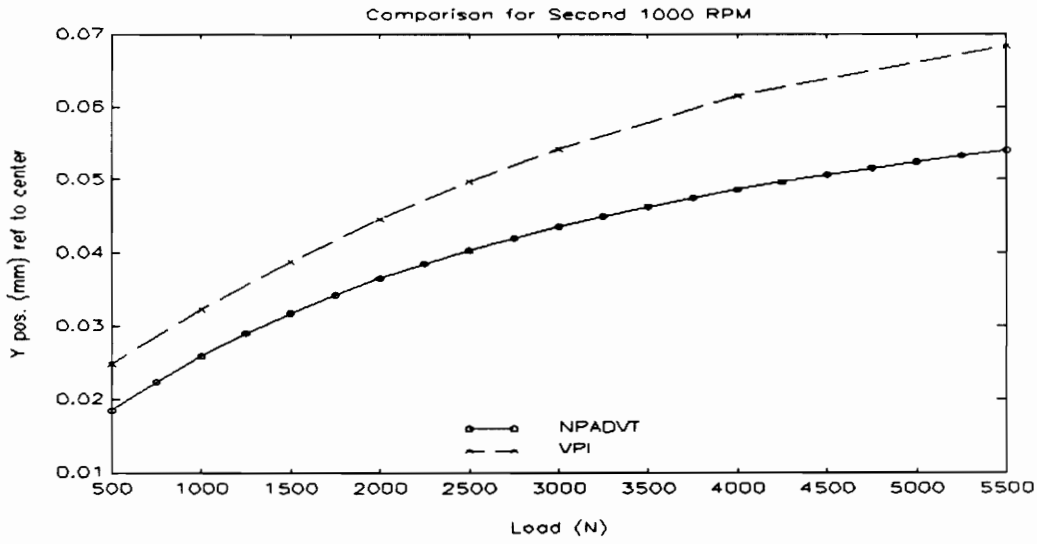

Fig. 174: 16.7 Hz Pocket Y-Position Comparison (Second Test Series)

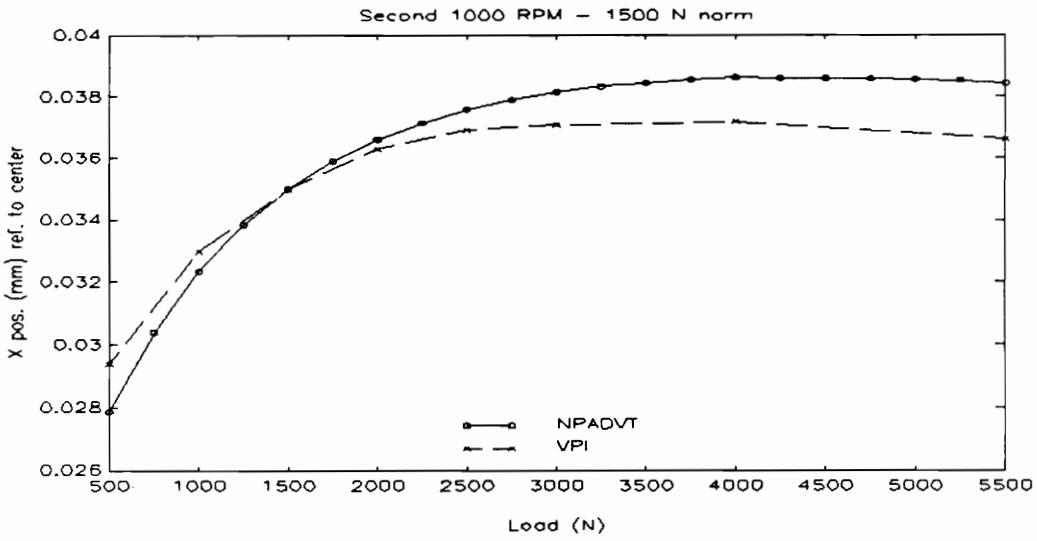

Fig. 175: 16.7 Hz Pocket X-Position 1500 N Normalized Comparison (Second Test Series)

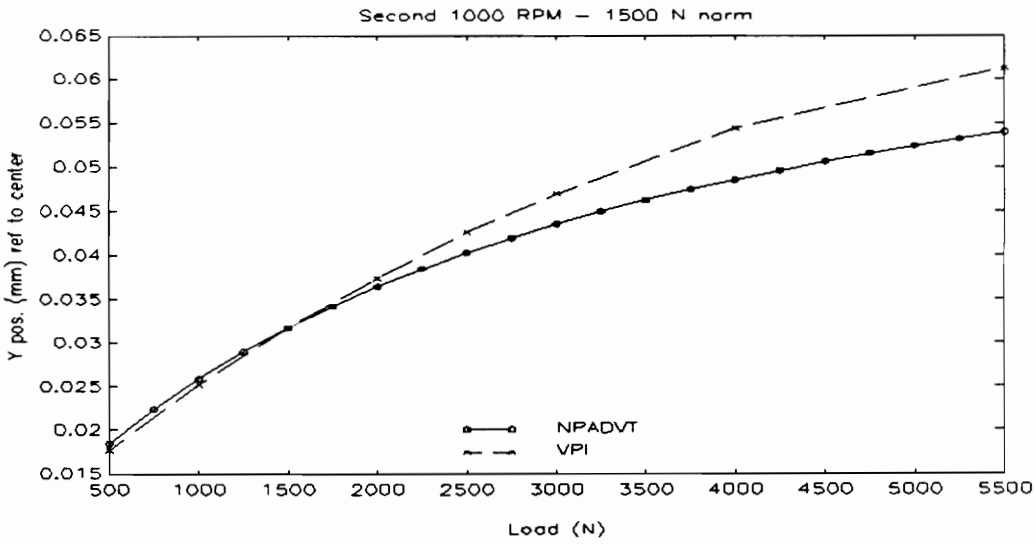

Fig. 176: 16.7 Hz Pocket Y-Position 1500 N Normalized Comparison (Second Test Series)

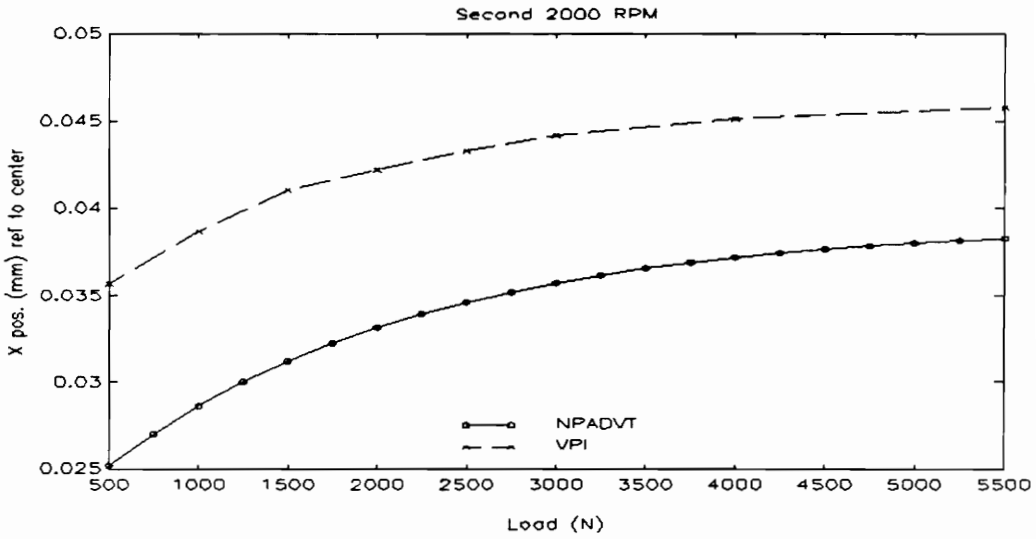

Fig. 177: 33.3 Hz Pocket X-Position Comparison (Second Test Series)

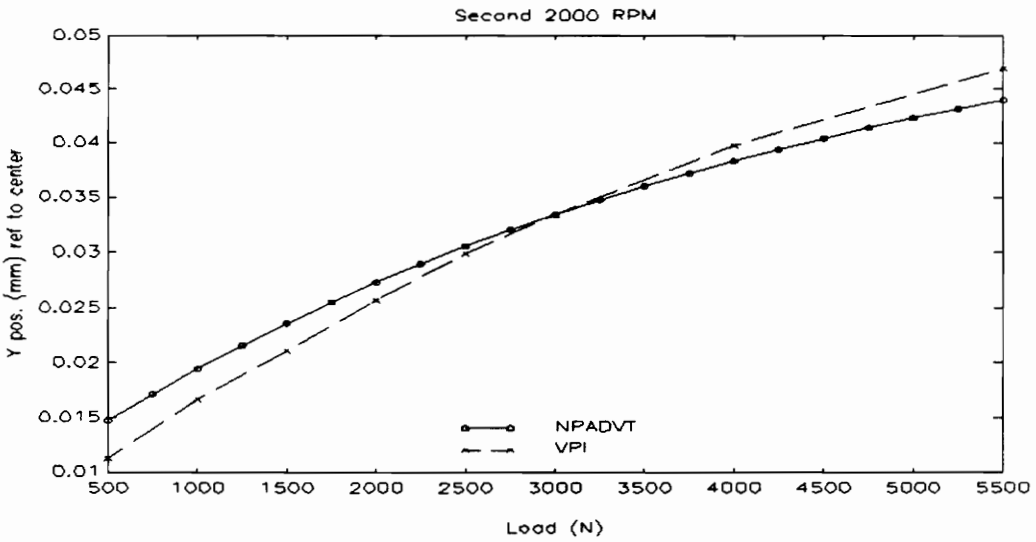

Fig. 178: 33.3 Hz Pocket Y-Position Comparison (Second Test Series)

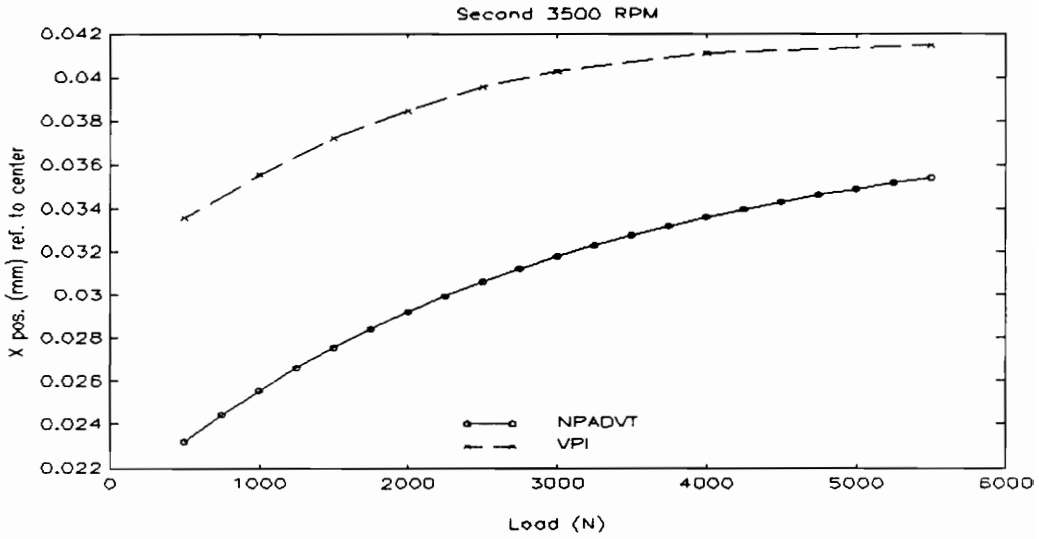

Fig. 179: 58.3 Hz Pocket X-Position Comparison (Second Test Series)

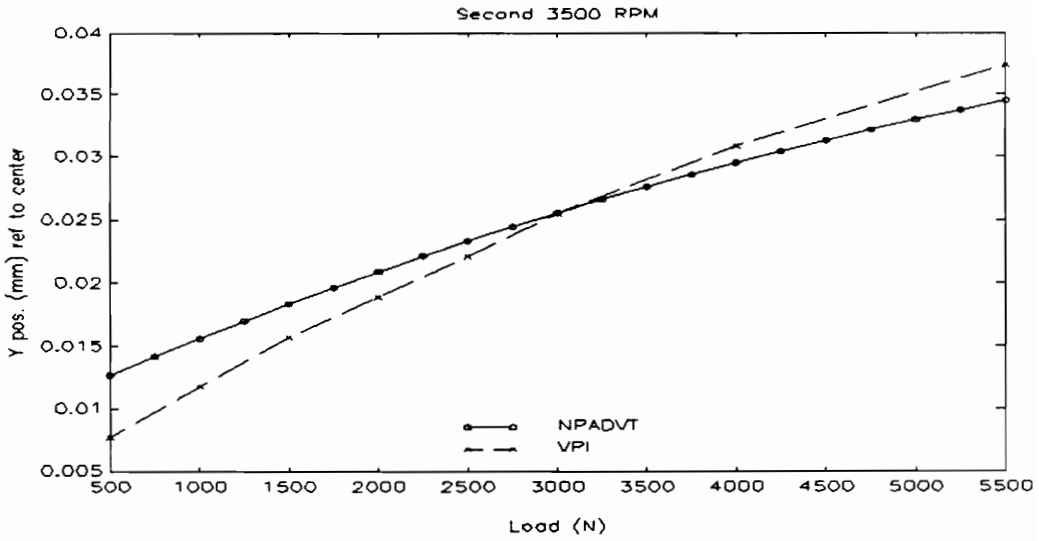

Fig. 180: 58.3 Hz Pocket Y-Position Comparison (Second Test Series)

6.4.6 Discussion of NPADVT vs. VPI for Pocket Bearing

16.7 Hz: Both of the comparisons for this speed exhibit a large x-position zero offset; the y-position zero in general looks quite good. This result tends to cast some doubt on the earlier hypothesis that the thermal effects primarily cause offsets in the y-position measurements. The x-position shaft locus also shows generally good agreement for the normalized plots, with increasing deviation as the load increases. This deviation may be, in part, caused by shaft bending and thermal effects. Interestingly though, for this bearing, the NPADVT results hint at the same slope sign reversal as the experimental data. The analytical and experimental y-position shaft locus also show a great deal of agreement, again deviating smoothly as load increases. Some portion of this disagreement may be related to shaft deflection; this point will be discussed in the conclusions to this chapter.

33.3 Hz: As with the 16.7 Hz data, the x-position zero in the actual data plot is considerably worse than the y-position zero, which shows fairly good agreement. The normalized plots also compare favorably. Again, the analytical x-positions are larger than those seen in the experimental

data, and the analytical y-positions are smaller than the experimental coordinates for larger loads (for normalized data).

58.3 Hz: The data for this speed repeat some of the trends observed earlier. The general shapes of the curves are very similar, with the analytical x-positions generally larger than experiment and the analytical y-positions generally smaller than the experimental values for large loads (in the normalized plots). The comparison of zero positions does not show as good agreement as before.

6.4.7 Comparison Between Pocket and Plain Bearing

To illustrate the alterations in shaft locus caused by the addition of a pocket to a plain bearing, Fig. 181 and Fig. 182 present, respectively, the NPADVT analytical curves and the experimental curves for 33.3 Hz. It should be noted that in both plots the plain bearing's clearance is slightly smaller than the pocket bearing's clearance. The plots are both in dimensional form. In the experimental data plot, areas for plus or minus two standard deviations about the mean, based on the last four load repetitions, are again indicated.

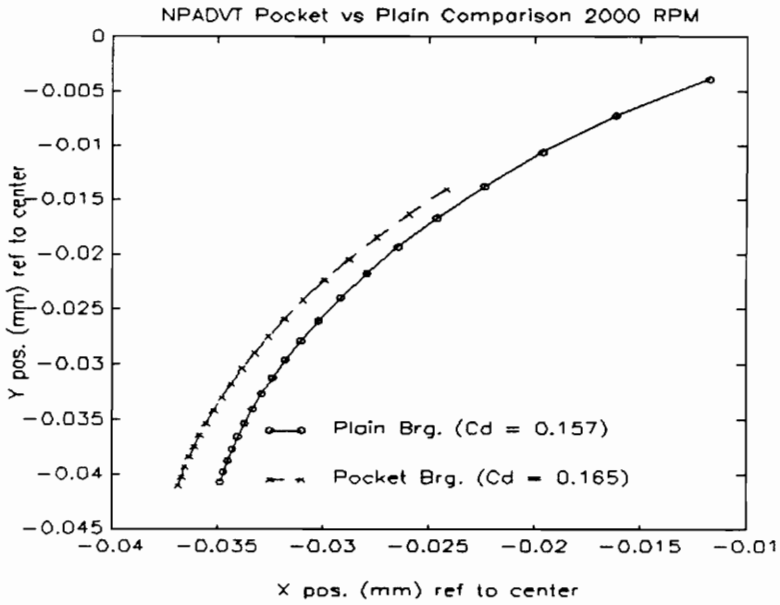

Fig. 181: Comparison Between Plain and Pocket Bearings, 33.3 Hz (NPADVT)

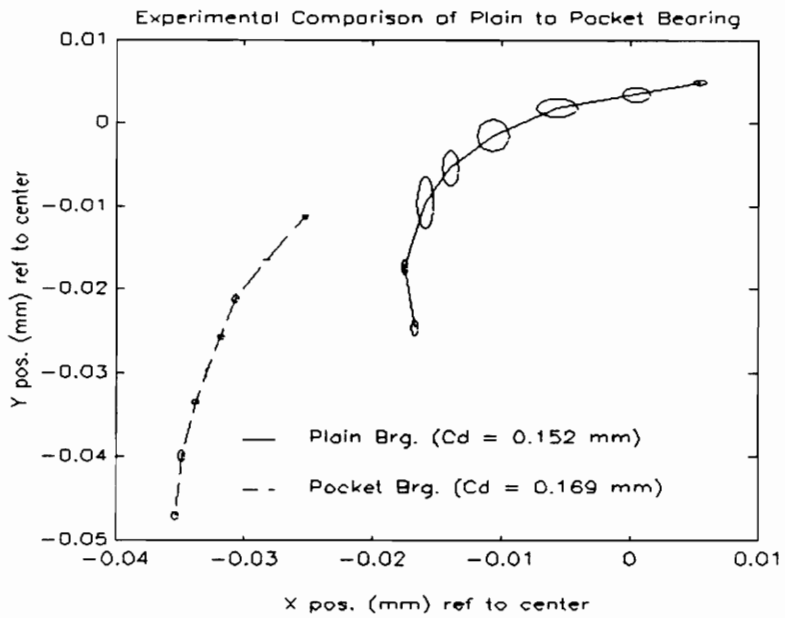

Fig. 182: Comparison Between Pocket and Plain Bearings, 33.3 Hz (Experimental)

6.4.8 Comments on Bearing Type Comparison

Although Fig. 181 and Fig. 182 present a rather different view of the changes in shaft locus caused by adding a pocket to a plain bearing, several observations can be made (the differences are probably the result of both analysis problems and experimental zero shifts). One observation is that in both cases the pocket does load the bearing down and away from the pocket (i.e., towards negative X and Y for a pocket starting at positive X and continuing counter-clockwise), as one would intuitively expect. It may also be observed that the shift causes a reduction in the magnitude of the cross-coupled stiffness (the locus curve is more nearly vertical for a given load), which would have a stabilizing effect. The final observation is that the pocket causes some reduction in load capacity/operating film thickness. The NPADVT analysis suggests that the effect on ultimate load capacity is slight, as the decrease in film thickness occurs primarily at light loads, and has less of an effect at higher loads, as one would intuitively expect. The experimental results shown a much more pronounced curve shift, although this shift may be in large part due to zero offsets and shaft deflection effects.

6.4.9 Comments and Discussion for Pocket Bearing

In general, the results for this bearing geometry show reasonably good agreement, especially with regard to slope. This agreement suggests that the stiffness values obtained from NPADVT may be reasonably useful for this bearing. Interestingly the NPADVT analysis shows a similar x-position slope sign reversal as seen in the experimental data; this similarity differs considerably from the plain bearing comparisons (the similarity is most apparent in the 16.7 Hz comparisons). Also, the differences between the NPADVT analysis and the experimental data are opposite those observed for the plain bearing (i.e., the NPADVT eccentricity is generally too small). This could be construed as suggesting that the bearing loading induced by the pocket overwhelms any thermally induced deformation effect. The comparisons between the NPADVT analysis and the experimental data also suggest that shaft slope may be causing a measurement error due to the systematic and smoothly increasing difference between the curves. This hypothesis also receives support from the observation that the difference between experimental data and the NPADVT analysis at the maximum load is of almost the same magnitude in each of the normalized comparisons. Based on these observations, an examination was made of the loading effect on the measured displacements with the shaft stationary. After obtaining the zero and clearance as in the experimental procedure, the shaft was loaded to each of

the experimental loads and the measured position was recorded. For the hypothesis of a load dependent measurement error to be correct, basic beam theory would indicate that an offset linearly dependent on applied load should be expected (assuming a constant pivot, etc.). Although a position error of the correct sign was observed and the relationship between the error and applied load was a smooth curve, it was not linear. Thus, although the measurements seem to suggest that there is a measurement error related to applied load, the exact mechanism is not simple shaft deflection, and should be examined further before a correction equation is specified. The possibility of some effect on the fluid/bearing interface as the result of shaft bending also seems likely.

Chapter 7

Conclusions and Recommendations

7.1 Conclusions for NPADVT

As seen in chapter 4, NPADVT seems to model the fluid mechanics of a fluid-film bearing in a sufficiently consistent fashion that it can be used as a yardstick for an initial evaluation of the VPI rig. In general though, the program has a number of shortcomings which need attention. NPADVT, although certainly a useful program, cannot be considered a highly accurate design tool. The program does seem to successfully capture the gross characteristics of a bearing, but misses many of the important details. Most significant is the fact that it does not do a good job of predicting the cross-coupled stiffness effect. This problem also casts doubt on the cross-coupled damping coefficients. In addition to the problems with the cross-coupled effects, other weaknesses include the lack of an option for user

spacing/placement of nodes, and the limit on the maximum number of nodes. These weaknesses are especially evident in the difficulties with successfully modeling the single groove bearing of Ref. 3. The analysis for this bearing also points out a problem in the temperature-viscosity iteration procedure, as the temperatures would sometimes start to diverge if too many temperature-viscosity iterations were employed. A final problem is that NPADVT is not very user-friendly, relying on formatted input and output files as a means of interacting with the user.

7.2 Conclusions for the VPI & SU Test Rig

From the comparisons between experimental data presented in chapters 5 and 6, it would appear that the VPI rig generally functions in a consistent manner (ignoring the zero offset problem). The data exhibit very good repeatability between repeated tests, particularly considering that in some sense the test rig is still in the early phases of debugging. The comparisons between VPI data and the NPADVT analyses show the same trends and exhibit generally the same level of, or better, agreement between NPADVT and experiment as do the comparisons in chapter 4 to the accepted published data. Thus, using as criteria both internal consistency and agreement with a calibrated external measure, it would seem reasonable to conclude that the VPI & SU test rig can be considered useable. This designation of useable carries with it the proviso that the rig still needs some work before it can be considered an operational,

precision test instrument. Suggestions for improvements and problem areas to be examined will be discussed following the recommendations regarding NPADVT.

7.3 Recommendations for NPADVT

Although the primary thrust of this work was not an evaluation of NPADVT, an appreciable amount of effort was expended in evaluating the program for use as a measure of the VPI rig's performance. Thus, the background for several recommendations concerning the program's analysis has been presented. Since the primary motivation for having an analytical analysis of fluid-film bearings is the need for dynamic bearing coefficients for use in a rotor dynamic analysis, the problems with the cross-coupled term(s) seen in almost all of the comparisons are in the greatest need of attention. The problem does not seem to be entirely related to the simple thermal model in NPADVT; some of the other assumptions may need to be questioned. The fact that the comparisons between analytical data and experimental data in Ref. 18, which uses essentially the same assumptions as NPADVT but a more complex thermal model, shows the same sort of disagreement with regards to the cross-coupled effect supports the hypothesis that there is some important factor being ignored in the analysis. One assumption that does not seem to have been examined at great length in the literature is the assumption of no significant mechanical deformation as the result of the film temperature gradients. There is a significant

temperature rise through the region of minimum film thickness; it would not seem too unreasonable to suppose that this gradient could give rise to sufficient mechanical deformation to alter the characteristics of the bearing. Although such deformation is generally dismissed as negligibly small, the combination of a thin film and the likelihood of very high bearing sensitivity to geometry changes in this region could contradict this assumption. One of the few works that addresses the issue, Ref. 20, presents analytical results which show changes in the static operating locus similar to those observed in the comparisons of Chapters 4-6. Preliminary work to quantify this effect is also currently underway at VPI & SU, and should be continued. The results of this investigation should also be coupled to an NPADVT analysis. Depending on the results of this work, some simple thermally induced mechanical deformation model may need to be incorporated into NPADVT.

Although there is some analysis (Ref. 18) which suggests that the simple NPADVT global energy balance is adequate, it would be useful to update NPADVT to include local film-temperature and viscosity variations. This local modelling would also be required if the results of the thermally induced deformation study show that there is a significant effect. It might also be fruitful to investigate the possible time savings resulting from going from the current two-layer solution approach of

1) approximate (closed form) solution,

2) full 2-D solution,

to a three level approach of:

1) approximate (closed form) solution

2) 1-D circumferential solution (assume an axial pressure profile as in Ref. 14),

3) full 2-D solution.

The logic behind this approach would be that the majority of the time is used in developing a good estimate of the shaft position, and a 1-D circumferential solution would be considerably faster in developing a good estimate. The estimate could then be refined by a more exact 2-D solution. It might also be helpful to include a better treatment of the cavitated region of the bearing. Finally, some effort to increase user friendliness and eliminate the occasional convergence problems with the temperature-viscosity iteration step would be helpful.

7.4 Recommendations for Test Rig

The recommendations for test rig upgrades/improvements and detailed study can be broken down into several general items:

1) Thermal Growth Effects

2) Other Misalignment Effects

3) Data Acquisition

4) Oil System

5) Speed Control and Miscellaneous Instrumentation

6) Rig Mechanical

7) Miscellaneous

Each of these items will be discussed separately below.

7.4.1 Thermal Growth Effects

The test rig seems to have some significant problems with thermal growth of components. Not only does the bearing bush itself measurably change diameter from warmed-up (i.e., at the oil inlet temperature) to operating conditions, but more significantly, the bearing housing itself experiences a large (relative to the magnitude of clearance and measurement accuracy) dimensional change between ambient and operating temperature. There is also some variation in housing dimensions which is correlated with operating load and speed. Since the rear support bearing does not mirror these changes, this growth causes misalignment problems. The misalignment effect alone is not too difficult to control; the rear support bearing could be readily mounted on a pair of (large) lead-screws to enable it to be moved to accommodate some misalignment. The problem is one of measurement. Unfortunately, it is difficult to imagine a means of measuring the actual operating bearing dimensional changes short of installing displacement probes in the test rig shaft. Although shaft

mounted probes have been employed (for examples, Ref. 18 or Ref. 30), the speed range (up to 500+ Hz) of the VPI rig would cause problems from a materials standpoint (centrifugal loading is extremely high at these elevated speeds), as well as problems with passing the signal from the shaft (this speed range seems likely to cause problems for slip-rings). The fact that the shaft would need to be bored to bring the signal leads to the turbine end where slip rings could be mounted is also a complicating factor. One simpler proposal for measuring the effects of the thermal growth is to monitor the center-line height of both bearing housings relative to the rig base and adjust the rear bearing housing height to match the thermal growth of the test bearing housing. This approach would only work for vertical growth, but this is probably the major housing growth effect. This approach will not help in reducing the effect of bearing diametral growth, but perhaps a means of rapidly stopping the rig and rapidly measuring the clearance can be devised. If taken rapidly enough, this measurement should reflect the actual operating geometry.

Another approach to controlling misalignment effects is to mount a pair of pressure transducers in the bearing, equidistant from the bearing centerline, and adjust the rear shaft position until the indicated pressures are equal. This approach has the advantage that shaft slope through the bearing caused by loading can also be reduced or eliminated. If two sets of transducers are mounted with sufficient angular separation,

this approach should work for misalignment in both X and Y directions. This approach, however, will only work for midplane symmetric bearings and requires the installation of two to four pressure transducers. Although this approach seems to be a very good solution to the misalignment problem, more study is warranted. The installation of two more displacement probes at the bearing outer measurement location would also be helpful, since dual probes would allow some of the effect of the housing growth on the measurement to be cancelled out. It is also possible that some form of active temperature control of the bearing housing could be of help in reducing the amount of thermal growth correlated with different load and speed conditions.

7.4.2 Other Misalignment Effects

In addition to the thermally induced misalignment, the applied shaft load introduces measurable shaft bow, which effectively causes some degree of misalignment at the bearing. Measuring this misalignment is not as great a problem as measuring thermal growth effects, since a reference shaft slope can be obtained at low load with the shaft stationary and the loading induced slope can be measured relative to this reference (this is presently done). Since this measurement is fairly easy to obtain, the larger problem is to remove the misalignment. Manually moving the rear bearing carrier is not a good option due to the mounting method, nor does moving the main bearing

housing seem to be a good idea. The most workable solution is, as suggested above, the installation of a pair of lead-screws which can be remotely operated (probably large studs with slightly different thread pitch on each end). If these lead-screws are of large diameter (for high stiffness) and the pitch of the threads at the ends is close (for fine adjustment), this approach would seem to be likely to work well. The possibility of an improved method of obtaining the initial alignment also needs to be investigated.

7.4.3 Data Acquisition

Although the current combination of stand-alone and PC-based instrumentation has proved workable for the static testing conducted to this point, it will be extremely difficult, if not impossible, to adapt it to dynamic coefficient identification. The combination of a slow integrator for measuring the average shaft position coupled with a separate 8-bit dynamic waveform measurement will not work very well for this purpose. Even with static testing, there are some recurrent problems. These problems include occasional communication glitches related to the fact that the stand-alone instrument is not designed for complete computer control. The instrument also has not proved to be an extremely reliable piece of equipment. The data transfer rate from this instrument is also too slow for real time display. It is also difficult to expand beyond the current 8 channel data acquisition capability. It seems most likely

that some combination of plug-in PC based instrumentation will be best suited to future and present needs, although the possibility of IEEE 488 or other external instrumentation should not be ruled out entirely. The future instrumentation needs and specifications need to be developed and the hardware upgraded. A portion of this upgrade will necessarily include a major software rewrite, which should be aimed at maintaining as general-purpose a test environment as possible, with a reliable, user-friendly interface.

Another data-acquisition problem that needs to be addressed is zero drift. The problems with regard to the displacement measurements has been discussed previously. The load measurement system also exhibits this problem. The effect is most strongly seen in the up load cell, where the zero commonly shifts some 10 to 30 N over the course of a day of testing. This problem is not entirely the signal conditioning, as similar drift is seen with a separate digital readout. It also is unlikely that this drift is completely caused by sensor temperature sensitivity. The drift mechanism needs to be identified and eliminated. The torque sensor, likewise, has a problem maintaining a zero setting, but this may largely be a result of shifts in the structure holding the air inlet to the air turbine. Zero drift in the temperature input board needs to be addressed as well.

Another instrumentation problem is the lack of expansion capability. As mentioned above, it would be helpful to add two more displacement probes to the outer measurement location of the test bearing. With current instrumentation, this addition would require eliminating the rear bearing measurements. Also, for dynamic measurements, it will be necessary to simultaneously sample both load and displacement measurements; this need will greatly increase the number of required data input channels. The ability to obtain data in real time would also be required for controlled excitation. It could also be helpful to have the option of adding load measurement to the rear support bearing and/or to the test bearing. A redundant load measurement obtained by measuring the magnet field strength could also have several advantages.

The final instrumentation issue concerns load cell calibration. Currently the load cells can only be calibrated in place via shunt calibration. It would be reassuring to develop some means of providing dead-weight calibration for the load measurement (even if this is not possible in-place, the availability of a method of providing a precise dead-weight calibration up to about 7000 N would be helpful).

7.4.4 Oil System

The rig oil system currently has two major shortcomings: the temperature regulation is not always as precise as desired, and the methods currently employed to eliminate entrained air only work at very low flow rates. The control problem is mainly related to the imbalance between the large oil cooler capacity and the small oil heating capacity. This imbalance manifests itself when the temperature goes far below the nominal setting by causing the recovery period to be extremely long. The proposed solutions are a combination of:

1) further reductions in cooler capacity (this will most likely entail a new, smaller cooler, as the current shell and tube cooler has already been reduced to a fraction of its capacity by eliminating half of the passes and blocking about half of the remaining tubes) and moving the cooler closer to the bearing oil inlet to reduce the time lag between the cooler and the controller sensor, and
2) adding more heater wattage.

If applied correctly, increased heater wattage could also aid in the removal of entrained air by heating the drain oil, thereby reducing its viscosity, thus allowing air bubbles to rise to the surface and release the air more rapidly. To improve the entrained air removal rate, the size of the settling pan and/or the drain piping should

be increased to increase the exposed oil surface area. Other options may also need to be explored.

7.4.5 Speed Control

Although the speed controller functioned adequately during the testing, it is far from being operable by an arbitrary user. There are two basic problems. The first is a problem with one or both of the software and/or signal conditioning which causes the controller to occasionally lose track of the speed signal. This signal loss causes the control valves to either both temporarily close (the recovery from this upset is usually graceful), or to both go wide open (this usually is not so graceful; generally the rig rapidly accelerates until the secondary controller closes the shut-down valve). This problem needs to be remedied. It would also be beneficial if the fix includes a redundant speed pick-up; if the current speed signal is lost due to sensor failure or cabling problem, the control valves would both go wide open, but the secondary controller would never provide the redundant shut-down capability. Most likely, the bearing and/or rig would be damaged. This upgrade is currently being pursued, and the hardware is on hand.

The second problem with the speed control system is that the small control valve is too big for the degree of control precision required. This problem, in turn, requires that the controller output changes be very small. These small control magnitudes make the controller unnecessarily sensitive to control parameters, which must be tweaked for different operating speeds to obtain the degree of speed control desired. The ideal fix would be to replace this air-to-close (i.e., the value is fully open when no control air pressure is applied) valve with a smaller air-to-open valve, thus improving control as well as gaining a better failure mode. The alternative is to fit the current valve with a reduced seat and valve stem. It would also be helpful to characterize the non-linear transfer function between the magnitude of the control valve control signal and the turbine output torque. An experimental determination of this transfer function would not be too difficult for the case of a locked rotor. The extension to running conditions could be made through use of the turbine operating curves.

Hardware on hand to allow the PC used for turbine control to also perform temperature monitoring for the two turbine bearings and the rig rear support bearings needs to be completed and installed. With this hardware, automatic monitoring of the bearing temperatures will enable automatic shutdown to be provided for abnormal temperatures. This hardware installation will ultimately include both warning as well

as trip settings. This monitoring capability also includes other rig temperatures, oil level switches and the minimum oil pressure switch. Air compressor remote condition monitoring could also be added (instrumentation would need to be added to the compressor). Compressor condition monitoring would be fairly inexpensive, but extremely beneficial.

7.4.6 Miscellaneous Instrumentation Upgrades

The current load cells have measurement uncertainties that could be improved upon, especially with regards to hysteresis. New, lower capacity load cells will also certainly be desired for dynamic load measurements of the magnitudes under consideration (typically 10 to 20 percent of the current load capability). The ability to provide an auxiliary load measurement through use of a magnetic field strength sensor could also be advantageous. This measurement would not be affected by inertial effects and could allow the magnitude of residual magnetism (and the resulting residual load) to be quantified. For dynamic coefficient extraction, load measurement at the test bearing will almost certainly be required. To eliminate inertial effects, the test bearing acceleration would also need to be measured if load cells are installed at this location. To reduce the problem of mass uncertainty in the inertial correction, it would be desirable to develop a load measurement system that would allow the mass of oil in the bearing to be ascertained. Any load measurement device at the test

bearing must also be extremely stiff, so as not to unduly affect the dynamic behavior of the test rig.

Another useful instrumentation addition, albeit a very difficult addition, would be shaft based instrumentation at the test bearing location. The problems discussed previously make the successful installation of such instrumentation unlikely. Finally, it could be helpful to have an accurate measurement of the bearing torque. This measurement could be useful in comparisons to analyses. The most obvious method of implementation is to mount the test bearing in a second, low friction bearing and measure torque by measuring the restraining force required to hold the assembly in place. The implementation of this approach could, however, be far more difficult than the benefits would justify.

7.4.7 Rig Mechanical

There are two primary mechanical problems with the test rig: the shaft run-out associated with the sleeve installation and the housing thermal growth. The thermal growth issue has been discussed previously and will not be discussed further. With regard to the sleeve run-out issue, although the use of shaft sleeves is appealing from the viewpoint of test rig flexibility, it is difficult, if not impossible, to reliably install a sleeve and maintain concentricity and parallelism on the order of 0.003 mm. The

best solution is to procure solid shafts of selected diameters. As most of the anticipated experimental work would be with U.S. standard dimensioned bearings, typical diameters of 4" and 2" would be good initial sizes. The current shaft could be modified to one of these diameters; a second solid shaft would have to be fabricated from scratch. Alternately, the current shaft could be retained as a backup, and two or more new shafts fabricated. The change to a solid shaft would require some modification of the current seal arrangement at the test bearing location, but this should not be too costly. This change is one of the priorities indicated below.

Some examination should also be made of the possibility of replacing the current duplex ball rear support bearing with a high pressure hydrostatic bearing. Although a certain amount of expense would be involved, it would be partially offset by eliminating the requirement to purchase a new set of bearings for new shafts. The hydrostatic bearing would offer several other advantages: very long life, possibly increased stiffness, increased damping, and potentially smoother operation (the current duplex ball bearing exhibits rather wild looking run-out, which could increase the noise level at the test bearing for dynamic measurements). The change to hydrostatic operation could also include a high capacity thrust bearing. Thrust capacity would become important for testing bearings such as the end fed damper seal (bearing) under consideration for use in a Space-Shuttle main engine turbopump, or the possibility of

seal testing with the loading magnets operating as a magnetic bearing in addition to a forcing input. This type of testing would most likely involve high pressure fluid creating a large thrust load on the end of the shaft at the test bearing end. Conventional bearings that can react high thrust loads at speeds of 500 Hz are quite expensive. A possible drawback to the hydrostatic bearing(s) would be a potential increase in the required drive power.

Finally, either the current right loading magnet needs to be mounted, or magnets optimized for dynamic loading need to be fabricated and installed. Either addition would allow arbitrary axis loading. One benefit of arbitrary loading is that the clearance could be determined for the entire bearing by loading at a number of angles. The ability to provide arbitrary loading could also be helpful in bearing evaluation.

7.4.8 Miscellaneous Recommendations

A number of other needs and items to investigate have become apparent over the last 8 months of rig operation. These items will be listed below in no particular order.

> Air compressor spares should be obtained. The source could include new parts, as well as acquisition of entire compressors to junk for usable parts, or parts that can be reconditioned. A spare air compressor would be an unlikely but even better option.

> Air turbine capacity reduction should be examined in detail. The current turbine power output far exceeds requirements. A removable reduction in the number of turbine nozzles could provide a useful level of rig capability, while reducing the drive air requirements. It would be helpful to be able to operate at reasonable speed and load from the shop air system. Such operation is not presently possible, but the turbine curves suggest this operation would be possible with a reduction in the number of nozzles. This same investigation would also point the way towards increasing drive power should this ever become needed (more air compressor capacity would be required).

> Although the muffler currently on the turbine exhaust provides a phenomenal degree of noise control, the noise is still objectionable for long periods of exposure and/or high speeds and loads. It would be desirable to construct a sound box around the muffler and the control valves (which also generate a surprising amount of noise). This project

could also be coupled with ducting to exhaust the drive air to the outside of the building.

> The loading control system needs to be upgraded; the current algorithm is slow and not very sophisticated. Better alternatives can be easily developed.

> Work needs to be done on the automation software to provide greater flexibility in testing and to allow other users to operate the test rig. These upgrades also tie in with the upgrades in condition monitoring. The ability to accommodate pressure probes also needs to be added to the data acquisition system.

> A knowledgeable lab technician would be very helpful. Not only could a good technician take over some of the physical upkeep of the rig, but such a person would also provide a greater degree of continuity between successive graduate students working with the test rig. Admittedly, such a person is difficult to find and retain.

7.4.9 Priorities

Since an array of possible rig improvements and items to examine has been presented in this chapter, this concluding section will present a prioritized list of some these

items based on cost, time, and potential future requirements. The items will be grouped as: Immediate, 1 Year, Long Term.

Table XII - Immediate Rig Improvement/Study Items

Immediate Items		
Item	Est. Cost	Est. Time
Solid Shaft/Hydrostatic Brg. Study and Acquisition	$2k - $5k	weeks to months (acquisition)
Find and Reduce Zero Drifts	Low	weeks
Add Pressure Probe Ability	$300 + Probes	days
Thermal Growth Study/Control	Unknown	days to weeks
Improve Temperature Control	Low + possible new cooler	days
Improve Speed Control	Low	days to weeks
Study Air Turbine Capacity Reduction	Unknown	days
Examine Alignment Methods	Low	days

Table XIII - 1 Year Rig Improvement/Study Items

1 Year Items		
Item	Est. Cost	Est. Time
Rear Bearing Running Adjustments	<$2k	weeks
Entrained Air Removal	low	days to weeks
Improve Speed Control	low	days to weeks
Large Thrust Capacity	$1k to <$10k	weeks to months
Thermal Growth Control	?	days to months
Shaft Deflection Control	?	days to months
Dynamic Measurements	??	days to months
Calibration Upgrades	<$1k	days to weeks
Instrument Compressor	<$500	days
Noise Control	<$200	days
Software Improvements	low	months
Air Compressor Spares	?	months
Instrumentation Upgrades	$1k to ?	months

Table XIV - Long Term Rig Improvement/Study Items

Long Term		
Item	Est. Cost	Est. Time
Dynamic Measurements	?	months
Instrumentation Upgrades	?	months
Torque Measurement	?	months
Software Improvements	low	months
Calibration Improvements	?	weeks
Air Compressor Spares	?	months

References

1. Allaire, P.E., Nicholas, J.C., Gunter, E.J., "Systems of Finite Elements for Finite Bearings." J. of Lubr. Tech., Trans ASME. **98,** 2, pp 187-197, 1977

2. Allan, T., "The Application of Finite Element Analysis to Hydrodynamic and Externally Pressurized Pocket Bearings." Wear. **19**, pp 169-206, 1972

3. Andrisano, A.O., "An Experimental Investigation on the Rotating Journal Surface Temperature Distribution in a Full Circular Bearing." J. of Tribology, **110**, pp 638-645, 1988

4. Booker, J.F., Huebner, K.H., "Application of Finite Element Methods to Lubrication: An Engineering Approach." J. of Lubrication TechTechnology **24**, 4, pp 313-323, 1972

5. Branagan, L.A., "Thermal Analysis of Fixed and Tilting Pad Journal Bearings Including Cross-Film Viscosity Variations and Deformations." PhD Dissertation, University of Virginia, Charlottesville, VA, 1988

6. Brockwell, "Measurements of Steady-State Operating Characteristics of a 5-Shoe Tilting Pad Journal Bearing." Tribology Transactions, **32**, pp 267-275, 1989

7. Coleman, H.W., Steele, W.G., Experimentation and Uncertainty Analysis for Engineers, Wiley-Interscience, 1989

8. DeChoudbury, P., "A Comparison of Film Temperatures and Oil Discharge Temperatures for Tilting Pad Journal Bearings." J. of Lubrication Technology, **103**, pp 115-119, 1981

9. Ferron, J., Frene, J., "A Study of Thermo-Hydrodynamic Performance of a Plain Journal Bearing, Comparison Between Theory and Experiement." J. of Lubrication Technology, **105**, pp 422-428, 1983

10. Flack, R.D., Allaire, P., "An Experimental and Theoretical Examination of the Static Characteristics of 3-Lobe Bearings." ASLE Trans., **25**, pp 88-94, 1982

11. Heller, S., "Static and Dynamic Performance of Externally Pressurized Fluid Film Journal Bearings in the Turbulent Regime." J. of Lubrication Technology, **96**, pp 381-390, 1974

12. Hinton, "Characteristics of a Statically Loaded Journal Bearing with Superlaminar Flow." J. of Mechanical Engineering Science, **22**, pp 79-94, 1980

13. Kirk, R.G., Input Instructions for Multi-Pad Fixed Bore Fluid Film Bearing Analysis ----NPADVT----. VPI&SU Rotor Dynamics Lab Manual, January (1990)

14. Knight, J.D., Barrett, L.E., Cornan, R.D., "The Effects of Supply Pressure on the Operating Characteristics of Two-Axial Groove Journal Bearings." ASLE Trans. **28**, pp 336-342, 1985

15. Leader, M.E., "Experimental Study of 3 Journal Bearings with a Flexible Rotor." ASLE Trans., **23**, pp 363-369, 1980

16. Orcutt, F., Arwas, "The Steady State and Dynamic Characteristics of the Full Circular Bearing and a Partial Bearing in the Laminar and Turbulent Regimes." J. of Lubrication Technology, **89**, pp 143-153, 1967

17. Lund, J., "Evaluation of Stiffness and Damping Coefficients for Fluid Film Bearings." Shock and Vibration Digest, **11**, 1, pp 5-10, 1979

18. Lund, J., Tonnesen, J., "An Approximate Analysis of the Temperature Conditions in a Journal Bearing. Part II: Application." J. of Tribology, **106**, pp 237-245, 1984

19. Lund, J.W., Sternlicht, B., "Rotor-Bearing Dynamics with Emphasis on Attenuation." ASME J. of Basic Engr **84**, pp 491-495, 1962

20. Morton, P.G., Keogh, P.S., "Thermoelastic Influences in Journal Bearing Lubrication." Trans. of the Royal Society of London **403**, pp 111-134, 1986

21. Murphy, B.T., et. al., "The Rocketdyne Multifunction Tester." The 6th Workshop on Rotordynamic Instability Problems in High-Performance Turbomachinery, May, 1990, Texas A&M, pp 347-374

22. Nicholas, J.C., "A Finite Element Dynamic Analysis of Pressure Dam and Tilting Pad Bearings." PhD Dissertation, University of Virginia, Charlottesville, VA, 1977

23. Nicholas, J.C. and Kirk, R.G., "Theory and Application of Multipocket Bearings for Optimum Turborotor Stability." ASLE Transactions, **24**, pp 269 - 275, 1981

24. Pinkus, M., Sternlicht, B., Theory of Hydrodynamic Lubrication, McGraw-Hill, New York, 1961

25. Rao, J.S., Rotor Dynamics, Wiley Eastern Limited, New Delhi, India, 1991

26. Read, "Temperature, Pressure and Film Thickness Measurement for Offset Half Bearing." Wear, **117**, pp 197-212, 1987

27. Reinhardt, E., Lund, J., "The Influence of Fluid Inertia on the Dynamic Properties of Journal Bearings.", J. of Lubrication Technology, **97**, pp 159-167, 1975

28. Reynolds, O., "On the Theory of Lubrication and its Application to Mr. Beauchamp Tower's Experiments, Including an Experimental Determination of the Viscosity of Olive Oil." Phil. Trans. Royal Soc. London, **177**, Part I, 1886

29. Someya, T., ed., Journal-Bearing Databook, Springer-Verlag, New York, 1988

30. Tonnesen, J., Hansen, P.K., "Some Experiments on the Steady State Characteristics of a Cylindrical Fluid-Film Bearing Considering Thermal Effects." J. of Lubrication Technology, **103**, pp 107-114, 1981

31. Tripp, H., Murphy, B.T., "Eccentricity Measurements on a Tilting Pad Bearing." STLE Trans. **28**, pp 217-224, 1985

32. Vance, J.H., Rotordynamics of Turbumachinery, Wiley, New York, 1988

Appendix A

Shaft Deflection Data

To quantify the shaft deflection due to load, the shaft was loaded down with 5800 N load at the magnet, and the displacement recorded at nine different locations. The procedure used is as follows:

1) Zero dial indicator at desired shaft location with no load applied
2) Apply load and note new dial indicator reading
3) Move to next shaft location

To check for the possibility of hysteretic effects, several locations were measured more than once. The repeated measurements exhibited good agreement with the initial measurements, suggesting the readings are reasonably accurate.

The measurement locations are shown graphically below in Fig. 183, the measured displacements and location relative to location "A" are shown in Table XV. The measurements reported are corrected for vertical displacement of the bearings. The measurements at H and I should be considered to be essentially zero, given the 0.003

mm divisions on the dial indicator used. The author would like to acknowledge the help of Mr. John Eddie in obtaining these measurements.

Appendix A - Shaft Deflection Data

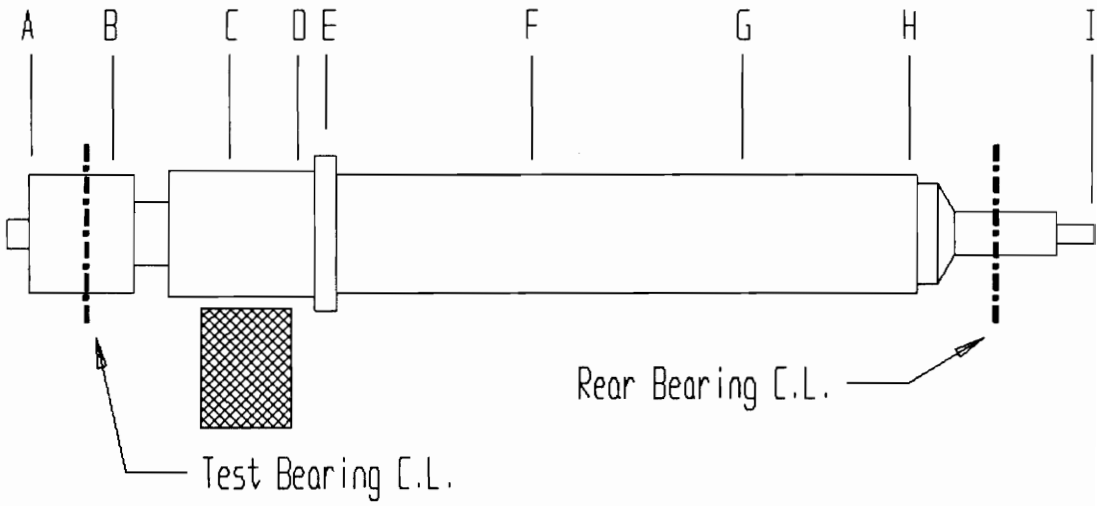

Fig. 183: Shaft Deflection Measurement Locations

Table XV - Shaft Deflections

Location	Distance From A (mm)	Deflection (mm)
A	0	0
B	70	-0.043
C	168	-0.082
D	225	-0.095
E	249	-0.087
F	405	-0.073
G	572	-0.028
H	722	0.008
I	876	-0.005

Appendix A - Shaft Deflection Data

Appendix B

Notes on Statistics

This appendix contains several items related to the statistical calculations employed in this work. The first is a sketch showing the development of the two standard deviation areas indicated on several of the plots of experimental data. The second is the Minitab analysis of variance output referred to in chapter 5. Finally, several sample uncertainty calculations from chapter 4 are provided to assist the reader in following the uncertainty discussion.

B.1 Confidence Areas

In Fig. 184, a typical set of four data points and the resulting two standard deviation area are shown. This confidence area is developed as follows:

1) Find the center of the group of points by computing the average x-coordinate and average y-coordinate of the group. The X and Y computed determine the center location of the confidence area

2) Compute the sample standard deviation, σ_x, of the x-coordinates. The x-axis (b) of the elliptical confidence area corresponds to $\pm$ 2 x σ_x , that is, b = 2 x (2 x σ_x)

3) Likewise, compute the standard deviation of the y-coordinates. The y-axis (a) of the elliptical confidence area corresponds to 2 x (2 x σ_y).

4) Draw an ellipse around the center location with x-axis and y-axis defined as above.

Note that $\pm$ 2 standard deviations about the mean of four data points is somewhat different from the 95% confidence interval. The appropriate limits for a 95% confidence interval for four points (using a Student's t distribution for n-1 = 3 degrees of freedom) would be $\pm$ 3.182 standard deviations about the mean. Thus, comparing data sets for the intersection of $\pm$ 2 standard deviation areas is, in fact, a stronger test than a t-test with a 95% confidence level.

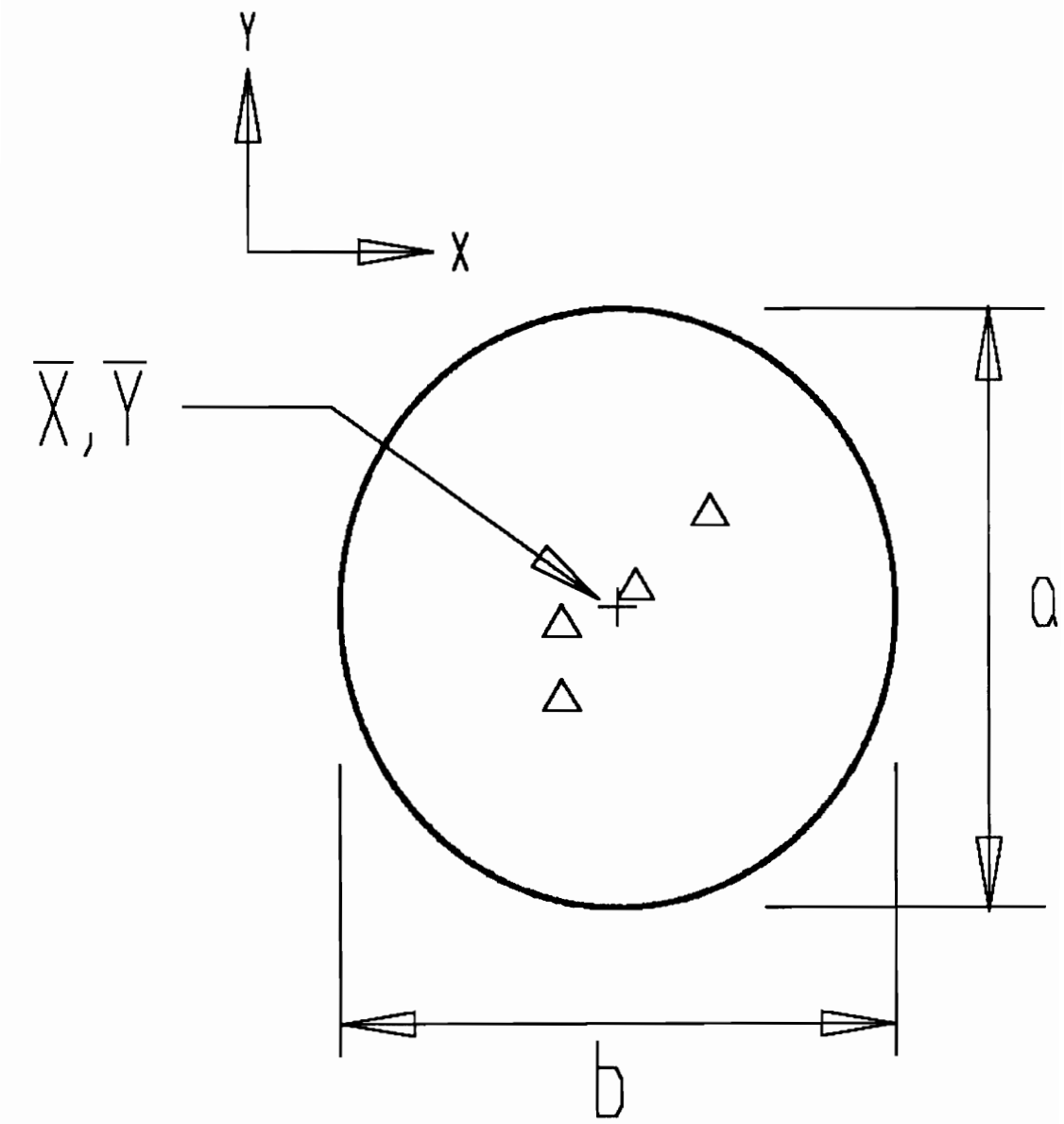

Fig. 184: Two Standard Deviation Area

B.2 Analysis of Variance Output

An analysis of variance (ANOVA) procedure was used in chapter 5 to examine the scatter (the difference between a data point and the mean for that load-speed-test combination) of the data from all of the tests with the original two-axial groove bearing for effects from load, speed, measurement axis and repetition. A total of 640 data points are in this aggregate data set. Annotated output from MINITAB is presented below for reference.

Scatter Statistics

	N	MEAN	MEDIAN	TRMEAN	STDEV	SEMEAN
data	640	-0.00003	-0.00005	-0.00008	0.00081	0.00003

	MIN	MAX	Q1	Q3
data	-0.00254	0.00508	-0.00041	0.00020

Note: All data multiplied by 1000 for further calculations

"Scatter Plot" of Data

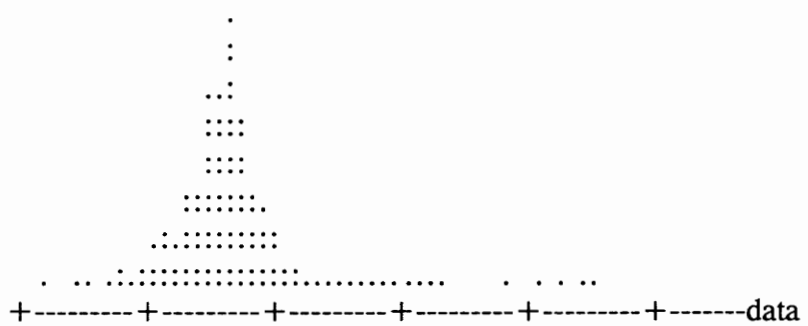

-3.0 -1.5 0.0 1.5 3.0 4.5

ANOVA Output

MTB > anova data = run|load|speed(run)|daxis(speed run)

Factor	Type	Levels	Values
run	fixed	2	1 2
load	fixed	8	1 2 3 4 5 6 7 8
speed(run)	fixed	4	1 2 3 4
daxis(run speed)	fixed	2	1 2

Analysis of Variance for data

Source	DF	SS	MS	F	P
run	1	0.5226	0.5226	0.64	0.420
load	7	0.0000	0.0000	0.00	1.000
speed(run)	6	3.1355	0.5226	0.65	0.689
daxis(run speed)	8	4.1806	0.5226	0.65	0.734
run*load	7	0.0000	0.0000	0.00	1.000
load*speed(run)	42	0.0000	0.0000	0.00	1.000
load*daxis(run speed)	56	0.0000	0.0000	0.00	1.000
Error	512	410.7863	0.8023		
Total	639	418.6250			

B.3 Sample Uncertainty Calculations

In chapter 4, a number of calculations are made in developing the uncertainty estimates. To help the reader in following these calculations, several sample calculations are included below.

B.3.1Sample Calculation #1 - Bearing Centerline Estimation

The first calculation in chapter 4 is the uncertainty in the estimation of the bearing centerline position from measurements on either side of the bearing. This uncertainty estimation uses the data reduction equation (8) from Chapter 4, repeated below for reference.

$$B_2 = \frac{P_1(Ref\backslash MProbe - Ref\backslash MBrg) + P_2(Ref\backslash MBrg - Ref\backslash IProbe)}{(Ref\backslash MProbe - Ref\backslash IProbe)} \qquad (8)$$

According to the approach of Ref. 7, the first step in evaluating the uncertainty is to compute the partials of the quantity (B_2 in this case) with respect to each item in the equation. This sample calculation will follow through the calculation due the to influence of the uncertainty in probe P_1.

1) Determine the partial with respect to P_1:

$$\frac{\partial B_2}{\partial P_1} = \frac{(Ref\backslash MProbe - Ref\backslash MBrg)}{(Ref\backslash MProbe - Ref\backslash IProbe)} \tag{12}$$

2) Substitute in nominal dimensions from chapter 4:

$$\frac{\partial B_2}{\partial P_1} = \frac{0 - 36.8}{0 - 67.6} = 0.5451 \tag{13}$$

3) Compute contribution to total uncertainty (substituting uncertainty data from chapter 4) to use in Eq. (7) as :

$$\frac{\partial B_2}{\partial P_1} U_{P1} = 0.5451 \times 0.0025 = 0.00138 \tag{14}$$

This number corresponds to the first entry in Table V, and is a random error. The remaining entries are computed in a similar fashion, as are the load uncertainties.

B.3.2 Sample Calculation #2 - Estimation of Number of Samples

At the end of the zeroth order uncertainty analysis for displacement in chapter 4, it is pointed out that the expected impact of repeated sampling on the uncertainty of the data can be computed. Although the text hints at the approach employed, a more complete discussion follows.

As noted in chapter 4, the RSS random error is expected to be $\pm 1.50 \times 10^{-3}$ mm for 95% certainty (i.e., one can be 95% certain that the true measurement lies within this interval if only random error sources are considered). Since 95% certainty corresponds to $\pm$ 1.96 standard deviations about the mean (for samples large enough to have a normal distribution), the expected standard deviation of a large data set is thus

$$\frac{1.50\times10^{-3}mm}{1.96} = 7.65\times10^{-4}\ mm$$

It can be shown that if multiple data points are averaged, the standard deviation of the data will decrease by approximately the square root of the number of samples averaged. Thus, the effect of averaging data is known. In addition, since small samples are involved, it is more appropriate to use the Student's t distribution for obtaining intervals as a function of the adjusted standard deviation. For example, if 10 samples are averaged, the calculations proceed as follows:

1) Find the interval for 95% coverage from a Student's t distribution. This interval corresponds to the area for 10-1 = 9 degrees of freedom, and 2.5% of the area in each tail. This number is $\pm$ 2.262. Denote this number by t(9, .025).

2) Find the adjusted standard deviation.

$$\frac{\sigma}{\sqrt{n}} = \frac{7.65\times10^{-4}mm}{\sqrt{10}} = 2.42\times10^{-4}mm$$

3) Compute the new interval.

$$t(9,0.025)\times\frac{\sigma}{\sqrt{n}} = \pm2.262\times(2.42\times10^{-4}mm) = \pm5.47\times10^{-4}mm$$

A similar procedure yields the remainder of the multiple averaged sample uncertainties shown in Chapter 4.

Vita

Erik Swanson was born January 1, 1967 in Newport-News, Virginia. Upon graduation from Bruton High School in York County, he entered Virginia Polytechnic Institute and State University, and spent five years as undergraduate, alternating semesters (or quarters) of school and co-operative education work experience at the Hopewell, Va. papermill owned by Stone Container. He graduated Magna Cum Laude with a Bachelor of Science Degree in Mechanical Engineering on May 5, 1990. After a considerable amount of development work with the VPI & SU Rotor Dynamics Lab's Fluid-Film Bearing Test Rig, he defended his Master's thesis on March 31, 1992. Erik plans to continue at VPI & SU, with the eventual goal of a doctoral degree in mechanical engineering.

Erik was a NASA Gradute Student Research Fellow throughout his tenure as a masters student and is a member of Tau Beta Pi, Pi Tau Sigma, and Sigma Xi Research Society.